Report No.
UCB/SEMM-2025/03

Structural Engineering
Mechanics and Materials

One-Way Shear Strength of Large Beams and Foundation Elements Containing High-Strength Longitudinal Reinforcement

By

Jerry Y. Zhai[1] and Jack. P. Moehle[2]

[1]Department of Civil and Environmental Engineering
University of California Berkeley

[2]Department of Civil and Environmental Engineering
University of California Berkeley

May 2025

Department of Civil and Environmental Engineering
University of California, Berkeley

ABSTRACT

Mat foundations for high-rise buildings have traditionally been constructed as relatively thick members without shear reinforcement and with relatively low longitudinal reinforcement ratio. Laboratory tests demonstrate that unit shear strength decreases with increasing depth and with decreasing longitudinal reinforcement. These effects are represented in the one-way shear strength design equations of ACI 318-19, which results in significantly reduced nominal strength compared with design strengths that were successfully used for foundation mats for decades. The introduction of high-strength longitudinal reinforcement raises further questions about the effects of increased longitudinal reinforcement strains on one-way shear strength. To explore the effects of depth, reinforcement ratio, and high-strength reinforcement on one-way shear strength, a series of seven one-way shear laboratory tests were conducted. The tests were supplemented by nonlinear finite element studies to extrapolate the test results to alternate member geometries and boundary conditions. Design recommendations are proposed based on the findings of the experimental and analytical studies.

ACKNOWLEDGEMENTS

The authors would like to thank the following individuals for their valuable insight and for graciously investing their time and energy into the project. Their involvement made this work possible and greatly improved the quality of the research results:

- David Fields, Magnusson Klemencic Associates, Seattle
- Neil Hawkins, University of Illinois, Urbana-Champaign
- Evan Bentz, University of Toronto
- Michael P. Collins, University of Toronto
- Dominic Kelly, Simpson Gumpertz & Heger

The authors would also like to thank the sponsors of the project for financial and material contributions to the project:

- Pankow Foundation
- ACI Foundation
- Magnusson Klemencic Associates Foundation
- Level 10 Construction
- Concrete Reinforcing Steel Institute
- nVent Lenton
- Cascade Steel Rolling Mills
- Sika

The authors would also like to thank the various managers and staff of the Structural Engineering Laboratory at UC Berkeley for their support and problem-solving abilities during the design, construction, and testing of the project.

The work described in this report was carried out by Jerry Y. Zhai in partial fulfillment of graduate degree requirements in Structural Engineering, Mechanics, and Materials of the Department of Civil and Environmental Engineering, University of California Berkeley, under the direction of Professor Jack P. Moehle.

CONTENTS

CHAPTER 1: LITERATURE REVIEW OF ONE-WAY SHEAR STRENGTHS WITH SPECIAL ATTENTION ON FOUNDATIONS

1.1. One-Way Shear Strength: Case Studies

Shear failures in reinforced concrete members must be prevented to ensure structural safety. In contrast with flexure failures in reinforced concrete, which can be controlled when reinforcement is correctly proportioned to achieve ductile failures, shear failures tend to be brittle and occur with little to no warning signs. Several shear failures in modern buildings and infrastructure have resulted in large financial losses, downtime, and loss of life. Several case studies are briefly presented below.

Figure 1-1: Concorde Overpass collapse (left) and column shear failure during Northridge earthquake in 1996 (right)

- Concorde Overpass in Laval Quebec, Canada (2006): The south half of the Concorde Overpass collapsed in 2006, killing five people and injuring another six. The bridge was designed with longitudinal reinforcement and no shear reinforcement, which satisfied the code requirements of the CSA S6 Design of Highway Bridges code during 1966. However, due to the unconservative code requirements of the CSA code in the 1960s, deterioration of the concrete, and lack of retroactive inspections and oversight, the bridge "essentially failed under its own weight" in shear. At the time of failure, the bridge was in service for 40 years, still reasonably within its service life [1].

- Holiday Inn in Van Nuys, Los Angeles during the Northridge earthquake (1994): The structure was built in 1966 as non-ductile seven-story concrete frame. During the 1994 Northridge earthquake, a shear failure was observed in the columns beneath the fifth floor due to a lack of ties. This led to significant spalling and buckling of longitudinal reinforcement in the column, nearly resulting in the axial failure of the column as well. As a result, the structure was red tagged following the earthquake due to the risk of imminent collapse. Fortunately, the gravity loads could be redistributed to the neighboring columns and total collapse was not experienced. The structure was successfully repaired and later retrofitted with shear walls [2].
- Wilkins Air Force Base (1955) and Robins Airforce Base (1956): The roofs of two similarly designed warehouses at two different United States Air Force bases collapsed. Inspections revealed that diagonal tension failure in shear was the primary cause of these failures. These roofs were part of a rigid frame structure and so it was thought that longitudinal shrinkage, insufficient design requirements, and overreliance on the concrete shear strength played a role in the inadequate design and subsequent collapse [3].

These case studies should illustrate the severe consequences of a shear failure. In cases 1 and 3, some signs of imminent failure were observed through excessive cracking and concrete spalling. However, large deformations were not observed and so the urgency of the failing concrete members was lost on the uninformed observers who were not concrete experts. For the Northridge case, the importance of ductile detailing during earthquakes is highlighted. For structures to be designed safely, the shear capacity and mechanisms of reinforced concrete members must be well understood and properly designed to avoid a sudden and brittle failure.

The research in this report is motivated by a few factors. Recent changes to the ACI 318-19 one-way shear equations have brought the issue of shear to the forefront once again as the updated code equations have reduced the nominal shear capacity of reinforced concrete members when compared with prior editions of the code. For structural elements traditionally designed without shear reinforcement, such as foundations or retaining walls, the reduced shear capacity in members without shear reinforcement has resulted in considerable increases in required member depths [4]. Understandably, practitioners are concerned about the safety of existing designs. Secondly, the increasing adoption of new technologies, namely high-strength steel reinforcement in mat foundations, requires additional investigation to confirm that existing data on shear strength are compatible with this new material. Finally, this report aims to provide design guidance by providing guidelines for one-way shear design.

Modern mat foundations are seeing increasing use of high-strength longitudinal reinforcement as a means of reducing steel quantities, resulting in improved construction efficiency and reduced carbon footprint. However, the shear strength of mats constructed with high-strength reinforcement is unclear due to the size effect and increased longitudinal strains. As mat foundations are traditionally lightly reinforced and can be as deep as 18 ft thick for some buildings, questions regarding their shear strength have prompted the experimental investigation described in this report.

1.2. Mechanisms Resisting One-Way Shear

The one-way shear strength of reinforced concrete can be discretized into several contributions. Figure 1-2 shows a simple beam loaded in 3-point bending but cut along a diagonal shear crack where failure may occur. Several force vectors are drawn to represent the forces along the cut surface. As both sides of the cut surface are subject to the same forces but in opposite directions, duplicates of the force vectors are not drawn for visual clarity. C refers to the forces in the compression zone plus compression reinforcement and T refers to the forces in the tension zone, primarily contributed by tension in the reinforcement and a small amount by tension stiffening in the concrete. The descriptions of each of the remaining force vectors and associated mechanisms are provided in the sections below.

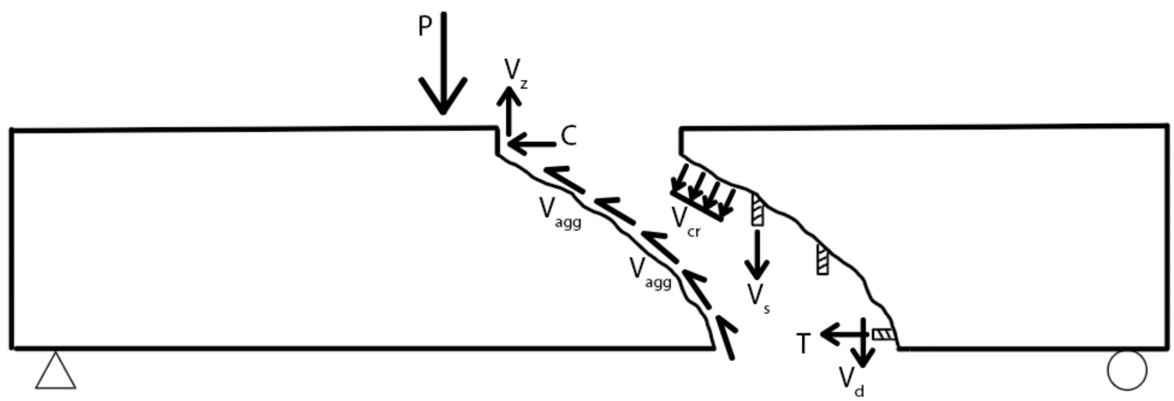

Figure 1-2: Free body diagram of diagonally cracked beam with shear resistance components.

1.2.1. Aggregate Interlock (V_{agg})

When concrete cracks due to flexure and shear, the crack typically forms along the weakest plane. For normal strength concrete, this is typically in the cement binder and therefore cracks around the aggregate particles. Due to the roughness of the crack, at reasonably small crack widths there is sufficient contact between the two surfaces such that interlocking between the aggregate particles can occur. One such relationship derived from the Modified Compression Field Theory (MCFT) suggests that the maximum interlocking stress on a crack is a function of the concrete strength (f_c'), aggregate size (a_g), and crack width (w) [5]:

$$v_{ci} = \frac{12\sqrt{f_c'}}{0.31 + \frac{24w}{a_g + 0.63}} \quad \text{(psi units)} \qquad 1\text{-}1\ )$$

Other factors such as the sphericity of the aggregate particles, quality of the aggregate, and inclusion of steel fibers can also affect the maximum shear strength but are not considered in this version of the MCFT equation.

Empirical and mechanistic models for aggregate interlock have been proposed by multiple authors, such as Bazant and Gambarova [6], Walraven and Reinhardt [7], and Vecchio and Lai [8] to name a few. The various models make different assumptions such as the roughness of the crack surface, degradation due to cyclic loading, and the path-dependency of the loading. These material models are generally calibrated from the results of panel tests, where stress states are well controlled on the panel element. As an example of how a typical crack behaves, Figure 1-3 presents the results of a panel test by Calvi et al. that investigates shear slip behaviors [9]. A reinforced concrete panel under constant transverse displacement is subject to cyclic shear to measure the shear slip behavior under some constant crack width. The pinched shape of the hysteretic curve in this case suggests the deterioration of the crack surface between load cycles. The envelope of maximum responses would represent the monotonic response leading up to failure, which can be calculated using Equation (1-1).

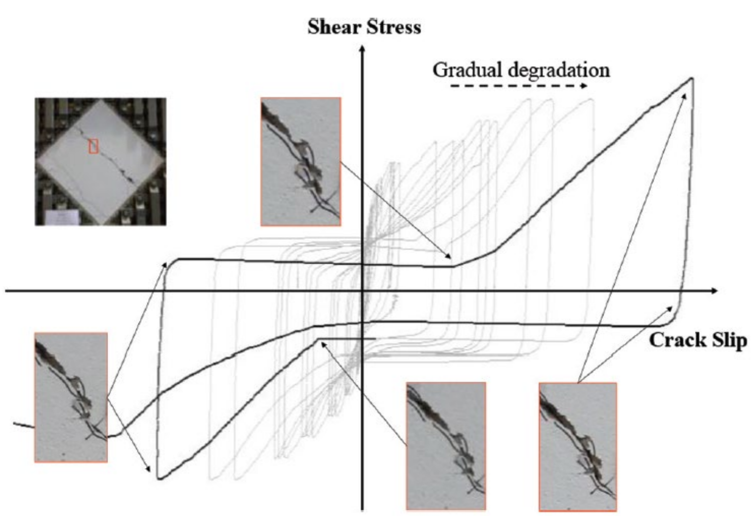

Figure 1-3: Shear stress versus crack slip response [9].

In terms of how aggregate interlock is applicable in a beam, additional complexities arise. There are changing stress conditions with depth in a beam due to variation in longitudinal strain and shear. Also, crack widths are generally nonuniform as they increase in width proportionally with the member's depth [10]. Some general observations can be made using Figure 1-2 as a reference. The figure shows that the aggregate interlock forces run parallel with the diagonal crack and therefore has a horizontal and vertical component. The vertical component contributes to the shear resistance of the member and is dependent on the effectiveness of the interlocking forces, which depend on both the crack geometry and crack width. Shear failures due to loss of aggregate interlock in beams containing normal strength concrete and no shear reinforcement typically occur when the crack is no longer able to sustain the shear forces on it and the crack begins to slip excessively. This assumes that the aggregate particles remain, for the most part, intact and not sheared.

For lightweight concrete and high strength concrete, adjustments must be made to the aggregate interlock models. This is because for these concrete mixes, the aggregate particles are typically weaker than the cement paste and so cracking tends to run through the aggregate particles rather than around them. The term "Interface Shear Transfer" or "Friction" is perhaps more appropriate here as the diagonal crack surface is smoother than that observed in normal strength concrete [11].

1.2.2. Shear in the Compression Zone (V_z)

In addition to vertical forces being carried as shear across the crack via aggregate interlock, some amounts of vertical shear forces can be carried as shear stresses inside the compression zone. As the compression zone is typically uncracked, this force transfer method is still valid though its effectiveness will depend on the longitudinal reinforcement configuration and presence of axial loads, both of which affects the depth of the compression block [11]. For a 55" (1.4 m) deep member with light longitudinal reinforcement, zero axial loading, and no shear reinforcement, Sherwood et. al. [12] found that approximately 24% of the vertical forces were carried by shear in the compression zone and the remainder through aggregate interlock mechanisms. For members without shear reinforcement and without distributed longitudinal reinforcement, it is well accepted that V_z and V_{agg} contribute the most to shear strength.

1.2.3. Residual Tension (V_{cr})

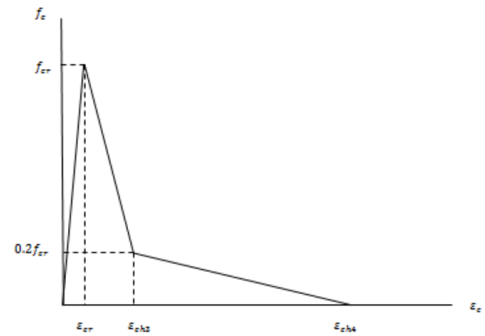

Figure 1-4: Tension softening behavior (adapted from Vecchio, et. al.) [13].

At very small crack widths immediately after cracking, the tension softening behavior of concrete means that not all tensile capacity is lost upon initial cracking. Figure 1-4 presents an example model of tension softening, sometimes called a crack opening law, where after initial cracking there remains tensile capacity until some threshold tensile strain or crack width. For beams with shallow depths of 4" (100 mm) or less, the residual tensile capacity can add significant amounts of shear capacity to the beam [11]. For larger members, due to the size effect (see Section 1.5.1) the effects of residual tension on a diagonal crack are generally negligible as crack widths are too wide for tension softening mechanisms to contribute any meaningful capacity.

Opening of the crack is generally related to the fracture energy of the crack (G_f). The fracture energy is defined as the amount of energy required for a crack to propagate through a unit area, with the units (Force/Length).

1.2.4. Presence of Shear Reinforcement (V_s)

Shear reinforcement, if present, can provide additional strength after initial formation of a diagonal crack. As observed in Figure 1-2, shear reinforcement forces run vertically across an inclined diagonal crack, enabling shear reinforcement to carry shear forces. Experimental evidence shows that shear reinforcement is activated when a diagonal crack crosses the bar and carries most of the shear force until the reinforcement is close to yielding [14]. Once yielded, the concrete then begins taking the shear demands until both V_s and V_c have reached their capacity.

The effectiveness of shear reinforcement depends on adequate anchorage or bond with the concrete. For shear reinforcement crossing a diagonal crack in regions outside of the bar's development length, the forces in the shear reinforcement crossing the crack are transmitted to the concrete via bond stresses. For shear reinforcement bars crossing a diagonal crack close to the crack's top or bottom, bars terminated with traditional hooks or bends may not provide enough development length to fully anchor the shear reinforcement bar. For this reason, ACI 318-19 specifies a maximum shear reinforcement spacing between *d/4* to *d,* depending on the application, and up to 24" to ensure multiple shear reinforcement bars run across the diagonal crack. Headed shear reinforcement has been shown to mitigate the issue of development since headed bars with a head area of at least $10A_s$ theoretically have no development length requirement, allowing immediate development of forces in regions close to the crack tail [15].

1.2.5. Dowel Action (V_d)

Dowel mechanisms can contribute to shear strength by acting to resist shear across a crack. This mechanism can fail in two ways: plastic hinging of reinforcement (Figure 1-5a) or parallel splitting in the concrete along the axis of the reinforcement (Figure 1-5b). In most beams, dowel forces are usually not significant to shear strength due to limited tensile strength of the concrete cover at the tension face [11]. However, dowel forces can be significant if very high longitudinal reinforcement ratios are present, or when distributed longitudinal reinforcement is present through the depth of the member. At times, plastic hinging in the longitudinal reinforcement due to severe vertical displacements after failure can provide some residual shear capacity if sufficient plastic rotation in the reinforcement and sufficient concrete splitting occur such that the reinforcement can act like a cable (see Figure 1-6). However, at this point all other shear mechanisms, namely shear in the compression zone, aggregate interlock, and shear reinforcement, have lost its capacity. Due to the relatively small contribution of the tensile capacity at the concrete cover and large displacement requirements to activate second-order dowel forces, dowel action mechanisms are generally neglected in the development of one-way shear equations.

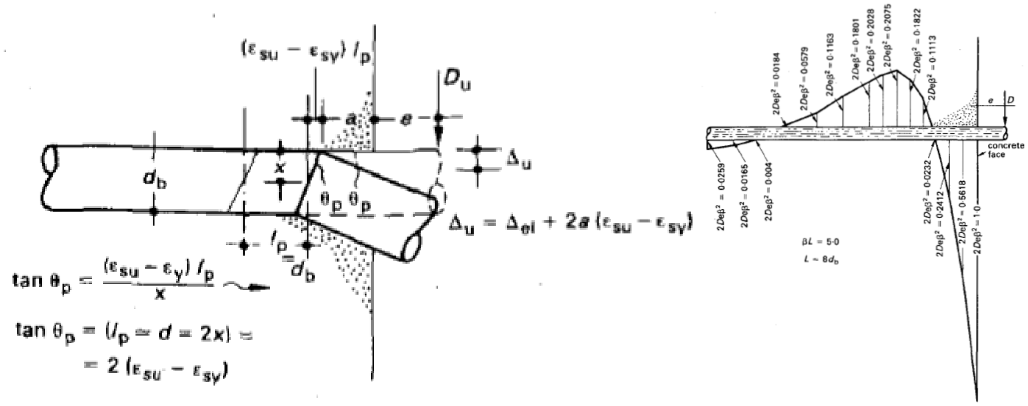

Figure 1-5: Dowelling action model of reinforcement in concrete. (a) Left figure shows failure by the reinforcement yielding and (b) right figure shows concrete tensile stresses leading to splitting failure [16].

Figure 1-6: Second order dowelling of longitudinal reinforcement after shear failure at the base of the shear crack. All other shear resisting mechanisms have broken down by this point.

1.3. Factors Affecting Concrete Contribution to One-Way Shear Strength

Current shear design practice depends on the structural element and loading. Typically, in seismic applications, shear reinforcement is placed to increase the shear capacity such that ductile flexural yielding controls the member behavior. For elements that may not traditionally contain shear reinforcement, such as footings, mat foundations, or retaining walls, the shear demands would be resisted solely by the concrete shear strength. In such cases, accurate equations and models for shear strength are necessary to ensure safe design.

There is extensive study on one-way shear strength of reinforced concrete members in shallow members. The DAfStb/ACI 445 database for one-way shear records the results of over 1000 documented shear tests [17]. Typical practice for comparing shear strength in reinforced concrete members is to normalize the shear force V_{test} causing failure by the web's cross-sectional dimensions and square root of the concrete strength to provide a normalized unit stress term α:

$$\alpha = \frac{V_{test}}{b_w d\sqrt{f_c'}} \quad \text{1-2)}$$

As shear actions are carried primarily in the web of the member, the width of the web (b_w) instead of the width of the member flange and the effective depth to the centroid of the longitudinal reinforcement (*d*) are used in the normalization. The term α in Equation (1-2) is typically reported in either psi or MPa units to compare with the results of other tests. The shear capacity of V_{test} depends on the convention with which the shear failure is assessed. For a point load, the shear force varies across the span due to the influence of self-weight, affecting the value of V_{test} depending on where along the shear span V_{test} is evaluated. For a distributed loading, the choice of evaluation section along the shear span changes the magnitude of V_{test} even more. Further discussion of this issue can be found in Section 1.3.5.

1.3.1. Influence of Member Depth (Size Effect)

The shear strength of reinforced concrete without shear reinforcement is strongly related to the member depth. Multiple test series by Bazant, Collins, and review of the DAfStb/ACI 445 shear database shows that the unit shear strength decreases with member depth [18, 19, 17]. This effect can be observed in Figure 1-7, which presents the shear strength of multiple one-way shear tests over a unit member width versus its member depth. The same plot shows the ACI 318-14 strength prediction which does not account for the size effect and therefore assumes that the shear strength scales proportionally with member depth. However, it is clear by the green and red dots representing experimental data points that the unit shear strength is not constant and the shear strength should therefore not scale proportionally with member depth.

This is typically attributed to the following mechanism. As the member increases in depth, the crack widths of the member increases in direct proportion with the increase in depth at the same longitudinal strain. When no shear reinforcement is present, the shear strength is provided by shear in the compression zone and aggregate interlock. Residual tensile forces are typically not significant when member sizes exceed 1 ft. As aggregate interlock depends on the crack width and it is generally impractical to scale aggregate size with member depth, the larger crack widths means that, by equation (1-1), shear capacity on the crack is lower and lowered unit shear strength with larger member depth are observed. For members with low longitudinal reinforcement ratios, aggregate interlock can account for most of the one-way shear strength [12].

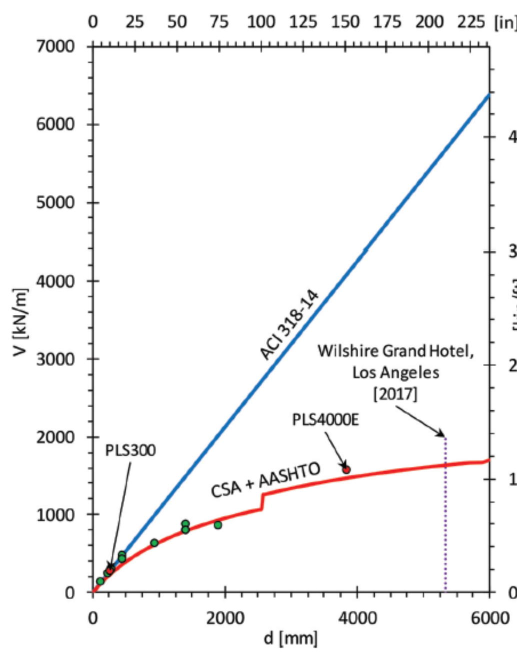

Figure 1-7: Size effect of reinforced concrete in one-way shear [19].

As the size effect is related to the width of diagonal cracks in members without shear reinforcement, shear reinforcement is effective in restraining the width of these cracks. Research by Lubell, et al. and Frosch have shown that shear reinforcement is effective in increasing the concrete contribution to shear strength and therefore helps overcome the size effect, allowing a proportional formula for shear strength to continue being used [20, 21, 22]. However, for shear reinforcement to be effective, maximum spacing requirements and adequate bond and anchorage must be provided as discussed earlier in Section 1.1.4.

1.3.2. Influence of Longitudinal Reinforcement Ratio (Strain Effect/ Longitudinal Reinforcement Ratio Effect)

In addition to the size effect whereby unit shear strength decreases with increased member depth, the unit shear strength also decreases with decreasing longitudinal reinforcement ratio. For a similar reason as the size effect, the crack width on the critical diagonal crack is influenced by longitudinal reinforcement. The reduced reinforcement ratio equates to a smaller flexural compression zone depth, increasing the reliance on aggregate in the cracked section. When the longitudinal reinforcement is distributed across the member depth, crack widths can be effectively controlled as the longitudinal reinforcement restrains the diagonal crack at multiple locations, acting almost as shear reinforcement in removing the size effect [11]. When the longitudinal reinforcement is concentrated in the flexural tension region, there is more limited restraint on the critical diagonal crack and so the longitudinal reinforcement effect is observed. This trend can be observed in the one-way shear database of Figure 1-8, where the scatter of unit shear strengths shows that lower longitudinal reinforcement ratios have lower average unit shear strengths.

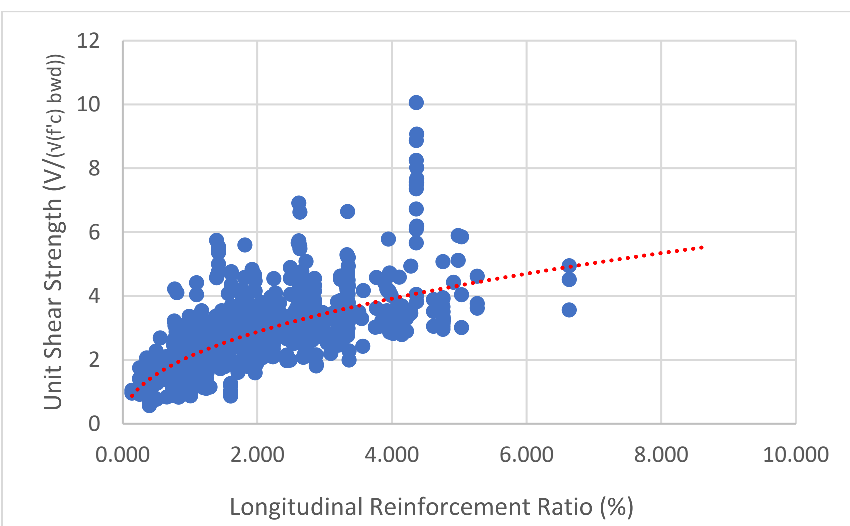

Figure 1-8: Longitudinal reinforcement ratio effect as observed from shear database [17].

1.3.3. Influence of Shear Span to Depth Ratio (Slenderness)

The shear span to depth ratio of concrete members affects the failure mode of a beam. Depending on the a/d or shear span to depth ratio of the beam, sometimes called the shear slenderness, either beam action or arch action controls the strength of the beam. Figure 1-9 illustrates the two mechanisms with the help of a finite element analysis of a transfer girder. For arch action on the left side, the principal compressive stresses are concentrated along a clearly defined "strut" in the left side where the slenderness is relatively low. These regions where the stress field is non-uniform are referred to as D-regions. By the ACI 318-19 definition, these regions are designated as d away from a force or geometric discontinuity, such as a support or location of a concentrated applied load, to name a few. In contrast, the higher slenderness on the right-side results in the forces distributed somewhat uniformly over the depth of the beam. These are called beam regions or B-regions, where sectional models for shear and moment provide reasonable predictions of strengths and the "plane sections" assumption holds relatively well.

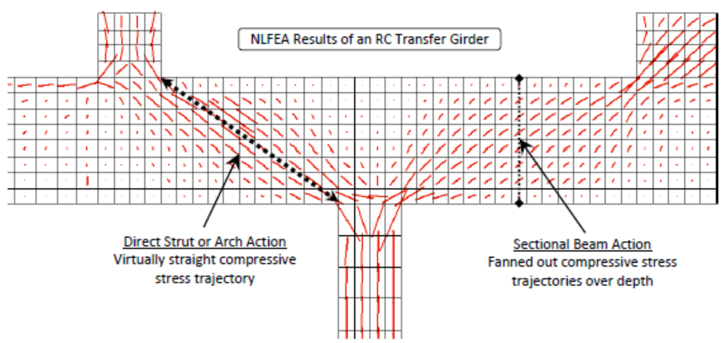

Figure 1-9: Arch action versus beam action in reinforced concrete beams [23].

Figure 1-10 shows the variation in shear strength with slenderness for a series of test beams tested by Kani et al. At low slenderness ratios, direct compression struts are the primary mechanism carrying applied loads, resulting in greatly increased shear strengths. For concrete members within this range, the strut-and-tie method is the appropriate analysis method for design and analysis. An *a/d* ratio of between 2.0 to 2.5 marks the transition between arch and beam action as the angle is generally too shallow to permit a clearly defined concrete strut. For *a/d* ratios larger than 2.5, failure is controlled by either one-way shear or flexure, depending on how the shear and longitudinal reinforcement are proportioned with respect to the *a/d* ratio.

The slenderness ratio implicitly influences the longitudinal reinforcement strains and associated one-way shear strength. Like the longitudinal reinforcement ratio effect, where reduced amounts of reinforcement results in lower one-way shear strengths, the increase in flexure strains due to increasing the slenderness ratio also results in larger longitudinal strains in the reinforcement. The larger reinforcement strains result in larger associated crack widths along diagonal shear cracks, resulting in reduced effectiveness of aggregate interlock and reduced shear strength. This can be observed in Figure 1-10, where the shear strength continues to decrease for *a/d* greater than 2.5, albeit at a much smaller rate and can effectively be regarded as constant with *a/d*. At sufficiently large *a/d* ratios, flexural failure begins to dominate the member response and shear capacity is no longer a concern.

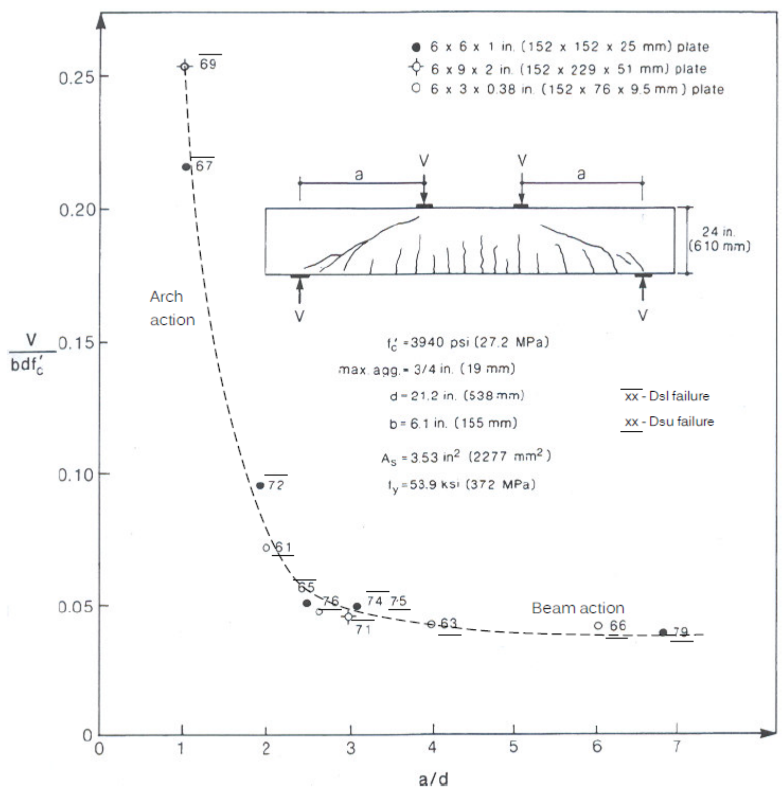

Figure 1-10: Effect of shear span to depth ratio on experimental shear strength (Presented by Mihaylov [24] and adapted from Collins and Mitchell [25]).

1.3.4. Influence of Aggregate Size

While it is impractical to scale the maximum aggregate size in construction due to regional supply constraints on coarse aggregate, the effects of aggregate size on shear strength were studied over a range of concrete mixes containing different maximum aggregate sizes. Three independent studies researched the influence of maximum aggregate size, which have been summarized below in Figure 1-11. Most of the data showed an increase in shear strength with increased aggregate size. The one exception was observed in the data from Sherwood on the right, where specimens with 50 mm coarse aggregate size showed lower observed shear strength than specimens with smaller coarse aggregate sizes. The authors attributed this to observing fractured aggregate particles, which resulted in smoother crack surfaces. This consequently lowered aggregate interlock capacity and resulted in lower shear strength when compared to some of the specimens with 30 mm (1.2”) maximum coarse aggregate size. This could be a consequence of the selected concrete mix with 50 mm (2”) maximum aggregate size and the specific minerology of the aggregate particles.

Outside of this one anomalous observation, all studies concluded that there was an observable increase in one-way shear strength with increased aggregate size. In reviewing the data, however, it appears that the difference in unit shear strength is generally within 15% of the mean value in each test series. Therefore, while there is an increase in capacity going from 10 mm to 40 mm in coarse aggregate size, the increase in capacity does not appear to increase by a very large amount and also subject to the natural variability in tested results.

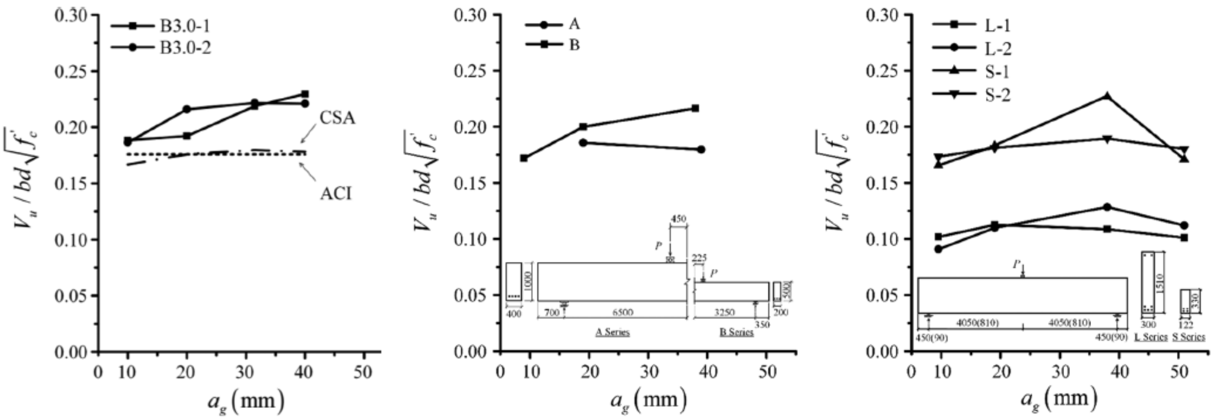

Figure 1-11: Influence of maximum aggregate size on unit shear strength (in SI units). Adapted from Deng et al. (left) [26] with data from Taylor et al. (middle) [27] and Sherwood et al. (right) [28]. Note that $0.17\sqrt{f_c'}$ (MPa) = $2\sqrt{f_c'}$ (psi)

1.3.5. Influence of Clamping (Point vs. Distributed Loads)

For simply supported beams loaded with a point load, the disturbed regions are located within *d* from a geometric or force discontinuity, namely within *d* of the two supports and the midspan applied load as illustrated in the upper beam of Figure 1-12. Within the zones marked as a D-Region, there are large variations in vertical stresses due to the support and loading plates. In contrast, zones marked as B-Regions have negligible vertical stresses as these zones are sufficiently far from the loading and reaction points.

Unlike a point load, where vertical stresses become negligible in B-Regions, distributed loads can induce vertical stresses in B-regions that improve shear strength by acting as positive restraint against crack opening. This is referring to as "clamping," which has been shown to improve the shear strength of shallow reinforced concrete slabs [29]. The same mechanism is thought to apply to the shear strength of other concrete elements subject to distributed loads, such as foundations or retaining walls. The influence of clamping is not captured in any major code equations, though it is often referenced as the reason behind the apparent increase in shear capacity in certain structural elements such as footings.

Acevedo et al. suggests that the beneficial influence of clamping is related to the ratio of clamping stress to shear stress. When the ratio is sufficiently high, clamping stresses provide an increase to one-way shear strength. Thus, the benefits of clamping will also depend on geometric qualities, such as the length of the shear span. A longer shear span results in larger area over which distributed loads can act, decreasing the effective clamping pressure. The distribution of said pressure, in the case of soil reactions, can also affect the effectiveness of clamping. The topic of soil pressure distributions will be discussed further in Chapter 1.7.

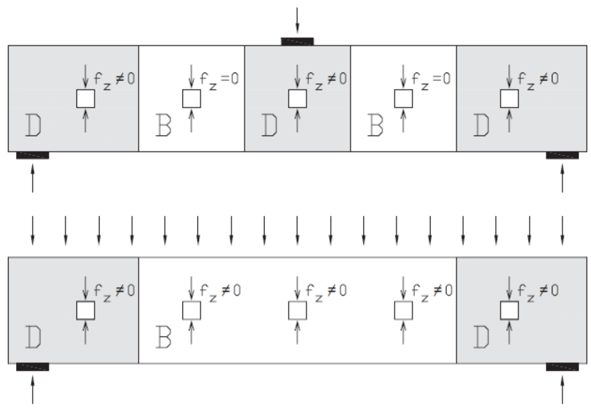

Figure 1-12: Clamping stresses introduced by supports, loads, and distributed loading (Taken from Avecedo et al.) [29]

1.3.6. Influence of Axial Loads

Axial loads in reinforced concrete beams and slabs can have positive or negative benefits on the one-way shear strength. When axial compression is present, the compressive strains act uniformly on the member cross section, delaying the onset of diagonal cracking. Most columns and shear walls have larger shear strengths when compared to beams due to the axial compression from gravity loading, and so these structural elements are typically unconcerned when it comes to the size effect. Given the abundant number of column and wall tests that do not exhibit diagonal-tension type shear failures, which is characterized by the beam "popping" open, it is certain that axial compression has a positive benefit on one-way shear strength up to a limit.

While most research on shear is conducted on members with axial compression, a handful of studies on members with tension have also been conducted. When axial tension is present, the increased tensile strains result in earlier onset of cracking. In addition to smaller cracking load, it is thought that there is a decrease in shear strength associated with the longitudinal stresses. Adebar, et al [30] and Ehmann, et al., [31] performed tests on beams without shear reinforcement subject to varying amounts of axial tension, with their respective results shown in below in Figure 1-13 and Figure 1-14. Interestingly, the two authors differed in their conclusions. Adebar concluded that there is a minor decrease in shear strength with increased axial tension, while Ehmann concluded that shear failure occurred independently of the axial tension. Both authors agreed that the cracking occurred earlier, but the proportional load decrease required to crack the beam was not indicative of the reduction in shear strength. In reviewing the data, it is the opinion of the authors that there is a decrease in shear strength with increased axial tension for the following reasons. Firstly, it is well established that longitudinal strains in the steel reinforcement correlate with the shear failure and axial tension serves to increase those strains. Secondly, in reviewing the Ehmann data it appears that there is a large drop in capacity when introducing a little bit of axial tension for both the *a/d=3* and *a/d=5* series of tests. Thirdly, Ehmann did not test a sufficiently large range of tension stresses. When normalized by the cross section, Ehmann's tests only investigated normal tensile stress ranging between 0 MPa to 6.6 MPa when calculated as $N/b_w d_v$ while Adebar's tests ranged up to 24 MPa in tensile stresses. The decrease in shear capacity could be obscured by an insufficient range in considered axial tension values and the natural variation in shear strength.

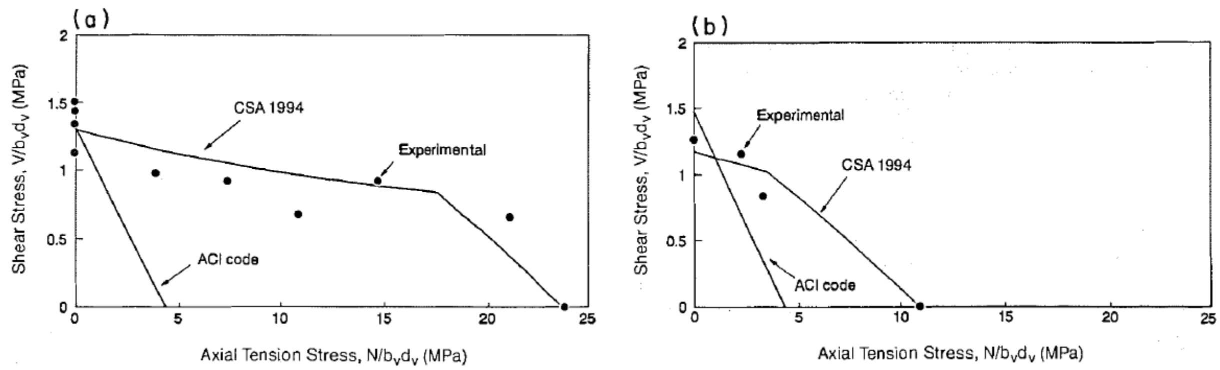

Figure 1-13: Variation in unit shear strength with axial load for (a) $\rho_w = 1.95\%$ and (b) $\rho_w = 1.0\%$ by Adebar, et al. [30]

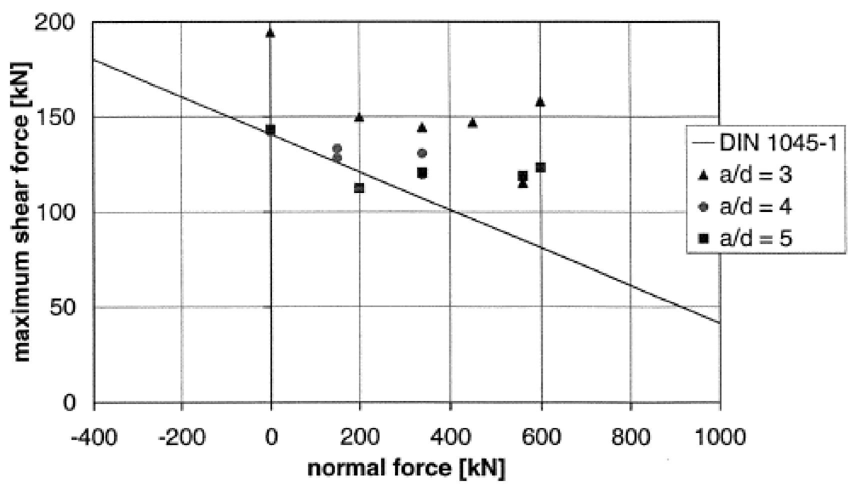

Figure 1-14: Variation in shear strength with axial load by Ehmann ($\rho_w = 1.6\%$) [31].

1.4. Empirical Methods of Analysis

Based on the preceding factors contributing to and affecting one-way shear strength in reinforced concrete members, many empirical equations have been proposed to predict the shear strength of beams. Each method focuses on different aspects of one-way shear and takes slightly different approaches towards a prediction.

Some common considerations among the different equations are listed below.

- All equations assume that concrete and steel contributions can be summed. That is, $V_n = V_c + V_s$.
- All equations consider member depth, width, and a surrogate of the tensile strength formulated in terms of the compressive strength f_c' to provide an estimate for V_n. However, there is limited consensus on the location along the shear span to take design forces and calculate V_n.
- Most equations also consider the influence of longitudinal strain. Some equations explicitly consider longitudinal strain as estimated by the bending moment, while others implicitly account for it by the longitudinal reinforcement ratio.
- Few equations explicitly consider the relative size between coarse aggregate diameter and member depth.

The most common code equations as well as a few empirical equations proposed by different authors are summarized below.

1.4.1. ACI 318-19

$$V_c = \left(8(\rho_w)^{\frac{1}{3}}\lambda_s\lambda\sqrt{f_c'} + \frac{N}{6A_g}\right)b_w d \quad \text{if } \mathrm{A_v} < A_{v,min} \text{ (psi units)}$$

$$V_c = \left(8(\rho_w)^{\frac{1}{3}}\lambda\sqrt{f_c'} + \frac{N}{6A_g}\right)b_w d \quad \text{or} \quad V_c = \left(2\lambda\sqrt{f_c'} + \frac{N}{6A_g}\right)b_w d \quad \text{(psi units)}$$

$$V_s = \frac{A_v f_{yt} d}{s} \qquad \lambda_s = \sqrt{\frac{2}{1+\frac{d}{10}}} \quad \text{(psi units)} \qquad \text{1-3)}$$

ACI 318-19 one-way shear equations include a longitudinal reinforcement term that reduces the shear strength with lower longitudinal reinforcement ratio, a size effect factor that reduces the shear strength, and axial load term that increases shear strength as a set ratio of the applied axial stress [32]. The size effect factor term is derived from the size effect work of Bazant, et al. [33]. The contribution of shear reinforcement considers the proportional area of shear reinforcement crossing a diagonal crack with an assumed angle of 45 to the horizontal. The section where shear strength is evaluated is taken at the point of highest shear without consideration of the moment at that section.

1.4.2. CSA A23.3:19 (Aggregate Interlock)

$$V_c = \lambda \frac{0.4}{1 + 1500\varepsilon_x} \cdot \frac{1300}{1000 + s_{ze}} \sqrt{f_c'}\, b_w d \qquad (MPa \text{ units})$$

$$\varepsilon_x = \frac{\frac{M}{0.9d} + V_u + 0.5N_u - A_{ps} f_{se}}{2\left(A_s E_s + A_{ps} E_p\right)}$$

$$s_{ze} = \frac{35 s_z}{15 + a_g} \qquad (MPa \text{ units})$$

$$V_s = \frac{A_v f_y d_v \cot\theta}{s} \quad , \quad \theta = 29 + 7000\varepsilon_x \tag{1-4}$$

$$s_z = \text{lesser of } (0.9d, \text{max. spacing of distributed longitudinal reinforcement})$$

The CSA A23.3 one-way shear equations are derived from the Modified Compression Field Theory (MCFT), which is a constitutive model for cracked concrete elements with reinforcement spanning across the crack. This method considers the effects of longitudinal reinforcement ratio through the longitudinal strain term (ε_x) and of relative member size through the equivalent crack spacing parameter (s_{ze}) [34]. Embedded in the equations is an emphasis on the aggregate interlock capacity of the inclined diagonal crack as a function of member depth and aggregate size.

The CSA General method is an iterative method that considers the loading of the beam. To apply the method, the loads on the beam (M , V_u, N_u) are increased based on the reference loading until the computed shear capacity (V_n) equals the shear demands (V_u) of the reference loading V_u.

The contribution of shear reinforcement is based on a variable angle, which depends on the longitudinal strain parameter. This implicitly depends on the amount of longitudinal reinforcement, where beams with lower amounts of longitudinal reinforcement tend to have a steeper compression field angle.

Evaluation with the CSA method requires checking the shear capacity at each end of the B-region. For design purposes without iteration, the simplified method removes the iteration requirements by assuming a longitudinal strain value of 0.85×10^{-3} and assuming an aggregate size of 20 mm. Evaluation is then limited to the point of highest shear like ACI 318-19 procedures.

1.4.3. Eurocode 2

$$V_c = \left[C_{Rd,c} \left(1 + \sqrt{\frac{200}{d}} \right) (100 \rho_w f_{ck})^{\frac{1}{3}} + \frac{k_1 N}{A_g} \right] b_w d \qquad (MPa \text{ units})$$

$$C_{Rd,c} = 0.18, \;\; k_1 = 0.15 \;\;\; \text{(Recommended)}$$

$$V_s = \min \left(\frac{A_v f_y d \; cot \, \theta}{s}, \frac{\alpha_{cw} b_w z v_1 \, f_{cd}}{\cot \theta + \tan \theta} \right) \qquad 1\text{-}5\;)$$

Eurocode 2 accounts for the size effect and longitudinal reinforcement ratio effect in very similar ways when compared to the ACI 318-19 code. The size effect is captured in the second term by $\sqrt{200/d}$ and strain effects captures by $(\rho_w)^{1/3}$ [35]. However, Eurocode differs from ACI 318-19 in the calculation of V_s. Like CSA A23.3, Eurocode permits a variable angle for the calculation of the compression field but allows the designer to select the angle provided that the compressive struts are adequate. This approach is based on plasticity theory and provides a lower bound to the shear reinforcement strength.

1.4.4. Depth of compression

Some authors suggest that the uncracked depth of concrete provides a better correlation with the shear strength. One such relation by Frosch, et al., is presented below [36]:

$$V_c = 5\lambda\sqrt{f_c'}\, b_w\, c\, \gamma_d$$

$$c = \left(\sqrt{2\rho_w n + (\rho_w n)^2} - \rho_w n\right) d \quad , \quad n = \frac{E_s}{E_c}, \quad \gamma_d = \frac{1.4}{\sqrt{1 + \frac{d}{10}}} \qquad \text{1-6)}$$

Instead of the depth of the concrete section, the cracked section neutral axis is used instead in the expression. The reasoning is that all shear failures occur in regions where longitudinal reinforcement is unyielded, below the neutral axis. The calculation for c also implicitly accounts for the stiffness of the longitudinal bars, expanding the equations to incorporate FRP reinforcement, which has different mechanical properties when compared to conventional steel reinforcement. The equation is derived based on the shear capacity of the uncracked compression zone while accounting for the influence of compression in this zone [37].

1.4.5. Evaluation Section

Various codes and empirical equations take different approaches with respect to the location along the shear span where shear strength is assessed. This primarily has to do with the disconnect between where is the largest shear force and where is the observed failure location. In the case of flexural failures, the evaluation section and observed failure location generally coincide at the point of highest moment for almost all observed tests. On the other hand, shear failure is more complicated as failure is not always observed where shear forces are highest due to the interaction between longitudinal strain caused by bending moment and shear force.

To illustrate this complexity, the bending moment and shear profile of a beam loaded in 3-point bending and a typical spread footing loaded in the middle with a uniformly reacting soil pressure are presented in Figure 1-15. For a beam-style loading, the point of highest moment occurs at the midspan and decreases to zero at the left or right support. The point of highest shear however occurs at the left and right supports and decreases to half of the applied load at midspan due to the influence of self-weight. The influence of self-weight on assessing the location where shear is evaluated is typically small in beams of shallow depth but becomes important to consider for very large beams. The question of where to evaluate shear strength is magnified for uniformly distributed loads since shear forces along the span vary faster than the point load case.

Since the shear failure depends on both bending moment and shear forces at a section, a shear failure can possibly occur anywhere along the span. Figure 1-16 shows an example of a beam loaded in 3-point bending and the associated failure cracks highlighted in red. On the left side, the failure crack runs at about 30 degrees to the beam's longitudinal axis and occurs at about halfway between the load and the support. On the right side, the failure crack runs at a similar angle, but forms close to the point of applied loading. If referencing the beam-style bending moment and shear diagrams in Figure 1-15, it is clear that neither failure occurred at the point of highest shear that is outside of a D-region (see Section 1.5.3 for B-regions and D-regions).

The failure location along the shear span will depend on the reinforcement configuration and member size. Specifically, the combination of these variables will induce slightly different stress states that change the degree to which the beam cracks, affecting the consequent failure location and applied load causing failure. Models developed from stress-field mechanics such as the MCFT have been applied successfully in predicting the failure load as well as the failure location of beam shear.

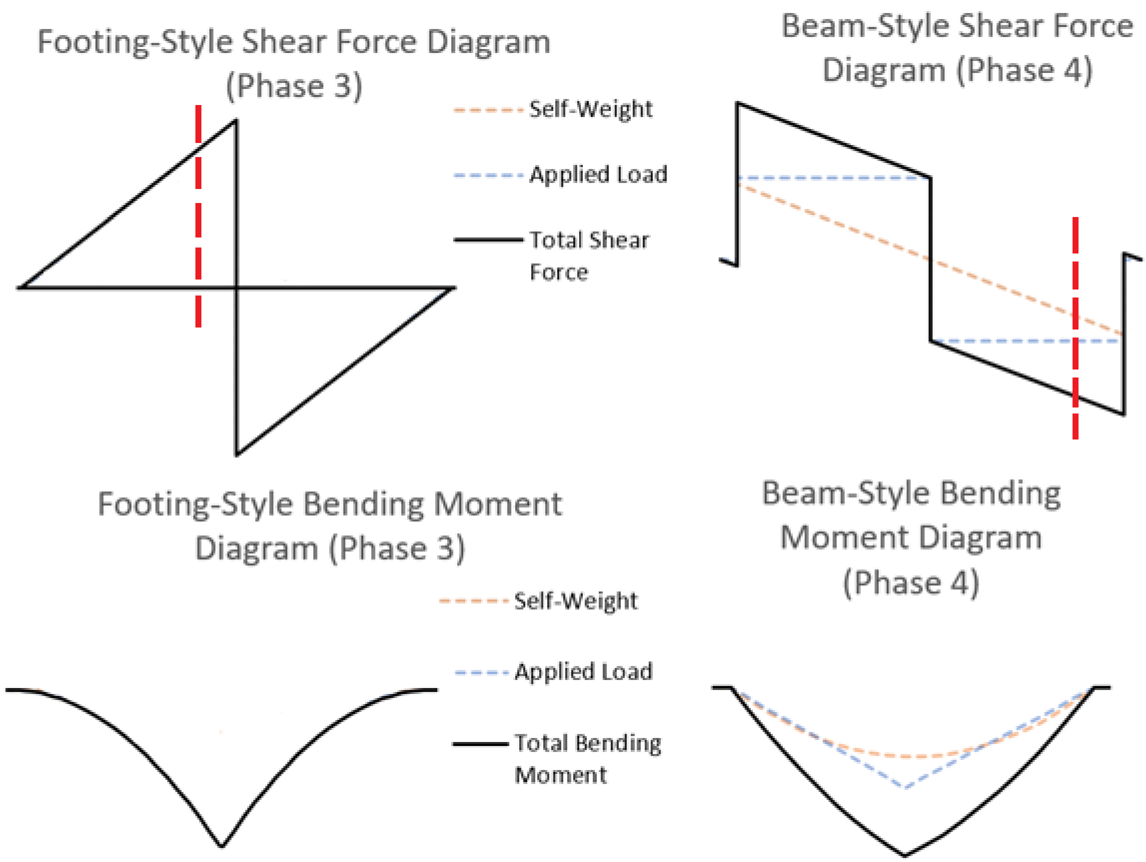

Figure 1-15: Shear force diagram and bending moment diagrams footing-style and beam-style loadings. Evaluation section by ACI 318 highlighted in red vertical dashed line.

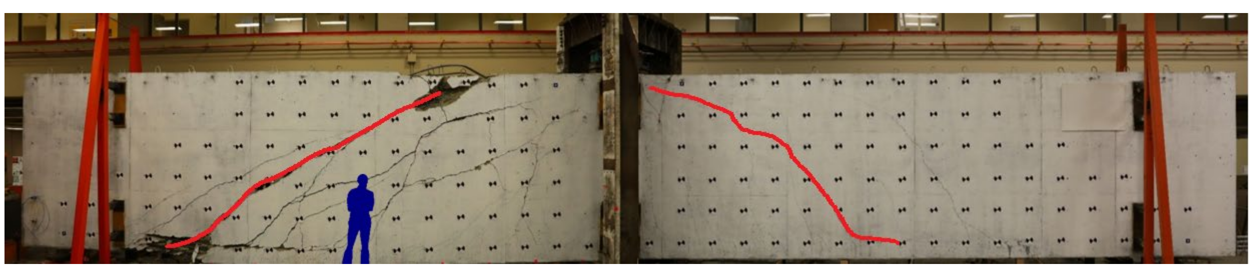

Figure 1-16: Example of shear failure locations. The beam is simply-supported in 3-point bending, with shear failure on different locations between the left and right sides.

The ACI 318-19 code takes the approach of evaluating shear strength at its highest point outside of disturbed or d-regions. ACI equations for shear strength rely solely on the shear force and do not explicitly rely on bending moments or longitudinal strains, which for point-loaded or uniformly loaded beams place the evaluation section for shear strength at the edge of the b-region close to a support. For beams with small depths, the shear force varies little across the shear span since self-weight contributions are small. The issue of best evaluation section is not ambiguous in a footing-style loading since moment and shear increases in tandem as shown previously in Figure 1-15, resulting in a single region where failure is possible. The issue is also mitigated when shear reinforcement is present, since the additional strength provided by its inclusion decreases the proportional contribution of self-weight to failure.

The question of the best location at which to evaluate shear failure is magnified for large beams without shear reinforcement since the self-weight loads vary significantly across the shear span and may contribute a significant proportion of the sectional shear stress causing failure. To illustrate this topic by presenting a high-level summary of the results of Phase 1, shear forces at a vertical section inside b-regions at failure would range between 71 k and 90 k, with self-weight contributions varying between 22% and 39 % respectively at the section close to the applied load and the section close to the support respectively. Evaluated as a normalized stress in terms of the cross-section, the failure shear stress for Phase 1 would range between 0.8 $\sqrt{f'c}$ and 1.0$\sqrt{f'c}$ depending on where along the shear span is evaluated.

1.5. Shear in Foundations

Foundations are designed to resist the vertical loads imposed by the superstructure and distribute the loads into the supporting soil beneath. Typically, foundations are classified as either a shallow foundation or a deep foundation (Figure 1-17). Shallow foundations rely on the bearing capacity of the supporting soil to resist vertical and overturning forces without any piles. When the supporting soil is inadequate to resist the loads or the required footing dimensions become uneconomical, deep foundations are used. Deep foundations are elements that rely on soil resistance at depth, such as driven or augered piles that rely on either friction with the soil or anchorage into solid bedrock to resist the vertical applied loads.

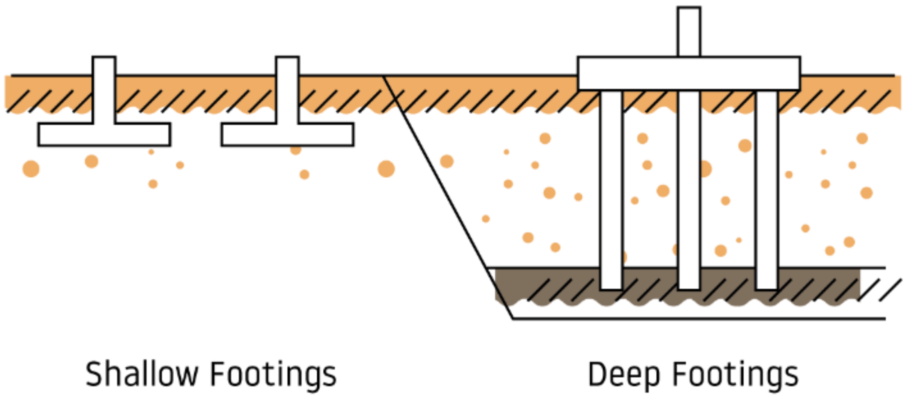

Figure 1-17: Shallow footing (left) versus deep footing (right) [38].

There are a few different types of shallow foundations. The simplest type is an isolated spread footing, which is the shallow footing shown in Figure 1-17. When overturning forces are large and the required footing footprint increases, it is common to connect adjacent spread footings into a connected footing to resist the overturning forces.

The foundation type that will be discussed at length are spread footings and mat foundations. Mat foundations are like connected footings but are suitable when the soil conditions result in unacceptable differential settlements across different points of the building. When the foundation is subjected to large overturning actions, a mat foundation system can help provide the large footprint required for adequate resistance. Mat foundations may also become suitable where the requirement for multiple connected footings takes up more than half of the building footprint, making it more economical to perform a monolithic concrete pour as opposed to multiple smaller connected footings. Mat foundations are a common foundation system for high-rise buildings on the western United States when the soil capacity and characteristics permit its construction.

1.5.1. Simplified Analysis of Foundations

A simplified approach for footing design and the procedure outlined by ACI 318-19 is to adopt the rigid footing, flexible soil assumption. Under this assumption, the stress distribution that resists against vertical loads and overturning moment on a footing is as shown in Figure 1-18:

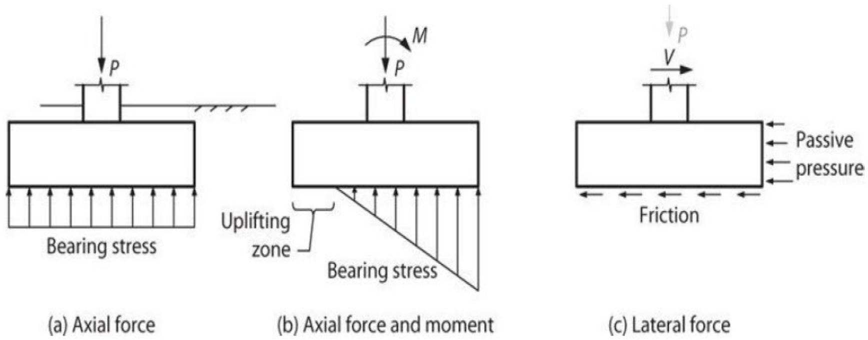

Figure 1-18: Resistance mechanisms for simple spread footings subject to vertical load and overturning [39].

$$\sigma_y = \frac{P}{A} \pm \frac{Mc}{I} \tag*{1-7)}$$

where c is the distance away from the centroid of the footing. Another way of presenting the above system is to recreate the overturning moment M by applying the force P at some eccentricity $e = M/P$. If uplift is undesirable, the eccentricity e must be within the “Kern Limit”, which can be derived as $L/6$ where L is the dimension from the footing centroid to its edge [40]. Some uplift is allowable under ultimate loading conditions, though it requires an iterative procedure. To determine the stress distribution underneath the mat under uplift, the effective length of the mat should be iteratively reduced based on the prior iteration of the mat length in compression until no point of the mat under the effective length assumption is in tension. This procedure will allow the eccentricity to exceed *L/6* and up to *L*, though it is not typical to get significantly more overturning resistance due to allowable bearing pressure limits in the soil.

To design for shear under the simplified model, assuming the configuration as shown in Figure 1-18 and Equation (1-7) for the stress distribution, an integration of σ_y across the bottom of the mat to determine the demand shear forces at *d* away from the center is then:

$$V_u = \int_d^L \sigma_y \, dx = \left(1 - \frac{d^2}{L^2}\right)\frac{3M}{4L} + \left(1 - \frac{d}{L}\right)\frac{P}{2} = \left(1 - \frac{1}{a_d^2}\right)\frac{3M}{4L} + \left(1 - \frac{1}{a_d}\right)\frac{P}{2} \tag*{1-8)}$$

Equation (1-8) provides some basic insights on the shear design for foundations mats. At small slenderness (a_d) ratios, increasing slenderness is very effective in increasing the shear strength but decreases in effectiveness at larger slenderness ratios. Changing the slenderness of the foundation allows proportionally more overturning moment to be applied than vertical load. This suggests there is a practical limit to how slender a mat foundation can be before it is not economical from a shear perspective.

$$P \leq \frac{V_u}{\left(1-\frac{1}{a_d}\right)} - \left(1-\frac{1}{a_d^2}\right)\frac{3M}{4L}\frac{1}{\left(1-\frac{1}{a_d}\right)} = -\frac{a_d+1}{a_d}\cdot\frac{3M}{4L} + \frac{a_d V_u}{a_d-1} \qquad \text{1-9)}$$

Equation (1-9) provides another arrangement of equation (1-8), which highlights the relationship between overturning moment and vertical load. The amount of vertical load that can be applied given some overturning moment, or vice versa, depends on the M/L ratio as well as the slenderness ratio a_d of the mat. Additionally, if uplifting of the toe of the footing is not permitted, then an additional constraint is added such that:

$$P \geq \frac{3M}{L} \qquad \text{1-10)}$$

The permissible design space for a footing would then be the intersecting regions provided by equations (1-9) and (1-10) under the rigid footing assumption.

1.5.2. Footing Tests with Simplified Stress Distributions Under Purely Vertical Loads

To understand the shear strength of foundations under the assumed soil distribution, researchers have conducted foundation tests on reinforced concrete footings of various reinforcement and geometric configurations. For most of these early tests, a uniform load is imposed on the footing specimen by using car springs, which are soft enough over a large range of displacement to impose a relatively uniform support reaction thereby simulating a uniform soil reaction.

Tests by Talbot in the early 1900s investigated the response of both one-way and two-way footings [41]. Various configurations of reinforcement ratio in footings without shear reinforcement were studied. Despite differences in material quality between the early 1900s and today, such as the lack of transverse ribs on steel reinforcement leading to poor bond or weaker concrete strength in the 1900s when compared to modern concrete, several key observations drawn from Talbot's series of tests are still applicable to modern footings. The tests for wall footings, which primarily are critical in one-way shear, suggested that a shear failure forms at some distance away from the column and recommended that this critical section be located at *d* away from the column. The work also recommended that well-formed web reinforcement should be used to avoid a diagonal tension shear failure.

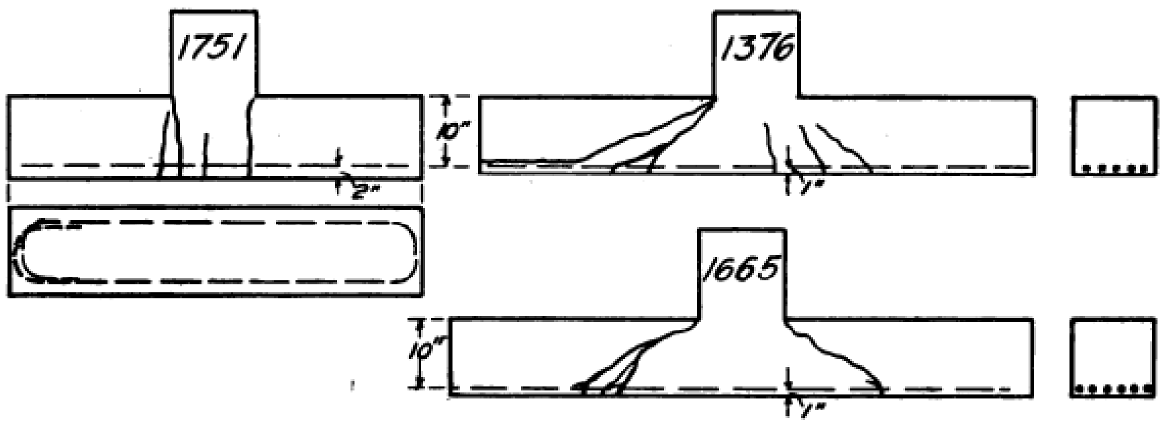

Figure 1-19: Talbot one way footing tests [41]

The next series of influential footing tests where a uniform soil reaction is imposed on the footing were conducted by Richart in the 1940s [42]. Richart primarily tested square and rectangular footings supported by car springs and constructed with a small column stub in the middle of the footing to simulate uniform soil reactions under vertical loads. Material properties used in these tests were more representative of modern materials. While most of these tests were conducted on square footings that failed in a punching mechanism, Richart found that the rectangular footings where the footing span was longer failed in one-way shear. These tests informed that footings, depending on the shear span slenderness, can be critical in either one-way or two-way shear. For Richart's specimens that failed predominantly in one-way shear, the shear slenderness ratio (*a/d*) of the longer dimension was 3.31.

More recently in 2011, Uzel et al. extended the findings of Talbot and Richart by testing one-way footings with a focus on investigating the size effect in one-way shear [43]. Uzel tested footings with similar geometries as Talbot's one-way specimens (see Figure 1-19) but mimicked a uniform soil reaction by applying loads from below with hydraulic cylinders that apply equal load. The findings of this research suggested that size effect is mitigated for footing specimens with *a/d* less than 2.5 because failure is characterized by crushing of concrete struts within the D-region. For footings with *a/d* over 3, a slight size effect is observed. Interestingly, this shear span slenderness ratio is like Richart's specimens that were critical in one-way shear, which consisted of rectangular footings with *a/d* of 3.31. Uzel also compared two specimens where one specimen is loaded uniformly across the entirety of the base and another specimen with uniform loads only outside of *d* of the support (see Figure 1-20). Both specimens had very similar unit shear strengths when evaluated at *d* away from the column, implying that loads applied within *d* of the column do not increase the one-way shear demand.

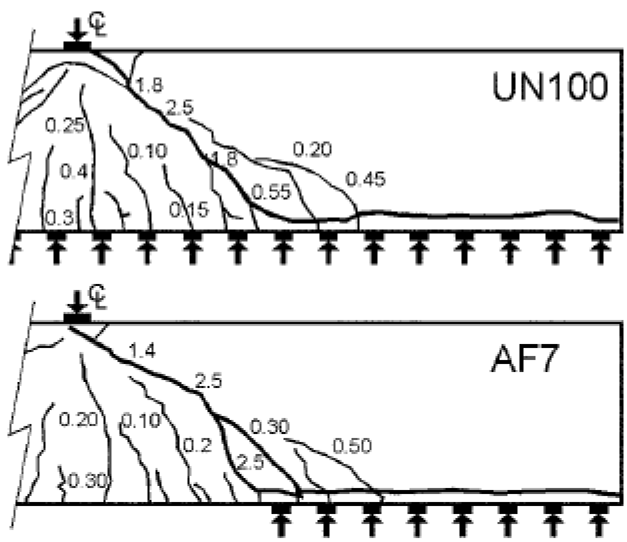

Figure 1-20: Uzel specimens investigating influence of applied loading on failure strength [43].

1.5.3. Realistic Soil Bearing Distributions Subject to Vertical Loads

The assumed stress distribution in the simplified soil pressure distribution under vertical load is applicable to the case where the footing is very stiff relative to the supporting soil. However, the reality is that soil pressure distributions will depend on the relative stiffness of the soil and the footing. When the compliance between the subgrade and superstructure is considered, soil pressure distributions may not be uniform under gravity load and linear under overturning moment as suggested by the simplified analysis outlined in Section 1.7.1. As the vertical stiffness of the footing decreases with distance away from the column, more loads tend to develop directly under the column and decrease in magnitude with distance from the column.

Hegger, et al., tested reinforced concrete footings on column stubs sitting on sand to evaluate the punching shear strength [44]. While the specimen's *a/d* ratio ranged between 1.45 to 2.5 and therefore did not fail in one-way shear, Hegger also recorded the soil pressure distribution beneath the footing. The authors defined a system rigidity (k_s) as a relative value between the stiffness of the soil and the stiffness of the foundation, with varying stiffnesses to observe the effects on the soil pressure distributions. The results summarized in Figure 1-21 show that there is a tendency for all footings (DF2-DF5) to have a slight concentration in soil pressure beneath the column. Only DF1 showed a somewhat uniform soil pressure distribution. Bonic, et al., tested similar specimens and attributed the concentration of soil pressures beneath the footing to the separation of the punching body from the footing due to diagonal shear cracking [45]. During the separation process, regions directly beneath the footing can develop direct compression struts to resist vertical loads, which is a relatively stiff mechanism. Areas outside the punching cone are failing in shear, resulting in reduced stiffness and leading to more load concentrating beneath the column.

The above studies were limited to smaller footings. Mat foundations are more complicated due to the concept of "dishing," which refers to the tendency for reduced soil stiffness at the center of the mat even under the assumption of uniform soil pressure [40]. Figure 1-22 presents a simple mat loaded uniformly from above with two sample points indicated for comparison. Under the uniform load assumption, the pressure would be the same under both Point A and Point B. However, the pressures at Point B dissipate much faster into the underlying soil column when compared to point A, resulting in increased deflection at point A when compared to point B. Further iteration likely results in a different soil pressure distribution and generally results in the deflected shape shown in Figure 1-22. Consideration of dishing effects can influence the bending moment demands.

It should be noted that for most footings which are a few feet in length or width, the small size of the footing reduces the impact of dishing. Additionally, most footings have relatively short spans and associated slenderness (*a/d*) ratios such that they are effectively rigid when compared to the stiffness of the underlying soil. For the case of mat foundations however, the large gravity loads applied on the mat by the core wall can result in soil pressures concentrating beneath the core. Dishing also increases the complexity of the foundation analysis, and so it becomes more important to consider the influence of pressure dispersion in the soil and its effect on settlement across the footprint of the mat.

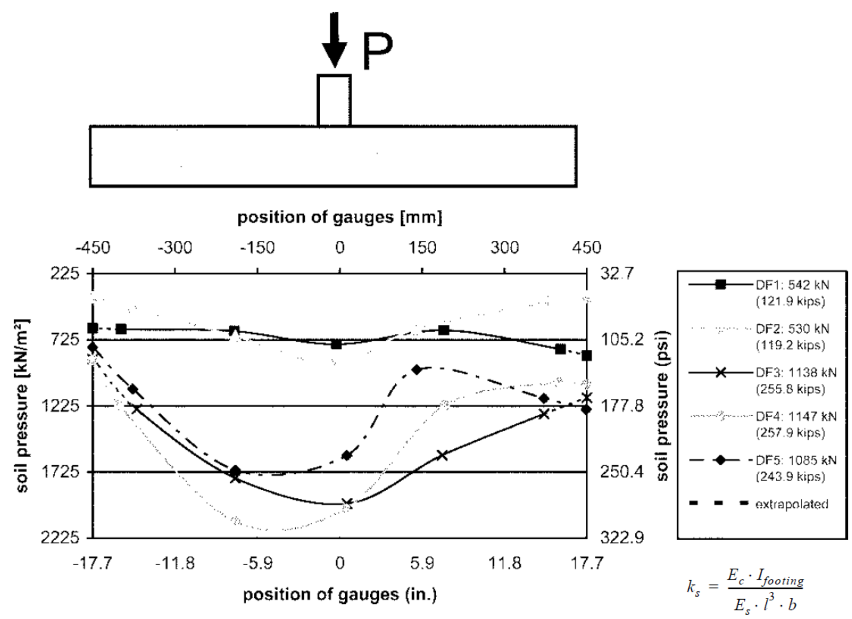

$$k_s = \frac{E_c \cdot I_{footing}}{E_s \cdot l^3 \cdot b}$$

Footing no.	d, mm (in.)	c, mm (in.)	a/d	$f_{c,cyl}$, MPa (psi)	$f_{ct,sp}$, MPa (psi)	E_c, GPa (ksi)	Bar size	ρ_l (ρ'_l), %	D	E_s, MPa (ksi)	k_s
DF1	150 (5.9)	150 (5.9)	2.5	20.2 (2929)	1.63 (236.4)	24.0 (3480)	14 (0.6)	1.03	0.339	44.2 (6.41)	0.497
DF2	150 (5.9)	150 (5.9)	2.5	22.0 (3190)	1.76 (255.2)	22.6 (3277)	14 (0.6)	1.03	0.851	80.1 (11.62)	0.258
DF3*	150 (5.9)	150 (5.9)	2.5	30.7 (4451.5)	2.33 (337.9)	25.8 (3741)	14 (0.6)	1.03	0.870	125.8 (18.25)	0.188
DF4	250 (9.9)	150 (5.9)	1.5	24.5 (3552.5)	1.97 (285.7)	24.0 (3480)	14 (0.6)	0.62	0.930	127.5 (18.49)	0.581
DF5	250 (9.9)	175 (6.9)	1.45	17.6 (2552)	1.51 (219)	23.3 (3378.5)	12/16 (0.5/0.6)	0.73	0.821	96.1 (13.94)	0.707

Notes: $f_{c,cyl}$ = cylinder compression strength; $f_{ct,sp}$ = splitting tensile strength; E_c = Young's modulus of concrete; ρ_l (ρ'_l) = flexural tensile (compressive) reinforcement ratio; D = compactness of sand packing; E_s = modulus of elasticity of soil; and k_s = system rigidity.

*DF3 included shear reinforcement (A_{sw} = 4070 mm^2 [6.32 in.^{2}]; s_0 = 75 mm [3.0 in.]; and s = 112.5 mm [4.4 in.]).

Figure 1-21: Soil pressure distributions under footing at failure [44].

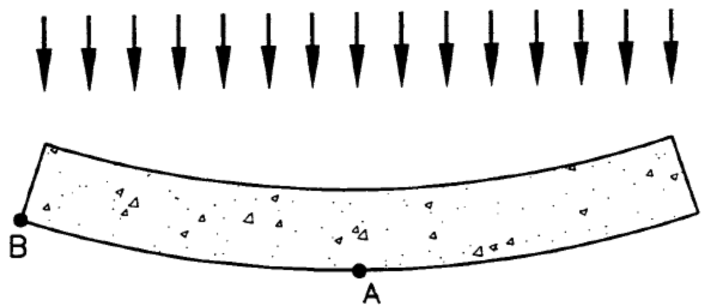

Figure 1-22: Dishing effect in mat foundation loaded uniformly [40].

1.5.4. Soil Pressure Distributions Subject to Eccentric Loads (Overturning)

Early studies on footing strength have primarily focused on purely vertical load with an emphasis on the punching shear strength. When overturning forces are considered, they are typically applied by testing eccentrically loaded footings to increase both vertical and overturning force until failure. Zhang, et al., tested a 7” deep square footing with *a/d* of 3.2 with “soil” reaction provided by rubber blocks that reasonably represented the stiffness of clay [46]. Figure 1-23 summarizes the reaction distributions of the soil-like rubber blocks, where the curves corresponding to 1-1, 2-2, and 3-3 represents reactions in the axis perpendicular to the axis of bending and 4-4, 5-5, and 6-6 representing reactions on an axis parallel to the axis of bending. These results show that in the bending direction, the linearly varying soil reaction of the simplified analysis is reasonably close to the measured reaction, while the transverse direction that does not resist overturning has soil pressures that are concentrated beneath the column.

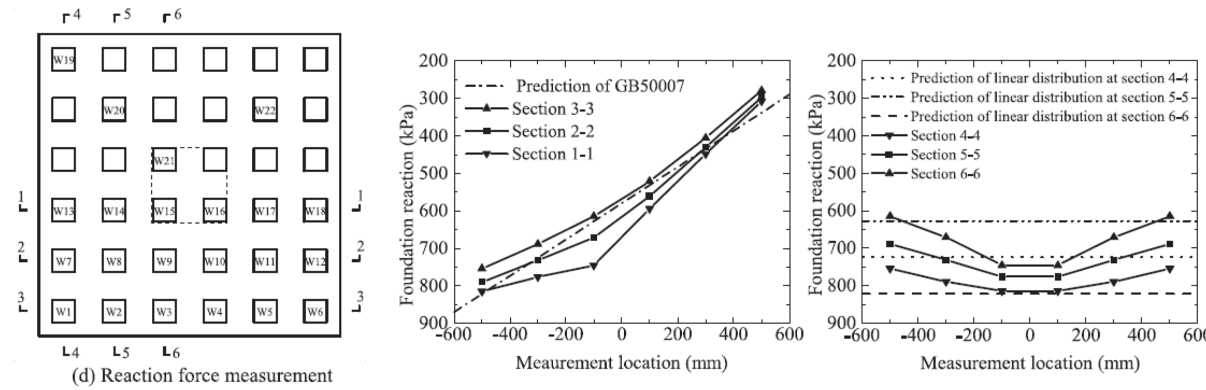

Figure 1-23: Subgrade reaction with footing subject to vertical and overturning moment [46].

In addition to experimental investigations that recorded the soil pressure distribution, analytical studies from a geotechnical perspective have also been performed to determine the maximum allowable bearing pressure for footings subject to vertical and overturning forces. Finite element analyses of soil with a perfectly rigid foundation element have been conducted by various authors to investigate the maximum allowable bearing stresses. One such analysis by Loukidis, et al., looked at the bearing capacity of strip footings under an inclined load with eccentricity [47], though it is the bearing pressure distribution that is of most interest here. Figure 1-24 shows the soil bearing pressures at failure. For the case with 0 eccentricity (i.e. purely vertical loading), the soil bearing pressures prior to failure in the soil are generally concentrated beneath the centerline of the footing, consistent with the findings of the prior research by structural engineers. As the overturning moments or eccentricity grows, the location of the peak soil pressure shifts with the amount of eccentricity.

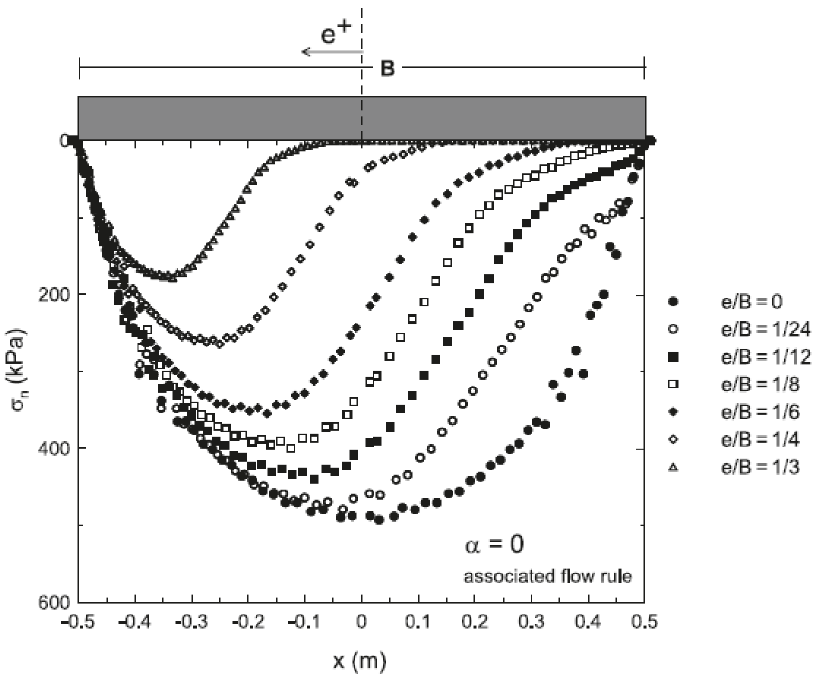

Figure 1-24: Distribution of soil bearing pressures at failure on eccentrically loaded rigid footings with no horizontal forces [47].

In reviewing the geotechnical engineering side, we see that there is a disconnect between structural and geotechnical analysis. The geotechnical engineers perform their soil finite element analysis with the assumption that the structural component above is perfectly rigid, while the structural engineers perform their footing finite element analysis with the assumption that the soil behaves like linear springs! The reality is that neither model is 100% correct as the subgrade and foundation interact. For most small footings, the issue is not a concern as the rigid footing assumption appears to be reasonable. However, it becomes important to consider the soil-structure interaction for mat foundations due to their sheer size and potential for the stiffnesses of the two elements to be relatively similar.

1.6. Current Practices for Mat Foundation Analysis

To facilitate the required collaboration between structural and geotechnical engineers, the Discrete Area Method proposed by Ulrich [48] is recommended by Horvilleur and Patel in 1995 [40] and more recently Klemencic et al. in 2012 [49] as a procedure to model the foundation demands given the nonlinearity and coupling of soil response across the footprint of the mat foundation. The steps are summarized below

1. The geotechnical engineer proposes a subgrade modulus given the dimensions of the mat foundation for preliminary analysis in the structural model. The choice of subgrade reaction is then modified according to empirical relations by other researchers and the geotechnical engineer’s own judgement.
2. The structural engineer uses the subgrade modulus in the foundation model. The foundation model is divided into small discrete areas to which a spring stiffness is assigned based on the provided subgrade modulus. The structural engineer is then able to run the foundation model with the forces from the overlying structure and obtain a set of displacements and contact pressures at each spring location. These pressures and deflections are returned to the geotechnical engineer.
3. The geotechnical engineer reviews the change in forces and deflections to ensure compatibility with the soil model. If discrepancies are found, new subgrade moduli are provided based on the provided pressures at the incompatible locations.
4. The structural engineer receives updated subgrade moduli for each of the discretized locations and analyzes the foundation model again with the respective subgrade modulus corresponding to each discrete area.
5. Steps 3 and 4 are repeated until the entire mat is compatible between the structural model and the soil model within some specified tolerance.

According to Ulrich, deflection compatibility can be achieved within three iterations. However, given that this procedure is necessary for every load case and that a mat foundation may have up to 50 different load cases that account for each of the gravity and seismic cases, the analysis can be quite cumbersome to perform. For this reason, upper and lower bound analysis based on a range of possible soil properties is sometimes recommended [49].

1.7. One-Way Shear in Mat Foundations

The prior review of one-way shear strengths in beams and of foundation loading effects can be generalized to mat foundations. Mat foundations are traditionally proportioned to resist the two-way punching shear demands without shear reinforcement. The flexure demands are then met by placing sufficient longitudinal steel throughout the mat. Typically, the same amount of steel is placed in the top and bottom of the mat [49]. Due to the large number of columns and large core wall anchoring into the mat and the large footprint and depth of the mat causing nonuniform soil response, the simplified approach for footings is usually not adopted and the more sophisticated analysis considering soil and mat stiffnesses is used.

Finite element software with the thick plate element formulation to account for shear deformations is typically used to model the mat with some stiffness modifier to account for cracking. The soil structure interaction with the underlying soil is usually performed with the Discrete Area method to iteratively obtain a compatible set of soil pressures and soil settlement.

Once the soil pressures are obtained, design strips and perimeters around columns and walls are designated for analysis. A perimeter of $d/2$ corresponds to the critical sections for checking punching shear strength while a distance of d applies for checking one-way shear strengths (see Figure 1-25). There is currently no consensus as to the effective width of the design strip for checking one-way shear strength in mats. As it is unlikely that the entire cross section of the mat can sustain the shear strength simultaneously, especially when shear reinforcement is not present, a conservative width on the order of d plus the core wall dimension have been proposed

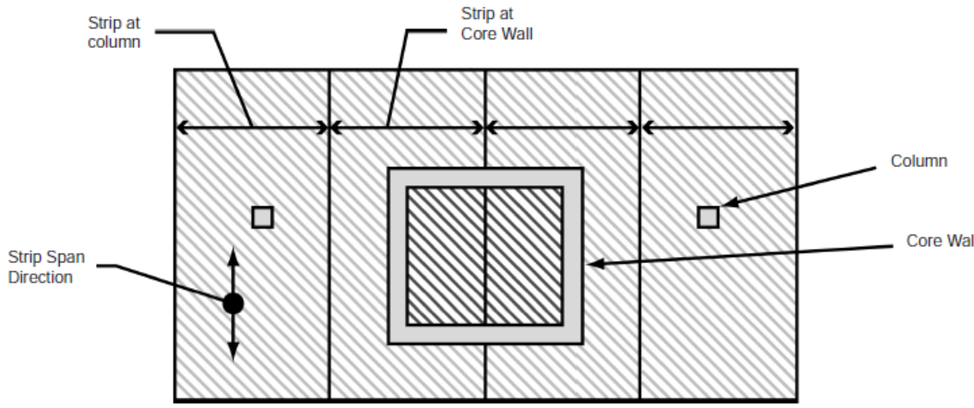

Figure 1-25: Example design strip layout for one-way shear and flexure design in mat foundations [49].

In addition to traditional vertical loads and overturning, a mat foundation is subject to additional factors that change the demand forces and one-way shear strength.

1.7.1. Backstay Effect

The backstay effect is applicable to buildings with multiple subterranean floors, which are typically used for the parking garages of high-rise buildings. The lateral loads and associated overturning moments can be partially resisted by a force couple acting on the basement walls as shown in Figure 1-26. The effectiveness of the backstay effect depends largely on the interaction between the basement walls, floor diaphragms, and the supporting soil. Design offices typically deal with the uncertainty in structural and soil stiffness by employing a sensitivity analysis considering upper and lower bounds on soil and structural stiffness, which reduces the amount of overturning resisted by the mat if the mat were at the ground level. Another common approach is to design the mat foundation for the full overturning moments at ground level without any reductions through considering the backstay effect.

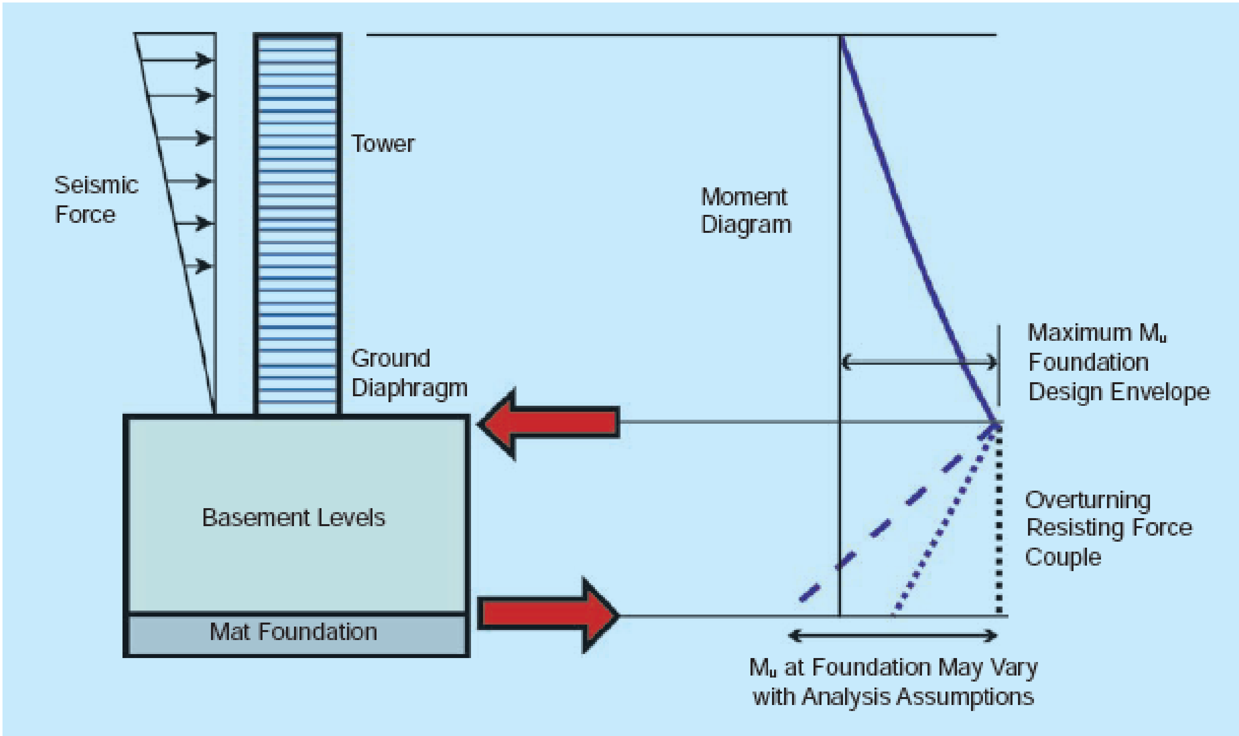

Figure 1-26: Backstay effect in high-rise buildings. Demands are reduced on the mat foundation based on the lateral stiffness of the soil [49].

1.7.2. Lateral Earth and Hydrostatic Pressures

As mat foundations are frequently constructed several stories beneath the ground surface, there are significant lateral loads imposed by the at-rest earth pressure on the mat foundation and basement walls. At the foundation level, these lateral loads apply on both sides of the mat, introducing additional axial compression. These axial loads are rarely accounted for in design since it is difficult to precisely quantify the extent of these loads. However, as Section 1.5.6 describes and most empirical equations suggests, axial compression provides positive benefits to the one-way shear strength.

For tall buildings in seismic regions, seismic activity typically imposes the most severe structural demands. In addition to overturning moments, the lateral loads applied to the structure during an earthquake must also be resisted by the foundation system. For tall buildings with multiple subterranean levels, the lateral seismic loads are resisted by a combination of passive or active earth pressure, friction on the basement walls, and friction along the base of the mat foundation [39]. Friction on the basement walls reduces the lateral demands on the foundation mat. The cases of passive or active earth pressure at the mat foundation level fall under the same category as the at-rest earth pressures, where lateral earth pressure applies axial compression in the mat. Lastly, friction on the bottom of the mat foundation will point contrary to the direction of sliding. As soil pressures are higher on the compressed side of the mat under overturning, it can be reasonably assumed that significant frictional forces will develop in these regions. These frictional forces on the base of the mat can provide actions that resemble axial load and are thought to also increase the one-way shear capacity as well. This behavior is as illustrated in Figure 1-27.

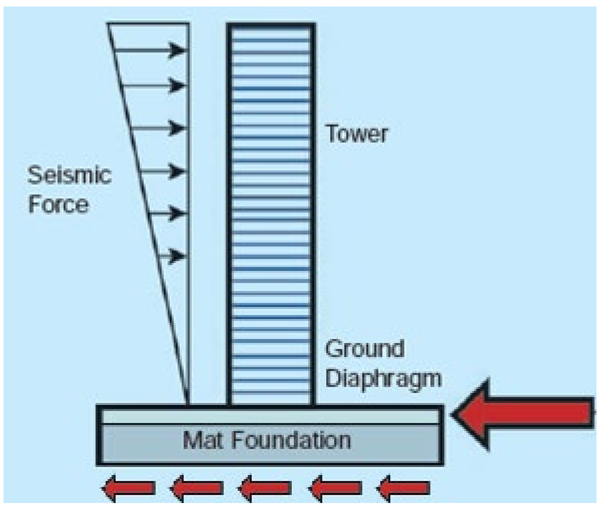

Figure 1-27: Friction on base of mat foundation (Adapted from Klemencic, et al.) [49]

1.7.3. Further Studies Required on One-Way Shear in Mat Foundations

Considering all discussed effects in mat foundations, further study is required to better understand one-way shear in mat foundations. One-way shear is influenced by both the bending moment and the demand shear forces, making the problem particularly sensitive to the soil pressure distributions. The soil pressures affect the design shear and moment greatly with only a small change in soil pressure distribution. As the bending moment depends on the second integral of the pressure distribution along a design strip, small changes in the soil pressures are amplified quadratically in the bending moment. One case study shows a 43% change in peak bending moment with only a 9% change in the maximum bearing pressure [40]. The influence of clamping on the shear strength is also a question.

To accurately analyze the mat's one-way shear strength, there are potentially up to 50 load cases that must be considered. Performing the Discrete Area method on 50 load cases and including sensitivity analyses to investigate one-way shear strengths is rarely performed in practice due to the sheer volume of computation and checks to be done. Foundation software models also usually do not consider reinforced concrete mechanics in detail and cannot predict failure. While design strips to obtain shear and moment demands are useful in design, the lack of accurate numerical simulations to predict one-way shear failure in foundations has resulted in one-way mat foundation shear being an open topic for research.

1.8. References

[1] D. Mitchell, J. Marchand, P. Croteau and W. D. Cook, "Concorde Overpass Collapse: Structural Aspects," Journal of Performance of Constructed Facilities, vol. 25, no. 6, pp. 545-553, 2011.

[2] K. D. Palmer, "Nonductile Concrete Frames," Structure Magazine, Nov 2019. [Online]. Available: https://www.structuremag.org/?p=15185. [Accessed June 2024].

[3] J. Feld, "Shear Failures in Frames and Slabs," Building Research and Practice, pp. 264-270, 1974.

[4] C. W. Dolan, "Observations on Concrete Shear Strength," Concrete International, vol. 42, no. 4, pp. 51-56, 2020.

[5] F. J. Vecchio and M. P. Collins, "The Modified Compression Field Theory for Reinforced Concrete Elements Subjected to Shear," ACI Journal Proceedings, vol. 83, no. 2, pp. 219-231, 1986.

[6] Z. P. Bazant and M. Gambarova, "Rough Cracks in Reinforced Concrete," Journal of the Structural Division, vol. 106, pp. 1947-1966, 1980.

[7] J. C. Walraven and H. W. Reinhardt, "Theory and Experiments on the Mechanical Behavior of Cracks in Plain and Reinforced Concrete Subjected to Shear Loading," HERON, vol. 26, 1981.

[8] F. J. Vecchio and D. Lai, "Crack Shear-Slip in Reinforced Concrete Elements," Jouranl of Advanced Concrete Technology , vol. 2, no. 3, pp. 289-300, 2004.

[9] P. M. Calvi, E. C. Bentz and M. P. Collins, "Pure Mechanics Crack Model for Shear Stress Transfer in Cracked Reinforced Concrete," ACI Structural Journal, vol. 114, no. 2, pp. 545-554, 2017.

[10] F. Cavagnis, J. T. Simoes, M. F. Ruiz and A. Muttoni, "Shear Strength of Members without Transverse Reinforcement Based on Development of Critical Shear Crack," ACI Structural Journal, vol. 117, no. 1, pp. 103-118, 2020.

[11] ASCE/ACI Committee 445 on Shear and Torsion, "Recent Approaches to Shear Design of Structural Concrete," Journal of Structural Engineering, vol. 124, no. 12, pp. 1375-1417, 1998.

[12] E. G. Sherwood, E. C. Bentz and M. P. Collins, "Evaluation fo Shear Design Methods for Large, Lightly-Reinforced Concrete Beams," Advances in Engineering Structures, Mechanics & Construction, pp. 153-164, 2006.

[13] P. S. Wong, F. J. Vecchio and H. Tromels, "VecTor2 & Formworks User's Manual Second Edition," VecTor Analysis Group, Toronto, 2002.

[14] J. J. Poldon and E. C. Bentz, "Shining a New Light on the Riddle of Shear," Concrete International, vol. 45, no. 2, pp. 17-25, 2023.

[15] A. Ghali and S. A. Youakim, "Headed Studs in Concrete: State of the Art," ACI Structural Journal, vol. 102, no. 5, pp. 657-667, 2005.

[16] E. N. Vintzeleou and T. P. Tassios, "Mathematical models for dowel action under monotonic and cyclic conditions," Magazine of Concrete Research, vol. 38, no. 134, pp. 13-22, 1986.

[17] K.-H. Reineck, E. C. Bentz, B. Fitik, D. A. Kuchma and O. Bayrak, "ACI-DAfStb Database of Shear Tests on Slender Reinforced Concrete Beams without Stirrups," ACI Structural Journal, vol. 110, no. 5, pp. 867-875, 2013.

[18] Z. P. Bazant and M. T. Kazemi, "Size Effect on Diagonal Shear Failure of Beams without Stirrups," ACI Structural Journal, vol. 88, no. 3, pp. 268-276, 1991.

[19] M. P. Collins, P. T. Quach and E. C. Bentz, "Shear Strength of Thick Slabs," ACI Structural Journal, vol. 117, no. 4, pp. 115-126, 2020.

[20] A. S. Lubell, E. C. Bentz and M. P. Collins, "Headed Shear Reinforcement Assemblies for One-Way Shear," ACI Structural Journal, vol. 106, no. 6, pp. 878-889, 2009.

[21] A. S. Lubell, E. C. Bentz and M. P. Collins, "Shear Reinforcement Spacing in Wide Members," ACI Structural Journal, vol. 106, no. 2, pp. 205-214, 2009.

[22] R. J. Frosch, "Behavior of Large-Scale Reinforced Concrete Beams with Minimum Shear Reinforcement," ACI Structural Journal, vol. 97, no. 6, pp. 814-820, November 2000.

[23] P. T. Quach, "Understanding and Safely Predicting the Shear Response of Large-Scale Reinforced Concrete Structures," Graduate Department of Civil Engineering University of Toronto, Toronto, 2016.

[24] B. Mihaylov, "Behaviour of Deep Reinforced Concrete Beams under Monotonic and Reversed Cyclic Load," University of Toronto, Toronto, 2008.

[25] M. P. Collins and D. Mitchell, Prestressed Concrete Structures, Response Publications, 1997.

[26] D. Qing, W.-J. Yi and F.-J. Tang, "Effect of Coarse Aggregate Size on Shear Behavior of Beams without Shear Reinforcement," ACI Structural Journal, vol. 114, no. 5, pp. 1131-1142, 2017.

[27] H. P. Taylor, "Shear Strength of Large Beams," Journal of the Structural Division, vol. 98, no. 11, pp. 2484-2488, 1972.

[28] E. G. Sherwood, E. C. Bentz and M. P. Collins, "Effect of Aggregate Size on Beam-Shear Strength of Thick Slabs," ACI Structural Journal, vol. 104, no. 2, pp. 181-190, 2007.

[29] A. B. Acevedo, E. C. Bentz and M. P. Collins, "Influence of Clamping Stresses in the Shear Strength of Concrete Slabs Under Uniform Loads," Journal of Earthquake Engineering, vol. 13, no. S1, pp. 1-17, 2009.

[30] P. Adebar and M. P. Collins, "Shear Strength of Members without Transverse Reinforcement," Canadian Journal of Civil Engineering, vol. 23, no. 1, pp. 30-41, 1996.

[31] J. Ehmann and U. Kuhlmann, "Shear Resistance of Concrete Bridge Decks in Tension," Composite Construction in Steel and Concrete V Proceedings, pp. 67-76, 2012.

[32] ACI Committee 318, Building Code Requirements for Structural concrete (ACI 318-19) and Commentary (ACI 318R-19, Farmington Hills, MI: American Concrete Institute, 2019.

[33] B. P. Zdenek, Q. Yu, W. Gerstle, J. Hanson and J. Ju, "Justification of ACI 446 Proposal for Updating ACI Code Provisions for Shear Design of Reinforced Concrete Beams," ACI Structural Journal, vol. 104, no. 5, pp. 601-610, 2007.

[34] E. C. Bentz and M. P. Collins, "Development of the 2004 CSA A23.3 Shear Provisions for Reinforced Concrete," Canadian Journal of Civil Engineering, vol. 33, no. 5, pp. 521-534, 2006.

[35] EN 1992 1-1, 1992, "Design of Concrete Structures, Part 1: General Rules and Ruels for Buildings (EuroCode 2)," European Committee for Standardization , Brussels, Belgium.

[36] R. J. Frosch, Q. Yu, G. Cusatis and Z. P. Bazant, "A Unified Approach to Shear Design," Concrete International, vol. 39, no. 9, pp. 47-52, 2017.

[37] A. K. Tureyen and R. J. Frosch, "Concrete Shear Strength: Another Perspective," ACI Structural Journal, vol. 100, no. 5, pp. 609-615, 2003.

[38] Haggar Construction, "Haggar Construction," [Online]. Available: https://haggarconstruction.co.uk/blog/installing-the-correct-groundworks-foundations/. [Accessed 2024].

[39] J. P. Moehle, Seismic Design of Reinforced Concrete Buildings, McGraw-Hill Education, 2015.

[40] J. F. Horvilleur and V. B. Patel, "Mat Foundation Design - A Soil Structure Interaction Problem," ACI Symposium Publication, vol. 152, pp. 51-94, 1995.

[41] A. N. Talbot, "Reinforced Concrete Wall Footings and Column Footings," University of Illinois Bulletin, 1913.

[42] F. E. Richart, "Reinforced Wall and Column Footings Part 2," ACI Journal Proceedings, vol. 45, no. 11, pp. 237-260, 1948.

[43] A. Uzel, B. Podgorniak, E. C. Bentz and M. P. Collins, "Design of Large Footings for One-Way Shear," ACI Structural Journal, vol. 108, no. 2, pp. 131-138, 2011.

[44] J. Hegger, A. G. Sherif and M. Ricker, "Experimental Investigations on Punching Behavior of Reinfored Concrete Footings," ACI Structural Journal, vol. 103, no. 4, pp. 604-613, July 2006.

[45] Z. Bonic, N. Davidovic, T. Vacev, N. Romic, E. Zlatanovic and J. Savic, "Punching Behavior of Reinforced Concrete Footings at Testing and According to Eurocode 2 and fib

Model Code 2010," International Journal of Concrete Structures and Materials, vol. 11, no. 4, pp. 657-676, 2017.

[46] W. Zhang, B. Li, H. Hwang, J. Zhang, L. Xiao and W. Yi, "Punching Shear Strength of Reinforced Concrete Columns Under Eccentric Compression," Engineering Structures, 2019.

[47] D. Loukidis, T. Chakraborty and R. Salgado, "Bearing capacity of strip footings on purely frictional soil under eccentric and inclined loads," Canadian Geotechnical Journal, vol. 45, no. 6, pp. 768-787, 2008.

[48] E. J. Ulrich, Jr, "Subgrade Reaction in Mat Foundation Design," ACI Symposium Publications, vol. 152, pp. 95-116, 1995.

[49] R. Klemencic, I. S. McFarlane, N. M. Hawkins and S. Nikolaou, "NEHRP Seismic Design Technical Brief No. 7: Seismic Design of Reinforced Concrete Mat Foundations - A Guide for Practicing Engineers (NIST GCR-917-22)," National Institute of Standards and Technology, Gaithersburd, MD, Aug 2012.

CHAPTER 2: SHEAR STRENGTH OF LARGE SHEAR-CRITICAL BEAMS WITH HIGH-STRENGTH REINFORCEMENT

Jerry Y. Zhai and Jack P. Moehle

2.1. Abstract

Laboratory tests of deep, lightly reinforced concrete members without shear reinforcement demonstrate that unit shear strength decreases with increasing depth and with decreasing tension longitudinal reinforcement ratio. Design procedures for one-way shear strength in ACI 318-19 incorporate these effects but result in relatively low design shear strengths for some members with both large depth and low reinforcement ratio. To better understand the effects of depth and longitudinal reinforcement on shear strength, tests were conducted on beams with varying depth, relatively low ratio of high-strength longitudinal reinforcement, and with either no shear reinforcement or minimum shear reinforcement. Loads were applied slowly and monotonically and included concentrated loads plus self-weight. Beam supports were either point supports, as in a beam, or uniformly distributed, as in a foundation. The test results demonstrate size and longitudinal reinforcement effects and suggest that a lower-bound unit shear strength may be applicable for design of some members with both large depth and low reinforcement ratio.

Keywords: foundation mat; shear; size effect, tension shift, high-strength reinforcement, shear reinforcement

2.2. Introduction

The ACI 318 building code [1] permits reinforced concrete slabs and shallow foundations to be designed without shear reinforcement if the concrete section alone is sufficient to resist the design shear forces. This allowance for foundations extends to relatively thick foundation mats that, in the case of tall buildings, can have a depth as much as 12 ft (3.7 m) or more. In these large concrete elements without shear reinforcement, a size effect is

---

Submitted for publication in ACI Structural Journal

observed whereby sectional shear stresses at failure decrease with increasing member depth [2]. Reinforced concrete elements without shear reinforcement also experience a longitudinal tension reinforcement ratio effect whereby sectional shear stresses at failure decrease with decreasing longitudinal tension reinforcement ratio [2]. These observations have prompted the introduction of new equations for nominal one-way shear strength in ACI 318-19 that incorporate a combined effect of both depth and reinforcement ratio for one-way members without shear reinforcement [3]. For members with both large depth and low reinforcement ratio, the new equations result in nominal shear strengths that may be much lower than the nominal one-way shear strength prescribed by previous ACI 318 Codes. The penalties of large member depth and low longitudinal reinforcement ratio can be avoided if ACI 318-19 minimum shear reinforcement is provided.

To test the effects of both thickness and longitudinal reinforcement ratio on the shear strength of one-way members, two large-scale beams were constructed and tested. The beams had total lengths of approximately 76 ft (23.2 m) with total depths of either 11'-8" (3.56 m) or 8'-0" (2.44 m). The beam longitudinal reinforcement ratio was varied within a range representative of that used in mat foundations. Spans either had no shear reinforcement or shear reinforcement corresponding to $A_{v,min}$ as defined by ACI 318-19. The beams were loaded either as simple, suspended spans or as spans supported from underneath by a uniformly distributed reaction. The large beam tests were supplemented by three additional beams with smaller spans and depths, as reported elsewhere [4]. The tests provide benchmark data on one-way shear strength and insights into design requirements.

2.3. Research Significance

Recent changes to provisions for one-way shear strength in ACI 318-19 can result in substantial reductions in nominal shear strength for deep members with low longitudinal reinforcement ratio and no shear reinforcement. Those same provisions indicate that the addition of minimum shear reinforcement restores the contribution of the concrete section to nominal shear strength. Additional provisions in ACI 318-19 permit the use of Grades 80 and 100 for longitudinal reinforcement, without a penalty to nominal one-way shear strength. The tests reported in this paper provide data on one-way shear strength of deep members with high-strength longitudinal reinforcement at low reinforcement ratios, both with and without minimum shear reinforcement.

2.4. Findings From Prior Studies

Analytical and experimental studies have demonstrated that the shear strength of normal-strength reinforced concrete members without shear reinforcement is primarily dependent on the aggregate interlock mechanism across flexure-shear cracks and a lesser contribution by shear in the uncracked compression zone [2]. As the member develops progressively wider inclined flexure-shear cracks with increased applied load, aggregate interlock resistance decreases. For relatively slender members, diagonal tension shear failure occurs when the aggregate interlock mechanism can no longer resist the applied loads, leading to sudden failure, commonly with minimal signs of distress prior to failure. The effectiveness of aggregate interlock in members without shear reinforcement is strongly affected by the member depth, an effect known as the size effect, and the longitudinal tension reinforcement ratio.

According to ACI 445 Shear and Torsion Committee, the main mechanism behind the size effect is the increased width of inclined cracks in deeper beams when compared with shallower beams at an equivalent stage in loading [2]. One effect of increased crack width is reduced effectiveness of the aggregate interlock mechanism since it is dependent on the crack width relative to aggregate particle size. It is generally impractical to mitigate this concern by adjusting the concrete mixture design to include larger nominal aggregate size as the beam depth increases. The size effect has been studied experimentally in multiple test series where test beams with controlled concrete, reinforcement, and geometric properties demonstrate a clear reduction in sectional shear stress at failure with increasing member depth [5, 6]. The ACI 445/DAfStb one-way shear database for similarly shows a downward trend in unit shear strength with increasing depth [7].

In a similar fashion as the size effect, a low longitudinal tension reinforcement ratio results in larger crack spacing and wider cracks, leading to reduced aggregate interlock and reduced shear strength [2]. This effect is demonstrated in tests by Lubell et al. and in analyses of the ACI445/DafStb one-way shear database [7, 8]. This effect has been predominantly demonstrated in beams of smaller depth, usually with $d < 4$ ft (1.22 m), where d is the distance from the extreme compression fiber to the centroid of the longitudinal tension reinforcement. It is less well demonstrated in larger members because most such tests have used reinforcement ratios less than 1.0% such that the effect of wider variations in reinforcement ratio are not clear.

Crack width may also increase when using high-strength longitudinal reinforcement, both because reinforcement ratios are decreased and because the reinforcement sustains higher working stresses. Recent trends of placing high-strength reinforcement in lightly reinforced members such as mat foundations have brought this issue to the forefront. The authors are aware of only eleven unique shear tests containing high-strength reinforcement with yield strength of $f_y \geq 80\ ksi$ (550 MPa) and reinforcement ratio of $\rho_w = A_s/b_w d < 0.5\%$, where A_s = area of longitudinal tension reinforcement and b_w = web width, all conducted with smaller beam depths [7]. Thus, the effect on shear strength of high-strength longitudinal reinforcement in deep, lightly reinforced members is unclear.

Shear strength is also affected by loading type and aspect ratio. Overall shear resistance of reinforced concrete beams is determined by beam action or arch action, with the transition between the two controlling mechanisms occurring at a shear span-to-effective-depth ratio (*a/d*) of about 2.5 [9]. At *a/d* larger than 2.5, beam action becomes the dominant failure mode as the angle between support and load is too shallow for a single compression strut to be effective for arch action. This observation is common to beams that are loaded from above by either a point load or a uniform load, with concentrated supports below the beam. The influence of shear span to depth ratios in footings is somewhat different. Footings generally resist applied loads via upwardly reacting soil pressures, which are often idealized for design as uniformly reacting on the base of the footing. To investigate one-way shear isolated from two-way shear in footings, Uzel et al. tested beams loaded uniformly from below to simulate uniform soil pressure conditions [10]. That investigation found that, at *a/d* ratios less than 2.5, size effects do not appear to apply because failures were characterized by failure of struts. However, footing design is also unlike beam design in that it needs to also consider two-way or punching shear mechanisms. Laboratory tests show that rectangular two-way footings tested with uniform or realistic soil support reactions, *a/d* ratios of up to 3, and depths within 20” (510 mm) generally failed in punching shear [11]. Only the deepest rectangular footings in Richart’s series 5 tests with *a/d* = 3.3 exhibited one-way shear failures [12], suggesting that the *a/d* ratio in footings where sectional shear controls is higher than that in beams. For mat foundations with relatively large depths, relatively large *a/d* ratios, and substantial overturning moment from lateral loads, one-way shear is again a concern.

To demonstrate the size effect in very deep beams and mats, one-way shear tests were conducted by Shioya et al. [13] and Collins et al. [14]. The Shioya beam was 9’-10” (3.0 m) deep with $\rho_w = 0.41\%$ and the Collins beam was 13’-2” (4.0 m) deep with $\rho_w = 0.66\%$. Both tests provide valuable experimental data illustrating how the size effect applies in large concrete elements. However, these specimens experienced relatively small peak longitudinal steel tensile strains at 0.0007 and 0.001, respectively, such that the effects of high strains on shear strength were not observable.

Shear reinforcement provides an alternative force path to carry shear forces after initiation of flexure-shear cracks [15]. It can also act as a restraint against further crack growth. Tests by Lubell et al. [16] [17] and by Frosch [18] demonstrate that ACI minimum shear reinforcement is effective in suppressing the size effect in 3 ft (0.91 m) deep specimens, provided spacing of shear reinforcement does not exceed ACI 318 limits of $d/2$ and 24" (0.61 m).

2.5. Specimen Details

Two large test beams, designated UCB Beams 1 and 2, were designed, constructed, and tested. Each beam had two spans, with different reinforcement or loading configuration in each of the two spans. Taken together, this results in a total of four different tests, designated Phases 1 and 2 for UCB Beam 1 and Phases 3 and 4 for UCB Beam 2. Both specimens were constructed with normal-weight concrete with specified compressive strength of 4000 psi (27.6 MPa) and A1035 Gr.100 (700 MPa) longitudinal steel. Figure 1 shows photographs of the two test beams and Table 1 presents a summary of the properties.

Figure 1: UCB Beam 1 (left) and UCB Beam 2 (right)

Table 1: Summary of test beams.

Beam	b_w in (mm)	a ft, (m)	d in (mm)	a/d	ρ_w %	f_c' psi (MPa)	a_g in (mm)	A_s in^2 (mm^2)	f_y psi (MPa)
Phase 1	10 (254)	35 (10.7)	130	3.23	0.46	4600 (32)	3/4 (19 mm)	6 (3900)	120**
Phase 2	10 (254)	35 (10.7)	131	3.21	0.84	4600 (32)	3/4 (19 mm)	11 (7100)	120**
Phase 3	10 (254)	35* (10.7)	93	4.52	0.22	4600 (32)	3/4 (19 mm)	2 (1300)	120**
Phase 4	10 (254)	35 (10.7)	93	4.52	0.22	5000 (34)	3/4 (19 mm)	2 (1300)	120**

* Shear Span over which uniform reaction is acting
** Yield strength by 0.2% offset method as no well-defined plateau exists for A1035 steel.
f_c' = concrete compressive strength measured at time of testing.
a_g = nominal maximum aggregate size.

Figure 2 shows the reinforcement and loading configuration of UCB Beam 1. The beam was configured to represent a full-scale slice through a mat foundation with bending about a single axis perpendicular to the test specimen span. The overall dimensions of the beam were 76 ft (23.16 m) long, 140 in (3.56 m) deep, and 10 in (0.25 m) wide. For testing, the beam was supported on "roller" supports centered at 3 ft (0.914 m) from each beam end, with loading provided by self-weight plus a concentrated downward force near midspan.

The east span of the beam, referred to as Phase 1, was constructed without shear reinforcement. The west span, or Phase 2, was provided with deformed No. 5 (16 mm) ASTM A615 Grade 60 (420 MPa) single-legged stirrups with heads at both ends, spaced at 35" (0.88 m) on centers, resulting in a provided value of $\frac{A_v}{b_w s}$ = 0.00089, where A_v = area of shear reinforcement within spacing s. The provided transverse reinforcement ratio corresponds to the minimum shear reinforcement $A_{v,min}$ of ACI 318, but the spacing exceeds the maximum permitted spacing of 24" (610 mm). The provision of shear reinforcement in the west span was expected to result in a significant increase in shear strength compared with the east span.

Longitudinal reinforcement was provided by deformed No. 9 (29 mm) ASTM A1035 Grade 100 (700 MPa) bars. For the east span of Beam 1, it was desirable to achieve a relatively large tensile strain, but not yielding, in the longitudinal tension reinforcement at the time of shear failure in that span. A total of eleven No. 9 bars were provided, but only six of them were bonded to the concrete, reaching an effective longitudinal reinforcement ratio of 0.46%. The remaining five No. 9 bars were positioned in ungrouted ducts. All longitudinal bars were spliced with mechanical couplers. For Phase 1 loading, the centrally located concentrated force P was increased until shear failure was achieved in the weaker east span. After failure, external shear reinforcement was post-tensioned to close the shear cracks and provide additional shear strength in the east span, and the five previously ungrouted longitudinal bars were grouted along the east span, effectively bonding the bars and increasing the flexural reinforcement ratio in both spans to 0.84%. The concentrated force P was then re-applied and increased in the Phase 2 test until failure was achieved in the west span with shear reinforcement.

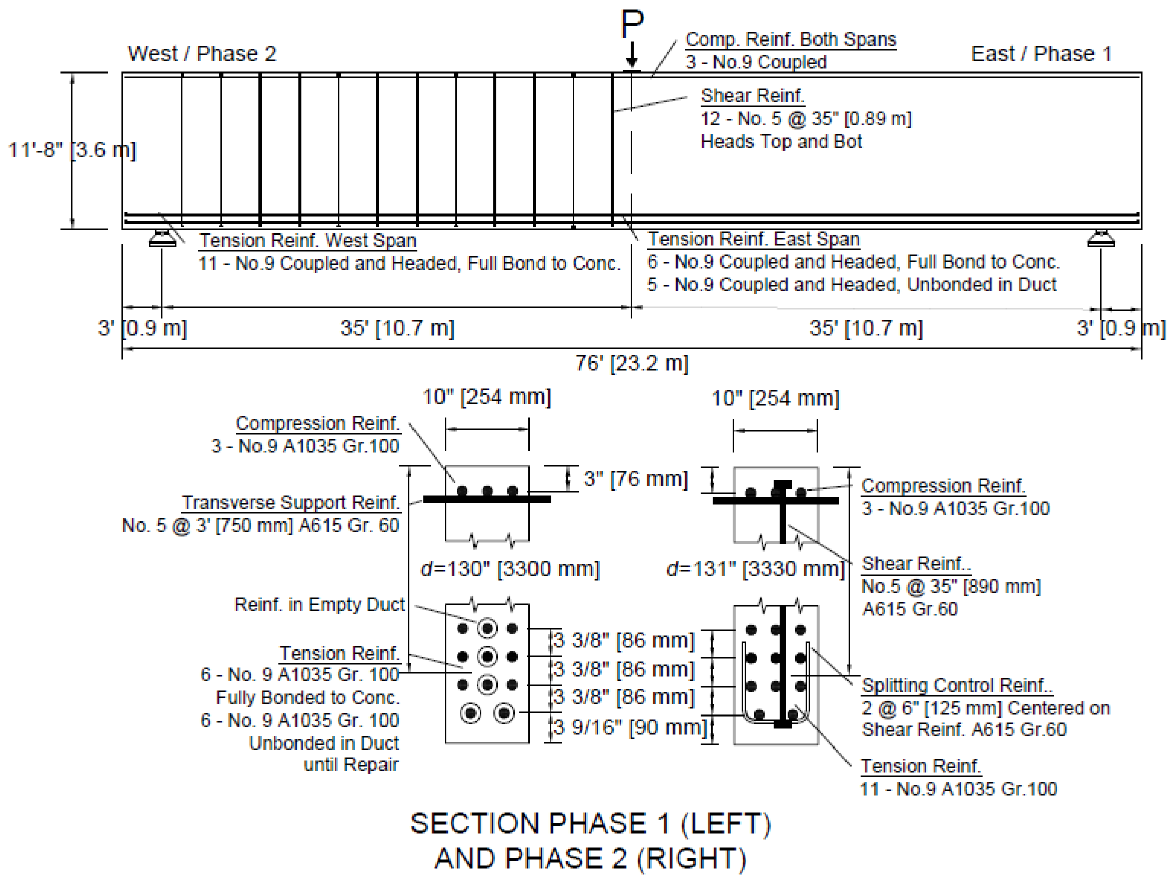

Figure 2: UCB Beam 1 details (all dimensions in US customary units).

Figure 3 shows the reinforcement and loading configuration of UCB Beam 2. The overall dimensions of the beam were 73 ft 6 in (23.16 m) long, 96 in (2.44 m) deep, and 10 in (0.25 m) wide. Longitudinal reinforcement was provided by two deformed No. 9 (29 mm) ASTM A1035 Grade 100 (700 MPa) bars top and bottom. The longitudinal reinforcement ratio was $\rho_w = \frac{A_s}{b_w d} = 0.22\%$, which meets the minimum required shrinkage and temperature reinforcement ratio of 0.18% required by ACI 318-19. If considered as a beam rather than as a footing, ACI 318-19 requires a minimum steel ratio $\rho_w = \frac{3\sqrt{f_c'}}{f_y} = 0.0024$ based on specified compressive strength $f_c' = 4000$ psi (27.6 MPa) and the maximum value of $f_y = 80$ ksi (550 MPa) permitted by ACI 318-19. If the cap on f_y is removed and f_y is taken as 100 ksi (690 MPa), then the minimum ratio becomes 0.19%, which this specimen satisfies. The small value of ρ_w was intended to result in high tensile strains in the longitudinal tension reinforcement at the onset of shear failure in either span.

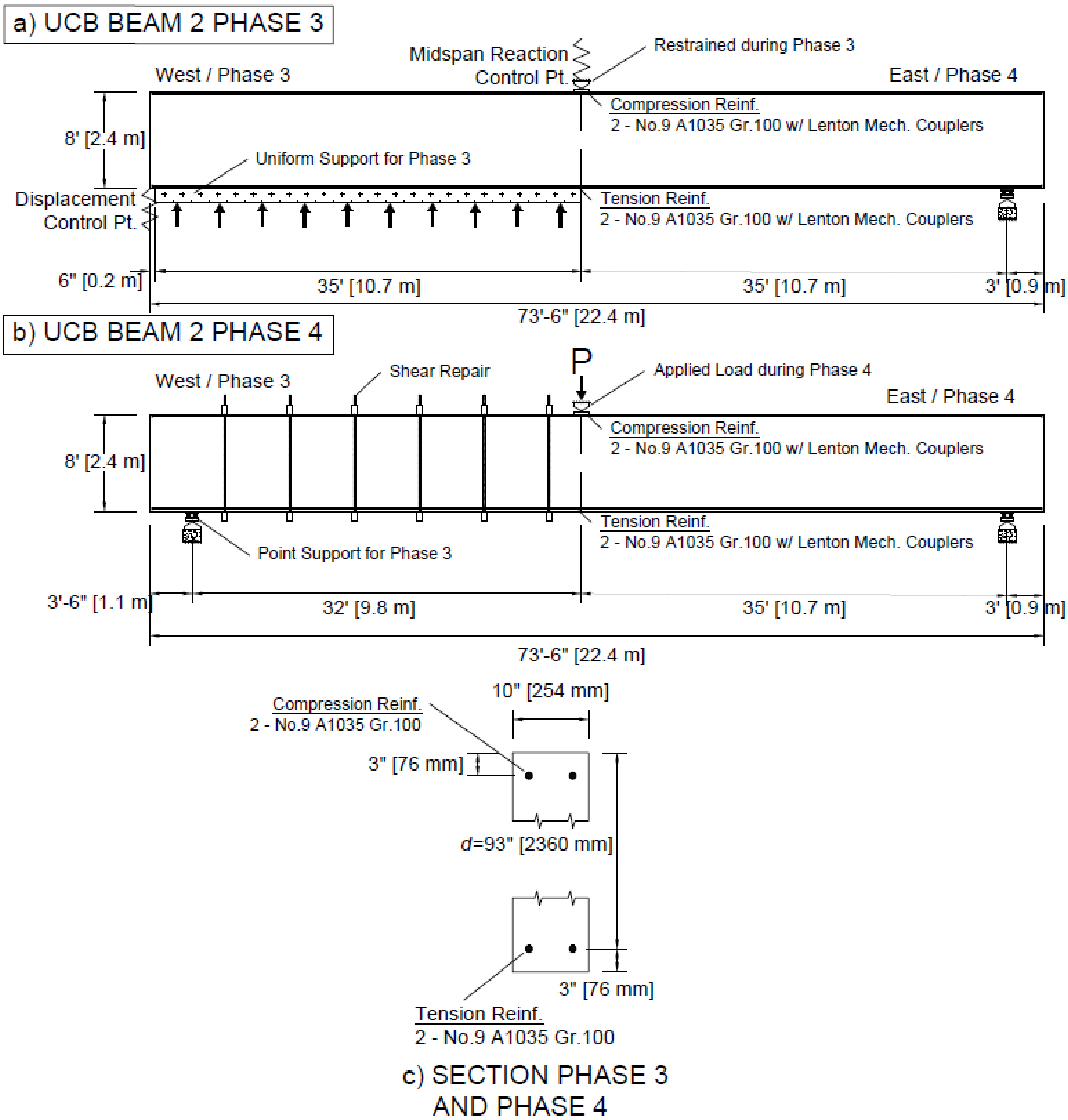

Figure 3: UCB Beam 2 details (all dimensions in US customary units).

Downward loads comprised self-weight plus a concentrated force *P* near midspan. For Phase 3 loading, the downward forces were resisted by a distributed support along the west half of the beam and a roller support at the east end of the beam (Figure 3a). The uniform reaction along the west half of the beam was intended to simulate an idealized footing-style loading in the west span. Failure for Phase 3 loading was expected to occur in the west half of the beam with the uniformly distributed reaction. For Phase 4 loading, the downward forces were resisted by roller supports at both ends of the beam (Figure 3b), which is more typical of a beam-style loading. The intent of this setup was to investigate differences between footing-style and beam-style loadings when both spans are identically reinforced and have the same shear span of 35 ft (10.67 m).

Figure 4 shows the shear and moment diagrams near the point of maximum loading for Phase 3 and Phase 4 loadings. It is noteworthy that the Phase 3 footing-style loading results in shear and moment diagrams in which the maximum shear and moment occur at the same beam section adjacent to the concentrated load (Figure 4a). In contrast, the Phase 4 beam-style loading results in the maximum shear and moment occurring at different beam sections (Figure 4b). Because the longitudinal tension reinforcement strain affects the shear strength, it is possible for the failure crack in a beam-style loading to occur anywhere within the shear span depending on detailing of the reinforcement and length of the shear span. Conversely, in a footing-style loading the failure surface is more likely to be located close to the concentrated midspan load because the region of maximum shear force and of maximum moment occur adjacent to that point.

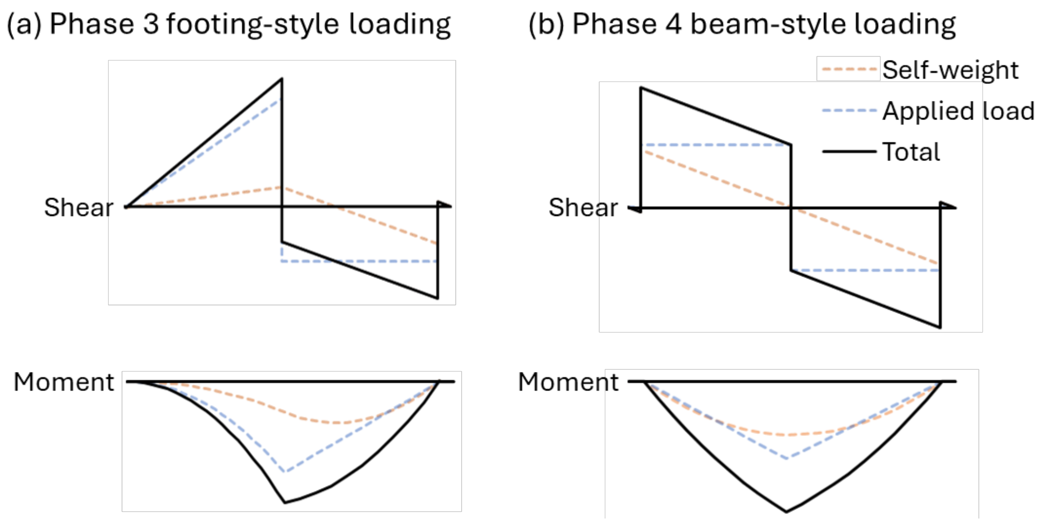

Figure 4: Shear force and bending moment diagrams for (a) Phase 3 footing-style loading and (b) Phase 4 beam-style loading.

For Phase 3 testing of Beam 2, the uniformly distributed reaction was achieved by using a line of ten equally spaced hydraulic jacks that applied equal vertical forces beneath the west span. During testing, the force in the upwardly acting jacks was increased until the beam was lifted off its temporary supports. After it was confirmed that the jacks fully supported the west span self-weight, the centrally located downward acting jack was activated and locked in position to provide a downward reaction P to resist further loading by the jacks beneath the west span. This achieves a pseudo uniform support on the west span, whose reaction was increased until failure occurred in the west span. After failure, the line of equally distributed jacks on the west span was removed and replaced with a “roller” support near the west end. External shear reinforcement was post-tensioned to close the shear cracks and provide additional shear strength in the west span. The centrally located jack was unlocked and used to apply a concentrated downward force *P*, which was increased in the Phase 4 test until failure was achieved in the simply supported east span.

2.6. Material Properties

Normal weight concrete had specified 28-day compressive strength of 4000 psi (27.5 MPa) with a maximum nominal aggregate size of ¾ inch (19 mm). A mixture design commonly used in mat foundations was selected, having high fly ash and slag content with no plasticizers. Companion 6 in by 12 in (150 mm by 300 mm) cylinders were stored adjacent to the test beams and were removed from their molds at the same time the forms were stripped from the test beams. The cylinders were tested at ambient moisture conditions around the same day as the beam tests, resulting in four different ages for the concrete cylinders corresponding to Test Phases 1 through 4, respectively. Figure 5 plots measured relationships between compressive stress and strain for concrete cylinders from each of the ready-mix trucks on test day. Mean compressive strength, splitting cylinder, and elastic modulus test results are summarized in Table 2.

Tensile tests were conducted on as-rolled reinforcing bars, with stress defined as tensile force divided by the nominal bar cross-sectional area and engineering strain based on the measured elongation divided by the initial gauge length of 8 in (200 mm). The ASTM A615 Gr. 60 reinforcement had a linear stress-strain relationship followed by a yield plateau at 70 ksi (483 MPa) and ultimate strength of 96 ksi (662 MPa). The ASTM A1035 Grade 100 reinforcement had a roundhouse stress-strain relationship with a yield strength of 120 ksi (830 MPa) by the 0.2% offset method. Due to difficulties in testing the Grade 100 bars, the stress-strain curve beyond the experimentally observed test beam steel strains was obtained but strains up to fracture of the bar were generally not obtained.

Table 2: Concrete material property summary.

	Phase 1	Phase 2	Phase 3	Phase 4
Age at Testing	43 days	65 days	28 days	41 days

Mean f_c'	4600 psi	4600 psi	4600 psi	5000 psi
Mean f_t (Splitting Tension)	426 psi	408 psi	443 psi	453 psi
Mean Elastic Modulus E_c	2730 ksi	2640 ksi	2740 ksi	2780 ksi

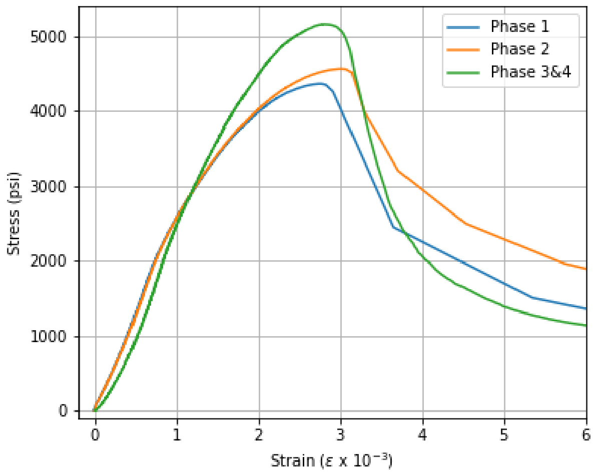

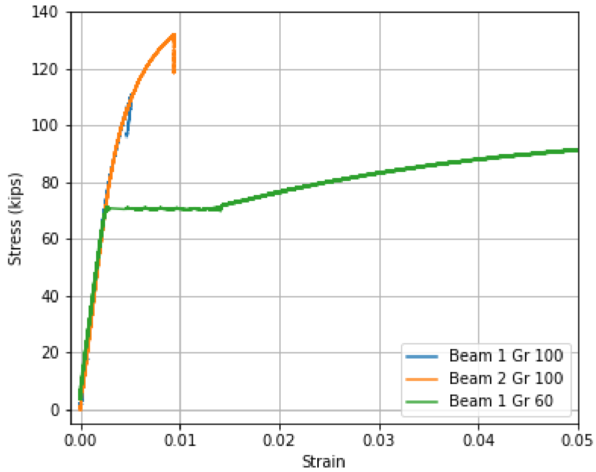

Figure 5a (left): Concrete stress-strain relationships and Figure 5b (right): Steel reinforcement stress-strain relationships.

2.7. Loading Apparatus And Instrumentation

The test apparatus and instrumentation for UCB Beams 1 and 2 had some common features and some features unique to each testing phase. Figure 6 shows the overall test geometry for Test Beam 1 and Test Beam 2. For the “roller” supports of all phases, a roller condition was simulated with a steel pivot block comprising two steel blocks with a machined semicircular slot into which a cylindrical steel bar was placed with grease to ensure near-zero moment resistance. The steel blocks were supported on heavily greased steel sheets that ensured near-zero horizontal resistance. A central frame was anchored to the strong floor and fitted with a hydraulic jack for downward loading. For Phases 1, 3, and 4, the central jack was displacement-controlled to apply either zero displacement or monotonically increasing displacement using a servo-valve up to the house pressure maximum of 3,000 psi. For Phase 2, the larger required loads required that the hydraulic system be powered pneumatically with an air pump to reach the jack’s maximum rating of 10,000 psi. Out-of-plane stability of the test beams was achieved via two pairs of A-frames installed near the roller supports and additional lateral supports mounted on the central frame. Low friction steel and greased brass plates at the interface between the lateral braces and the concrete surface enabled sliding with minimal resistance.

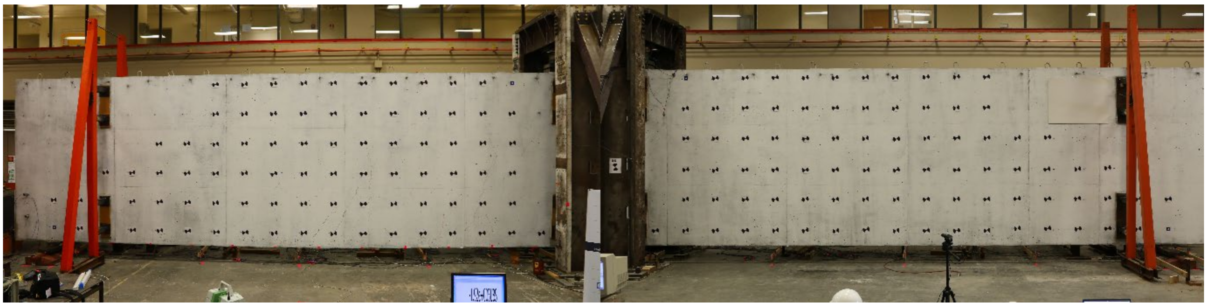

Figure 6a: Phase 1 and Phase 2 loading configurations.

Figure 6b: Phase 3 and 4 loading configurations.

Figure 7 shows the external shear reinforcement that was provided to close cracks and increase the shear strength of the west span of UCB Beam 2 following initial failure of that span during Phase 3 testing. A similar arrangement on the east span of Beam 1 was used following Phase 1 testing. The reinforcement comprised a yoke of two post-tensioned steel rods, one alongside each face of the beam, with steel tube anchor blocks bearing on the top and bottom faces of the beam.

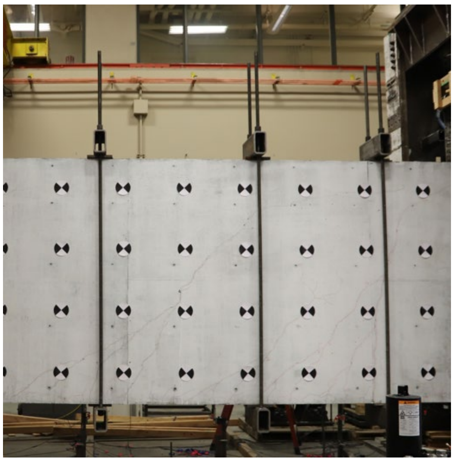

Figure 7: Shear repair brackets.

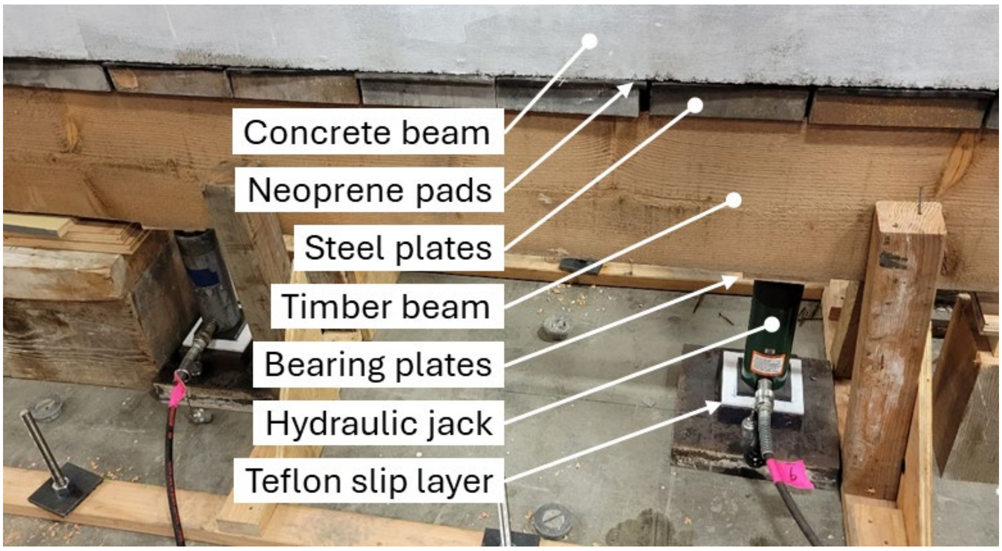

Figure 8: Phase 3 uniform loading setup.

For Test Beam 2 in its Phase 3 configuration, the west span was uniformly supported with hydraulic jacks. The jacks that composed the uniform support were manifolded together and controlled from a single point to develop equal force in all the jacks. A hand pump was used to ensure that the system pressure equalized uniformly and that the force was applied in a slow and controlled manner. As shown in Figure 8, the uniform support comprised, in order from bottom to top, white Teflon slip layers, two 20-k hydraulic jacks, steel bearing plates for the jacks, segmented timber beam spanning across a pair of jacks, segmented steel plates, and neoprene pads. This configuration was intended to allow the jacks to slide horizontally and avoid introducing longitudinal restraint on the concrete beam while distributing the jack forces uniformly beneath the concrete beam.

Each beam was instrumented with load cells, strain gauges, various displacement transducers at locations of interest, and 3D coordinate measurements of black and white "bowtie" targets as depicted in Figure 6. These targets were scanned with a laser scanner and recorded in a point cloud, enabling both generalized surface measurements as well as precise measurements of the target movements.

2.8. UCB Beam 1 Phase 1: Response Of Span Without Shear Reinforcement

Phase 1 emphasized the behavior of the east span of Beam 1 without shear reinforcement because that span was expected to be much weaker than the west span. Loading began on September 29, 2021, taking place over 2 days and approximately 9 hours of testing. Figure 9 shows the measured relationship between midspan applied force P and midspan deflection, with loading paused at seven load stages (LS) to mark crack locations, measure crack widths, and scan the surface of the beam with a laser scanner to record the spatial coordinates of the beam. Displacements start at 0 and do not include self-weight deflections.

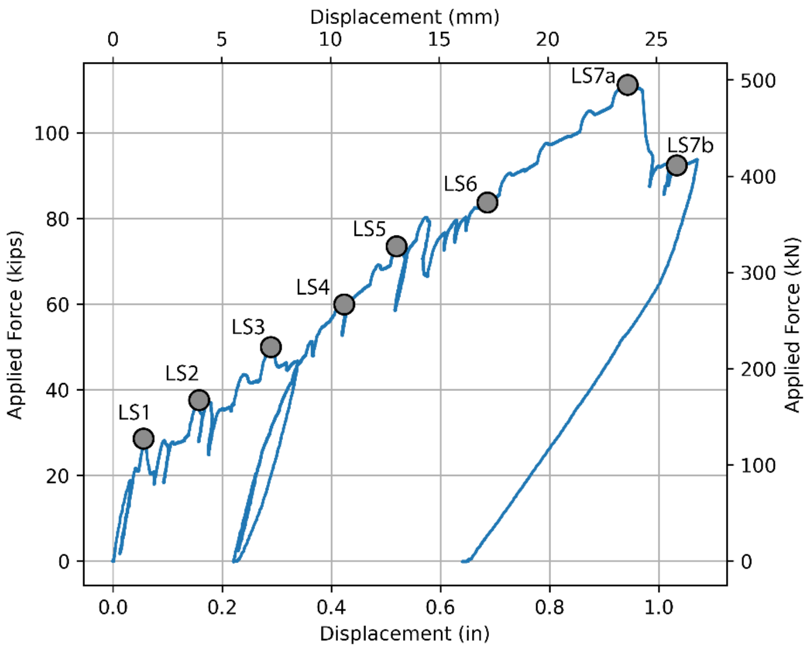

Figure 9: Measured relationship between applied force P and midspan displacement for Phase 1.

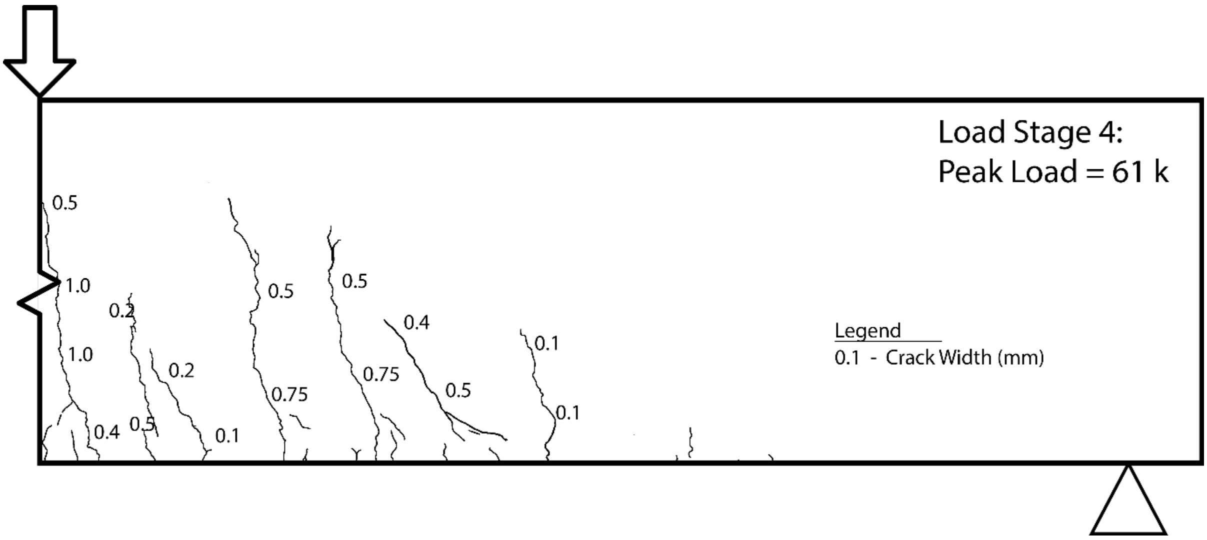

Figure 10a: Crack diagrams during Phase 1 Load Stage 4 (LS4).

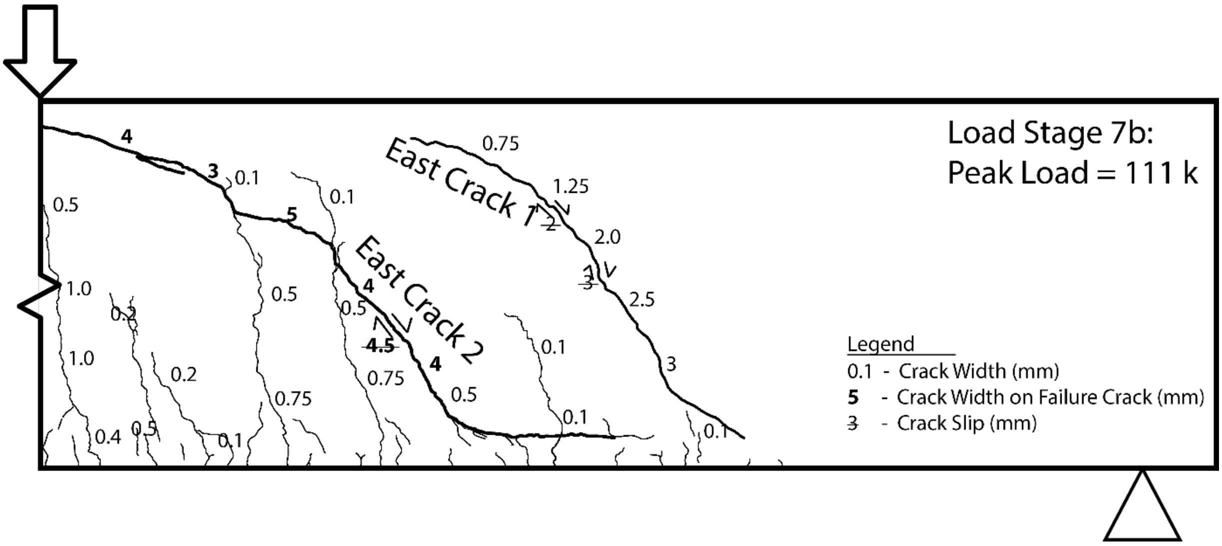

Figure 10b: Crack diagrams during Phase 1 Load Stage 7b (LS7b).

First flexural cracking occurred around 26 k (116 kN) of applied force P. Further loading developed several nearly vertical cracks close to the midspan. Around LS4, several cracks gradually inclined toward the loading point (Figure 10a). By LS5, all new and existing cracks developed at an inclination relative to vertical. LS6 was the last stage for which cracks were hand marked as the beam began to show signs of shear distress with crack widths reaching 0.03” (0.75 mm). At LS7a (Figure 9), the crack labeled “East Crack 1” (Figure 10b) appeared to be nearing capacity due to the increasing crack width and subtle reorientation toward the loading point.

At applied load of P = 111 k (494 kN), the applied load suddenly dropped by 18% of the maximum value to LS7b (Figure 9), as a second major crack labeled “East Crack 2” (Figure 10b) formed at an angle approximating 30 degrees. This new failure crack formed rapidly by branching between existing adjacent cracks at a shallower angle, extending from an existing flexure-shear crack on the bottom and projecting toward the point of load application. Further loading resulted in the observed plateau in the force-displacement curve near LS7b (Figure 9), with the failure crack growing to an estimated width of 0.2” (5 mm) as the deflection increased from 0.98” (24.9 mm) to around 1.1” (27.9 mm). The test was stopped to preserve the integrity of the flexural compression zone, which is necessary to repair the east span. After removing the load P, inspections showed that the concrete sections on opposite sides of this crack had slipped by 0.2” (4.5 mm) relative to one another. A residual displacement of 0.65” (16.5 mm) was observed as well as a 50% decrease in the unloading stiffness relative to the unloading stiffness at LS4 (Figure 9). At the end of Phase 1, the maximum width at mid-depth of “East Crack 1” was approximately 0.08” (2 mm) compared with the main failure crack “East Crack

2”, which had a maximum width of approximately 0.2” (5 mm).

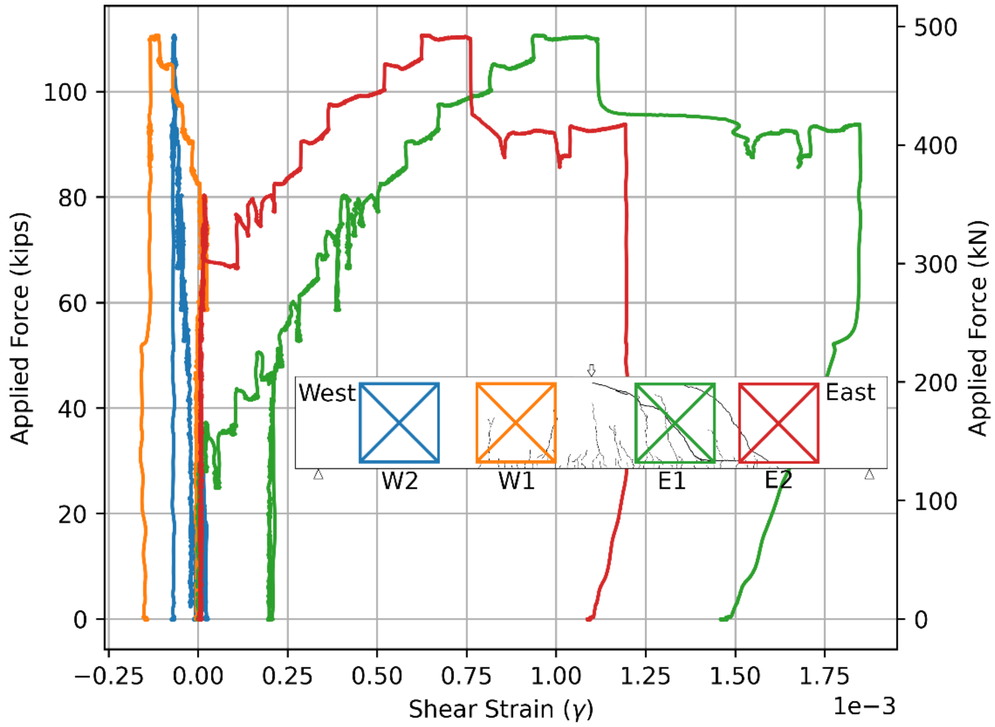

Figure 11: Average shear strain response over panel.

Figure 11 plots the applied load P vs. average shear strain over four correspondingly colored panels as depicted in the inset. All the relationships start at zero strain under self-weight, and a convention is selected where panel zones W1 and W2 in the west span develop negative shear strain and panel zones E1 and E2 in the east span develop positive shear strain under this loading. The shear stiffness of the east span without shear reinforcement decreases markedly when an inclined crack forms in the panel zone. Just after reaching the peak load of 111 k (494 kN), the applied load drops to 90 k (401 kN) and the midspan displacement increases from 0.98” (24.9 mm) to 1.0” (25.4 mm) (Figure 9), while the shear strain on panel E1 increases from 1×10^{-3} to 1.5×10^{-3} (Figure 11), illustrating the apparent shear failure along panel zone E1. Further imposed vertical displacement results in increased shear strain without developing additional resistance, suggesting that the beam is accommodating vertical displacements via widening of and slip along the inclined cracks. In contrast with the softening east span, the west span with shear reinforcement responds in the nearly linearly elastic range of response.

2.9. UCB Beam 1 Phase 2: Response Of Span With Aci Minimum Shear Reinforcement

The purpose of Phase 2 loading was to fail the west span of Beam 1 containing ACI minimum shear reinforcement. First, the span without shear reinforcement that had failed during Phase 1 testing was strengthened by grouting the previously ungrouted longitudinal reinforcement ducts and adding external shear reinforcement to increase the moment and shear strengths. Loading was then resumed on October 21, 2021, 65 days after casting.

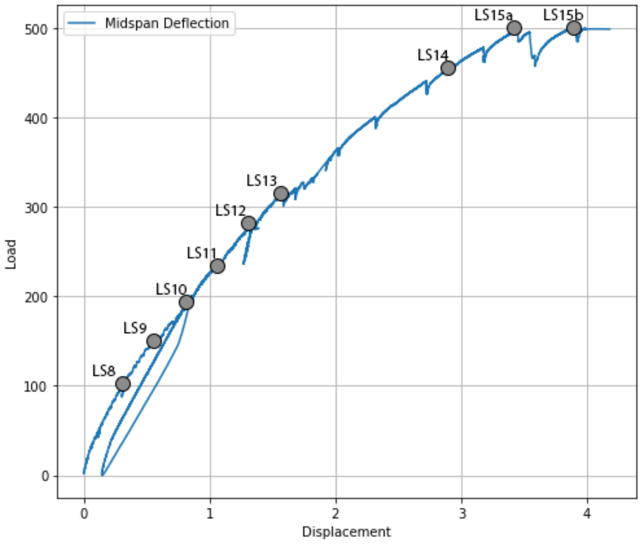

Figure 12: Load Displacement at midspan of Phase 2.

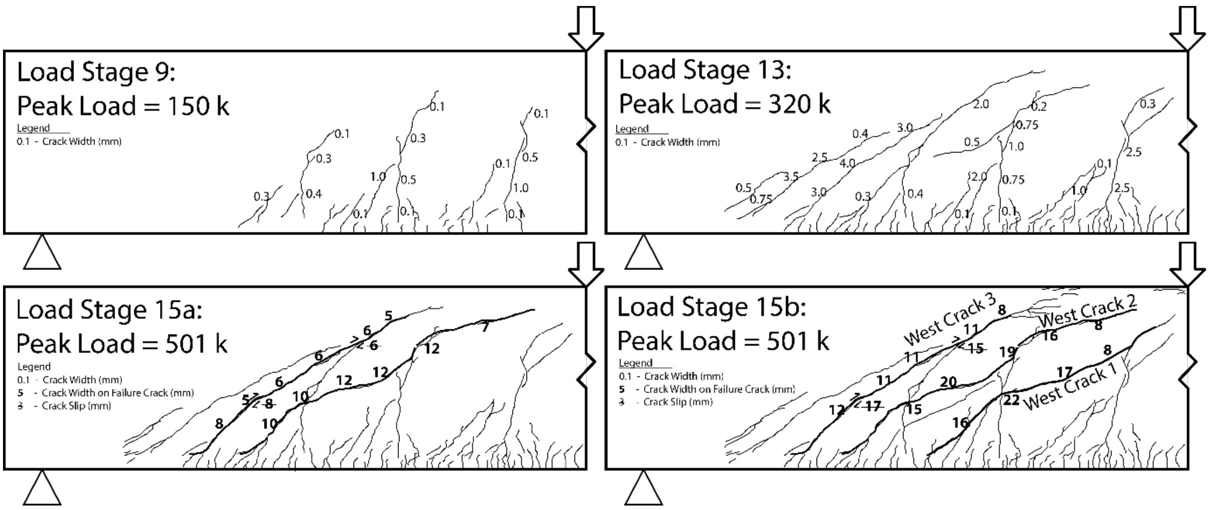

Figure 13: Crack patterns during Phase 2.

Figure 12 shows the measured relationship between midspan applied force P and midspan deflection and Figure 13 shows crack maps at selected load stages during Phase 2. Displacements at the start of Phase 2 are taken as 0 because shear strain data from the previous Phase 1 loading indicated that the west span had behaved almost linear elastically. As the beam had residual cracks from Phase 1, no new cracks were observed until the beam was loaded past the previous peak of 111 k (494 kN).

At LS9, observed cracks rose upwards at an angle of about 60 degrees to the horizontal and bent toward the point of load application. At LS11 and onwards, new and existing cracks tended to form at an inclination of about 45 degrees. These cracks would extend and grow in width until the value of P reached 320 k (1420 kN) at LS13. At this point, new cracks formed at a reoriented 35-degree angle and branched between existing cracks. These new cracks periodically ejected fine concrete dust, indicating damaging shear stresses along the cracked plane as the cementitious material and aggregate was ground to dust. Between a load of 320 k (1420 kN) at LS13 and 500 k (2230 kN) at LS15a, no noteworthy new cracks were observed. Instead, existing cracks widened to as much as 0.5” (12 mm) under increasing load.

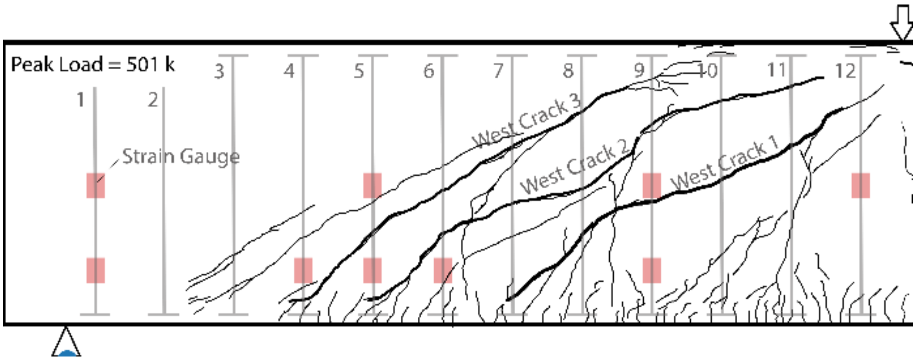

Figure 14: Phase 2 cracked state at failure, overlain on transverse reinforcement at LS 15a.

Figure 14 shows the crack diagram at LS15b overlain on the locations of the transverse reinforcement and strain gauges. Several strain gauges had been damaged during the concrete casting, resulting in the sparse arrangement of gauges seen here. Between LS15a and LS15b, West Crack 1 formed and increased to approximately 0.8” (20 mm) in width. Correspondingly, the upper gauge on the transverse bar labeled 9 experienced a large increase in strain, developing from near zero strain to the largest readout of 1.3% strain. However, the lower strain gauge on bar 9 and the gauge on bar 12 both remained near zero. This suggests that a strut and tie type mechanism formed in the region near the loading head, but the compressive force in the concrete strut was developed along the transverse reinforcement via bond stresses rather than at a CTT node at the bottom of the shear reinforcement as idealized in typical strut-and-tie models.

At this stage, three main cracks of interest had formed, as labeled in Figure 14. Crack 1 crossed transverse bars 7 to 11 and had opened to as wide as 0.8” (20 mm) at mid-depth. Crack 2 was at a shallower angle with similar crack width, running nearly the entire depth of the beam and crossing transverse bars 5 to 11. Despite the large crack widths, negligible crack slip was observed on either crack, indicating that aggregate interlock was likely not strongly engaged. This suggests that, while beam action mechanisms using aggregate interlock may have broken down on West Crack 1 and 2, a strut-and-tie mechanism was possible as this is within the "disturbed" region close to the loading head.

Unlike Cracks 1 and 2, Crack 3 had smaller crack widths, on the order of 0.4" (10 mm), at failure, but experienced slip of about 0.7" (17 mm) prior to failure, making it plausible that aggregate interlock occurred and contributed to shear resistance. The beam failed suddenly along Crack 3 as shown in Figure 15. Post-failure inspections showed that all transverse bars crossing Crack 3 had fractured.

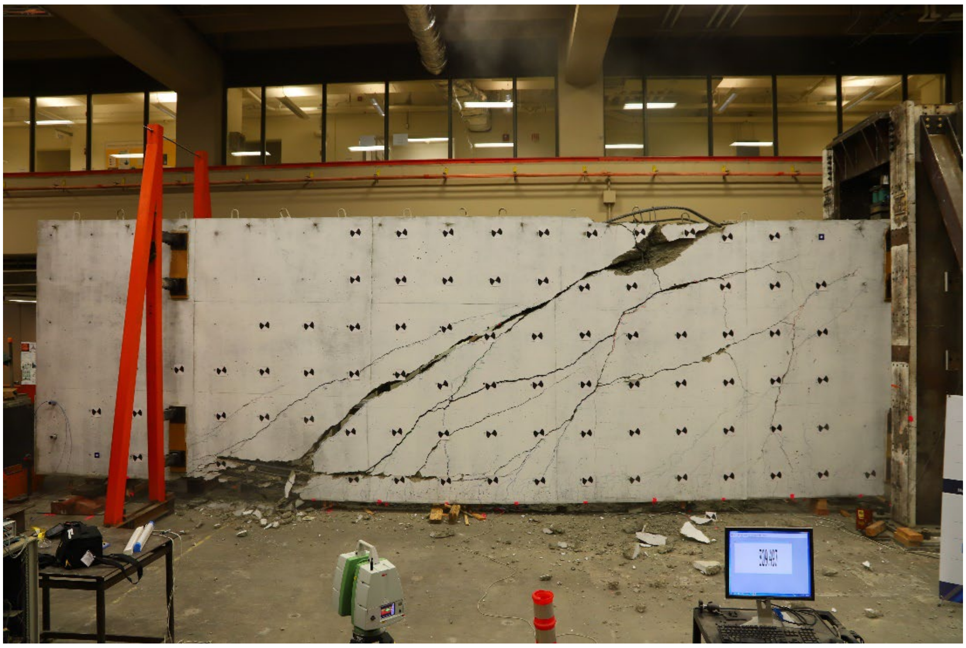

Figure 15: Failure state of UCB Beam 1 during Phase 2

Given that the tested shear strength (V_n) was 278 k (1240 kN) and is the sum of the concrete contribution (V_c) and steel contribution (V_s), V_c can be estimated by applying an assumption for V_s. Under the upper bound assumption on V_s that all five shear reinforcement bars crossing Crack 3 can carry a force corresponding to the fracture strength (f_u) simultaneously, the concrete normalized shear stress is estimated at $1.5\sqrt{f'_c}$ psi ($0.12\sqrt{f'_c}$ MPa). Although this is not a full $2.0\sqrt{f'_c}$ ($0.17\sqrt{f'_c}$ MPa) as the ACI code allows, the assumption here that all bars fractured simultaneously is a lower bound on the calculated concrete contribution to shear strength; if the yield strength (f_y) is used instead of f_u in the preceding calculating, the normalized shear stress becomes $1.9\sqrt{f'_c}$ psi ($0.16\sqrt{f'_c}$ MPa). Thus, there is good indication that minimum shear reinforcement is effective in increasing V_c to reach close to the full strength of $2.0\sqrt{f'_c}$ psi ($0.17\sqrt{f'_c}$ MPa) as allowed by ACI 318-19 even when high tensile strains are present in the high-strength longitudinal reinforcement.

2.10. PHASE 3: RESPONSE OF SPAN LOADED AS A FOOTING

Phase 3 testing with a uniform support reaction took place over 7 hours on March 29, 2023. Figure 16 presents the load-displacement plot for Phase 3. The y-axis can be interpreted as the vertical applied load P at midspan that is resolved by a uniform support reaction on the west (left) span and a point support on the east (right) span. Displacements are measured at the west tip of the beam relative to the initial position prior to applying the uniform reaction. It should be noted that beam flexibility on the opposite east span, including effects of cracking, influences the load-displacement plot.

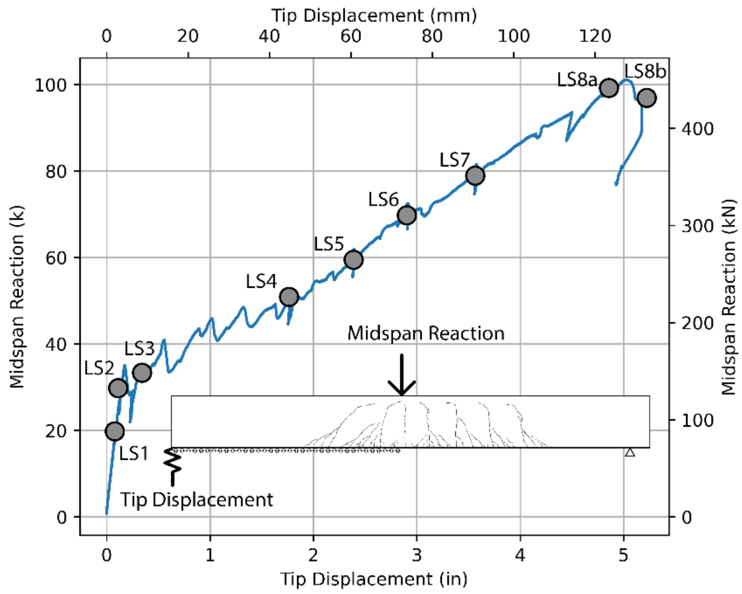

Figure 16: Load displacement at beam tip during Phase 3

Figure 17 presents crack progression for the west span in Phase 3. The footing-style west span first developed a steeply climbing flexural crack at LS4, followed by some smaller flexure-shear cracking that developed over the next few load stages. Between LS4 and LS7, all cracks developed at an inclination primarily within *d* of the applied load.

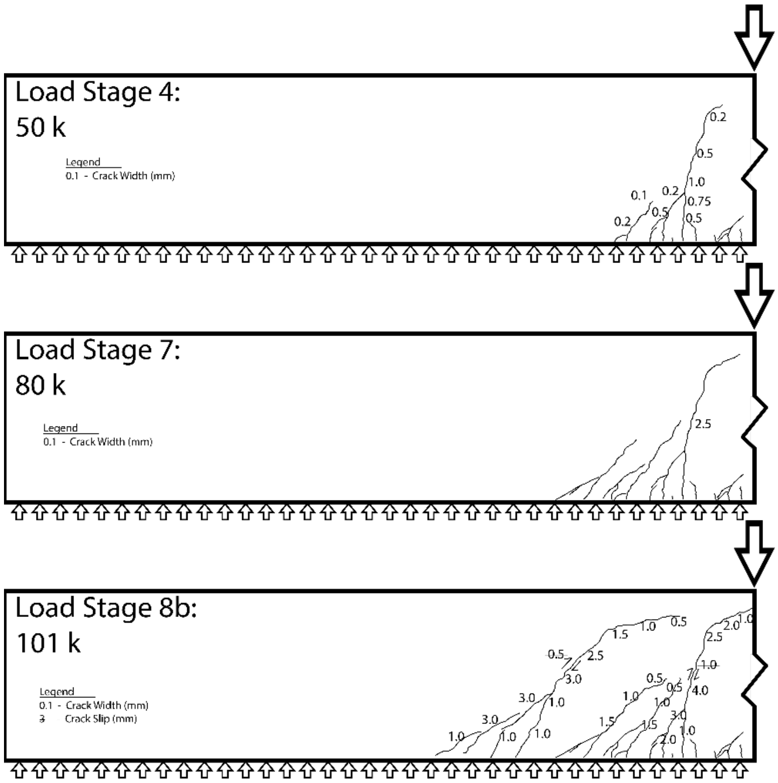

Figure 17: Phase 3 west span crack progression.

This crack pattern remained relatively stable with cracks widening to as much as 0.12" (3 mm) until near failure at about 101 k (450 kN) downward applied load. At loads approaching failure (LS8a), it was observed that a shallower inclined crack 1.5*d* from the loading head was developing rapidly. Over the next 0.1" increase in tip displacement, this crack grew in height and width to 0.12" (3 mm). When fine concrete dust was observed being ejected from this new crack, the test was paused and ultimately stopped. After unloading a nominal amount to enable safe beam inspection, the crack was observed to have slipped approximately 0.02" (0.5 mm). Post-test analysis showed that, when the concrete dust was ejected, there was a small drop in load and small increase in vertical tip displacement, but a large increase in the average shear strain on the beam surface (Figure 18). This suggested that the beam had reached or was nearing its capacity, and it was unlikely to develop significant additional load.

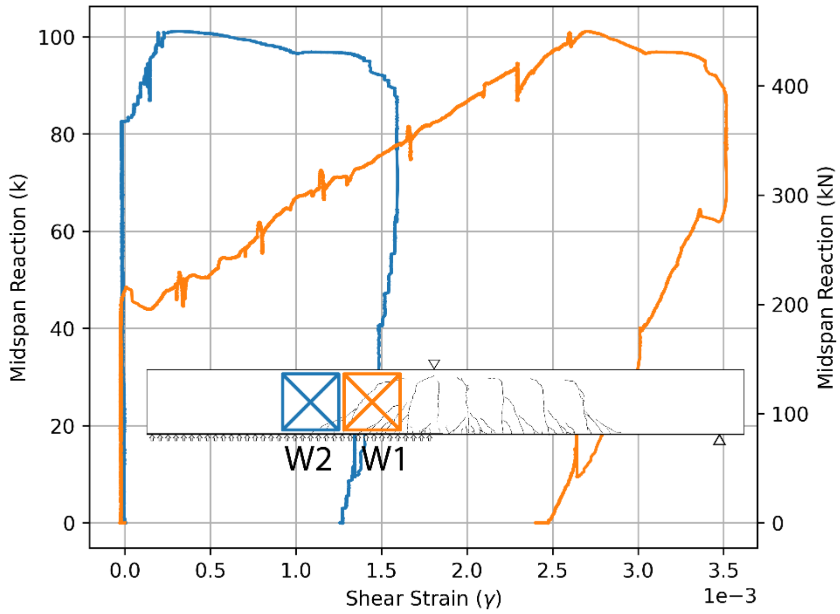

Figure 18: Phase 3 west span shear strain response.

The shear strain data are derived from diagonal displacements measurements on the corresponding panels, as drawn in Figure 18. Post-test processing of this data showed that most of the shear strain response came from the tensile diagonal while the compressive diagonal deformation was essentially zero. Considering the position of the instruments relative to primary cracks (Figure 18), the tensile diagonal of both W1 and W2 measured the crack width of the newly formed crack at LS8b. The increase in crack opening on W2, which reflects the opening of the crack tail, is approximately twice that of W1, which reflects the opening of the crack at mid-depth, when looking beyond the peak load of 101k. As there are no other cracks located near the failure crack, this observation provides further evidence that the kinematics of crack opening can be reasonably described by a rotation centered at the tip of the crack. The same observation was also made in the deep beam test reported by Collins et al. [14].

2.11. Phase 4: Response Of Span Loaded As A Beam

Phase 4 began with the removal of the uniformly reacting support on the west span and replacement with a "roller" support located 3'-6" (1.07 m) from the west end. This increased the contribution of self-weight to the reaction at the east support while maintaining the same load pattern as during Phase 3 on the east span. Response during Phase 3 is connected to Phase 4 by monitoring the rotation at midspan during Phase 3 and matching the support reactions on the east span. Using this approach, the equivalent midspan load and equivalent displacement for both Phase 3 and Phase 4 are plotted in Figure 19. The equivalent midspan load on the y-axis starts at -22 k (-98 kN) because less self-weight is carried on the east span in Phase 3 than in Phase 4. For the Phase 4 apparatus to achieve the response in Phase 3, the central jack must lift the beam. Due to this testing arrangement, the proper interpretation is that the beam would develop its first flexural crack under its own self-weight or shortly after applying load in a 3-point bending configuration.

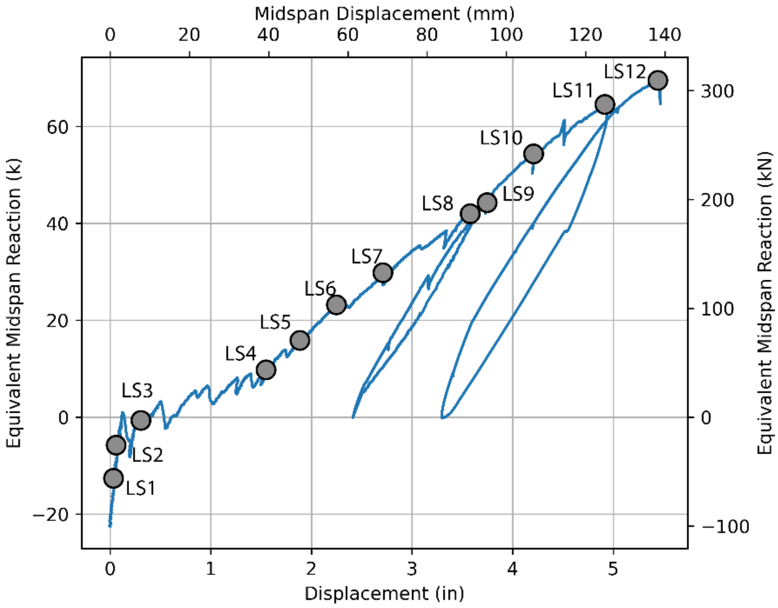

Figure 19: Phase 4 response to beam-style loadings.

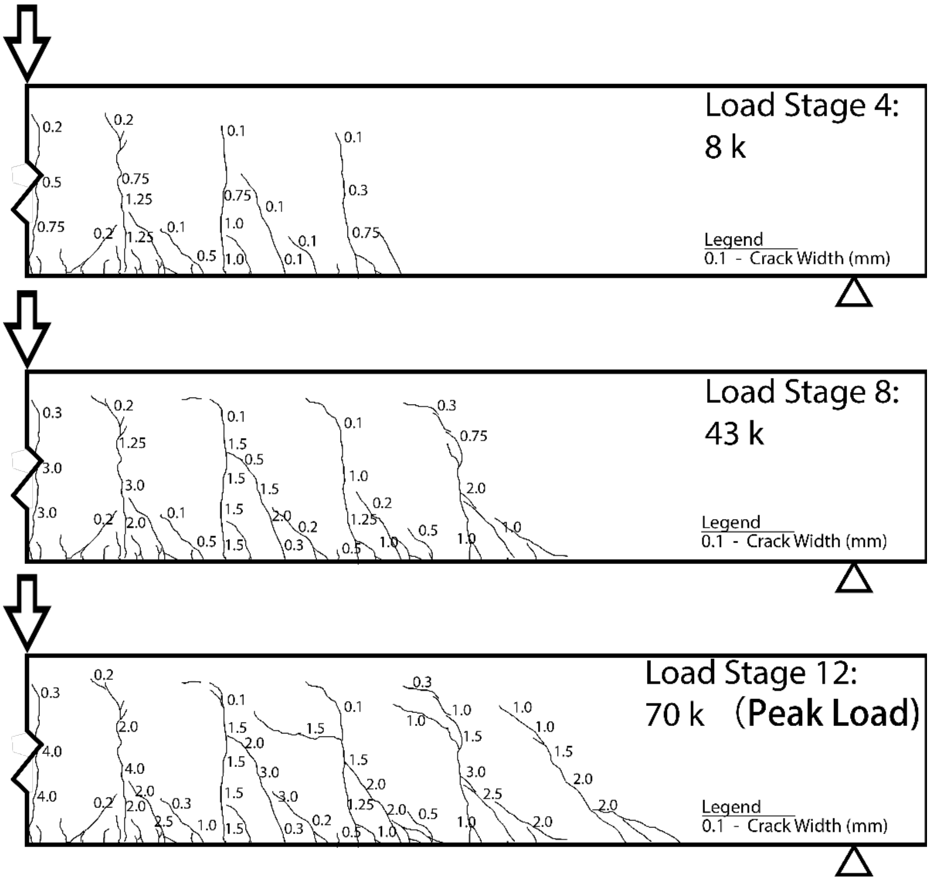

Figure 20: Phase 4 crack patterns at select load stages.

Figure 20 shows the cracked state of the east span. Due to the very low cracking moment and cracked stiffness of this beam, the span loaded as a beam cracked immediately prior to LS3. Consecutive development of flexural cracks resulted in reduced load-displacement stiffness between LS3 and LS4 when compared with loading beyond LS4. At LS8, the beam was unloaded upon failure of the west span. Loading resumed under Phase 4 in 3-point bending, and it is observed that the load-displacement slope recorded during Phase 4 agrees well with the processed results of Phase 3. At LS8, the flexural cracks increased in height, spaced regularly at about 5 ft (1.5m) intervals, and bent toward the central load P below the flexural compression zone. In addition to the flexural cracks, several shallower flexure-shear cracks can be seen extending from the tension face and climbing to join existing flexural cracks at mid-depth.

The beam ultimately failed along the right-most crack closest to the east support. The indicated failure crack grew rapidly during a 3-kip (13.4 kN) increase in applied load. Seconds prior to failure, an audible cracking sound was heard before the beam failed suddenly. The critical shear crack “ripped” open and the sudden thrust pushed the compression reinforcement off the top face as the beam settled into the arched shape seen in Figure 21. No other warnings or degradation in the load-displacement curve were observed, highlighting the brittle and sudden nature of shear failures.

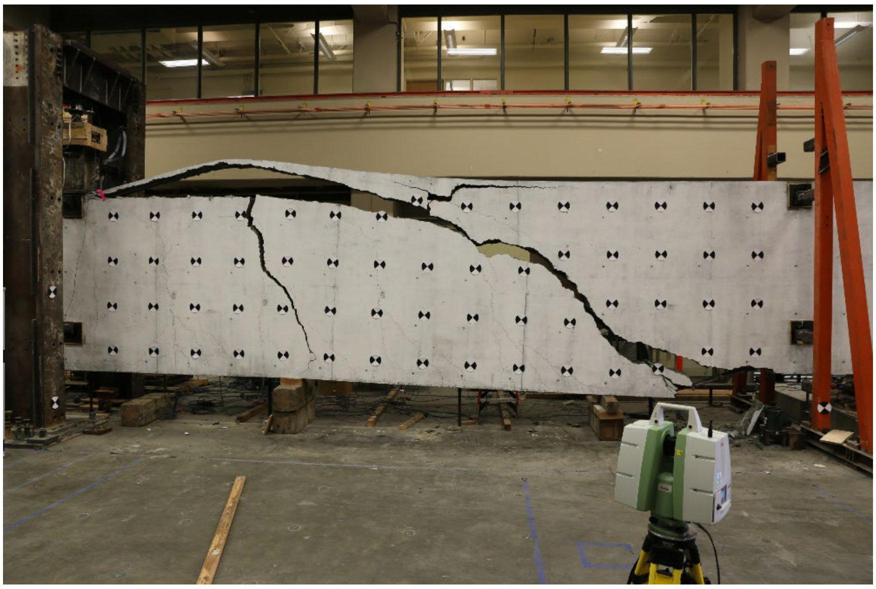

Figure 21: UCB Beam 2 failure on east span during Phase 4.

2.12. Longitudinal Reinforcement Strain Response

Figure 22a and Figure 22b presents measured and calculated tensile strains on longitudinal reinforcement alongside the observed cracking patterns for Phase 3 and Phase 4. Measured strains are based on readings from foil strain gauges attached to the longitudinal reinforcement, which were zeroed prior to the beams supporting self-weight and external loads. Calculated strains are based on conventional sectional analysis considering the bending moment on the section and ignoring effects of creep and shrinkage [19].

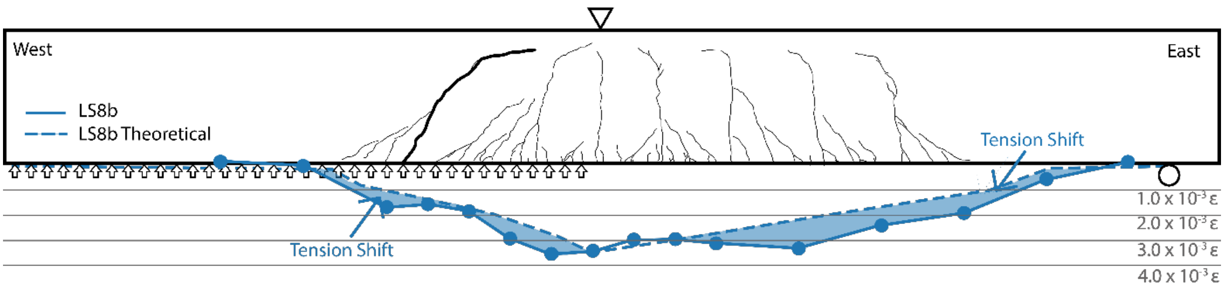

Figure 22a: Longitudinal strains and crack pattern at failure for Phase 3 during LS8b.

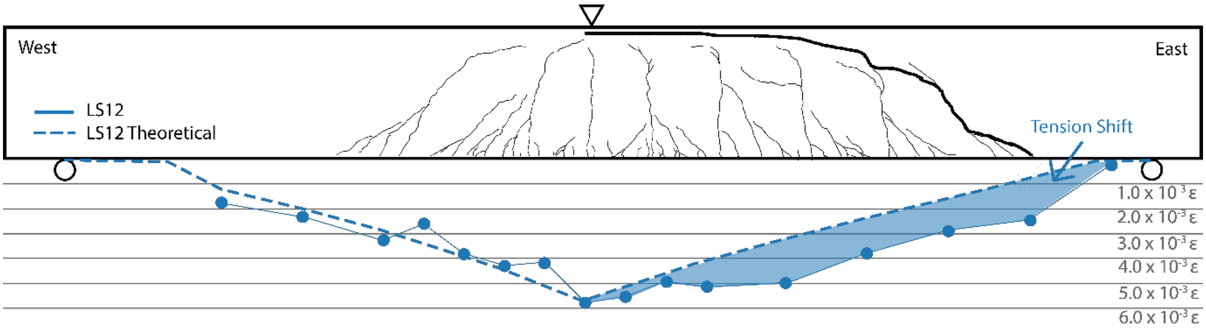

Figure 22b: Longitudinal strains and crack pattern at failure for Phase 3 during LS8b.

Figure 22a shows the distribution of longitudinal tension reinforcement strains at failure for Phase 3, which had the footing-style loading. The peak longitudinal tensile steel strain was 0.0034, corresponding to 86 ksi (593 MPa) at midspan or about three times the values observed at failure in tests reported by Shioya et al. [13] and Collins et al. [14]. Steel strains are near-zero for most of the west span, increasing only in the vicinity of cracking near midspan. The measured and calculated tensile strains compare well along the West span and beneath the concentrated load P, but measured strains tend to exceed calculated strains along the East span. This observation for the East span is consistent with the phenomenon known as tension shift, whereby tensile strains in longitudinal reinforcement exceed those calculated by flexural theory because of compression struts along concrete diagonals between inclined cracks [2]. Tension shift effects appear to be smaller in the west span with a footing-style loading when compared with the east span with a beam-style loading.

The peak longitudinal tensile steel strain observed in Phase 4, with the beam-style loading (see Figure 22b), was 0.0057, which corresponds to a tensile stress of 113 ksi (780 MPa). Although relatively high tensile strains extend well into the beam span because of tension shift, failure ultimately occurred at a section with lower tensile strain near the right support, which is the section with highest sectional shear stress when considering self-weight.

Despite having very different shear, moment, and tensile strain profiles along the span, the vertical shear forces carried by the failure crack during Phase 3 and Phase 4 were quite similar. The vertical shear forces were about 54 k (240 kN) and 55 k (245 kN), or $0.86 b_w d \sqrt{f_c'}\ psi$ and $0.84 b_w d \sqrt{f_c'}\ psi$, for Phase 3 and Phase 4, respectively. Reinforcement tensile strains at the bottom of the failure crack for Phase 3 and Phase 4 were both around 0.002.

2.13. Size Effect Of Large Concrete Members Containing High Strength Shear Reinforcement

To understand how the one-way shear tests outlined in this paper fit into existing trends for one-way shear strengths, Figure 23 presents a size effect series composed of Phase 1, 3, and 4 and three similarly reinforced companion beams of 1 ft (0.3 m), 2 ft (0.6 m), and 3 ft (0.9 m) deep [4]. Additionally, various size effect series identified by Bentz in the DAfStb/ACI 445 shear database for members loaded with point and distributed loads and no shear reinforcement are presented for comparison [6, 7]. The unit shear strength is reported as the shear force at the point of highest shear, typically located at *d* from the support for beams. Broken curves fitted to the data using a power law show the general trend of each test series.

The UC Berkeley size effect series shows a clear decrease in unit shear strength with decreasing longitudinal reinforcement ratio and increasing member depth that is consistent with the similarly reinforced Low Rho series at 0.35%. ACI 318-19 nominal shear strength for each series is also presented in the correspondingly colored continuous curves. Comparison between the curve-fitted broken curves and the ACI predictions (continuous curves) shows that the ACI 318-19 equation is conservative by a factor of 1.5 – 2.0 for all size effect series. The data additionally shows that unit shear strengths tend to a lower bound of about $1.0\sqrt{f_c'}$ psi (0.083 $\sqrt{f_c'}$ MPa) for each size effect series.

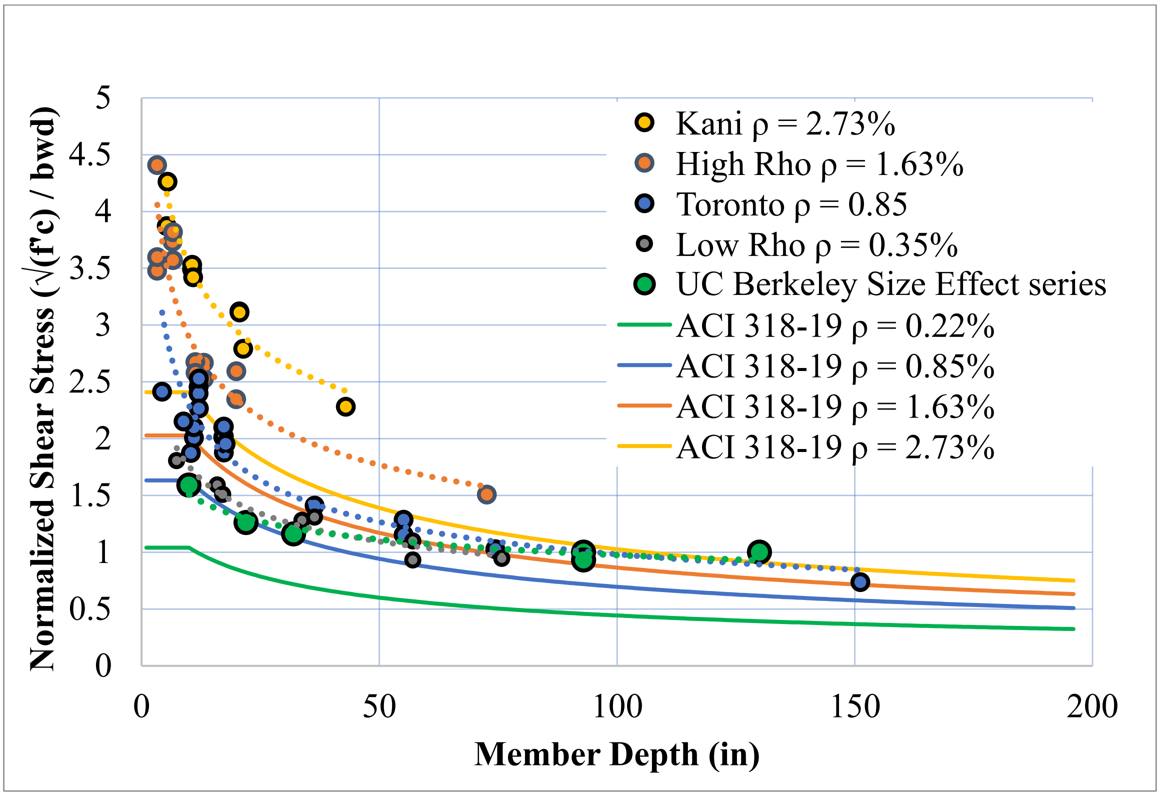

Figure 23: UCB size effect series versus similar size effect series.

2.14. Summary And Conclusions

Four unique shear tests were conducted on two large beams containing high-strength [Grade 100 (690 MPa)] longitudinal reinforcement and normal-weight nominal 4000-psi (28 MPa) compressive strength concrete. The focus was to evaluate the effects of size, longitudinal reinforcement ratio, strain in the longitudinal reinforcement, and provision of ACI minimum shear reinforcement on the unit shear strength of large beams. The four tests were designated Phases 1 through 4, as summarized below.

The Phase 1 test involved a three-point beam-style test with centrally located point load, self-weight, and two "roller" supports. The beam developed maximum tensile stress of approximately 50 ksi (345 MPa) in the longitudinal reinforcement before failing in shear at a nominal shear stress of a 1.0 $\sqrt{f_c'}$ in psi units (0.083$\sqrt{f_c'}$ MPa units). The corresponding nominal shear stress according to the ACI 318-19 one-way shear equations is 0.5 $\sqrt{f_c'}$ in psi units (0.042$\sqrt{f_c'}$ MPa units), or about 50% of the measured shear strength.

The Phase 2 test had the same member depth and shear span as the Phase 1 test but the span was provided longitudinal tension reinforcement ratio of 0.84% with minimum shear reinforcement $A_{v,min}$ as specified in ACI 318-19. The beam developed maximum tensile stress of 90 ksi (621 MPa) in the longitudinal reinforcement before failing in shear by fracturing all transverse reinforcement. The nominal shear stress resisted by the concrete at failure was between 1.5$\sqrt{f_c'}$ psi (0.125$\sqrt{f_c'}$ MPa) and 1.9$\sqrt{f'_c}$ psi (0.16$\sqrt{f'_c}$ MPa) depending on whether the transverse reinforcement stress was assumed equal to f_{su} or f_{sy}, respectively. The failure load was 1.15 times the nominal shear strength specified by ACI 318-19.

The Phase 3 test was a footing-style test that contained no shear reinforcement and was loaded with a uniformly distributed reaction beneath the test span. The beam developed maximum tensile stress of approximately 86 ksi (593 MPa) in the longitudinal reinforcement before failing in shear at a nominal shear stress of 1.0 $\sqrt{f_c'}$ psi (0.083$\sqrt{f_c'}$ MPa). The ACI 318-19 nominal shear strength, assuming the member to be a beam, is 0.44 $\sqrt{f_c'}$ psi (0.037$\sqrt{f_c'}$ MPa), or about 0.44 of the measured strength. Assuming the member to be a footing, such that the size effect factor of ACI 318-19 would not apply, the ACI 318-19 nominal shear strength is 1.04 $\sqrt{f_c'}$ psi (0.086$\sqrt{f_c'}$ MPa), or 1.04 of the measured strength.

The Phase 4 test was nominally identical to the Phase 3 test except the span was tested as a beam-style test with concentrated central load, self-weight, and roller supports. The span developed maximum tensile stress of approximately 113 ksi (780 MPa) in the longitudinal reinforcement before failing in shear at a nominal shear stress of 0.93 $\sqrt{f_c'}$ psi (0.077$\sqrt{f_c'}$ MPa). The shear strength is nearly identical to the value measured in a nominally identical beam tested as a footing-style test. The ACI 318-19 nominal shear equations, assuming the member to be a beam, is the same as that calculated for Phase 3, being 0.44 $\sqrt{f_c'}$ psi (0.037$\sqrt{f_c'}$ MPa). This is approximately 0.47 of the tested shear strength.

The results of the four beam tests were compared with results of other tests of deep beams with varying longitudinal reinforcement ratios. On the basis of these tests, the following conclusions are made:

1. Headed shear reinforcement corresponding to the minimum shear reinforcement ratio of ACI 318-19 minimizes the size effect and allows the concrete contribution to reach close to if not the full 2.0 $\sqrt{f_c'}$ psi (0.17$\sqrt{f_c'}$ MPa).
2. The ACI 318-19 equations for one-way shear are very conservative for large members without shear reinforcement. The ratio of code prediction to experimental one-way shear value ranged between 0.44 to 0.50 for Phases 1, 3, and 4 when treating the specimens as a beam. Trends for different size effect series additionally show that unit shear strengths tend to a lower bound of about 1.0$\sqrt{f_c'}$ psi (0.083 $\sqrt{f_c'}$ MPa).
3. The shear strength of members containing high-strength longitudinal reinforcement appears consistent with the shear strength of members containing Gr.60 reinforcement when the reinforcement ratios are similar. This is true even at large *a/d* ratios, where specimens containing regular Gr.60 longitudinal reinforcement would have failed in flexure before shear.
4. Tension shift in specimens loaded as a beam results in large increases in longitudinal reinforcement strain relative to cracked-section predictions. Tension shift should be considered in the moment reinforcement design if bar cutoffs are used.
5. Minimal differences between Phase 3, the footing-style loading, and Phase 4, the beam-style loading, were observed in terms of the observed shear strength at the evaluation section, suggesting that differences in shear strength between beams and footings are closer than the ACI 318-19 code may imply and that any observed differences in strength are likely due to other factors.

2.15. References

[1] ACI Committee 318, Building Code Requirements for Structural concrete (ACI 318-19) and Commentary (ACI 318R-19, Farmington Hills, MI: American Concrete Institute, 2019.

[2] ASCE/ACI Committee 445 on Shear and Torsion, "Recent Approaches to Shear Design of Structural Concrete," *Journal of Structural Engineering,* vol. 124, no. 12, pp. 1375-1417, 1998.

[3] D. A. Kuchma, S. Wei, D. H. Sanders, A. Belarbi and L. C. Novak, "Development of the One-Way Shear Design Provisions of ACI 318-19 for Reinforced Concrete," *ACI Structural Journal,* vol. 116, no. 4, pp. 285-295, 2019.

[4] J. Y. Zhai and J. P. Moehle, "SEMM Report," Structural Engineering Mechanics and Materials Report, Civil and Environmental Engineering, UC Berkeley, Berkeley, 2024.

[5] Z. P. Bazant and M. T. Kazemi, "Size Effect on Diagonal Shear Failure of Beams without Stirrups," *ACI Structural Journal,* vol. 88, no. 3, pp. 268-276, 1991.

[6] E. C. Bentz, "The Toronto Size Effect Series," *ACI Symposium Publication,* vol. 328, pp. 2.1-2.12, 2018.

[7] K.-H. Reineck, E. C. Bentz, B. Fitik, D. A. Kuchma and O. Bayrak, "ACI-DAfStb Database of Shear Tests on Slender Reinforced Concrete Beams without Stirrups," *ACI Structural Journal,* vol. 110, no. 5, pp. 867-875, 2013.

[8] A. S. Lubell, E. C. Bentz and M. P. Collins, "Influence of Longitudinal Reinforcement onOne-Way Shear in Slabs and Wide Beams," *Journal of Structural Engineering,* vol. 135, no. 1, pp. 78-87, 2009.

[9] M. W. Huggins, Kani on shear in reinforced concrete, Toronto: Department of Civil Engineering, University of Toronto, 1979.

[10] A. Uzel, B. Podgorniak, E. C. Bentz and M. P. Collins, "Design of Large Footings for One-Way Shear," *ACI Structural Journal,* vol. 108, no. 2, pp. 131-138, 2011.

[11] C. E. Ospina and N. M. Hawkins, "Effect of Flexural Reinforcement Ratio, Effective Depth and Slenderness Ratio on Punching Strength or Spread Footings," *ACI Symposium Publication,* vol. 353, pp. 50-72, 2022.

[12] F. E. Richart, "Reinforced Wall and Column Footings Part 2," *ACI Journal Proceedings,* vol. 45, no. 11, pp. 237-260, 1948.

[13] T. Shioya, M. Iguro, H. Akiyama and T. Okada, "Shear Strength of Large Reinforced Concrete Beams," *ACI Symposium Publication,* vol. 118, pp. 259-280, 1990.

[14] M. P. Collins, P. T. Quach and E. C. Bentz, "Shear Strength of Thick Slabs," *ACI Structural Journal,* vol. 117, no. 4, pp. 115-126, 2020.

[15] J. J. Poldon and E. C. Bentz, "Shining a New Light on the Riddle of Shear".

[16] A. S. Lubell, E. C. Bentz and M. P. Collins, "Headed Shear Reinforcement Assemblies for One-Way Shear," *ACI Structural Journal,* vol. 106, no. 6, pp. 878-889, 2009.

[17] A. S. Lubell, E. C. Bentz and M. P. Collins, "Shear Reinforcement Spacing in Wide Members," *ACI Structural Journal,* vol. 106, no. 2, pp. 205-214, 2009.

[18] R. J. Frosch, "Behavior of Large-Scale Reinforced Concrete Beams with Minimum Shear Reinforcement," *ACI Structural Journal,* vol. 97, no. 6, pp. 814-820, 2000.

[19] J. P. Moehle, Seismic Design of Reinforced Concrete Buildings, McGraw-Hill Education, 2015.

CHAPTER 3: ANALYTICAL STUDY OF ONE-WAY SHEAR FAILURES IN MAT FOUNDATIONS

3.1. Abstract

Predicting the one-way shear strength of mat foundations is challenging due to the lack of experimental data on the shear strength of large reinforced concrete members, leading to uncertainties regarding their shear strength due to the size effect. Additionally, complex interactions between the mat and the soil, along with the uncertain shear spans in large mats, require sophisticated models for accurate shear strength prediction. These models must account for size effects, longitudinal reinforcement effects, clamping effects, and soil-structure interaction. This paper presents the calibration of Finite Element models using results from large shear specimens tested under boundary conditions representative of beams and of foundations. Parametric studies using the calibrated model are conducted to investigate the one-way shear strength under boundary conditions specific to mat foundations.

3.2. Introduction

Mat foundations are commonly used to support high rise buildings in the Western U.S. where soil conditions allow and are critical in safely resisting the lateral forces and overturning moments generated during earthquakes. The distribution of axial forces, shear forces, and bending moments within the mat depends on its configuration and on the soil-structure interaction. However, the one-way shear strength under various boundary conditions and soil reactions remains insufficiently addressed [1]. With mat foundations reaching 18' (5.5 m) deep in some structures like the Wilshire Grand in Los Angeles, further study is required to ensure that the foundation boundary conditions result in shear strength that align with current design practices.

To explore the complex interactions between one-way shear strength and various soil reactions, this paper presents Finite Element (FE) models of large reinforced concrete beams modeled using the software ATENA. The FE models are calibrated using the large 11.7 ft (3.6 m) and 8 ft (2.4 m) deep one-way shear specimens tested at UC Berkeley in 2021 and 2023 (See

In preparation for submission to ACI Structural Journal

Chapter 2 and Appendix A). A parametric study is then performed with the calibrated models under simplified boundary conditions to assess the sensitivity of one-way shear strength to various soil reactions and loading conditions that a mat foundation may experience.

3.3. Research Significance

Experimental testing is essential for addressing questions about one-way shear strength in mat foundations and for calibrating code equations and analytical models. However, conducting large-scale shear tests for all possible variables is prohibitively expensive. As an alternative, well-calibrated finite element models that accurately replicate existing test results are developed to investigate foundation boundary conditions, including the effects of clamping, axial compression, and variable soil pressure distribution under overturning actions.

3.4. Literature Review

The one-way shear strength of a mat foundation depends on several factors. In the absence of shear reinforcement, the ACI 318-19 one-way shear equations suggest that shear strength is a function of member depth, whereby unit shear stress at shear failure decreases with increased member depth [2]. Shear strength is also a function of the longitudinal reinforcement ratio, whereby unit shear stress at failure decreases with reduced amounts of longitudinal steel [3]. These are often referred to as the size effect and longitudinal reinforcement effect, respectively. Other design codes, such as CSA A23.3, explicitly include the effect of longitudinal strain by accounting for demand bending moments or prestressing forces in the shear strength calculation [4]. Additionally, clamping stresses —vertical compression stresses due to distributed loads, such as those from uniform loads or soil pressure — can increase shear strength [5].

While many of these interactions are experimentally verified and documented in shear databases, most tests are limited to smaller beams, typically up to 4 ft (1.2 m) in depth [6]. Consequently, there is a lack of experimental data for large specimens where size effects become significant. Further complicating the issue, the uncertainties in soil response contributes to greater uncertainty in the distribution of vertical and horizontal soil reactions under lateral forces and overturning moments. As mat foundations also support numerous walls and columns, the variability in loading makes the effective shear span unclear, potentially impacting its one-way shear strength.

Traditional design practice for mat foundations is to size the mat as deep as required to satisfy the shear demands without shear reinforcement and then place sufficient longitudinal steel to satisfy the moment demands [1]. This style of design is beneficial with respect to construction efficiency but makes the mat foundation susceptible to the size effect. Longitudinal reinforcement ratios are also typically low, resulting in further penalties on shear strength. The shear strength of beams reinforced like mat foundations without shear reinforcement can be as low as $0.7\sqrt{f_c'}$ psi ($0.041\sqrt{f_c'}$ MPa) as reported by Collins in the 2015 Toronto shear test on a 13.1 ft (4.0 m) deep specimen [7] and $1.0\sqrt{f_c'}$ psi ($0.083\sqrt{f_c'}$ MPa) for specimens 8 ft (2.4 m) and 11.7 ft (3.6 m) deep by Zhai and Moehle. In comparison, ACI 318-14 and prior would permit a unit shear strength of $2.0\sqrt{f_c'}$, though it was common practice in the Western United States to reduce the unit shear strength to $1.0\sqrt{f_c'}$ when proportioning mat foundations without minimum shear reinforcement to account for the size effect [1].

Typical analysis practice for one-way shear in mat foundations is to use the thick plate formulation to represent a mat foundation that is supported on idealized soil springs with an initial subgrade modulus [8]. Based on the forces from the superstructure model and iterations with the geotechnical engineer, a soil pressure distribution on the mat's bottom can be determined for each load case. After calculating the shear demands along design strips at *d* away from any columns or walls, the one-way shear demands for design can be obtained. Demand shear and bending moments are highly sensitive to the soil bearing pressure, with one case citing up to 43% change in peak design moment with only a 9% change in maximum bearing pressure [8].

Practitioners have observed that there is a tendency for reduced soil stiffness at the center of the mat, resulting in "dishing" of the mat's deflected shape. Vertical forces also tend to concentrate beneath the core wall, resulting in less shear forces carried outside of *d* from the core wall. However, the effects of shear spans and clamping on the mat's shear strength remain unclear. Additionally, the effects of overturning moments on shear strength in mat foundations are not well addressed and have generally not been studied.

3.5. Finite Element Model Using ATENA

The nonlinear finite element (FE) software for reinforced concrete ATENA was used in this study to model the results of UCB Beam 1 and Beam 2. The concrete model combines fracture and plastic concrete behaviors in a smeared crack band model by representing the total strain as the sum of elastic (ε^e), plastic (ε^p), and fracture (ε^f) strains [9]. In tension, the material behaves elastically until fracture based on the Rankine criterion, wherein failure occurs when the principal tensile stress reaches the defined tensile strength. The ATENA model accounts for discrete cracking using Bazant and Oh's crack band approach [10], which smears a crack over a crack band length (L_t). The crack width (*w)* can then be defined as the product of the crack band length (L_t) times the fracture strain (ε^f):

$$w_t = \varepsilon^f L_t \qquad (3\text{-}1)$$

The crack band length is taken as the projection of the element dimension normal to the crack angle and further modified by relations proposed by Cervenka et al. to reduce the effects of mesh sensitivity, provided that the element size is reasonable [11]. Opening of the crack and the crack opening stiffness are related to ε^f as a function of the fracture energy (G_f). The Mode II shearing stiffness of the crack is assumed to be proportional to the crack opening stiffness, where the proportionality constant is denoted as the shear factor (s_F). The maximum shear stress that a crack can support is drawn from the MCFT relation [12]:

$$v_{max} = \frac{2.2\sqrt{f_c'}}{0.31 + \dfrac{24w}{a_g + 0.63}} \quad \text{(psi units)} \qquad (3\text{-}2)$$

3.6. Calibrated Finite Element Models for UCB Beam 1

The FE model was calibrated based on the results of UCB Beam 1, with an emphasis on Phase 1. The Phase 1 test was a symmetric 3-point bend test of a reinforced concrete beam loaded monotonically to failure in the east span without shear reinforcement (see Figure 3-1). The beam was 140 inches deep (3.56 m) with an effective depth *d* to the longitudinal tension reinforcement of 130 inches (3.3 m) and *a/d* ratio of 3.23. The concrete compressive and splitting tension strengths were 4600 psi (31.7 MPa) and 416 psi (2.8 MPa), respectively. The longitudinal reinforcement was A1035 Gr.100 high strength steel and shear reinforcement was A615 Gr. 60 steel. Additional details of the experiment can be found in Chapter 2 and Appendix A.

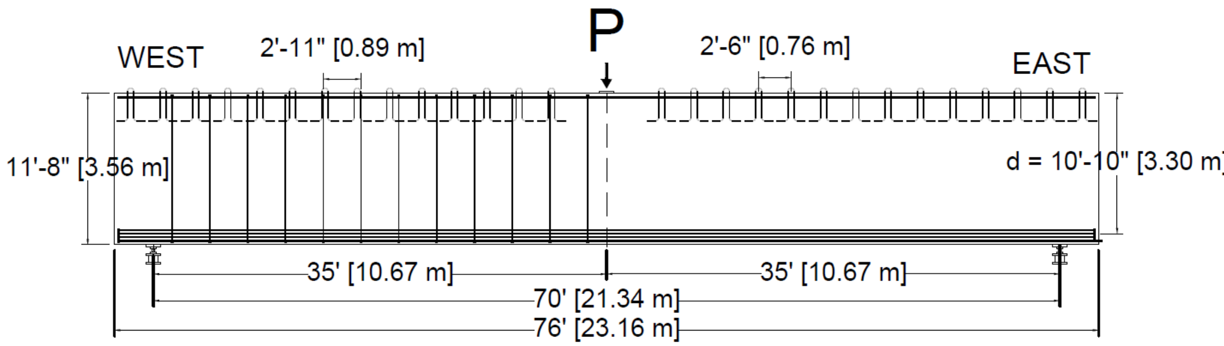

Figure 3-1: Test setup of UCB Beam 1. Phase 1.

ATENA was selected for use in this study because of its excellent results in the 2015 blind prediction competition of a 13.1 ft (4.0 m) deep one-way shear test at the University of Toronto. Using their FE software ATENA, Cervenka Consulting simulated the failure load of PLS4000 East to within 9% and correctly simulated the cracking pattern [13]. Based on the recommendations from Cervenka et al., a similar approach was used to calibrate an ATENA FE model of UCB Beam 1 Phase 1.

Mesh sensitivity in the FE model depends on the crack band size such that the dimension of the crack band reasonably approximates the concrete and reinforcement behavior. Cervenka et al. found based on a parametric study of the Toronto shear test that sensitivity in simulated peak load can be reduced by using quadratic elements. Thus, the FE model was set up using 2D plane stress 8-node rectangular elements with a 2-by-2 integration scheme. Both longitudinal and shear reinforcement were modeled as discrete 1-D truss elements with tested stress-strain relations. Perfect bond to the concrete was assumed. The full beam with both shear spans was modeled due to asymmetry in the reinforcement configuration in the east and west spans. Calibration of the FE model to the results of Phase 1 involved finding a combination of variables that, within their reasonable range, best fit the load-displacement slope, peak load, and crack pattern of Phase 1.

Based on recommendations for mesh size by Cervenka et al. [14], the element size was set at 6” (150 mm) or approximately 8 times the maximum aggregate size for the remainder of this study to ensure reasonable runtimes for all models. As the shear factor (s_F) defines the stiffness of crack slip as proportional to the crack opening stiffness, which opens based on a function of fracture energy (G_F), the quality of the FE model’s crack pattern and peak strength was most affected by input values for both s_F and G_F. Concrete compression strength, tension strengths, and elastic modulus used values obtained from material testing. The maximum aggregate size of the concrete mixture was 0.75" (19 mm). Fracture energy used the relation recommended by *fib* ModelCode 1990 [15]:

$$G_F = G_{Fo}(f_{cm}/f_{cmo})^{0.7} \tag{3-3}$$

This equation was used to obtain an estimate of fracture energy as aggregate size is considered through the term G_{Fo}, providing $G_F = 0.45\ lbs/in\ (79\ N/m)$. All other values used the software default since it was determined that values corresponding to tension and cracking were the most important for calibration.

All numerical models for Phase 1 presented in Figure 3-2 were computed in displacement-control with every load step fully meeting a convergence criterion of 0.5% for the relative displacement norm, energy norm, relative residual 2-norm, and relative residual max norm. Each FE model used approximately 300 load steps leading up to the peak load. For most steps, the Newton-Raphson method was used to solve the nonlinear system of equations and Arc-Length was used when Newton-Raphson struggled or failed to converge.

Comparison of the midspan load versus midspan displacement response is presented in Figure 3-2 for several models varying in the shear crack stiffness factor (s_F). Using the average elastic modulus value of 2730 ksi (18800 MPa) and average splitting cylinder tensile strength of 416 psi (2.9 MPa), the pre-cracking stiffness and cracking load is well estimated in all models. It was important to calibrate the shear factor (s_F) because this parameter determines the stiffness of crack slip, which had a major impact on the model outputs.. As observed in Figure 3-2, models with low s_F values underestimate the shear stiffness, resulting in a softer load-displacement curve and poorer quality simulation of the peak load. When the s_F factor is in the range between 60 to 100, the FE models correctly estimated the peak load and the load-displacement slope before and after cracking. Models with higher values for s_F had the right load-displacement slopes but overestimated the peak strength and so are not presented.

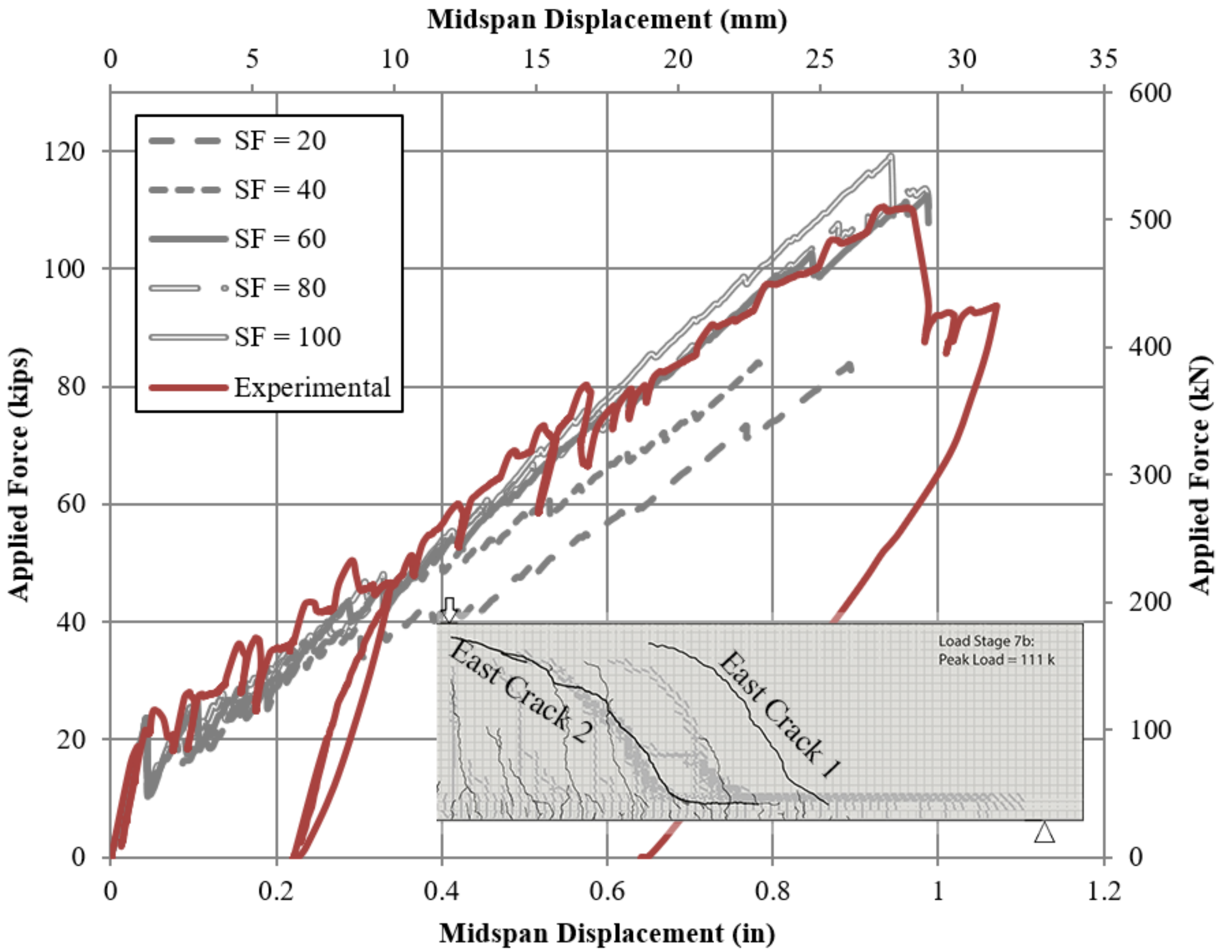

Figure 3-2: Midspan applied load versus midspan displacements for UCB Beam 1 Phase 1 and ATENAwith variable s_F values. Inset shows crack pattern of $s_F = 60$ model compared with experimental crack pattern.

It was observed that models with low s_F values of 20 tended to result in premature horizontal splitting along the top layer of the longitudinal tension reinforcement in a pattern resembling dowel cracks. This behavior is attributed to lower crack sliding stiffness resulting in excessive slip of the crack plane; the model necessarily accommodates the larger displacements by splitting horizontally along the reinforcement. However, as horizontal splitting cracks were not observed in the Phase 1 experiment until shear failure, the best crack patterns were observed with s_F values around 60, where horizontal splitting and widening of the critical crack occurred simultaneously in the numerical model.

Failure in the numerical models was characterized by severe opening of a diagonal crack over a small increase in displacement, increasing the maximum crack width to approximately 0.2” (5 mm). The FE model would at times allow for additional strengthening through horizontal dowel cracks, resulting in an unrealistic failure pattern where the beam unzips horizontally along the top layer of longitudinal tension reinforcement yet still increases in strength. In the case of this ambiguity, the crack widening behavior around 0.2” (5 mm) maximum crack width was set as the stopping criterion. It is believed that the additional strengthening in the FE model comes from the model’s inability to model true separation, resulting in overestimating the ductility of the critical diagonal crack and artificial strengthening of horizontal dowel cracks.

The best performing model was judged based on the simulated peak strength, likeness of the load-displacement plot, and the likeness of the resulting crack pattern. Based on these criteria, the model that was used for further modeling and extrapolation corresponded to s_F = 60 (see Figure 3-2). Peak load in this model was 112 k, whereas the experimental peak load was 111 k. The experiment for Phase 1 observed that East Crack 1 formed first at about 80 k (360 kN) of applied load and East Crack 2 formed at failure; this progression of cracking was also represented by this FE model. The location of East Crack 2 is modeled accurately, though the location of East Crack 1 was closer to the midspan when compared with the experimental results. A description of the FE model parameters is summarized in Table 3-1 and comparison of key results are presented in Table 3-2.

Table 3-1: ATENA FE model input parameters

	ATENA Model Input
Element Type	Quadrilateral 8 node
Mesh Size	6” × 6” (150 mm × 150 mm)
f_c'	4600 psi (31.7 MPa)
f_t	416 psi (2.8 MPa)
G_F	0.45 lbs/in (79 N/m)
s_F	60
E	2730 ksi

ν	0.2
$a_{g,max}$	0.75” (19 mm)
Fixed Crack	1.0

Table 3-2: Phase 1 ATENA vs Experimental Values

	Experimental	ATENA
Peak Load	111 k (494 kN)	112 k (498 kN)
Cracking load	23 k (102 kN)	28 k (125 kN)
Peak Displacement	0.93” (24 mm)	0.99” (25 mm)
Maximum Crack Width	0.20” (5 mm)	0.18” (4.5 mm)
Max. Longitudinal Reinforcement Tensile Strain at Peak Load	0.0017	0.0017
Max. Longitudinal Reinforcement Tensile Stress at Peak Load	50 ksi (345 MPa)	48.9 ksi (337 MPa)

3.7. Finite Element Models of Beam 2 Using Models Calibrated From Beam 1

UCB Beam 2 was an 8 ft deep specimen with *a/d* ratio of 4.5 in both spans. This specimen explored differences in shear strength when supported with a uniform reaction (Phase 3) and a point reaction (Phase 4) while experiencing very large steel strains. The uniform support reaction is intended to replicate boundary conditions like that underneath a mat foundation and to observe differences in shear strength when a nominally identical section is reacted with a point support. The beam was reinforced identically in both spans using A1035 Gr.100 high strength longitudinal reinforcement at 0.23% reinforcement ratio. The reinforcement ratio was selected at this low value to also observe the effects of high steel strains on shear strength. No shear reinforcement was present in either span. Concrete compression and splitting tension strengths measured 4600 psi (31.7 MPa) and 414 psi (2.86 MPa), respectively.

Phase 3 of loading begins by applying a uniform load via a line of hydraulic jacks beneath the west span until failure is observed in that span. Following failure, the west span is repaired with external shear reinforcement and the uniform load is replaced with a point support. The beam is reloaded during Phase 4 with a hydraulic jack from above in a 3-point bending configuration until the east span fails in shear. Additional details of the tests can be found in Chapter 2 and Appendix A.

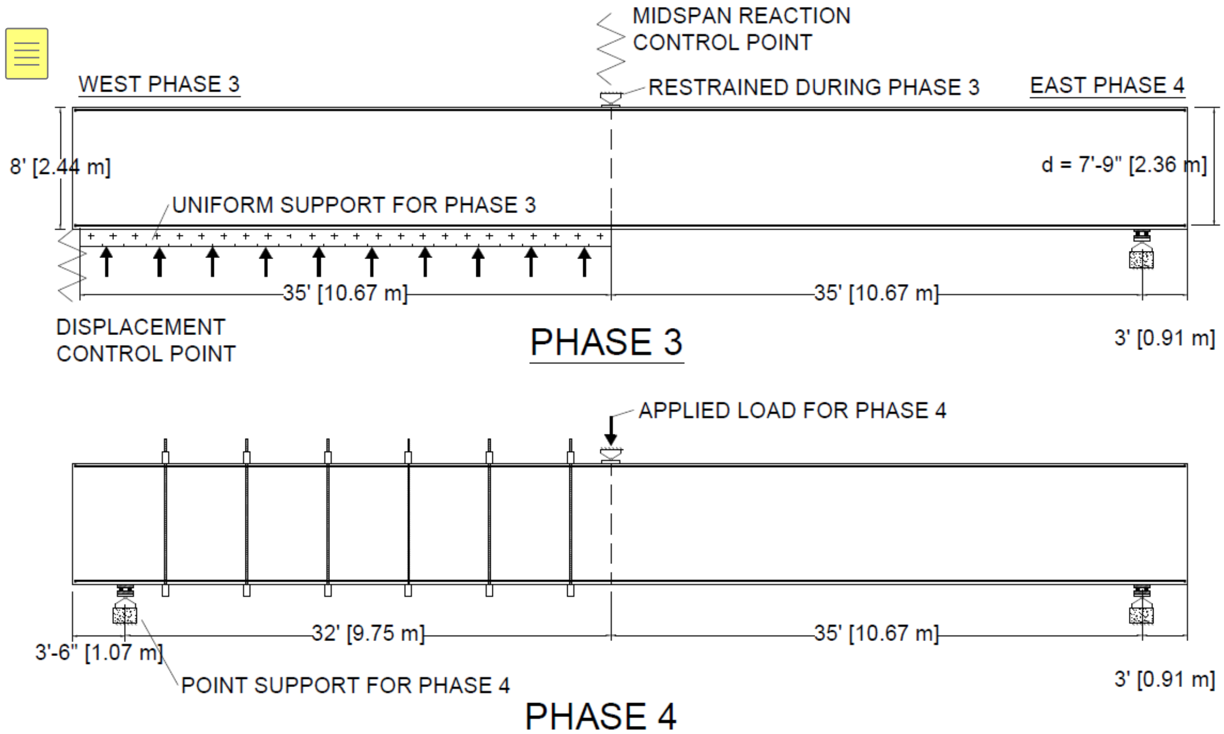

Figure 3-3: UCB Beam 2 specimen details and testing configuration

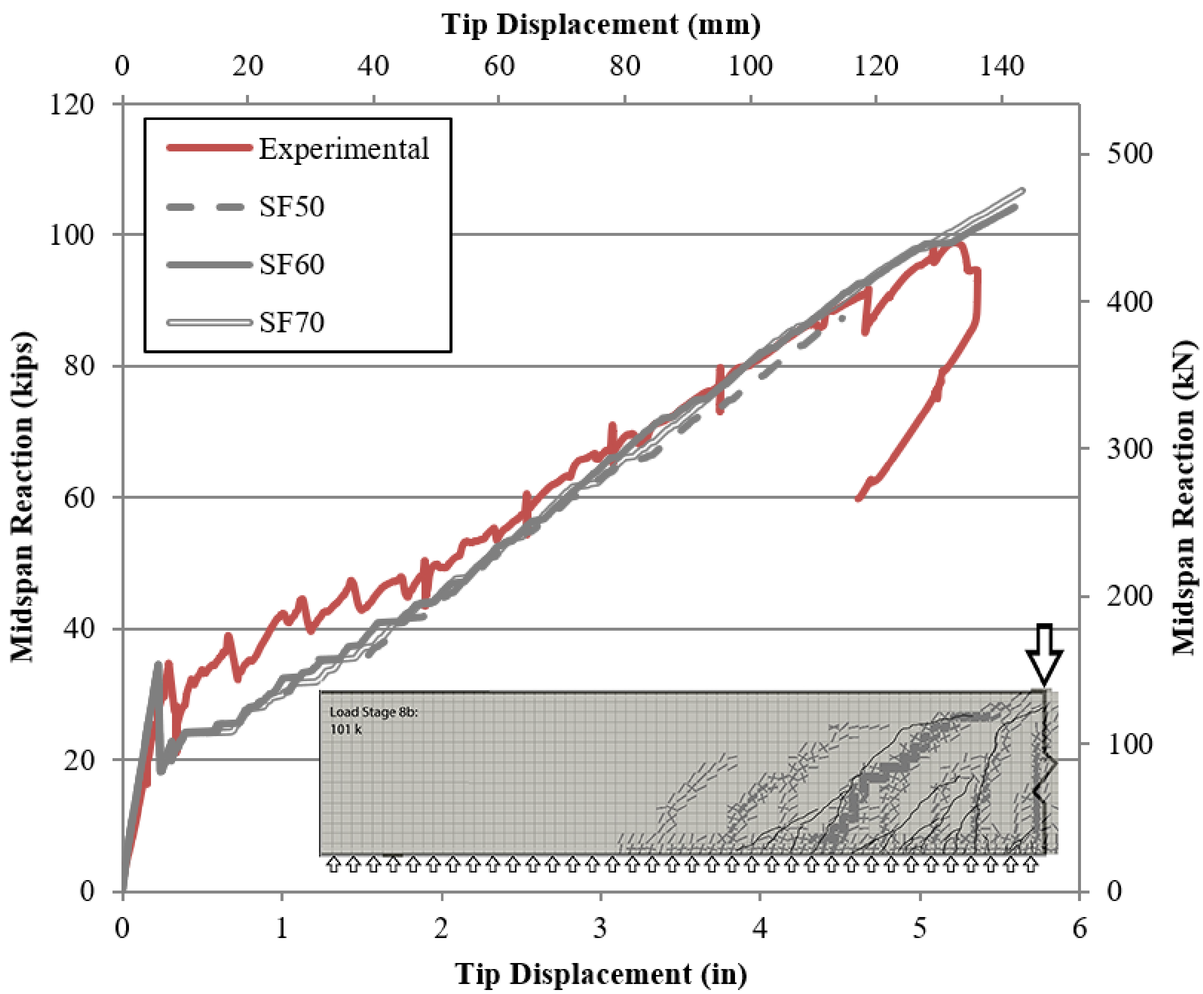

Figure 3-4: UCB Beam 2, Phase 3 experimental data and FE simulation of load-displacement and crack comparisons.

The best performing FE model for Phase 1, with the described parameters in Table 3-1 and Table 3-2, is used to model the load-displacement curve for Phase 3. Two additional models varying in the shear factor are also used to check the variability in the simulations. There were a few key differences between the model for Phase 1 versus Phase 3. The jacks providing a uniform support reaction were represented as a line load underneath the west span and the midspan was restrained against movement from above. As indicated in Figure 3-3, load-displacement relationships during Phase 3 were recorded in terms of the load developed at the midspan restraint and the displacement at the west end of the beam.

The FE model was analyzed in force-control rather than displacement-control since the displacements corresponding to a uniform support reaction were unknown. Most load steps used a Newton-Raphson solver to find a convergent solution, which will always increase the load increment between load steps. For the load steps immediately after initial flexure cracking, an arc-length solver with a very small step size was used to solve what is numerically a snap-through behavior.

Figure 3-4 presents the FE model of Phase 3, using the material properties of the best calibrated Phase 1 model with no alterations. Good agreement in the load-displacement response and the crack pattern is observed between the experimental values and the ATENA simulation. It is noted that reinforcement and concrete were of the same specifications and sourced from the same mills and concrete batch plant for Phase 3 as Phase 1. Additionally, the concrete properties on the test day for Phase 1 and Phase 3 were nearly identical, which was beneficial to the Phase 3 simulation since the material was essentially the same. Due to these factors, the peak load was simulated to within 14 %, 3%, and 7% for each of the models with s_F = 50, 60, and 70, respectively. Other key test variables are compared in Table 3-3, which show generally good agreement between experimental and simulated variables.

The FE model overestimates the drop in load after initial flexure cracking, which is attributed to the assumption of homogenous material properties. While the cracking load was simulated reasonably well, the FE model provides lower forces after cracking until 70 k midspan reaction, after which the lines corresponding to the FE models and experimental data appear to rejoin at a similar slope.

The failure criterion used for calibrating the Phase 1 model did not need to be used here as there was no horizontal splitting of concrete along longitudinal reinforcement. Instead, failure was simply characterized by the lack of numerical convergence and the severely deformed shape of the last load step in the converged model. A comparison of key test values against the ATENA simulation is summarized in Table 3-3, where most quantities were represented correctly. However, the ATENA model overestimated crack widths, likely because the Phase 3 test was halted before total failure to ensure the span remained repairable.

Table 3-3: Phase 3 ATENA vs Experimental Values

	Experimental	ATENA
Peak Load	101 k	104 k
Cracking Load	35.0 k	34.5 k
Peak Displacement	5.03”	5.61”
Maximum Crack Width	3 mm	12 mm
Max. Longitudinal Reinforcement Tensile Strain at Peak Load	0.0035	0.0036
Max. Longitudinal Reinforcement Tensile Stress at Peak Load	86 ksi	91.9 ksi

The FE model results of Phase 4 are presented in Figure 3-5. Since shear strength was the primary variable to predict, the FE model for Phase 4 is configured in a 3-point bending configuration and loaded monotonically to failure. To ensure that the east span of interest fails, the west span was artificially strengthened by increasing s_F to 300. The strength for each of the models with s_F = 50, 60, and 70 were relatively close to the failure load, providing estimates within 8% of the experimental failure load of 70 k. Displacement and stiffness estimates were less accurate, as it appears the stiffness of the FE model was higher than the recorded results during Phase 3 and Phase 4. This is attributed to artificially strengthening the east span, which increased its stiffness and affected the load-displacement stiffness. The data processing was also different than how the FE model was set up. However, as the beam is determinate, this should have minimal effects on the ultimate strength. Comparison of key data points using the best model (s_F= 60) is summarized in Table 3-4.

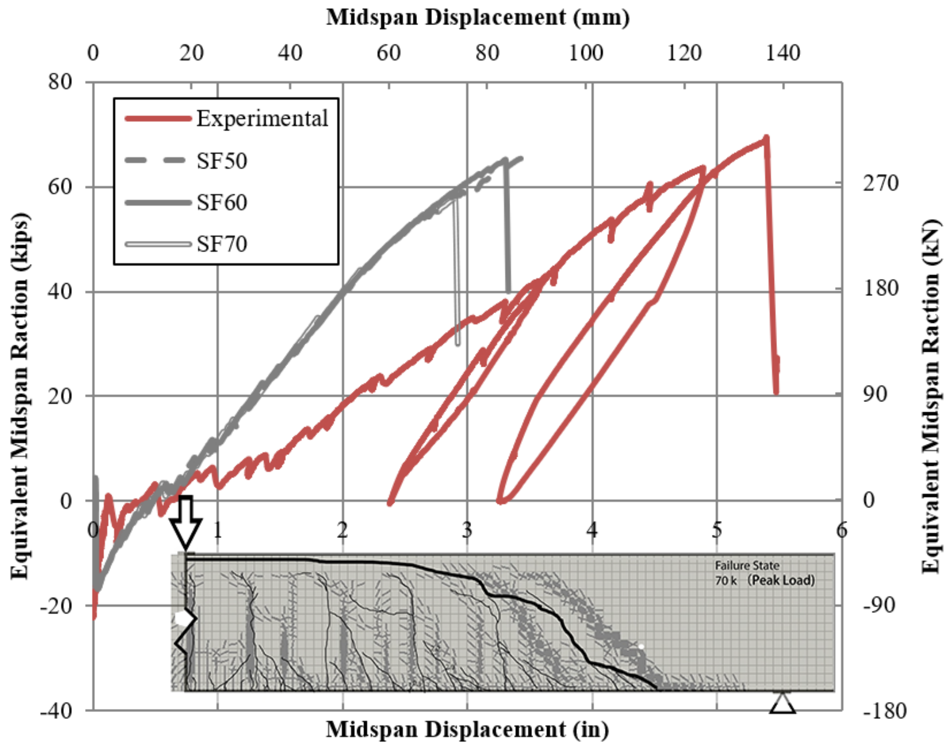

Figure 3-5 Load-displacement of FE model for Phase 4.

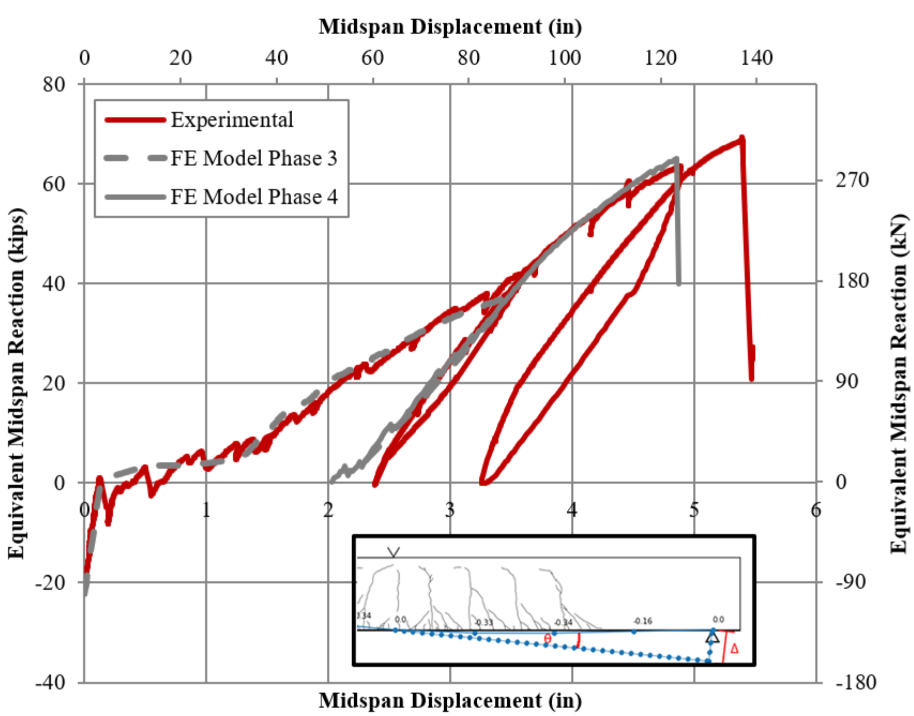

Figure 3-6: Load-displacement of Phase 4 model calibrated to fit displacements.

Table 3-4: Phase 4 ATENA vs. Experimental Values

	Experimental	ATENA
Peak Load	70 k	65 k
Cracking Load	1.0 k	4 k
Peak Displacement	5.4”	3.5
Maximum Crack Width	2.0 mm before failure (estimated)	6 mm
Max. Longitudinal Reinforcement Tensile Strain at Peak Load	0.0057	0.00483
Max. Longitudinal Reinforcement Tensile Stress at Peak Load	113 ksi	106 ksi

To improve the likeness of the FE model’s load-displacement response, it was essential to replicate the loading history and mimic how data were processed in the experimental setup. The experimental data stitches the response of the beam under Phase 3 loading with the uniform support reaction to Phase 4 by monitoring the rotation at midspan during Phase 3 (see inset picture in Figure 3-6). This provides a tangent line at the midspan that is used to extrapolate a perpendicular distance to the right support, providing an approximate estimate for the midspan displacement if the east span were loaded in 3-point bending during Phase 3.

To accurately reproduce the load-displacement plot, the complex loading history and repair procedure had to be incorporated in the FE model. An FE model was first analyzed in the Phase 3 test setup. After failure is reached, the model is unloaded and repaired with external shear reinforcement. The model is then reloaded in 3-point bending until failure. Displacement data were extracted from the FE model using the same processing method as described by the inset in Figure 3-6.

When the loading history is accounted for, the FE model replicates the experimental FE results adequately, as shown in Figure 3-6. A much better estimate of the load-displacement curve is reached with a similar peak load for Phase 4.

3.8. Parametric Study of Shear Strengths on Foundation Mat Slices Subject to Different Boundary Conditions

The success of the FE models to replicate the load-displacement relations of Phase 1, Phase 3, and Phase 4 increased confidence in the ability to extend those models for conducting parametric studies to investigate boundary condition effects on one-way shear strength in beams and foundations. To facilitate comparison, the shear strength is normalized as follows:

$$\alpha = \frac{V}{b_w d\sqrt{f_c'}} \quad \text{(psi or MPa units)} \tag{3-4}$$

where V is the assessed shear strength taken from the FE model, b_w is the web width, d is the distance from the centroid of the reinforcement to the extreme compression fiber, and f'_c is the concrete compressive strength.

3.8.1. Shear Span and Clamping Effects on Mat Foundation Shear Strength

Foundations and beams experience different boundary conditions that affect how they resist applied loads. While beams primarily resist downward forces by reactions at discrete points along their length, foundations distribute these reactions over their footprint, transferring them to the supporting soil. This soil reaction introduces vertical stresses, often termed clamping stresses [5], along the foundation's shear span (see Figure 3-7) that inhibits the formation and growth of diagonal cracks. In contrast, vertical stresses in beams with point loads are only significant within the disturbed regions, typically taken as regions within d of the support or loading point.

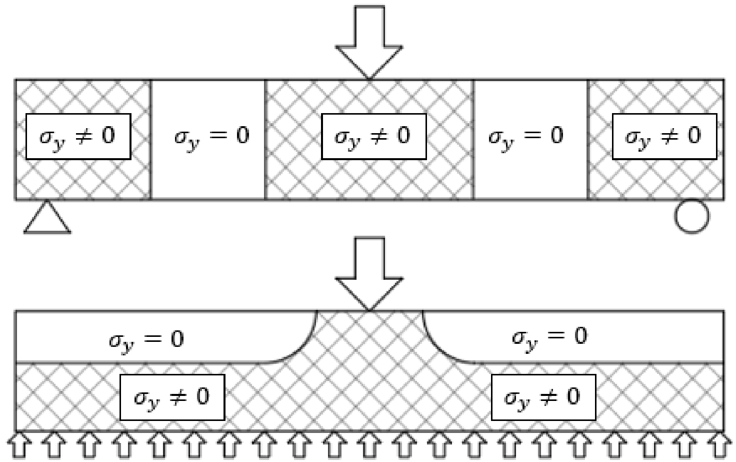

Figure 3-7: Vertical clamping stresses in beams (above) and foundations (below) based on linear FEM analysis.

There is currently little research in the relationship between shear slenderness and shear strength in foundations. Notably, neither shear span effects nor clamping stresses are explicitly considered in the ACI 318-19 one-way shear equations. To investigate the influence of shear slenderness on shear strength in beams and foundations, two cross sections and two boundary conditions were considered in Figure 3-8. The cross sections corresponded to the Phase 1 cross section (P1), with a member depth of 140 inches (3.56 m) and a reinforcement ratio of 0.45%, and the Phase 3 and Phase 4 cross sections (P3), both with a member depth of 96 inches (2.44 m) and a reinforcement ratio of 0.22%. The P1 and P3 cross sections are indicated in maroon and blue, respectively.

FE models using these cross sections were subjected to two loading conditions. In the first boundary condition, labeled "beam," a point load was applied above the beam at midspan and two supports at each end for resistance. In the second boundary condition, labeled "foundation," a point load was applied from above while a uniformly distributed line load along the bottom face provided resistance. The "beam" boundary condition is indicated with a hollow diamond marker, while the "foundation" boundary condition is indicated with a filled-in square marker. The shear strength was measured at the location along the member span corresponding to mid-depth of the failure crack. The FE models calibrated to the experimental results are circled in red and labeled as V_{test}.

Figure 3-8 presents the relationship between shear strength and *a/d* ratio for the four FE model series. At *a/d* ratios below 3, the P1 beam series shows an increase in one-way shear strength with decreasing *a/d*. This is consistent with strut-and-tie theory, which states that the shear strength of beams with sufficiently small *a/d*, typically below 2.5, is governed by arching action [16]. However, this trend is absent in the P3 beam series, where shear strength remains relatively constant with *a/d*, even for *a/d* ratios below 2.5. This may be because the FE model is calibrated to sectional shear mechanisms but not to strut-and-tie mechanisms, resulting in inaccurate responses.

Generally, the shear strength increases with decreasing *a/d* for the P1 foundation and P3 foundation series. This is attributed to two factors. First, a smaller slenderness pulls the centroid of the soil reaction towards the core wall, leading to smaller relative bending moments and reduced longitudinal tension strains. The reduced tension strains result in smaller crack widths, increasing shear strength [2]. Second, the reduced foundation slenderness increases soil pressure, which increases the vertical clamping pressures in the foundation. These vertical clamping stresses inhibit diagonal crack formation and crack growth, leading to increased shear strength as well.

For the P1 and P3 foundation series at *a/d* = 6, the shear strengths are $1.3\sqrt{f_c'}$ and $0.8\sqrt{f_c'}$, respectively. Their shear strengths increase to $2.7\sqrt{f_c'}$ and $1.6\sqrt{f_c'}$, respectively, at *a/d* = 2. The twofold increase in shear strength with reduced slenderness in the foundation FE models aligns with the experimental findings of Uzel et al., who observed that the size effect is mitigated in one-way foundation specimens with *a/d* ratios below 2.5 [17].

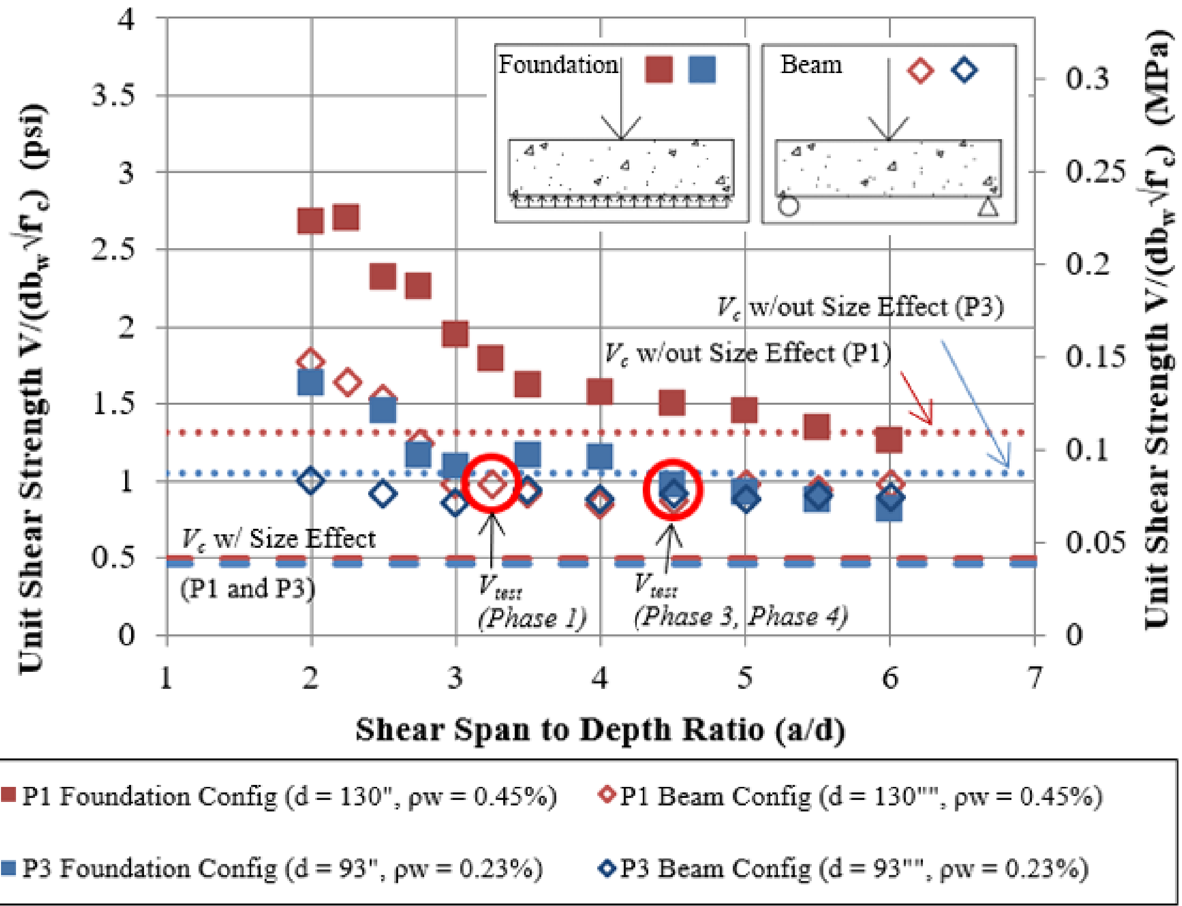

Figure 3-8: Change in unit shear strength with variable *a/d* for loading as a beam versus loading as a foundation.

Comparison between P1 foundation and P1 beam FE models supports the view that the shear strength of foundations is larger than its beam counterpart for all *a/d* ratios, with the two data sets appearing to converge in strength at a point beyond *a/d = 6*. Likewise, comparison between P3 foundation and P3 beam FE models shows that foundation shear strengths are larger than beam shear strengths for *a/d* less than 4, and similar in shear strength beyond an *a/d* of 4. The *a/d* ratio at which foundation shear strength equals the beam shear strength may depend on the member cross-sectional properties and requires further study.

The ACI 318-19 nominal shear strength equation and size effect factor (λ_s) are as follows in (eq. 3-5) and (eq. 3-6):

$$V_c = 8\lambda_s \lambda (\rho_w)^{1/3} \sqrt{f_c'} \quad \text{(eq. 3-5)} \qquad\qquad \lambda_s = \sqrt{\frac{2}{1+\frac{d}{10}}} \quad \text{(eq. 3-6)}$$

The nominal shear strength (eq. 3-5), considering the size effect (eq. 3-6), for the P1 beam and P3 beam cross-sections is plotted in Figure 3-8 using horizontal dashed lines, which equates to treating the P1 beam and P3 beam FE series as beams or slabs. On average, the ACI 318-19 expression results in a nominal shear strength approximately half the finite element strengths for P1 and P3 beams for *a/d* between 3 and 6.

ACI 318-19 permits ignoring the size effect factor ($\lambda_s = 1$) for shallow foundations and mat foundations. The nominal shear strength (eq. 3-5) with the size effect exemption ($\lambda_s = 1$) is plotted with dotted maroon and blue horizontal lines, which correspond to the P1 foundation and P3 foundation FE series, respectively. Comparing the FE model series to their colored dotted lines, the nominal shear equation with the size effect exemption appears to provide a lower bound for the P1 foundation series. The FE model P3 foundation series drops marginally below the ACI 318-19 value for larger *a/d* values.

This study using four FE model series shows that while the ACI 318-19 shear equations underestimate the strength of beams and slabs, the same equations with the size effect exemption for shallow foundations can provide reasonable lower bound estimates for the shear strength of mat foundations. However, this is achieved by taking the size effect factor as 1, which is not consistent with experimental results since foundations and beams are equally affected by the size effect. This was demonstrated experimentally by the Phase 3 and Phase 4 tests, which were tested as a foundation and as a beam, respectively, and observed similar shear strengths of $1.0\sqrt{f_c'}$ and $0.93\sqrt{f_c'}$. Additional study of effects of size on thick foundation elements is recommended.

3.8.2. Axial Loading Effect on Mat Foundation Shear Strength

In addition to vertical loads from the superstructure and supporting soil, a mat foundation must also resist various lateral loads. Under service loads, the mat resists at-rest earth pressures plus hydrostatic pressures at its free edge, inducing axial compression across the entire mat. During an earthquake, lateral loads are resisted by the foundation system through active or passive soil pressures on the mat edges, as well as friction on the mat base, as depicted in Figure 3-9 . To resist these lateral forces, axial compression is induced in the mat. Tension may also occur on the uplifting side due to friction, as drawn in Figure 3-9. However, this side of the mat is not expected to control the design for two reasons. First, the uplifting side experiences reduced vertical soil pressures, resulting in lower shear demand. Second, because friction is proportional to soil pressure, the decrease in soil pressures also reduces friction, thereby limiting axial tension. Consequently, this study focuses on the side of the mat that compresses into the soil under the combined effects of lateral load and overturning moments.

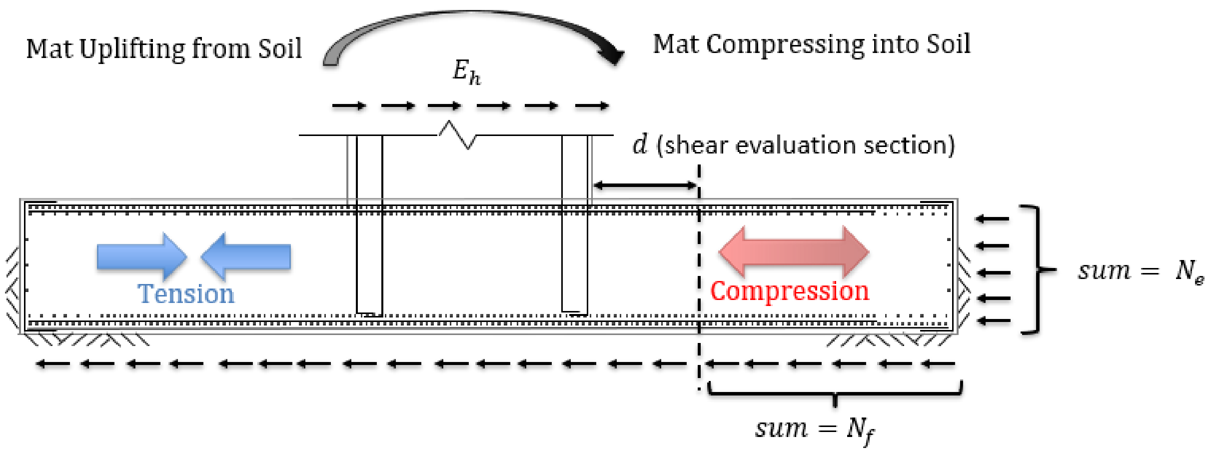

Figure 3-9: Frictional forces and lateral earth pressures inside mat foundations.

While axial compression provides benefits to one-way shear strength, the extent of these benefits in mat foundations is unclear. To investigate the effects of axial compression on shear strength, the FE models focused on the portion of the mat extending from the core wall to the compressed edge under overturning action, as shown in the inset figures of Figure 3-10. Two foundation configurations were considered: the Phase 1 geometry, which had *d=130", ρ_w=0.45%, a/d = 3.25*, and the Phase 3 geometry, which had *d=93", ρ_w=0.22%, a/d = 4.5*. The FE models for each configuration were loaded with a uniform stress applied normal to the end of the mat, representing lateral soil pressures. The total applied force sums to N_e, as shown in Figure 3-9. Another series of FE models applied friction as a uniform line load parallel to the bottom of the mat, totaling N_f over the distance from d from the core wall to the mat edge, as shown in Figure 3-9. The models are initially subjected to a constant amount of either normal force or friction, followed by a monotonically increasing uniform upward pressure until shear failure. For comparison, each friction model with an axial force of N_f had a corresponding model with normal force N_e, where $N_e = N_f$. The maximum considered N_f was the frictional load at which flexure cracking occurred on the top of the mat. Shear strength is assessed at *d* from the core wall, as indicated.

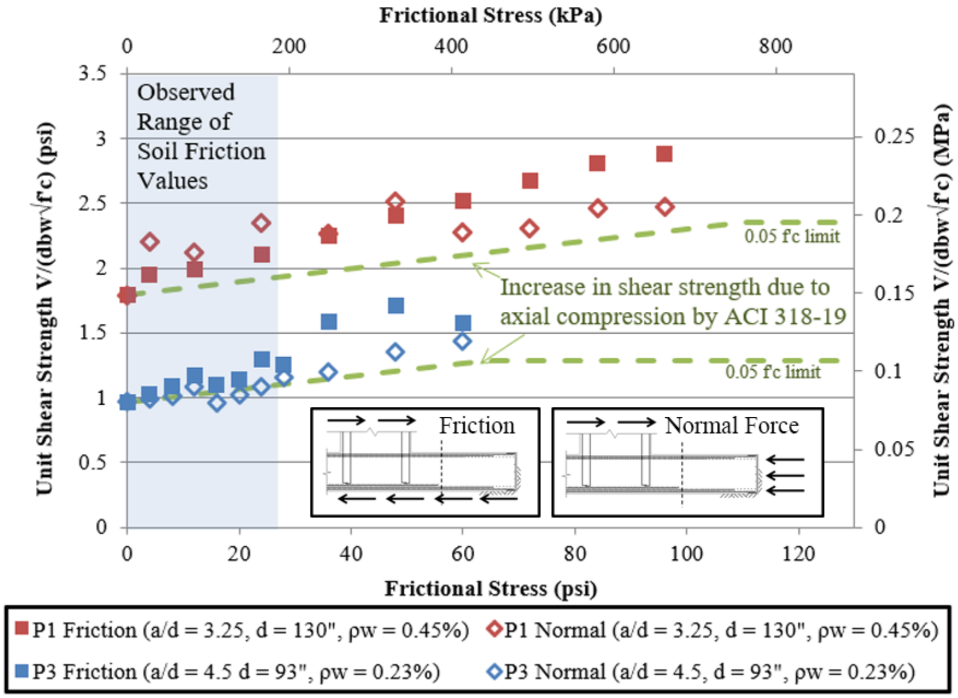

Figure 3-10: Increase in one-way shear strength with increase in axial compression, acting on mat as either friction on the base or as normal forces on the edges.

Figure 3-10 presents the shear strength of FE models with varying amounts of axial compression. For models loaded with normal forces, the axial compression is reported in terms of the equivalent frictional stresses at the mat base that would generate the same axial compression at *d* from the core wall ($N_e = N_f$). The frictional stress (τ) is related to the axial compression by:

$$\tau = \frac{N_f}{b_w\,(a/d - 1)d} \tag{3-7}$$

In general, the shear strength of all four FE series increases with greater friction at the mat base and higher axial load. At the largest considered frictional stress for each FE series, where cracks began forming on the top of the mat, shear strength increases by about 50% compared to the case with zero axial stress for all 4 FE series.

Based on an internal study, it was found that frictional stresses in mat foundations under lateral earthquake loads can be as high as 25 psi (180 kPa), covering the shaded region in Figure

3-10. At this frictional stress or equivalent amount of normal force, a modest 20% increase in shear strength is observed for all FE models on average. As there is also large uncertainty in quantifying frictional forces and lateral earth pressures, it is not recommended to incorporate these effects to improve design shear strength in mat foundations.

The ACI 318-19 one-way shear equation, with the axial load term included, is:

$$V_c = \left[8\lambda\lambda_s(\rho_w)^{\frac{1}{3}}\sqrt{f_c'} + \frac{N_u}{6A_g}\right] b_w d \tag{3-8}$$

The term representing the contribution of axial load to shear strength, $N_u/6A_g$, is limited to a stress of $0.05f_c'$. This equation also assumes that the axial loads are applied uniformly over the cross-section, whereas friction forces act along the base of the foundation.

The green dashed line in Figure 3-10 shows the expected benefits of increasing axial compression on shear strength, where the FE model's shear strength under zero axial load is taken as the y-intercept instead of $8\lambda\lambda_s(\rho_w)^{\frac{1}{3}}\sqrt{f_c'}$. The line appears to provide a lower bound on shear strength when compared with the FE model strengths for both friction and normal force loading cases. This suggests that the $N_u/6A_g$ term provides a reasonable estimate for increases in shear strength due to axial compression for either normal forces or frictional forces for the limited cases presented here.

3.8.3. Influence of Overturning Forces on Mat Foundation Shear Strength

The topic of shear forces in the mat foundation due to overturning moments is not well addressed in the literature. Under purely vertical loads, soil pressures tend to concentrate beneath core walls or columns rather than being uniformly distributed [17]. This concentration benefits shear design as more of the total load is concentrated within *d* of the supported wall or column, reducing the shear demands at *d* away from the wall or column. On the other hand, resistance against overturning moments requires a sufficiently large lever arm between the uplifting and compressed edge of the mat, pushing the soil pressures outwards toward the mat edges. It is unclear how this shift in soil pressure away from the supported wall or column affects the one-way shear strength.

FE models of 2D foundation slices were used to study a simple soil-supported mat foundation, as shown in Figure 3-11. The FE model is loaded with two point loads (*P/2*) to represent the vertical loads from the core wall. Two shear spans are modeled on either side of the core wall for resistance against vertical load and overturning moment. The FE models B11 and B22 had the same cross-sectional properties and shear span as the experimental tests Phase 1 and Phase 3, respectively, with the geometric properties as shown in Figure 3-11. Shear strengths are assessed at *d* away from the core wall, as indicated.

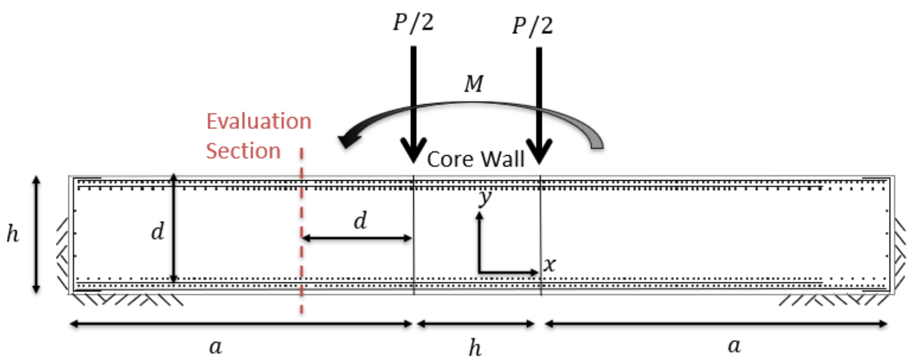

	Mat B11 (*Phase 1*)	Mat B22 (*Phase 2*)
h	140”	96”
d	130”	93”
ρ_w	0.45%	0.23%
a	420”	420”
a/d	3.25	4.5

Figure 3-11: Summary of overturning model geometry and reinforcement configuration.

Assuming the foundation is infinitely rigid relative to the soil, the soil pressure along the base of the mat is uniformly distributed under vertical loads (*P*) and linearly varying with distance under overturning moments (*M*) according to equation (3-9):

$$\sigma_y = \frac{P}{A} \pm \frac{Mx}{I} \tag{3-9}$$

where the A is the area of the mat base, I is the moment of inertia of the mat in the same bending axis as M, and x is the distance along the mat base according to the coordinate system shown in Figure 3-11. This soil pressure distribution corresponding to contributions from P and M are depicted in the inset drawings in Figure 3-12.

The FE models B11 and B22 were analyzed for their one-way shear strength under the assumed soil pressure distribution in equation (3-9). First, a set amount of vertical load is applied, followed by incremental increases in overturning moments until shear failure is observed. Various combinations of vertical load and overturning moment are considered until uplift occurs at the free edge.

Figure 3-12 presents the shear strengths of FE models B11 and B22. Model B11 exhibits a minor decrease in shear strength with increased overturning moments. In contrast, the shear strength of B22 remains constant, irrespective of the applied overturning moment. This is attributed to the following mechanism: as overturning moments increase, the centroid of the soil pressure shifts away from the core wall towards the free edge. This increases the moment demands, thereby increasing the effective shear span (*M/Vd*). This increase in effective shear span (*M/Vd*) appears consistent with the findings of section 3.8.1 (Figure 3-8), where the P1 foundation model decreased in shear strength with increasing *a/d* while the P3 foundation model had a constant shear strength beyond *a/d = 4*.

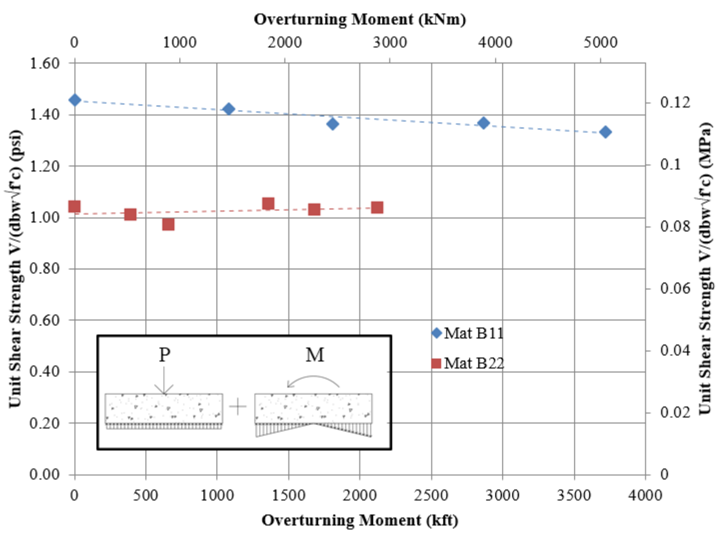

Figure 3-12: Unit shear strengths with increasing amount of overturning moment under assumed soil pressure distributions.

To enhance the realism of the FE model, the assumed soil pressure distribution was replaced with linear compression-only springs to represent the soil, allowing for a basic consideration of soil-structure interaction. Based on reviews of geotechnical reports for existing mat foundations, a subgrade modulus of 40 lbs/in^3 (270 kN/m^3) was selected, representative of a softer soil. Softer soil was preferred in this study to observe larger shifts in soil pressures away from the core wall. Like the previous FE model, a constant vertical load (*P*) is first applied to the FE model, followed by an overturning moment (*M*) that is monotonically increased until failure.

Figure 3-13 shows the change in unit shear strength with increasing overturning moment for FE models B11 and B22. The maximum moment considered corresponds to uplift of approximately 30% of the shear span, which was deemed a reasonable limit for uplift. The fitted trendline shows an observable decrease in the unit shear strength for both FE model series, although some inherent scatter is present in the FE results. The reduction in unit shear strength from a purely vertical load to the maximum considered overturning moment is about 20% and 30% for model series Mat B11 and Mat B22, respectively.

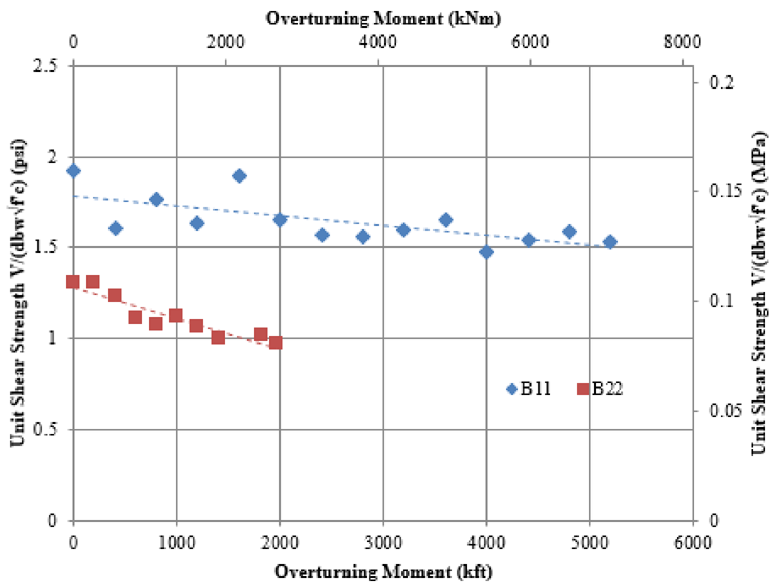

Figure 3-13: Unit shear strengths with increasing amount of overturning moment with mat supported by soil springs.

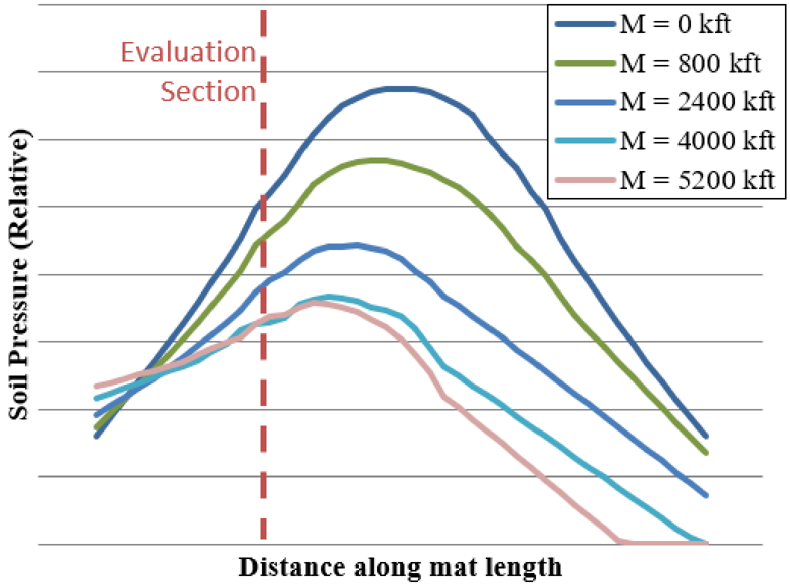

Figure 3-14: Foundation soil pressure distributions at shear failure under varying combinations of axial load and overturning moment for model B11.

Figure 3-14 shows the soil pressure distribution, considering soil-structure interaction, along the base of the mat for various levels of overturning moment. Under zero overturning moment, a concentration of soil pressure is observed beneath the core wall. Compared with the case with uniformly distributed soil pressures under vertical loads, soil-structure interaction results in reduced shear demand at *d* from the core wall.

As overturning moments increase, the centroid of the soil pressure shifts away from the core wall, increasing the effective shear span (*M/Vd*) and reducing shear strength. Additionally, a greater proportion of the soil pressures is pushed beyond *d* from the core wall, raising the shear demands on the compressed edge of the mat. This behavior is consistent with the observations of Figure 3-12.

In addition to the increase in *M/Vd* with greater overturning moment, soil pressures and associated clamping stresses at the evaluation section also decrease. Since clamping stresses restrain the growth and formation of diagonal cracks, their proximity to the diagonal crack is a critical factor. In this FE model, the failure crack consistently forms at the evaluation section, approximately *d* from the core wall. As shown in Figure 3-14, the soil pressure at the evaluation section decreases significantly with increased overturning moment, resulting in reduced restraint on diagonal crack formation and is thought to lower shear strength as well.

3.9. Conclusions

A set of physical one-way shear tests were modeled in the nonlinear finite element software ATENA. The FE model was calibrated using data from Phase 1, Phase 3, and Phase 4. General observations and ATENA-specific observations from the calibration process are summarized below:

1. Mechanisms relating to the mechanics along the failure crack (crack stiffness, crack opening parameters) were most influential in fine tuning FE model's failure mode. In ATENA, these are the shear factors, fracture energy, and unloading factors. They may go by different names in other FE software depending on the implemented constitutive models.
2. FE models with the best failure load simulations also tended to produce an accurate crack pattern when compared with the experimental results.
3. There is some inherent variability in the FE modeling process. A sensitivity analysis is recommended when resources permit to observe the scatter in FE load-displacement response.

Using the calibrated FE models, the one-way shear strength of mat foundations subject to various loading effects and boundary conditions was investigated. The results of these parametric studies are summarized below:

1. FE models showed that the shear strength of a soil-supported foundation is equal to or greater than the shear strength of the same member loaded as a beam in 3-point bending. The differences are attributed to the presence of vertical clamping stresses in foundations. Other variables, such as member depth and longitudinal reinforcement ratio, are likely to affect the effectiveness of clamping stresses on shear strength but require additional study.
2. When subject to axial loads generated by earth pressure or horizontal friction, shear strength can increase by modest amounts. However, quantifying soil friction or lateral earth pressures in a foundation mat can be difficult and highly variable. It is not recommended to consider axial compression in mat foundations due to the relatively small benefit and large uncertainty in determining axial compression.
3. The axial compression term in the ACI 318-19 shear equations appears to reasonably estimate the increase in shear strength.

4. One-way shear strength is reduced when a mat foundation is subject to significant overturning moment due to increased effective shear spans (M/Vd) and reduced clamping action near the critical section. Designing a mat foundation using procedures for a beam (i.e., considering the size effect) provides a lower bound on design shear strength and is recommended until further studies are able to more fully quantify these effects.

3.10. References

[1] R. Klemencic, I. S. McFarlane, N. M. Hawkins and S. Nikolaou, "NEHRP Seismic Design Technical Brief No. 7: Seismic Design of Reinforced Concrete Mat Foundations - A Guide for Practicing Engineers (NIST GCR-917-22)," National Institute of Standards and Technology, Gaithersburd, MD, Aug 2012.

[2] ASCE-ACI Committee 445 on Shear and Torsion, "Recent Approaches to Shear Design of Structural Concrete," *Journal of Structural Engineering,* vol. 124, pp. 1375-1417, December 1998.

[3] ACI Committee 318, Building Code Requirements for Structural concrete (ACI 318-19) and Commentary (ACI 318R-19, Farmington Hills, MI: American Concrete Institute, 2019.

[4] CSA A23.3-14, Design of Concrete Structures, Mississauga ON, Canda: Canadian Standards Association, 2014.

[5] A. B. Acevedo, E. C. Bentz and M. P. Collins, "Influence of Clamping Stresses in the Shear Strength of Concrete Slabs Under Uniform Loads," *Journal of Earthquake Engineering,* vol. 13, no. S1, pp. 1-17, 2009.

[6] K.-H. Reineck, E. C. Bentz, B. Fitik, D. A. Kuchma and O. Bayrak, "ACI-DAfStb Database of Shear Tests on Slender Reinforced Concrete Beams without Stirrups," *ACI Structural Journal,* vol. 110, no. 5, pp. 867-875, 2013.

[7] M. P. Collins, P. T. Quach and E. C. Bentz, "Shear Strength of Thick Slabs," *ACI Structural Journal,* vol. 117, no. 4, pp. 115-126, 2020.

[8] J. F. Horvilleur and V. B. Patel, "Mat Foundation Design - A Soil Structure Interaction Problem," *ACI Symposium Publication,* vol. 152, pp. 51-94, 1995.

[9] V. Cervenka, L. Jendele and J. Cervenka, "ATENA Program Documentation Part 1 - Theory," Cervenka Consulting, 31 March 2021. [Online]. Available:

https://www.cervenka.cz/assets/files/atena-pdf/ATENA_Theory.pdf. [Accessed 2024].

[10] Z. P. Bazant and B. H. Oh, "Crack Band Theory for Fracture of Concrete," *Materials and Structures,* vol. 16, no. 3, pp. 155-177, 1983.

[11] V. Cervenka, R. Pukl, J. Ozbolt and R. Eligehausen, "Mesh Sensitivity Effects in Smeared Finite Element Analysis of Concrete Fracture," in *Proceedings FRAMCOS-2 Aedificatio publishers*, Freiburg, Germany, 1995.

[12] F. J. Vecchio and M. P. Collins, "The Modified Compression Field Theory for Reinforced Concrete Elements Subjected to Shear," *ACI Journal Proceedings,* vol. 83, no. 2, pp. 219-231, 1986.

[13] V. Cervenka, J. Cervenka, R. Pukl and T. Sajdlova, "Prediction of Shear Failure of Large Beam Based on Fracture Mechanics," in *9th International Conference on Fracture Mechanics of Concrete and Concrete Structures*, 2016.

[14] J. Cervenka, V. Cervenka and S. Laserna, "On Crack Band Model in Finite Element Analysis of Concrete Fracture in Engineering Practice," *Engineering Fracture Mechanics,* vol. 197, pp. 24-47, 2018.

[15] fib. The International Federation for Structural Concrete, "Fib bulletin 2. Structural concrete textbook on behaviour, design and performance updated knowledge of the CEB/FIP model code 1990 volume 2," fib. The International Federation for Structural Concrete, 1999.

[16] M. P. Collins and D. Mitchell, Prestressed Concrete Structures, Response Publications, 1997.

[17] J. Hegger, A. G. Sherif and M. Ricker, "Experimental Investigations on Punching Behavior of Reinfored Concrete Footings," *ACI Structural Journal,* vol. 103, no. 4, pp. 604-613, July 2006.

[18] A. Uzel, B. Podgorniak, E. C. Bentz and M. P. Collins, "Design of Large Footings for One-Way Shear," *ACI Structural Journal,* vol. 108, no. 2, pp. 131-138, 2011.

CHAPTER 4: SUMMARY AND CONCLUSIONS

4.1. Overall Summary

Mat foundations for high-rise buildings have traditionally been constructed as relatively thick members without shear reinforcement and with relatively low longitudinal reinforcement ratio. Laboratory testing have previously shown that the unit shear strength decreases with increasing depth and with decreasing longitudinal reinforcement. These effects are represented in the one-way shear strength design equations of ACI 318-19, which results in significantly reduced nominal strength when compared with design strengths that were successfully used for foundation mats for decades. The introduction of high-strength longitudinal reinforcement raises further questions about the effects of increased longitudinal reinforcement strains on one-way shear strength. To explore the effects of depth, reinforcement ratio, and high-strength reinforcement on one-way shear strength, a series of seven one-way shear laboratory tests were conducted. The tests were supplemented by nonlinear finite element studies to extrapolate the test results to alternate member geometries and boundary conditions. Design recommendations are proposed based on the findings of experimental and analytical studies.

4.2. Experimental Studies

Four unique shear tests were conducted on two large beams containing high-strength [Grade 100 (690 MPa)] longitudinal reinforcement and normal-weight nominal 4000-psi (28 MPa) compressive strength concrete. The focus was to evaluate the effects of size, longitudinal reinforcement ratio, strain in the longitudinal reinforcement, and provision of ACI minimum shear reinforcement on the unit shear strength of large beams. The four tests were designated Phases 1 through 4, as summarized below.

The Phase 1 test involved a three-point beam-style test with centrally located point load, self-weight, and two “roller” supports. The beam developed maximum tensile stress of approximately 50 ksi (345 MPa) in the longitudinal reinforcement before failing in shear at a nominal shear stress of a 1.0 $\sqrt{f_c'}$ in psi units (0.083$\sqrt{f_c'}$ MPa units). The corresponding nominal shear stress according to the ACI 318-19 one-way shear equations is 0.5 $\sqrt{f_c'}$ in psi units (0.042$\sqrt{f_c'}$ MPa units), or about 50% of the measured shear strength.

The Phase 2 test had the same member depth and shear span as the Phase 1 test but the span was provided longitudinal tension reinforcement ratio of 0.84% with minimum shear reinforcement $A_{v,min}$ as specified in ACI 318-19. The beam developed maximum tensile stress of 90 ksi (621 MPa) in the longitudinal reinforcement before failing in shear by fracturing all transverse reinforcement. The nominal shear stress resisted by the concrete at failure was between $1.5\sqrt{f_c'}$ psi ($0.125\sqrt{f_c'}$ MPa) and $1.9\sqrt{f_c'}$ psi ($0.16\sqrt{f_c'}$ MPa) depending on whether the transverse reinforcement stress was assumed equal to f_{su} or f_{sy}, respectively. The failure load was 1.15 times the nominal shear strength specified by ACI 318-19.

The Phase 3 test was a footing-style test that contained no shear reinforcement and was loaded with a uniformly distributed reaction beneath the test span. The beam developed maximum tensile stress of approximately 86 ksi (593 MPa) in the longitudinal reinforcement before failing in shear at a nominal shear stress of $1.0\sqrt{f_c'}$ psi ($0.083\sqrt{f_c'}$ MPa). The ACI 318-19 nominal shear strength, assuming the member to be a beam, is $0.44\sqrt{f_c'}$ psi ($0.037\sqrt{f_c'}$ MPa), or about 0.44 of the measured strength. Assuming the member to be a footing, such that the size effect factor of ACI 318-19 would not apply, the ACI 318-19 nominal shear strength is $1.04\sqrt{f_c'}$ psi ($0.086\sqrt{f_c'}$ MPa), or 1.04 of the measured strength.

The Phase 4 test was nominally identical to the Phase 3 test except the span was tested as a beam-style test with concentrated central load, self-weight, and roller supports. The span developed maximum tensile stress of approximately 113 ksi (780 MPa) in the longitudinal reinforcement before failing in shear at a nominal shear stress of $0.93\sqrt{f_c'}$ psi ($0.077\sqrt{f_c'}$ MPa). The shear strength is nearly identical to the value measured in a nominally identical beam tested as a footing-style test. The ACI 318-19 nominal shear equations, assuming the member to be a beam, is the same as that calculated for Phase 3, being $0.44\sqrt{f_c'}$ psi ($0.037\sqrt{f_c'}$ MPa). This is approximately 0.47 of the tested shear strength.

The results of the four beam tests were compared with results of other tests of deep beams with varying longitudinal reinforcement ratios. On the basis of these tests, the following conclusions are made:

1. Headed shear reinforcement corresponding to the minimum shear reinforcement ratio of ACI 318-19 reduces the size effect and allows the concrete contribution to reach close to if not the full $2.0\sqrt{f'c}$ psi ($0.17\sqrt{f'c}$ MPa).

2. The ACI 318-19 equations for one-way shear are very conservative for large members without shear reinforcement. The ratio of code nominal strength to measured one-way shear strength ranged between 0.44 to 0.50 for Phases 1, 3, and 4 when treating the specimens as a beam. Trends for different size effect series additionally show that unit shear strengths tend to a lower bound of about 1.0 $\sqrt{f'c}$ psi (0.083 $\sqrt{f'c}$ MPa).
3. The shear strength of members containing high-strength longitudinal reinforcement appears consistent with the shear strength of members containing Gr.60 reinforcement when the reinforcement ratios are similar. This was observed at large a/d ratios, where only specimens containing high-strength longitudinal reinforcement would fail in shear and specimens containing Gr. 60 reinforcement would fail in flexure before shear.
4. Tension shift in specimens loaded as a beam results in large increases in longitudinal reinforcement strain relative to cracked-section predictions. In comparison, the tension shift effect was less significant for the footing-style loading.
5. Minimal differences between Phase 3, the footing-style loading, and Phase 4, the beam-style loading, were observed in terms of the observed shear strength at the evaluation section, suggesting that differences in shear strength between beams and footings are closer than the ACI 318-19 code may imply and that any observed differences in strength are likely due to other factors.

4.3. Analytical Studies

The set of physical one-way shear tests were modeled in the nonlinear finite element software ATENA. The FE model was calibrated using data from Phase 1, Phase 3, and Phase 4. General observations and ATENA-specific observations from the calibration process are summarized below:

1. Mechanisms relating to the mechanics along the failure crack (crack stiffness, crack opening parameters) were most influential in fine tuning FE model's failure mode. In ATENA, these are the shear factors, fracture energy, and unloading factors. They may go by different names in other FE software depending on the implemented constitutive models.

2. FE models with the best failure load simulations also tended to produce an accurate crack pattern when compared with the experimental results.
3. There is some inherent variability in the FE modeling process. A sensitivity analysis is recommended when resources permit to observe the scatter in FE load-displacement response.

Using the calibrated FE models, the one-way shear strength of mat foundations subject to various loading effects and boundary conditions was investigated. The results of these parametric studies are summarized below:

1. FE models showed that the shear strength of a soil-supported foundation is equal to or greater than the shear strength of the same member loaded as a beam in 3-point bending. The differences are attributed to the presence of vertical clamping stresses in foundations. Other variables, such as member depth and longitudinal reinforcement ratio, are likely to affect the effectiveness of clamping stresses on shear strength but require additional study.
2. When subject to axial loads generated by earth pressure or horizontal friction, shear strength can increase by modest amounts. However, quantifying soil friction or lateral earth pressures in a foundation mat can be difficult and highly variable. It is not recommended to consider axial compression in mat foundations due to the relatively small benefit and large uncertainty in determining axial compression.
3. The axial compression term in the ACI 318-19 shear equations appears to reasonably estimate the increase in shear strength.
4. One-way shear strength is reduced when a mat foundation is subject to significant overturning moment due to increased effective shear spans (M/Vd) and reduced clamping action near the critical section. Designing a mat foundation using procedures for a beam (i.e., considering the size effect) provides a lower bound on design shear strength and is recommended until further studies are able to more fully quantify these effects.

Appendix A. EXPERIMENTAL SUMMARY AND TEST DATA

Table of Contents

Seven individual shear tests, six of which included members without shear reinforcement and one with ACI minimum shear reinforcement, were tested and reported in this document. Each of the test beams served to investigate some aspect of foundation or beam design and all specimens together evaluates the one-way shear strengths of concrete members with very low reinforcement ratios and containing A1035 Gr.100 high-strength longitudinal reinforcement. A summary of the key parameters for all seven shear tests is provided below in Table A-1 and a summary of test results provided in Table A-2. The shear force is reported in two ways. V_{c-d} refers to the concrete contribution to shear force at d away from the support, the section of highest shear where code checks are performed. V_{c-c} refers to the shear force carried across the failure crack, which is calculated by considering a free-body diagram formed from cutting the beam in two along the diagonal crack. After summing any applied loads, support reactions, and self-weight, the remaining unbalanced vertical forces are attributed to V_{c-c}.

Table A-1: Overview of one-way shear tests

Beam	a	d	a/d	b_w	A_s	ρ_w	f_y^*	f_c'	Testing Age	a_g
Phase 1	35’	130”	3.23	10”	6 in^2	0.46%	120 ksi	4.6 ksi	43	3/4"
Phase 3	35’ **	93”	4.52	10”	2 in^2	0.22%	120 ksi	4.6 ksi	28	3/4"
Phase 4	35’	93”	4.52	10”	2 in^2	0.22%	120 ksi	5.0 ksi	41	3/4"
CB3	8’-6”	34”	3.0	12”	0.93 in^2	0.23%	124 ksi	5.4 ksi	93	3/4"
CB2	5’-6”	22”	3.1	12”	0.62 in^2	0.23%	124 ksi	5.4 ksi	93	3/4"
CB1	2’-10”	11”	3.1	12”	0.40 in^2	0.30%	131 ksi	5.5 ksi	113	3/4"
Phase 2***	35’	131”	3.23	10”	11 in^2	0.84%	120 ksi	4.6 ksi	65	3/4"

* Yield stress defined by 0.2% offset method

** Shear span for uniform load

*** Contains ACI minimum shear reinforcement at 0.089%.

Table A-2: Summary of test results

Beam	(a) V_{c-c}	(b) $\frac{V_{c-c}}{b_w d\sqrt{f_c'}}$	(c) V_{c-d}	(d) $\frac{V_{c-d}}{b_w d\sqrt{f_c'}}$	(e) $\frac{V_{Code}}{b_w d\sqrt{f_c'}}$ (ACI)	(f) $\frac{V_{c-d}}{V_{Code}}$ (ACI)	(g) $\frac{V_{Code}}{b_w d\sqrt{f_c'}}$ (CSA)***	(h) $\frac{V_{c-d}}{V_{Code}}$ (CSA)	(i) Max. Steel Strain and (Stress)
Phase 1	69 k	0.78 (psi units)	90 k	1.0	0.5	2.0	0.82 (n.s.)	1.22	0.17% (50 ksi)
Phase 3	54.1 k	0.86 (psi units)	64 k	1.0	0.46	2.2	0.67 (n.l)	1.5	0.35% (86 ksi)
Phase 4	55.2 k	0.84 (psi units)	61 k	0.93	0.46	2.0	0.74 (n.s.)	1.3	0.57% (113 ksi)
CB3	33.9 k	1.13 (psi units)	34.9 k	1.16	0.71	1.63	0.90 (n.l)	1.3	0.45% (107 ksi)
CB2	24.3 k	1.26 (psi units)	24.5 k	1.26	0.85	1.48	1.01 (n.l)	1.2	0.42% (103 ksi)
CB1	>15.5 k	>1.59 (psi units)	>15.5 k	>1.59	1.13	1.4	1.15 (n.l)	1.4	0.62% (133 ksi)
Phase 2	>128 k	>1.45* (psi units)	205 k	2.3**	2.0	1.15	1.52 (n.l)	1.5	0.38% (90 ksi)

* Since *V* = *Vs* + *Vc-c, Vs* estimated as *fu* times number of bars crossing crack. Equation is solved to provide lower bound on *Vc-c*.

** Since *V* = *Vs* + *Vc-d, Vs is* taken as (*As)(fy)(d)/(s)* as per ACI 318-19 and the equation is solved for *Vc-d.*

*** The CSA method evaluates the shear strength along the shear span. The critical location is indicated as n.s. = near support and n.l. = near load.

A.1. Common Observations of Tests without Shear Reinforcement

Based on the observations of six one-way shear tests that span depths as large as 130" deep to as small as 12" deep, several trends are identified. These are listed and described below.

- **Accuracy of ACI 318-19 Equations:** To compare the accuracy of the ACI and CSA equations with the test results, the normalized value for V_{c-d} is compared with the ACI prediction in column (f) of Table A-2. This comparison shows that, for combinations of no shear reinforcement, large depth, and low reinforcement ratio, the ACI equations are conservative by about a factor of 2. For the shallower Companion Beams, the ACI equations are conservative by about 1.5.

- **Accuracy of CSA A23.3 Equations:** The CSA general method is an iterative method for shear strength that considers the bending moment at the shear section in the strength prediction. Predictions with CSA are also conservative but are closer to the experimental value as observed in column (h). The predicted values by the Canadian method at *d* from the support are lower for Phase 3 than for Phase 4 even though the two spans are reinforced identically. This is because the CSA code considers the influence of longitudinal strain on shear strength and Phase 3 has higher longitudinal strains at the evaluation section when compared to Phase 4. This results in CSA code predictions being lower for the Phase 3 critical section, but this effect was not observed in the testing data of Phase 3 and Phase 4. This may imply CSA would be more conservative for foundations than for beams.
- **Correlation of Steel Strains at Crack Tail with Failure Shear Forces:** Comparing the steel strains and shear forces across the crack at failure between Phase 3 and Phase 4, it is found that both failure cracks carry essentially the same forces when normalized by the cross section and $\sqrt{f_c'}$. It is also found that the steel strains at the tail of the crack recorded very similar amounts, with both Phase 3 and Phase 4 recording about 0.2% elongation respectively. Because steel strains on the tension face correlate well with the widths of cracks in this region, there may be better correlation between the strains at the base of the crack and the failure load.
- **Shear Strength Similarities between Foundations and Beams:** With regards to the one-way shear strength between a foundation like loading (Phase 3) and a beam-like loading (Phase 1,4, CB1, CB2, CB3), no differences in the mechanics of one-way shear were observed. Failure loads for Phase 3 and Phase 4, the tests directly comparing foundation and beam strengths, showed little difference in failure shear strength. This is because loads applied by the supporting jacks outside of *d* from the loading head would tend to fan out into a uniform stress field. Since one-way shear mechanisms are typically more critical at mid-depth of the beam instead of at the tension face, the resulting stress field is similar to the case where a point support is used. Any observed

differences in one-way shear strength between foundations and beams would come from other sources, such as the influence of clamping forces in foundations, non-uniform stress distributions from the supporting soil, or axial restraint imposed by the boundary conditions of a foundation element.

- **Large Tension Shift:** Tension shift was observed in all shear tests except CB1 and CB2. The tension shift zone typically extends from the point of highest moment, which is generally underneath the point of load application or restraint on the top face of the beam. The steel strains remain plateaued until some distance away from the point of highest moment, which is observed in some cases to coincide with the base of a diagonal shear crack. This is because the presence of a diagonal shear crack and associated aggregate interlock forces require larger tensile steel forces at the crack base, manifesting as tension shift to maintain equilibrium balance. The amount of tension shift is influenced by the loading, specifically the gradient of the bending moment diagram as observed in the small tension shift zones of Phase 3. Otherwise, the zone can extend to as far as about $1.7d$ of the point of maximum moment, which corresponds to a right triangle with hypotenuse angled at a 30-degree angle to the horizontal.
- **Effectiveness of Shear Reinforcement:** Plots of the average beam surface shear strain for all the tests show that when shear reinforcement is not present, the beam suffers a dramatic decrease in the shear stiffness upon initial cracking. When shear reinforcement is present, the shear stiffness shows a more gradual degradation instead. Shear reinforcement also adds a minor amount of ductility to shear failures, allowing crack widths to open much larger than their counterparts without shear reinforcement. Failures in specimens without shear reinforcement are sudden and often occur very subtly via rapid crack lengthening and crack widening. Minimum shear reinforcement is quite effective in overcoming the size effect, allowing V_c to be taken as the full $2\sqrt{f_c'}$. It is also very effective in increasing the shear strength, with an observed increase of from 90 k to 285 k in shear strength at failure between Phase 1 and Phase 2.
- **Crack Widths and Member Depth:** The crack observations from 6 tests show that smaller beams experience failure at smaller crack widths, whereas larger beams have larger crack widths before failing. Aggregate interlock models suggest that it is this larger crack width that causes the size effect since the maximum shear stress transferred

by a crack decrease with increasing crack width. Additionally, the smaller crack widths means that residual tensile capacity via tension softening mechanisms are possible in resisting shear forces for the smaller beams, whereas the large crack widths of the deeper beams prohibit this mechanism from activating.

- **Surface Deformation Concentrated at Cracks:** Measurements of the surface deformations for each beam show that the largest surface deformations occur via opening of the cracks. Relative to the crack movement, surface strains of the beam are in comparison very small. Kinematic models that concentrate most of the surface deformation at the cracks should provide a reasonable estimate of the deformation field.

A.2. Evaluation of High-Strength Longitudinal Reinforcement Effects on Shear Strength

The effects of high-strength longitudinal reinforcement on one-way shear strengths can be observed over a range of depths through the six shear tests outlined in this report. These tests are compared against similar size effect series identified at the University of Toronto [1], which are shown below in Figure A-1 and Figure A-2. The data in each test series is obtained using similar testing, material, and construction practices to ensure that the only variable investigated is shear strength variation with depth. The shear strength is reported in two ways, either at a distance *d* away from a support at the section of highest shear as typically done in design or taken directly as the shear force carried by the failure crack at failure, which considers the geometry of the failure crack. Figure A-1 additionally includes the ACI 318-19 prediction for a series of beams with the same reinforcement ratio as the beams tested in this report to illustrate the size effect and differences between the ACI 318-19 one-way shear equation and the test results.

The UC Berkeley size effect series, which covers the six shear tests described in this report, has reinforcement ratios between 0.22% to 0.45%. The UC Berkeley size effect series is most consistent with the Low Rho Size Effect which has an average reinforcement ratio of 0.35% but contains regular Gr. 60 longitudinal reinforcement. Regardless of how the shear force is reported, the UC Berkeley Size Effect series and the Low Rho Size Effect series are always the closest.

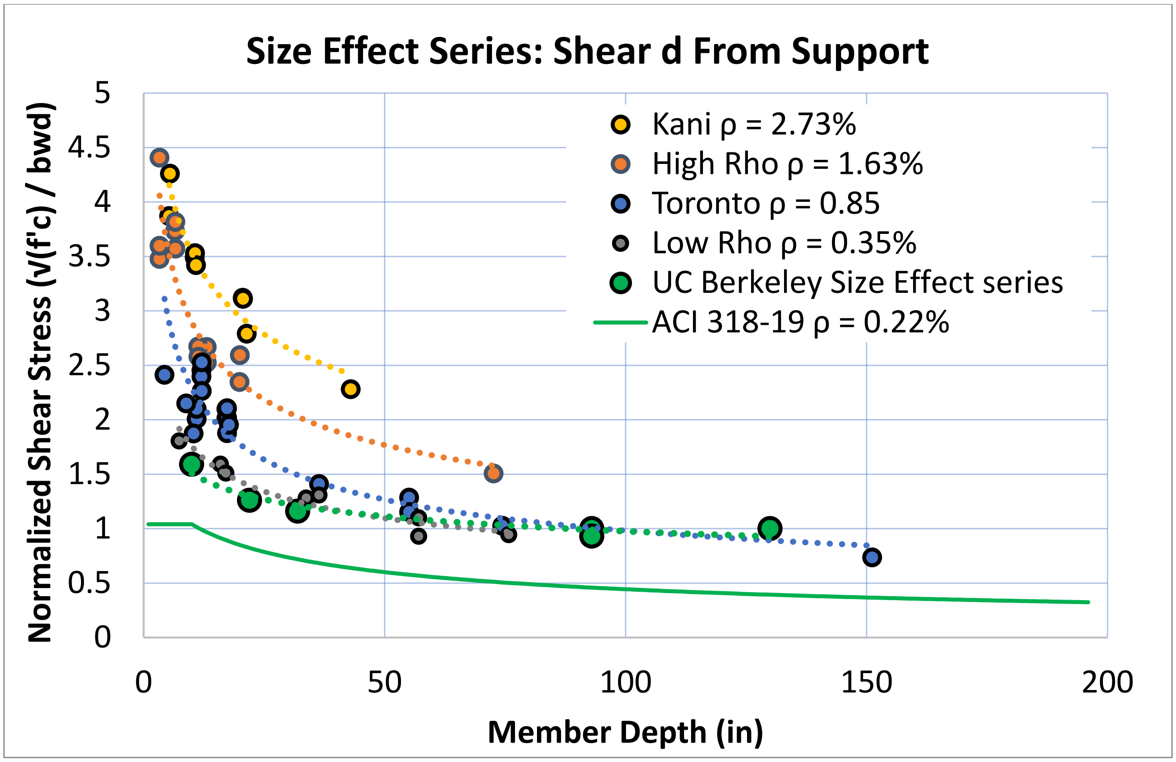

Figure A-1: Size effect series at *d* from support

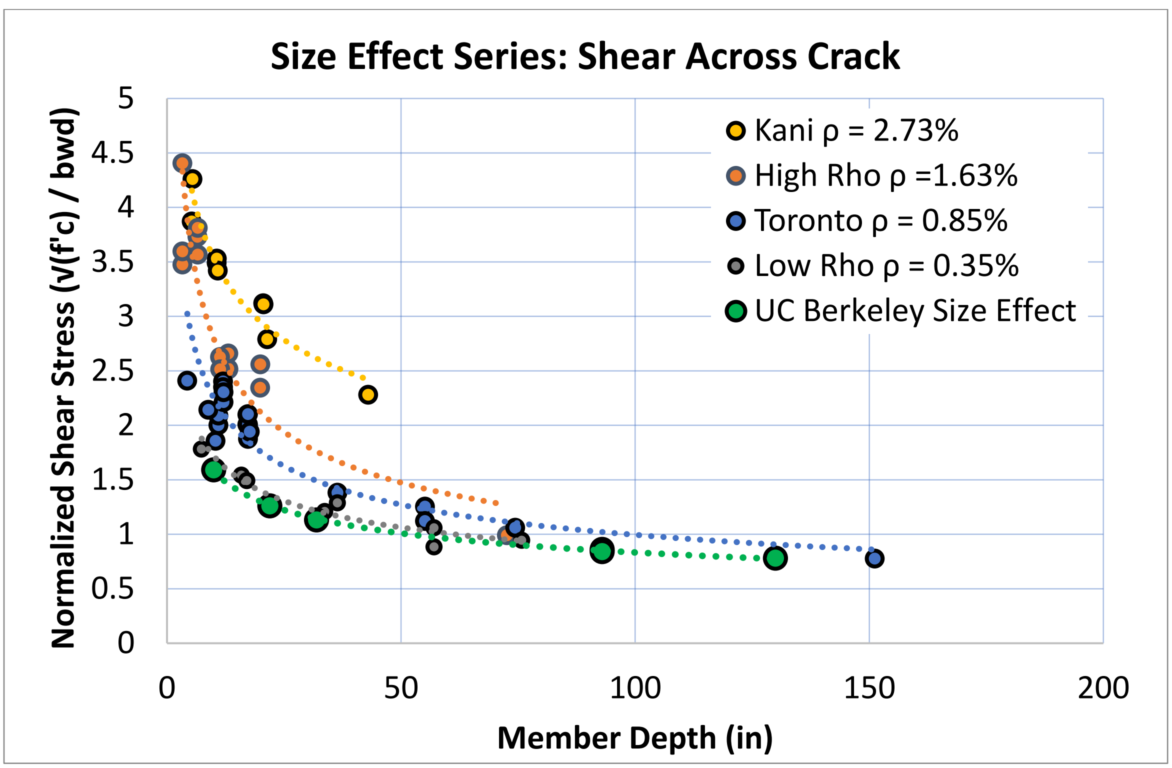

Figure A-2: Size effect series taken with shear across crack

With regards to designing mat foundations with high-strength reinforcement, the following points should be considered in the transition to high-strength longitudinal reinforcement:

- Headed shear reinforcement is highly effective and compatible with high-strength longitudinal reinforcement. No significant decreases in the shear strength are observed when steel stresses are close to "yielding" since the experimental value for V_c is around $2\sqrt{f_c'}$. Both ACI and CSA codes provide a slightly conservative estimate of the shear strength when shear reinforcement is used in the design.
- If no shear reinforcement is present and the same quantity of longitudinal steel is used with Gr.100 steel instead of Gr. 60 steel, the moment strength will increase greatly but the shear strength will not, possibly changing the failure mode from flexure to shear. This is because whether a beam fails in flexure or one-way shear depends on the shear span to depth ratio (*a/d*). When using high-strength longitudinal reinforcement, one-way shear failure is observed starting at around *a/d=2.5* but the largest *a/d* ratio at which a shear failure is still observed increases. For the deep beam tests outlined in this report, the shear strength does not appear to decrease at larger *a/d* ratios where steel stresses exceed 100 ksi. In this view, high-strength reinforcement does not negatively affect the shear strength of beams without shear reinforcement.
- If no shear reinforcement is present and Gr.100 or higher grade longitudinal reinforcement is used to match the flexural strength of a design with Gr. 60 longitudinal reinforcement, there will be roughly a two-fold decrease in the reinforcement ratio. For this scenario, the shear strength will decrease in accordance with the longitudinal reinforcement effect and be consistent with the shear strength of a member containing Gr. 60 longitudinal reinforcement at an equivalent reinforcement ratio. This is true even if steel strains in the high-strength steel are close to "yield". This means that designers can use the provided f_y of high-strength reinforcement for moment design while using existing equations for shear strength that have been calibrated with members containing Gr. 60 steel.

A.3. Material Properties

Companion concrete cylinders were casted from each concrete truck and stored in similar ambient conditions as the test specimens, with the cylinders removed from the cylinder molds at the same time the specimens were removed from the formwork

Test beam 1 was cast in 3 equal lifts from 4 ready-mix trucks. Test beam 2 was cast in 3 equal lifts from 3 ready-mix trucks. Specimens CB1, CB2, and CB3 were all cast from the same truck.

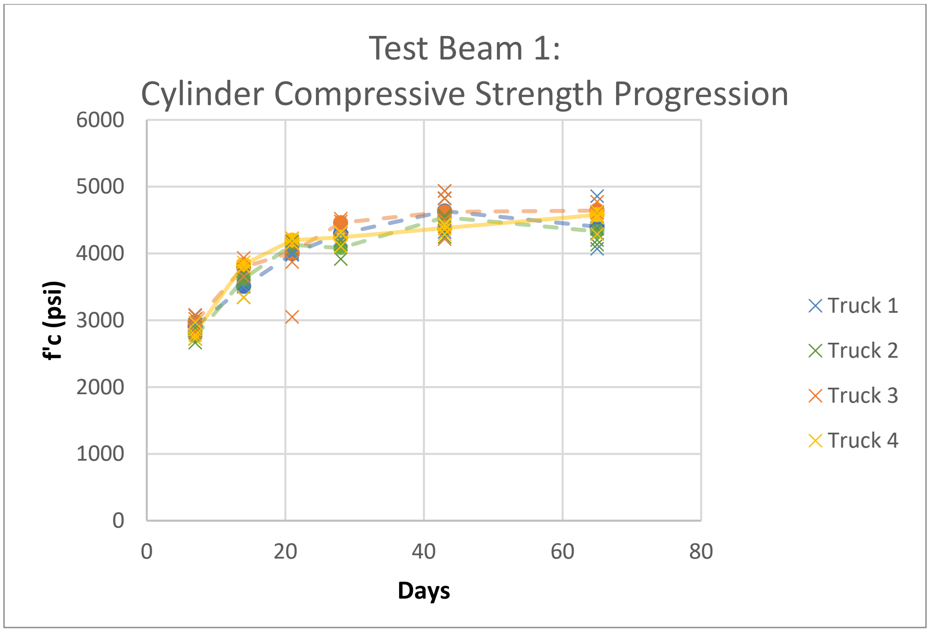

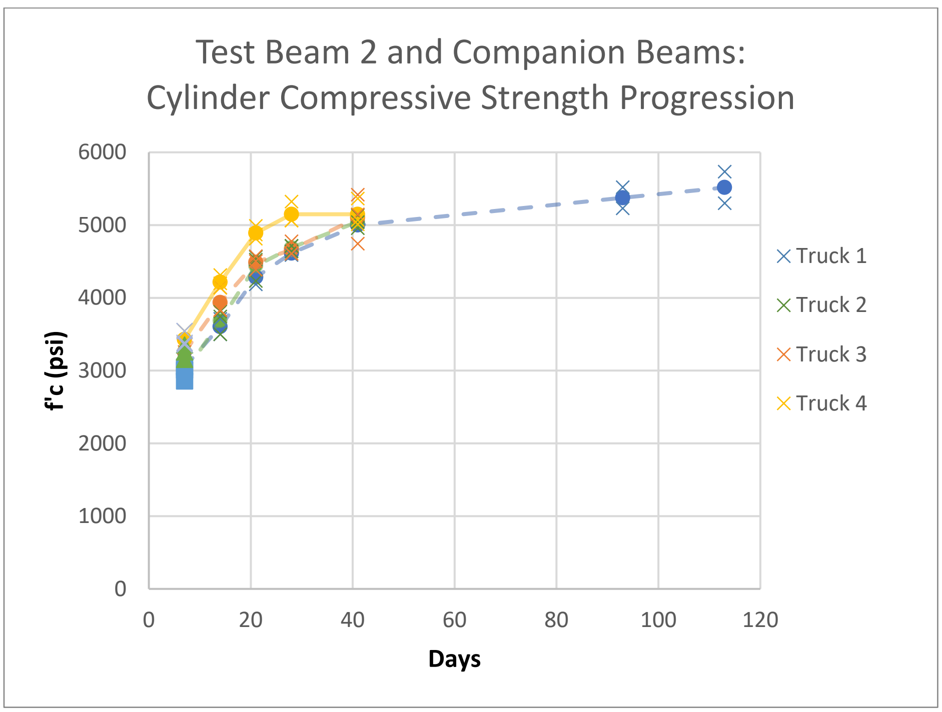

Figure A-3: Development of concrete cylinder compressive strength with time.

Table A-3: Compressive strength of concrete cylinders for UCB Beam 1

	7 Day (psi)	14 Day (psi)	21 Day (psi)	28 Day (psi)	Test Day 1 45 Day (psi)	Test Day 2 65 Day (psi)
Truck 1 (P1, P2)	2723 2936 3069 Avg: 2909	3672 3503 3343 Avg: 3506	4016 3995 3978 Avg: 3996	4210 4292 4381 Avg: 4294	4322 4453 4936 4822 Avg: 4633	4296 4381 4071 4856 Avg: 4401
Truck 2 (P1, P2)	2666 2724 2886 Avg: 2759	3698 3608 3563 Avg: 3796	4181 4058 4149 Avg: 4129	3917 4135 4190 Avg: 4081	4824 4530 4565 4247 Avg: 4542	4133 4368 4202 4616 Avg: 4330
Truck 3 (P1, P2)	2822 2081 3033 Avg: 2975	3656 3798 3934 Avg: 3796	4162 3872 ~~3051~~ Avg: 4017	4381 4520 4478 Avg: 4460	4507 4828 4936 ~~4215~~ Avg: 4757	4616 4608 4571 4773 Avg: 4642
Truck 4 (P1, P2)	2968 2774 2725 Avg: 2822	3866 3803 ~~3347~~ Avg: 3835	4231 4214 4152 Avg: 4199	4105 4317 4307 Avg: 4243	4421 4443 4288 4367 Avg: 4380	4537 4628 ~~4288~~ 4567 Avg: 4505

Concrete from Trucks 1-3 occupied the lower 8 ft of the concrete beam and are used as the basis for assessing concrete strength:

Test Day 1 (Phase 1) f’c = (4633 + 4542 + 4757)/3 = 4644

Test Day 2 (Phase 2) f’c = (4401 + 4330 + 4642)/3 = 4458

The average of the cylinder strengths appears to decrease between Test Day 1 to Test Day 2. The lumped average was used across both Day 1 and Day 2 since it is likely the cylinder strengths remained constant.

Collective Test Day 1 (Phase 1) and Test Day 2 (Phase 2) f’c = (4644 + 4458)/2 = 4551 psi.

Table A-4: Compressive strength of concrete cylinders for UCB Beam 2 and Companion Beams

	7 Day (psi)	14 Day (psi)	21 Day (psi)	Phase 3 28 Day (psi)	Phase 4 41 Day (psi)	CB2, CB3 93 Day (psi)	CB4 113 Day (psi)
Truck 1 (CB1, CB2, CB3)	3137 2960 Avg: 3049	3498 3710 Avg: 3604	4381 4185 Avg: 4283	4640 4589 Avg: 4615	-- --	5230 5520 5524 5224 Avg: 5375	5300 5733 Avg: 5517
Truck 2 (P3, P4)	3008 3049 2857 Avg: 2971	3499 3813 3743 Avg: 3685	4524 4232 4562 Avg: 4439	4512 4716 4638 Avg: 4622	5042 4958 5137 5050 Avg: 5047	-- --	-- --
Truck 3 (P3, P4)	3256 3154 3352 Avg: 3254	3834 4142 3830 Avg: 3935	4386 4573 4505 Avg: 4488	4778 4605 4605 Avg: 4663	5417 5146 4744 4610 Avg: 4979	-- --	-- --
Truck 4 (P3, P4)	3382 3357 3544 Avg: 3428	4137 4199 4313 Avg: 4216	4870 4988 4813 Avg: 4890	5061 5064 5322 Avg: 5149	5365 5011 5071 5534 Avg: 5245	-- --	-- --

For the second test beam (Phase 3 and Phase 4), concrete from Truck 2 composed the lower 3 ft, concrete from Truck 3 composed the next 3 ft, and concrete from Truck 4 composed the upper 2 ft. As most of the shear behavior occurs in the lower 2/3 of the beam's depth, strengths from Truck 2 and Truck 3 are most appropriate in determining response. Thus Truck 4 was not considered in average calculations.

Phase 3 f'c = (4622 + 4663) / 2 = 4640 psi.

Phase 4 f'c = (5047 + 4979) / 2 = 5010 psi.

Table A-5: Cylinder Split Tension Strengths

	Phase 1 45 Day (psi)	Phase 2 65 Day (psi)	Phase 3 28 Day (psi)	Phase 4 41 Day (psi)	CB2, CB3 93 Day (psi)

Truck 1	401 421 406 Avg: 419	453 369 408 Avg: 410	-- --	-- --	~~433~~ 570 542 Avg: 556
Truck 2	416 397 486 Avg: 433	392 386 376 Avg: 385	416 414 454 Avg: 428	415 ~~496~~ 412 Avg: 414	-- --
Truck 3	365 520 433 483 Avg: 427	384 567 391 483 Avg: 419	420 382 398 Avg: 400	409 440 458 Avg: 436	-- --
Truck 4	386 445 512 447 Avg: 426	395 408 347 447 Avg: 417	478 515 515 Avg: 503	481 501 513 Avg: 498	-- --

Table A-6: Elastic Modulus

	Phase 1 45 Day (ksi)	Phase 2 65 Day (ksi)	Phase 3 28 Day (ksi)	Phase 4 41 Day (ksi)	CB2, CB3 93 Day (ksi)
Truck 1	2735	2634	--	--	2705 3016 3114 Avg: 2945
Truck 2	2556	2431	2692	2729	--
Truck 3	2967	2850	2818	2837	--
Truck 4	2672	2634	2707	2788	--

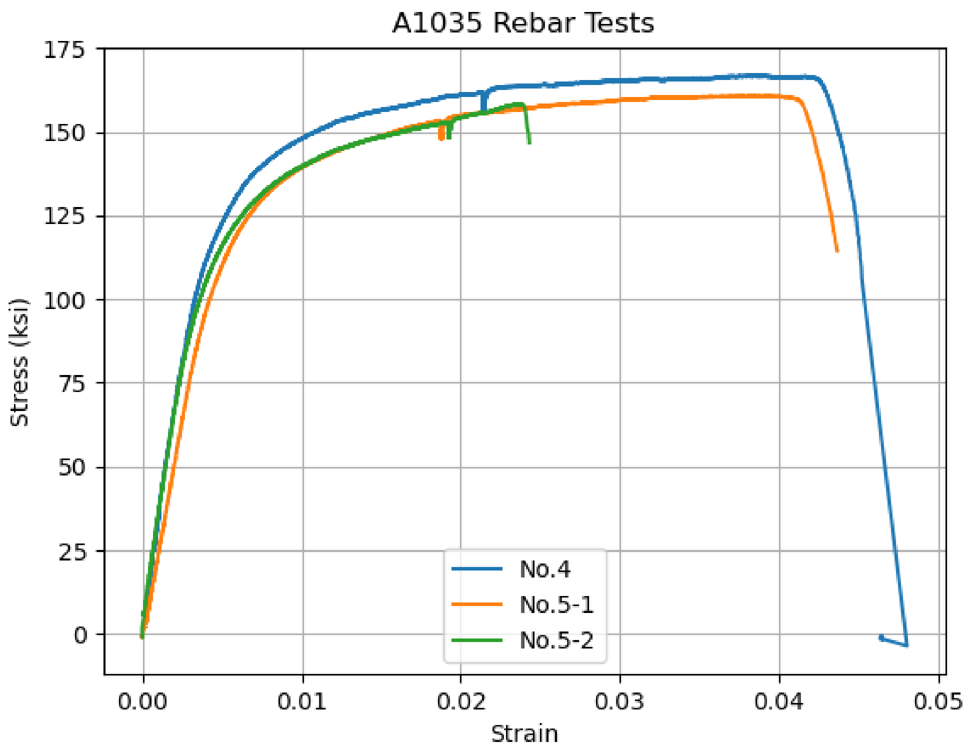

Figure A-4: A1035 Gr. 100 No.4 and No.5 stress strain curves

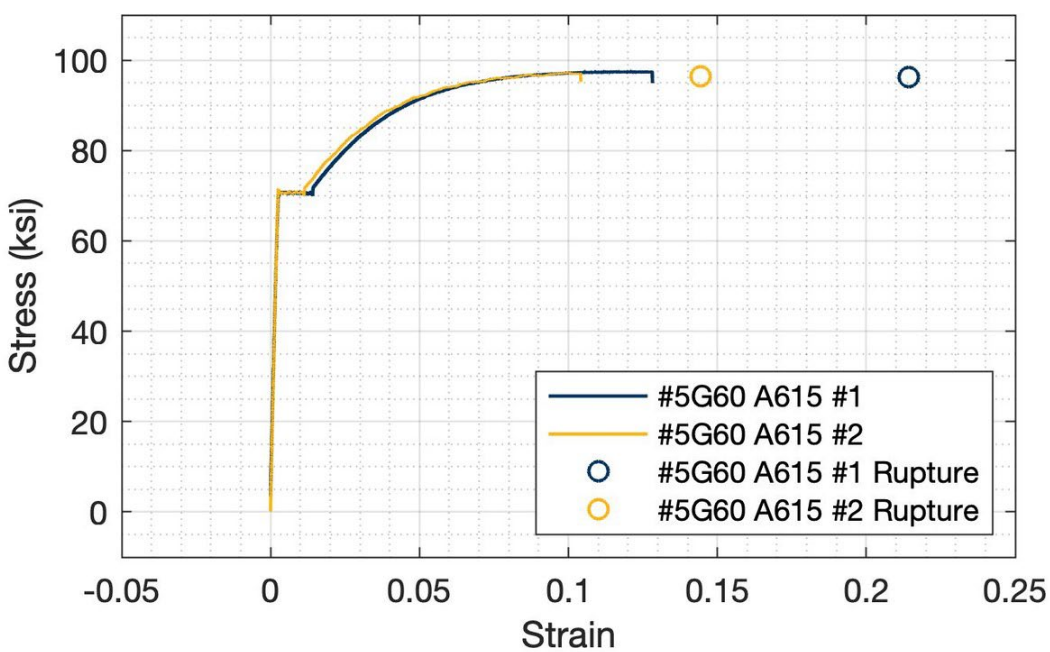

Figure A-5: A615 Gr. 60 No.5 stress strain curves

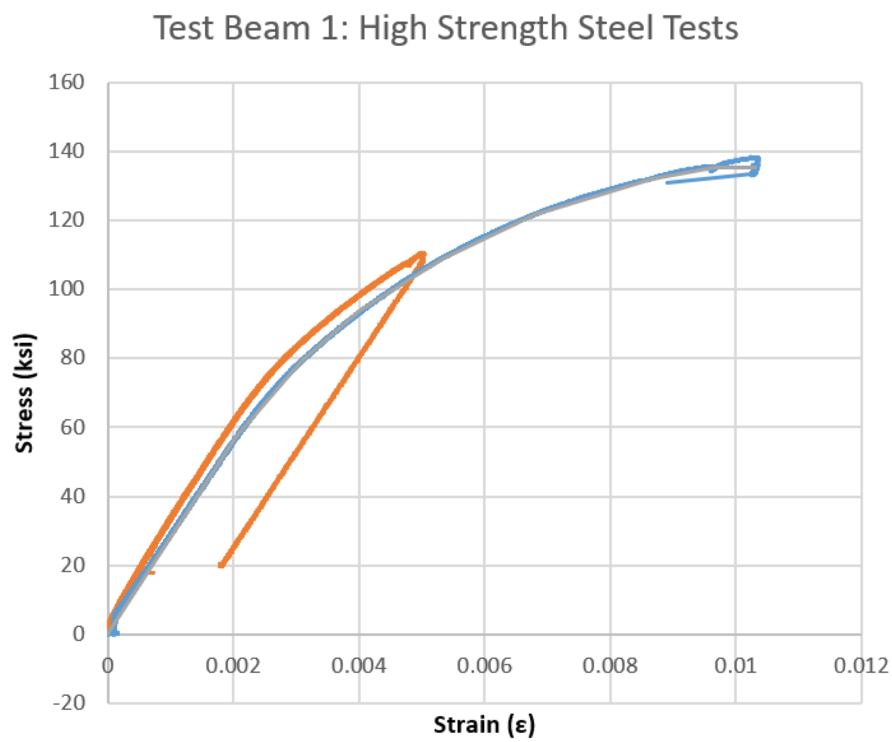

Figure A-6: A1035 Gr. 100 No.9 stress strain curves for Test Beam 1

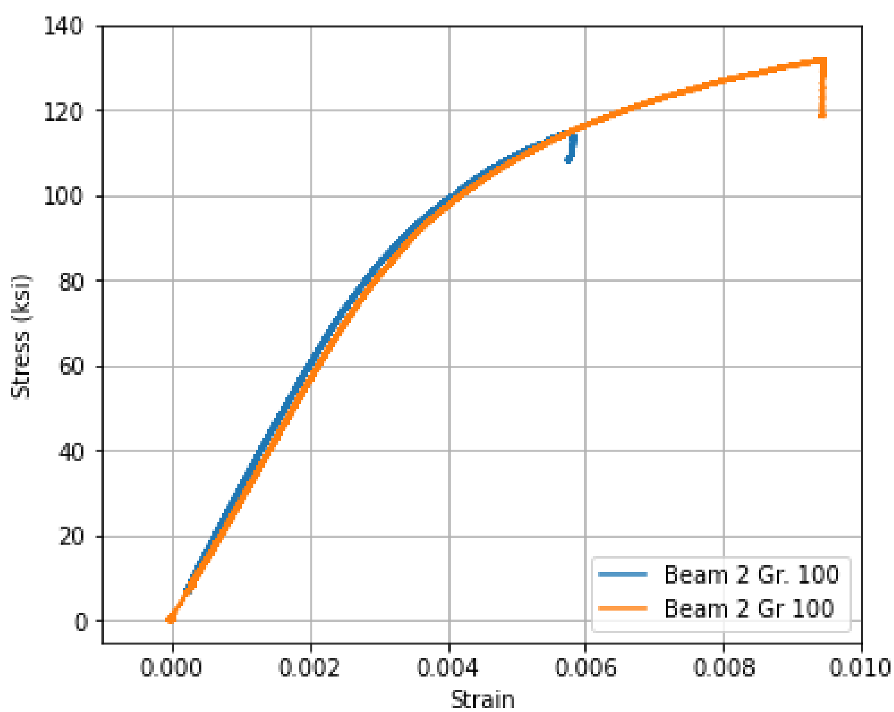

Figure A-7: A1035 Gr. 100 No.9 stress strain curves for Test Beam 1

A.4. Shear Repair and Moment Strengthening Details

During the transition between Phase 1 and Phase 2, it was necessary to repair the shear damage on the east span following Phase 1 testing and to increase the flexural reinforcement ratio in the east span to avoid an unwanted flexural failure. This was achieved via multiple sets of steel brackets that clamped the beam together from above and below, effectively acting as external shear reinforcement. The moment strengthening was achieved by pressure grouting the empty ducts containing additional longitudinal reinforcement on the east span. Drawings of the shear repair can be found in section A.6 and photos are documented in A.7.

The shear repair was validated during the test as the east span did not fail following installation of the steel brackets. To validate the effectiveness of the moment repair, data from steel strains at midspan is reported below in Figure A-8. for Phase 1 and Phase 2. Phase 1 is the response with 6 cast-in-place bonded reinforcement bars while Phase 2 is the response with 11 bonded reinforcements, 6 of which are cast-in-place and 5 were sitting in empty ducts that were grouted. The increase in stiffness by about 2 times before and after the moment strengthening provides good indication that the reinforcing bars are fully bonded to the concrete and participating in the flexural response.

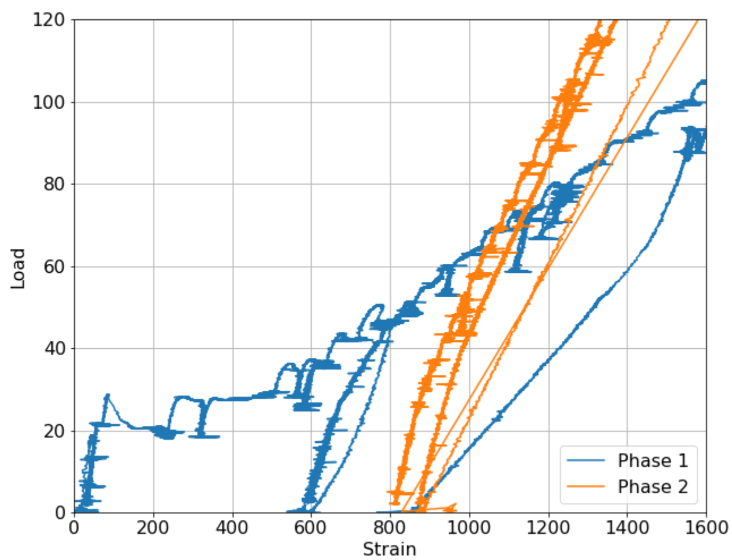

Figure A-8 Midspan reinforcement strains before and after shear repair, denoted by Phase 1 and Phase 2 respectively

A.5. Instrumentation Photos and Purpose

Linear Potentiometers for Vertical and Horizontal Movement

For all measurements involving horizontal or vertical movement, a linear potentiometer mounted to a magnetic block is used. The magnetic block is then mounted to a test stand, which is usually a steel angle welded to a steel plate to ensure stability.

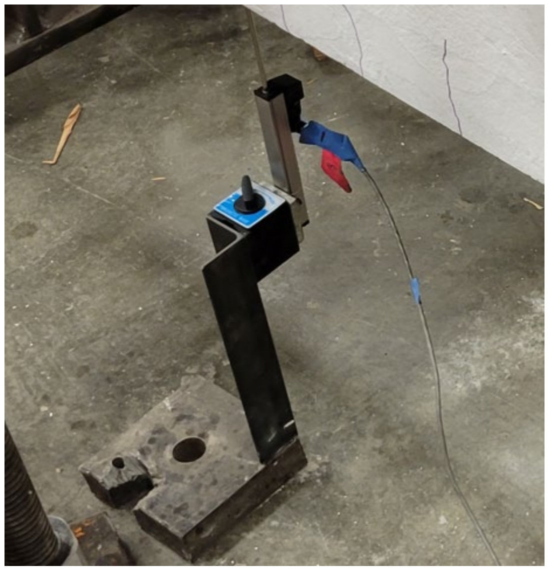

Figure A-9: Linear potentiometer for horizontal and vertical measurements

Diagonal Shear Strain for Companion Beam 2 and Companion Beam 3.

All diagonal measurements are taken with a linear potentiometer mounted between the upper and lower points of interest. A steel rod makes up the distance between the instrument and the lower instrument. An eyebolt fitted with a swivel bearing and steel rod is attached to the instrument to record any change in distance between the upper and lower anchor points.

The average (engineering) shear strain can be estimated from measured values for diagonal displacements $\Delta L_1, \Delta L_2$ for each of the diagonals respectively and the original length L between the anchor points:

$$\gamma = \frac{\Delta L_1 - \Delta L_2}{L}$$

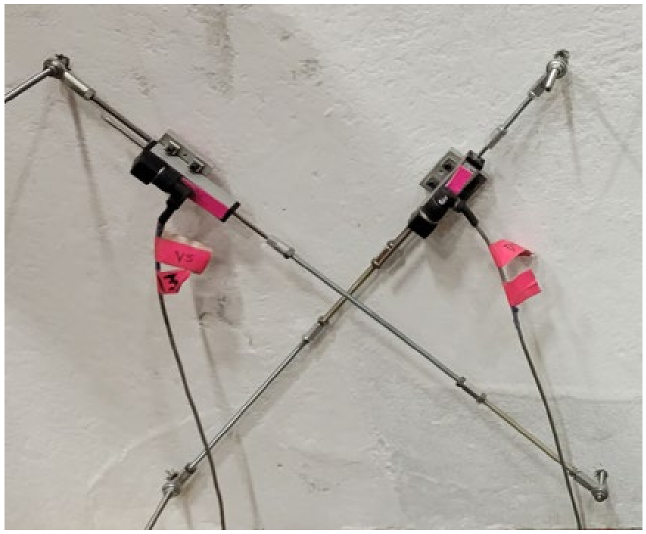

Figure A-10: Diagonal mounted potentiometers

<u>Diagonal Shear Strain for Test Beam 1 and Test Beam 2.</u>

Likewise, all diagonal measurements on the surface of the beam are taken by mounting an anchor and wire at the upper point of interest. The wire is a low-stetch steel and attached on either end with a compression sleeve to ensure that the wire does not slip out. At the lower point of interest, the wire is attached to a wire potentiometer. The wire potentiometer is installed close to the lower anchor point, and the wire is redirected around the anchor point with a smooth ball bearing. The intent of this setup is to ensure consistent diagonal measurements and ensure that the wire exiting the wire potentiometer is perfectly perpendicular to the instrument. By ensuring that the upper and lower anchor points are precisely installed, the only uncertainty would be in any movement between the instrument and the lower anchor point, which is generally small. Due to the long lengths, it was decided that a conventional approach with a steel threaded road would vibrate excessively. The same formula to estimate shear strains are used as above.

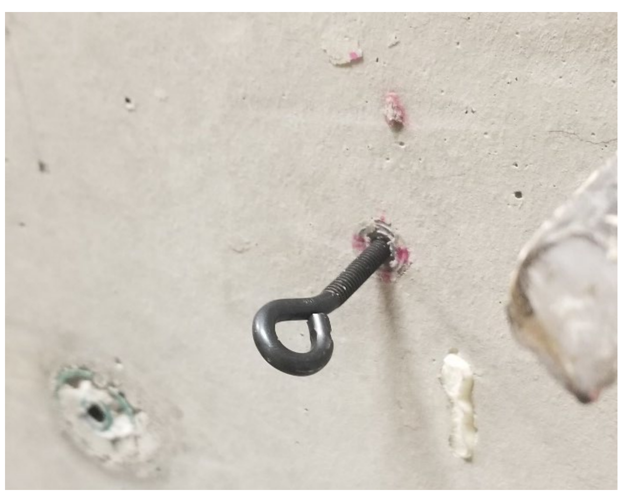

Figure A-11: Anchor for wires

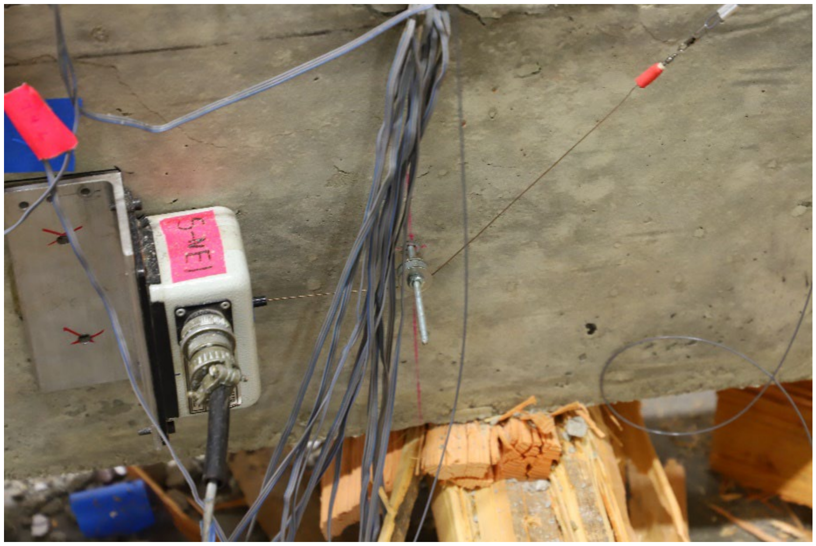

Figure A-12: Anchoring of diagonal wire potentiometers

<u>Strain Gauge on Steel Reinforcement</u>

Strain gauges are installed on reinforcement on the neutral axis of the beam. Since mechanical couplers are used to splice the longitudinal reinforcement, special care is taken to ensure that the neutral axis of all bars lie on the same surface once the bars are connected. Where possible, the transverse ribs of the bar are grinded down instead of the longitudinal rib. Installation of strain gauges involves first grinding the surface down with either a pneumatic belt sander or with a steel file. When using the belt sander, a well-worn belt is used to avoid removing too much material. The strain gauge is waterproofed by applying a layer of wax, followed by a sticky putty-like material, and finally a layer of epoxy to protect against external impacts. Despite these efforts, the strain gauge is still sensitive to vibrations from contacting a concrete vibrator. This unfortunately resulted in many damaged gauges on shear reinforcement and compression steel where contractors had access to the steel.

Figure A-13: Installation site for strain gauge on No.9 bar

Figure A-14: Installed strain gauge on No.9 bar

Laser Scanning Targets for Surface Deformations

To record the surface displacements of the beam, 150 mm circular "bow-tie" targets are printed out and positioned at 2 feet intervals on the beam surface. A hard stock paper is glued to the back surface to keep the paper stiff. A laser guide is used to ensure that the targets are generally horizontal and vertical in the intended grid layout, though this is not as important since the laser scanner records position of the targets on the beam surface, not displacements.

The laser scanner used for recording the surface displacements of the beam are the Trimble TX6 for Phase 1 and Phase 3. For Phase 2 and Phase 4, the Leica C10 was used. The choice of scanner was based on availability at the time, though last-minute changes were sometimes inevitable due to unforeseen issues. These scanners shoot a laser from a stationary point and record the spatial coordinates and color of the point relative to the scanner. This enables a spatial measurement of the beam surface while the contrast in color between the black and white quadrants of the target allows a computer software to determine the center of the target by interpolating lines between the black and white quadrants and finding its intersection point.

Figure A-15: Laser Scanner

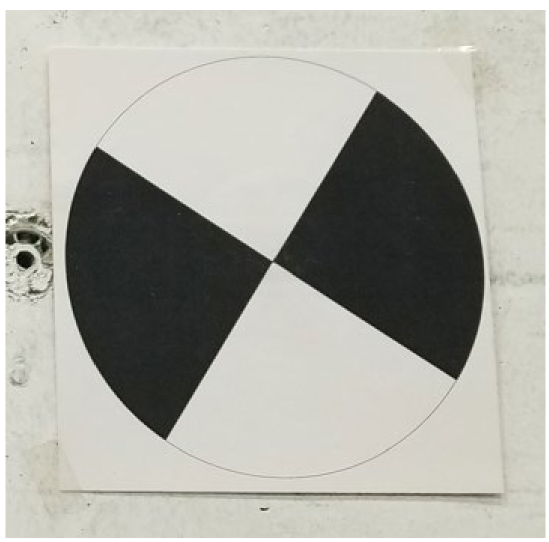

Figure A-16: Laser scanning paper target

Fiber Optic Strain Gauges

In addition to regular strain gauges installed on the steel reinforcement, fiber optic strain gauges were embedded alongside the longitudinal tension reinforcement as another way of monitoring longitudinal strains. These fiber optic strain gauges could record the concrete strains and provide estimates of crack widths along the span by a deconvolution method. The specifics of the data conversion and processing are deferred to the authors of this method [2].

Figure A-17: Fiber optic strain gauges embedded alongside steel reinforcement

Digital Image Correlation (DIC)

DIC was performed only on CB2 and CB3 but not on CB1. DIC was also not performed on the larger beams because of uncertainty in how to effectively apply it on a large surface. To perform the DIC analysis, black speckles were painted on the surface of the beam using a custom roller, ink pad, and regular ink. A stationary camera is set up to take photos of the surface at regular intervals. Unfortunately, only JPEG files were taken of the beam surface, which is a compressed image file, instead of the recommend RAW file formats. This may explain why the magnitude of the strains were inaccurate for CB2 and CB3. Nevertheless, crack mapping was quite intuitive with the DIC approach. The DIC was performed using Ncorr, an open source 2D DIC program written in MatLab [3]. A sample of the DIC pattern is shown below.

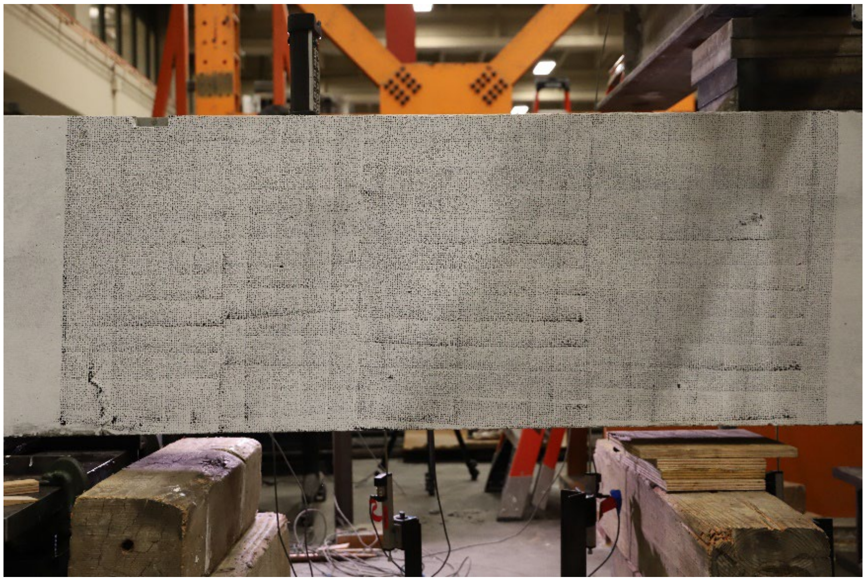

Figure A-18: Sample DIC pattern for CB3

A.6. Test Beam 1 (Phase 1 and Phase 2) Drawings

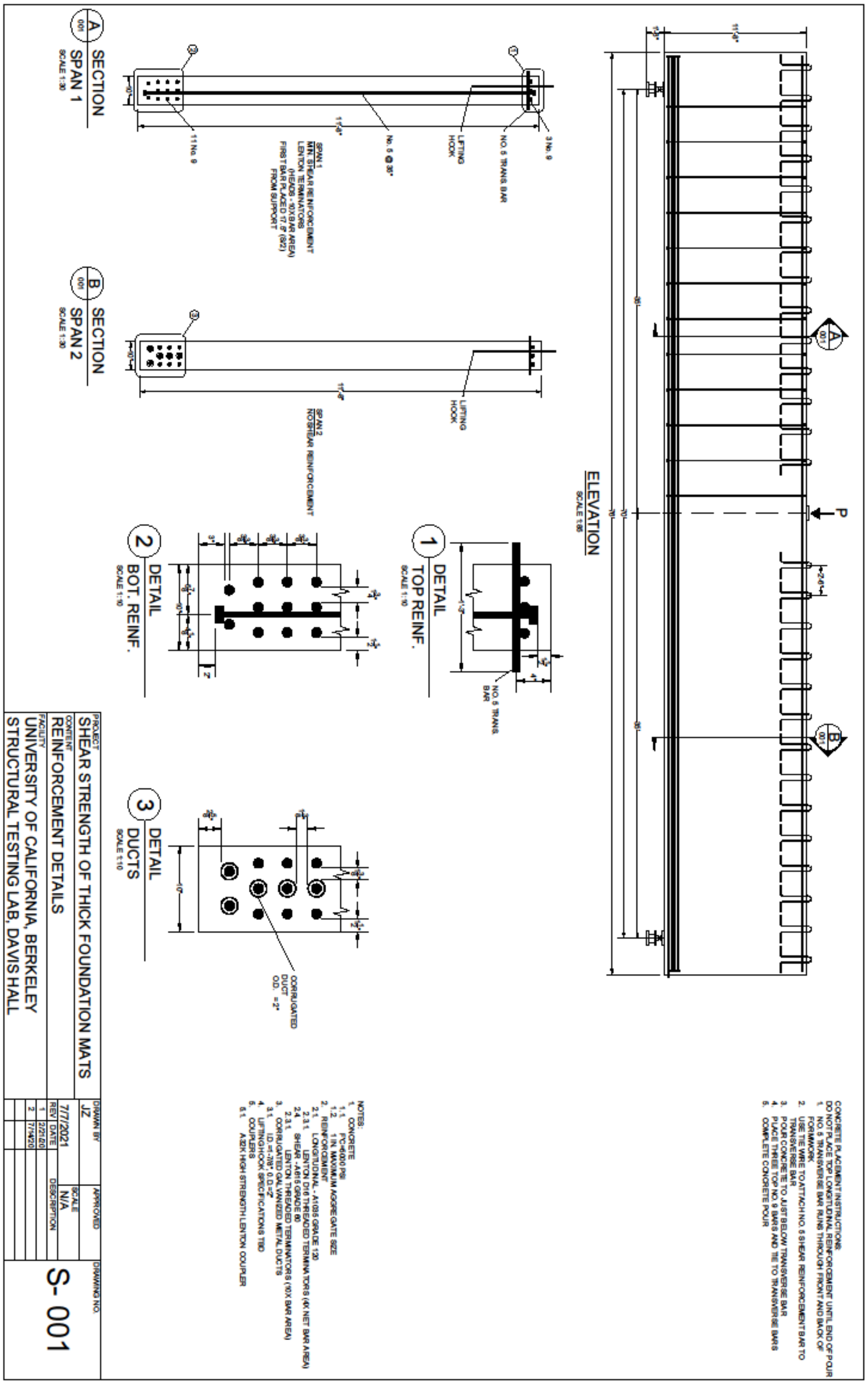

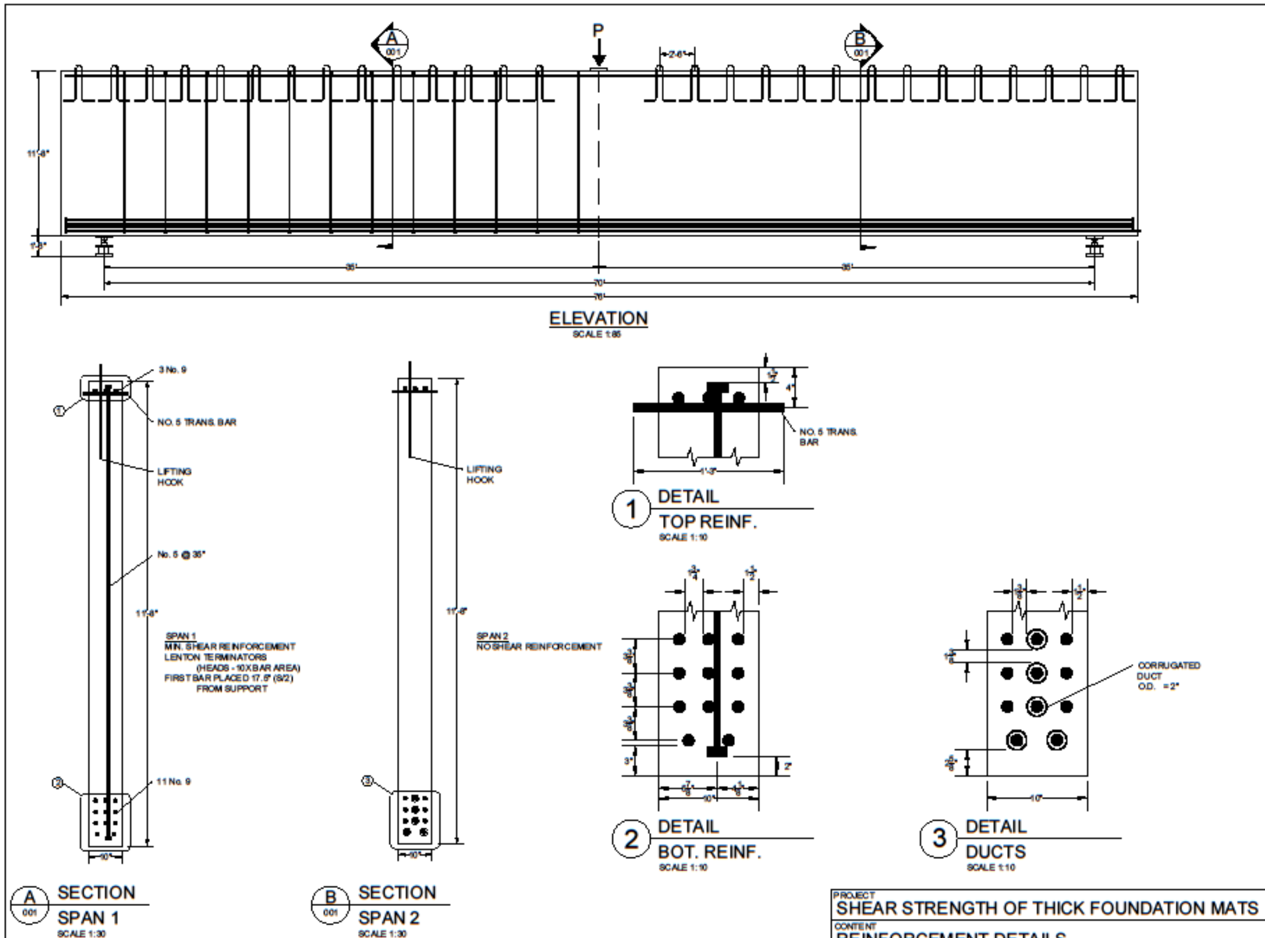

CONCRETE PLACEMENT INSTRUCTIONS:

DO NOT PLACE TOP LONGITUDINAL REINFORCEMENT UNTIL END OF POUR

1. NO. 5 TRANSVERSE BAR RUNS THROUGH FRONT AND BACK OF FORMWORK
2. USE TIE WIRE TO ATTACH NO. 5 SHEAR REINFORCEMENT BAR TO TRANSVERSE BAR
3. POUR CONCRETE TO JUST BELOW TRANSVERSE BAR
4. PLACE THREE TOP NO. 9 BARS AND TIE TO TRANSVERSE BARS
5. COMPLETE CONCRETE POUR

NOTES:

1. CONCRETE
   1.1. F'C=6000 PSI
   1.2. 1 IN. MAXIMUM AGGREGATE SIZE
2. REINFORCEMENT
   2.1. LONGITUDINAL - A1035 GRADE 120
      2.3.1. LENTON D16 THREADED TERMINATORS (4X NET BAR AREA)
   2.4. SHEAR - A615 GRADE 60
      2.3.1. LENTON THREADED TERMINATORS (10X BAR AREA)
3. CORRUGATED GALVANIZED METAL DUCTS
   3.1. I.D.=1-7/8", O.D.=2"
4. LIFTING HOOK SPECIFICATIONS TBD
5. COUPLERS
   5.1. A32K HIGH STRENGTH LENTON COUPLER

PROJECT SHEAR STRENGTH OF THICK FOUNDATION MATS	DRAWN BY JZ	APPROVED	DRAWING NO. S- 001
CONTENT REINFORCEMENT DETAILS	7/7/2021	SCALE N/A	
FACILITY UNIVERSITY OF CALIFORNIA, BERKELEY STRUCTURAL TESTING LAB, DAVIS HALL	REV / DATE 1 / 2/21/20 2 / 7/14/20	DESCRIPTION	

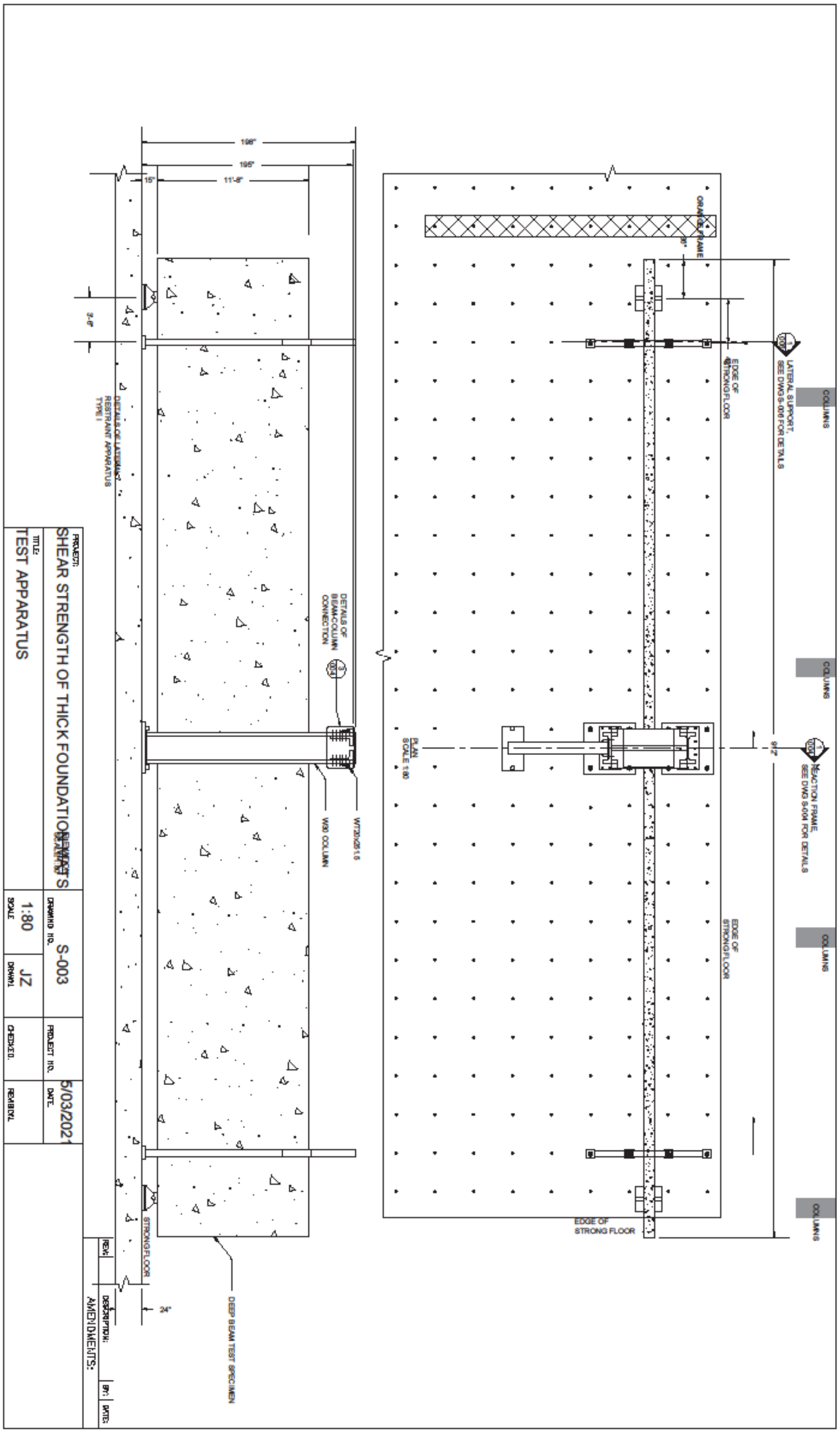

PROJECT:
SHEAR STRENGTH OF THICK FOUNDATION MATS
TITLE:
TEST APPARATUS
DRAWING NO.
S-003
SCALE
1:80
DRAWN
JZ
CHECKED
PROJECT NO.
DATE
5/03/2021
REVISION
AMENDMENTS:
REV.
DESCRIPTION:
BY:
DATE:
DEEP BEAM TEST SPECIMEN
STRONG FLOOR
W30 COLUMN
DETAILS OF BEAM-COLUMN CONNECTION
DETAILS OF LATERAL RESTRAINT APPARATUS TYPE I
PLAN
SCALE 1:80
LATERAL SUPPORT, SEE DWG S-006 FOR DETAILS
REACTION FRAME, SEE DWG S-004 FOR DETAILS
EDGE OF STRONG FLOOR
COLUMNS
ORANGE FRAME

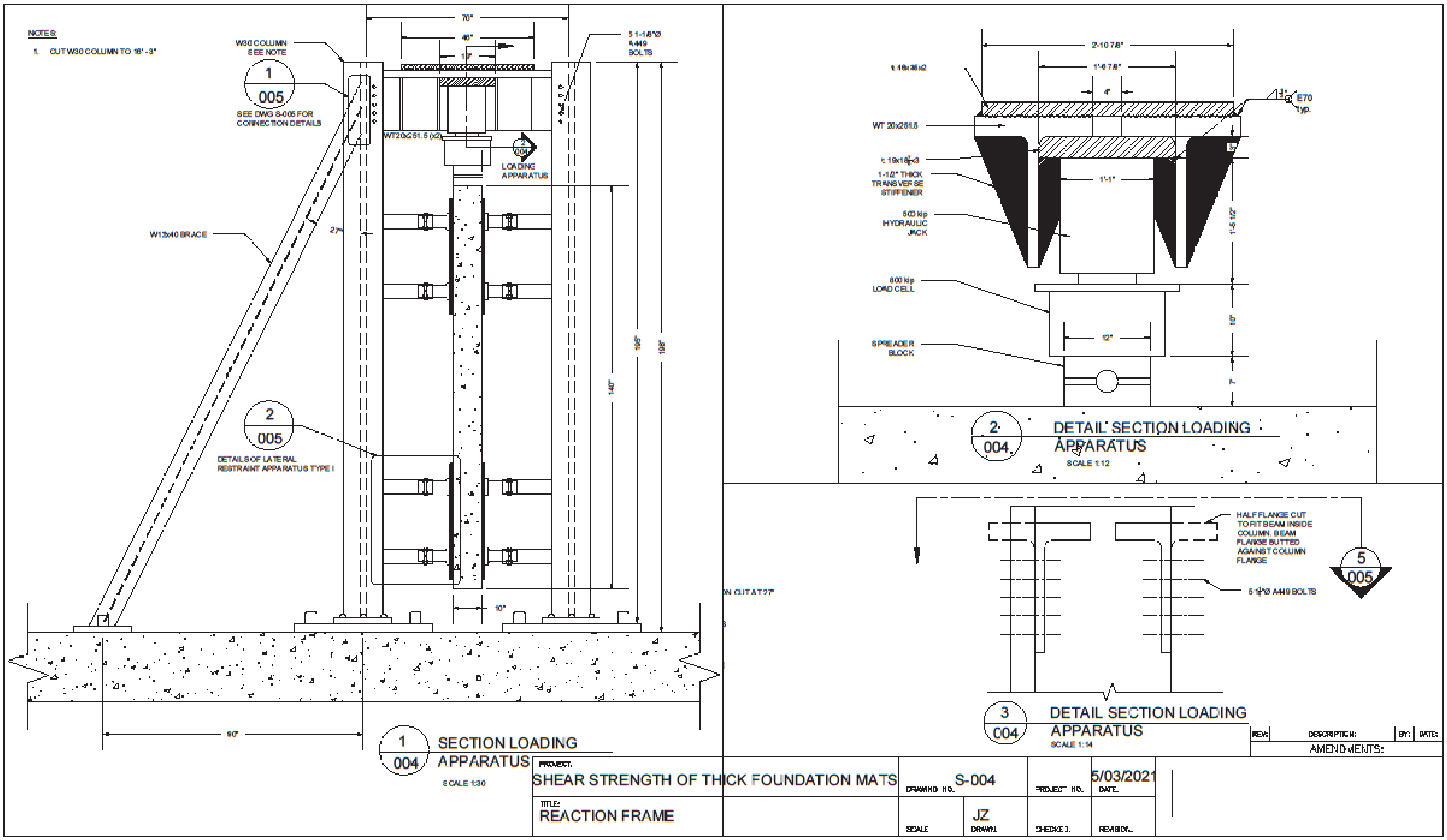

NOTES:
1. CUT W30 COLUMN TO 16' - 3"
W30 COLUMN SEE NOTE
1 005
SEE DWG S-005 FOR CONNECTION DETAILS
W12x40 BRACE
WT20x251.5
LOADING APPARATUS
2 005
DETAILS OF LATERAL RESTRAINT APPARATUS TYPE I
70"
46"
17"
140"
195"
198"
10"
60"
1 004 SECTION LOADING APPARATUS
SCALE 1:30
2 004 DETAIL SECTION LOADING APPARATUS
SCALE 1:12
WT 20x251.5
1-1/2" THICK TRANSVERSE STIFFENER
500 kip HYDRAULIC JACK
800 kip LOAD CELL
SPREADER BLOCK
E70 typ.
2'-10 7/8"
1'-6 7/8"
4"
1'-1"
1'-5 1/2"
12"
10"
7"
HALF FLANGE CUT TO FIT BEAM INSIDE COLUMN. BEAM FLANGE BUTTED AGAINST COLUMN FLANGE
5 005
3 004 DETAIL SECTION LOADING APPARATUS
SCALE 1:14
REV: DESCRIPTION: BY: DATE:
AMENDMENTS:
PROJECT: SHEAR STRENGTH OF THICK FOUNDATION MATS
DRAWING NO. S-004
PROJECT NO.
DATE: 5/03/2021
TITLE: REACTION FRAME
SCALE
DRAWN: JZ
CHECKED.
REVISION.

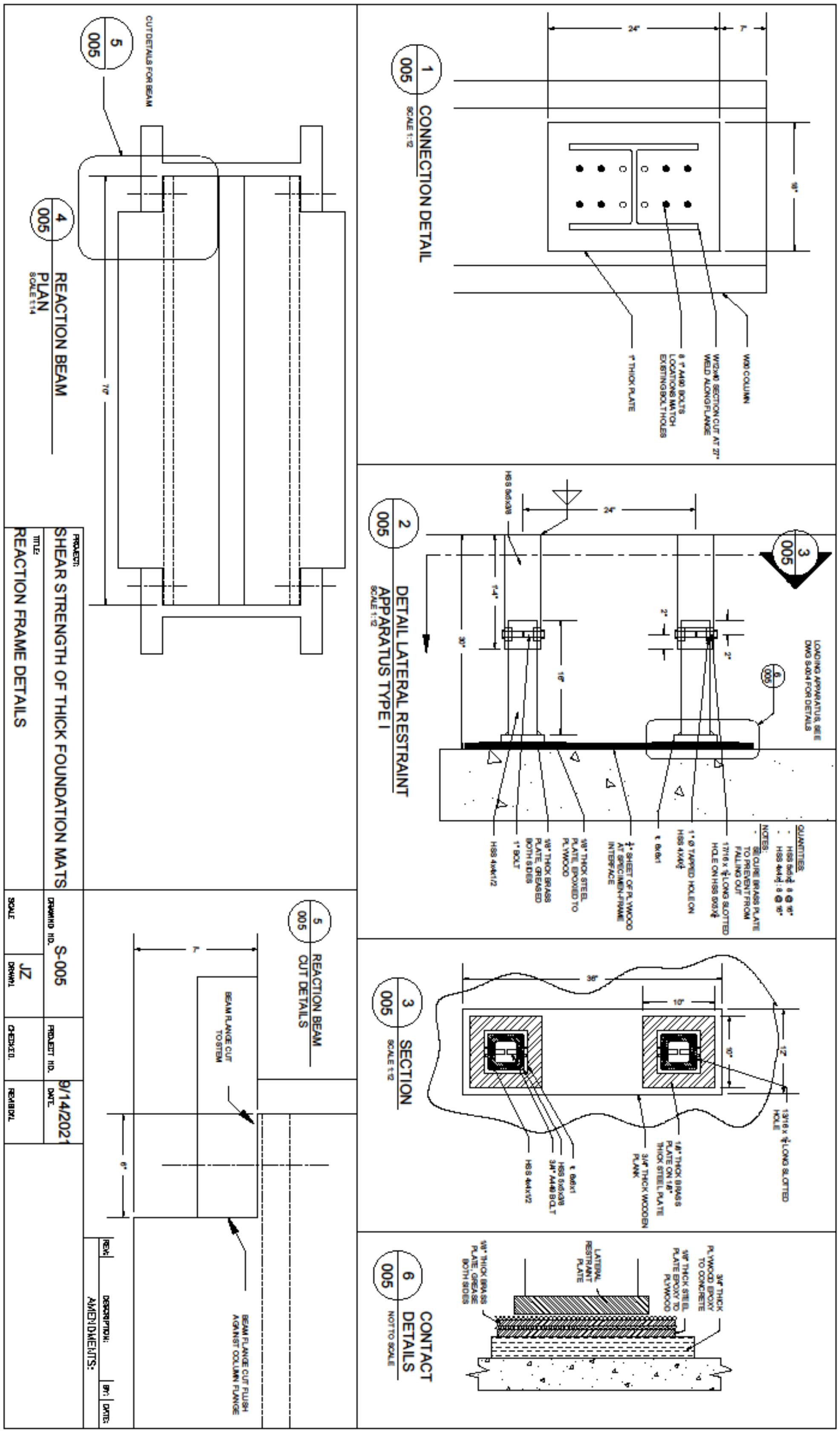

1
005
CONNECTION DETAIL
SCALE 1:12
24"
7"
18"
W30 COLUMN
W12x40 SECTION CUT AT 27" WELD ALONG FLANGE
8 1" A490 BOLTS LOCATIONS MATCH EXISTING BOLT HOLES
1" THICK PLATE
2
005
DETAIL LATERAL RESTRAINT APPARATUS TYPE I
SCALE 1:12
HSS 5x5x3/8
1'-4"
30"
18"
2"
LOADING APPARATUS, SEE DWG S-004 FOR DETAILS
3
005
SECTION
SCALE 1:12
36"
10"
12"
1/8" THICK BRASS PLATE ON 1/8" THICK STEEL PLATE
3/4" THICK WOODEN PLANK
HSS 5x5x3/8
3/4" A490 BOLT
HSS 4x4x1/2
6
005
CONTACT DETAILS
NOT TO SCALE
3/4" THICK PLYWOOD EPOXY TO CONCRETE
1/8" THICK STEEL PLATE EPOXY TO PLYWOOD
LATERAL RESTRAINT PLATE
1/8" THICK BRASS PLATE, GREASE BOTH SIDES
5
005
CUT DETAILS FOR BEAM
4
005
REACTION BEAM PLAN
SCALE 1:4
10'
5
005
REACTION BEAM CUT DETAILS
7"
6"
BEAM FLANGE CUT TO STEM
BEAM FLANGE CUT FLUSH AGAINST COLUMN FLANGE
PROJECT:
SHEAR STRENGTH OF THICK FOUNDATION MATS
TITLE:
REACTION FRAME DETAILS
DRAWING NO. S-005
PROJECT NO.
DATE: 9/14/202
SCALE
DRAWN: JZ
CHECKED:
REVISION:
REV:
DESCRIPTION:
AMENDMENTS:
BY:
DATE:

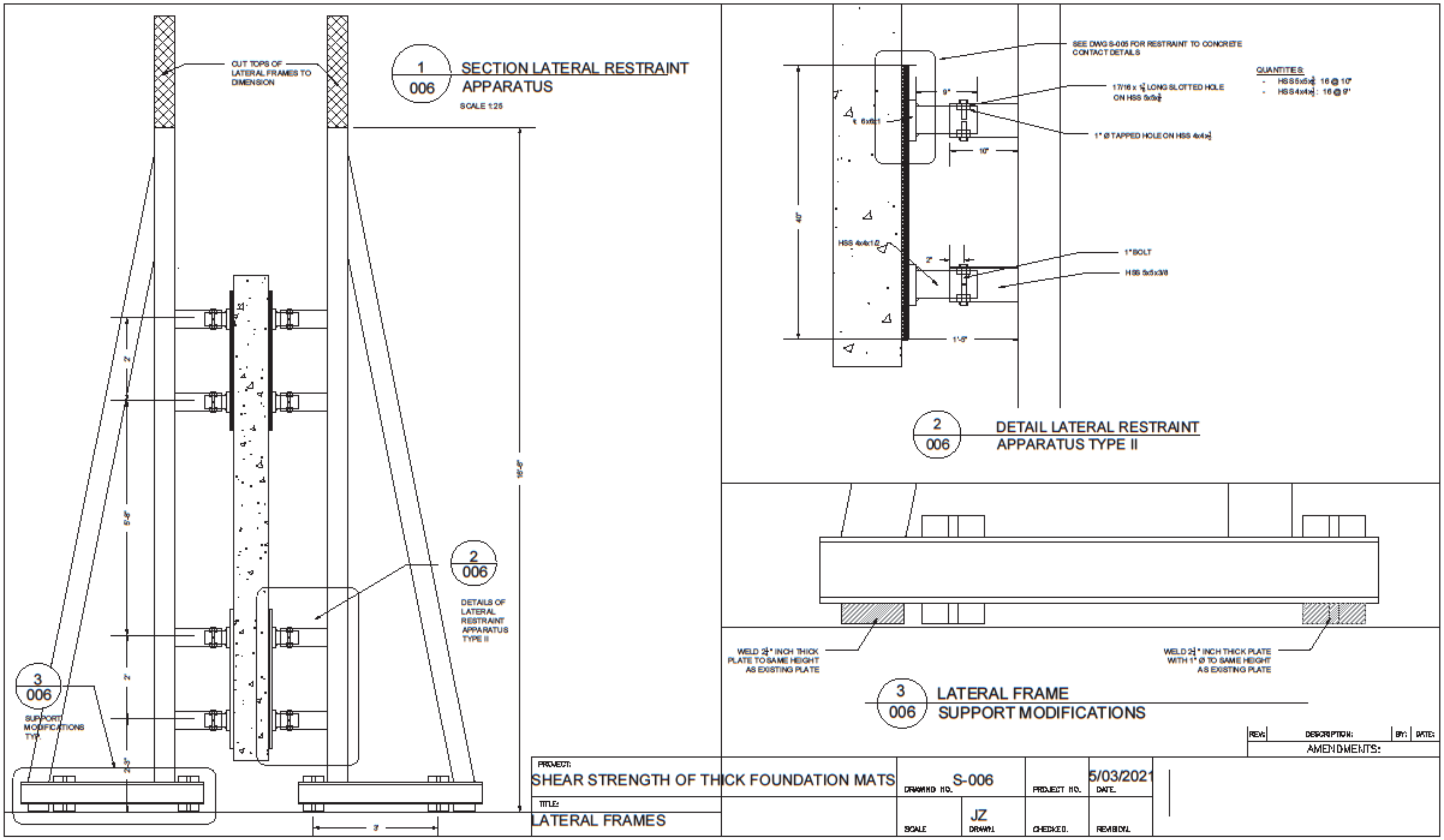
CUT TOPS OF LATERAL FRAMES TO DIMENSION
1
006
SECTION LATERAL RESTRAINT APPARATUS
SCALE 1:25
2
006
DETAILS OF LATERAL RESTRAINT APPARATUS TYPE II
3
006
SUPPORT MODIFICATIONS TYP.
SEE DWG S-005 FOR RESTRAINT TO CONCRETE CONTACT DETAILS
QUANTITIES:
1" BOLT
2
006
DETAIL LATERAL RESTRAINT APPARATUS TYPE II
WELD 2¼" INCH THICK PLATE TO SAME HEIGHT AS EXISTING PLATE
3
006
LATERAL FRAME SUPPORT MODIFICATIONS
REV: DESCRIPTION: BY: DATE:
AMENDMENTS:
PROJECT:
SHEAR STRENGTH OF THICK FOUNDATION MATS
DRAWING NO. S-006
PROJECT NO.
5/03/2021
DATE.
TITLE:
LATERAL FRAMES
SCALE
JZ
DRAWN
CHECKED.
REVISION.

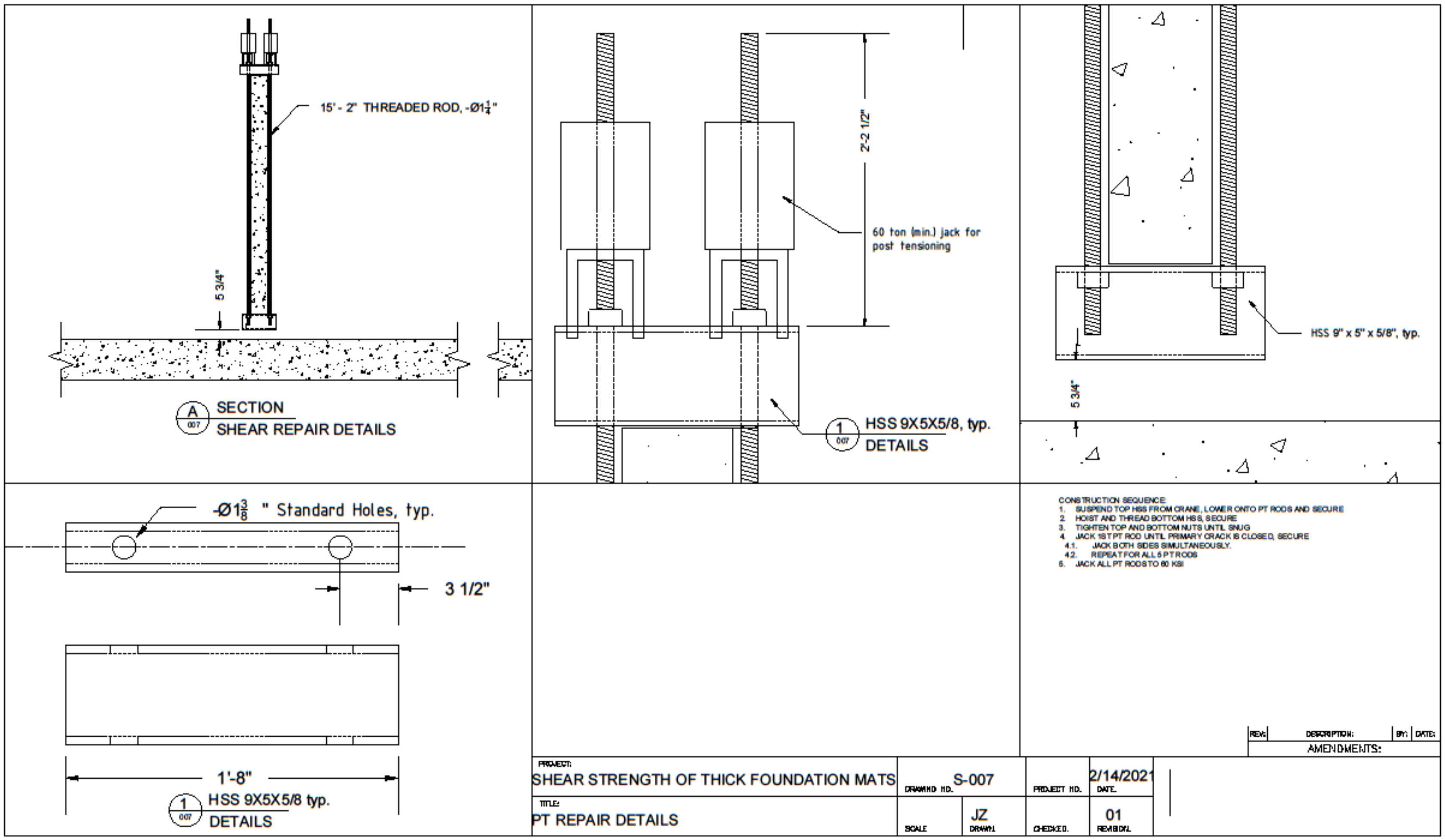
15' - 2" THREADED ROD, -Ø1¼"
5 3/4"
A 007 SECTION
SHEAR REPAIR DETAILS
2'-2 1/2"
60 ton (min.) jack for post tensioning
1 007 HSS 9X5X5/8, typ.
DETAILS
HSS 9" x 5" x 5/8", typ.
5 3/4"
-Ø1⅜ " Standard Holes, typ.
3 1/2"
1'-8"
1 007 HSS 9X5X5/8 typ.
DETAILS
CONSTRUCTION SEQUENCE:
1. SUSPEND TOP HSS FROM CRANE, LOWER ONTO PT RODS AND SECURE
2. HOIST AND THREAD BOTTOM HSS, SECURE
3. TIGHTEN TOP AND BOTTOM NUTS UNTIL SNUG
4. JACK 1ST PT ROD UNTIL PRIMARY CRACK IS CLOSED, SECURE
4.1. JACK BOTH SIDES SIMULTANEOUSLY.
4.2. REPEAT FOR ALL 5 PT RODS
5. JACK ALL PT RODS TO 60 KSI
REV: DESCRIPTION: BY: DATE:
AMENDMENTS:
PROJECT:
SHEAR STRENGTH OF THICK FOUNDATION MATS
DRAWING NO. S-007
PROJECT NO.
DATE: 2/14/2021
TITLE:
PT REPAIR DETAILS
SCALE
DRAWN: JZ
CHECKED:
REVISION: 01

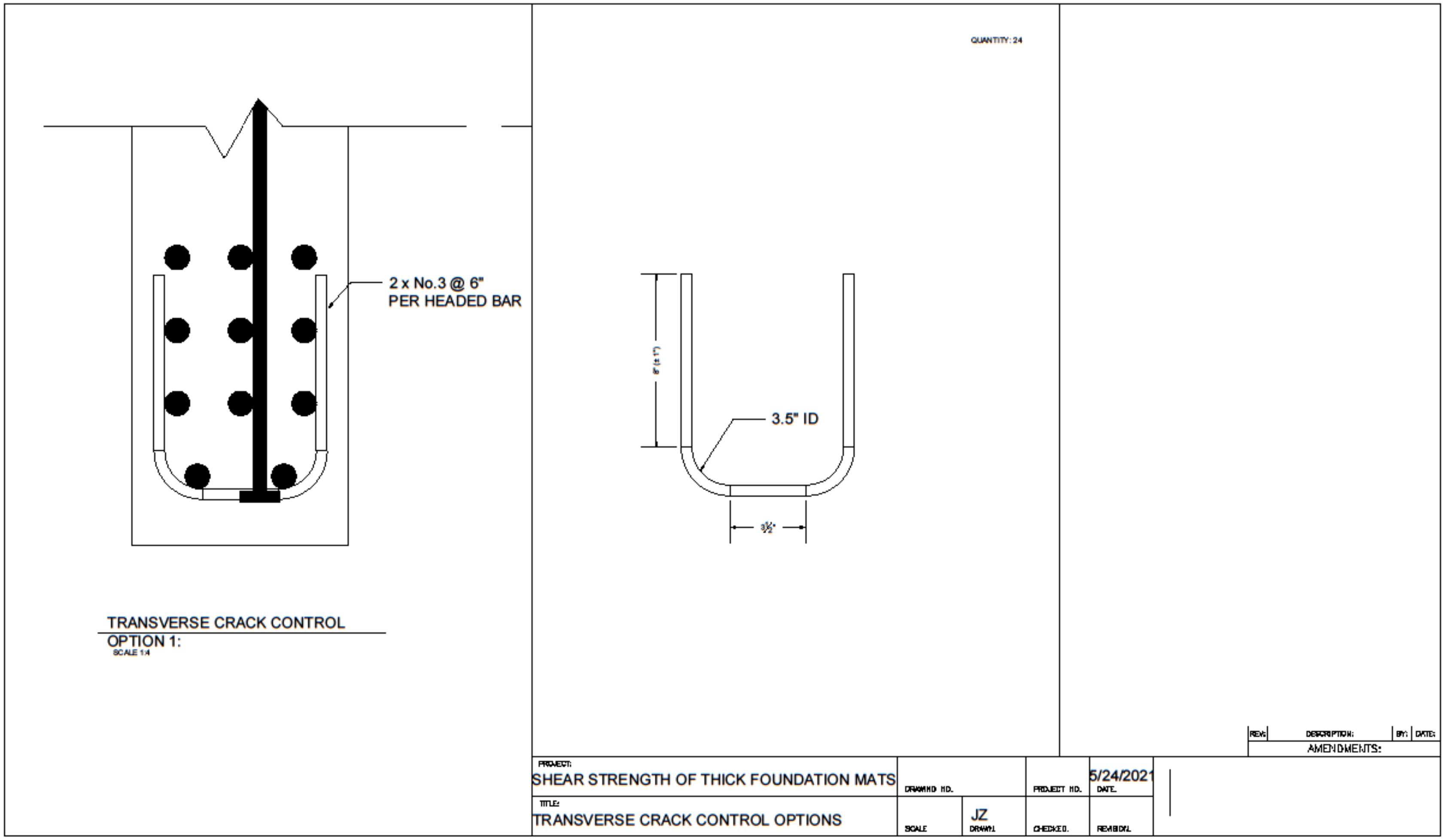
2 x No.3 @ 6"
PER HEADED BAR
TRANSVERSE CRACK CONTROL
OPTION 1:
SCALE 1:4
QUANTITY: 24
8" (± 1")
3.5" ID
3½"
REV: DESCRIPTION: BY: DATE:
AMENDMENTS:
PROJECT:
SHEAR STRENGTH OF THICK FOUNDATION MATS
DRAWING NO.
PROJECT NO.
5/24/2021
DATE
TITLE:
TRANSVERSE CRACK CONTROL OPTIONS
SCALE
JZ
DRAWN
CHECKED
REVISION

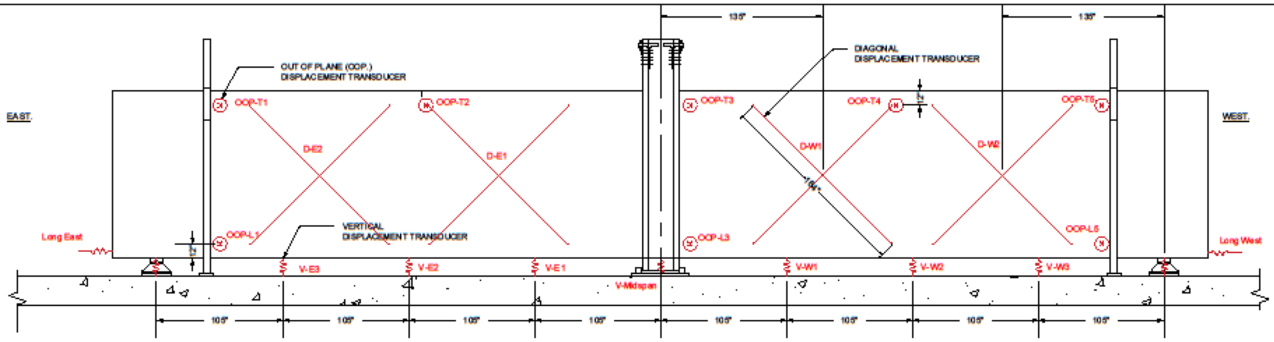

EXTERNAL INSTRUMENTATION LOCATIONS
(BACK FACE)

NOTES:
- DO NOT ZERO INSTRUMENTATION FOR PHASE 2 OF TEST.

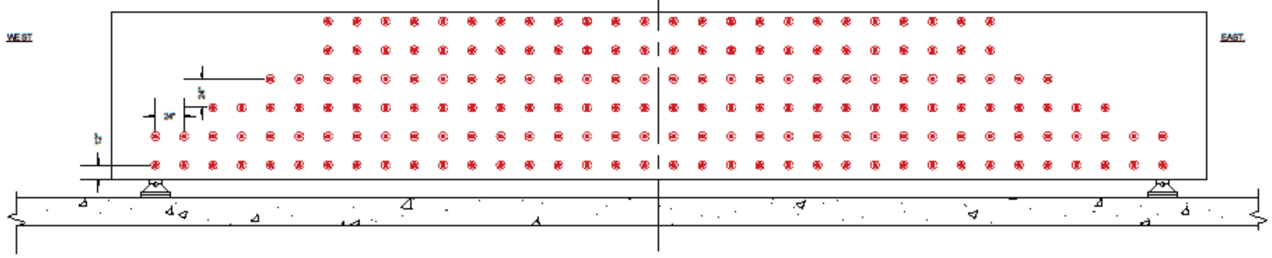

LASER SCANNER TARGET POINTS
(FRONT FACE)

REV:	DESCRIPTION:	BY:	DATE:
	AMENDMENTS:		

PROJECT: SHEAR STRENGTH OF THICK FOUNDATION MATS	DRAWING NO. S-011	PROJECT NO.	DATE: 6/23/2021
TITLE: EXTERNAL INSTRUMENTATION	SCALE	DRAWN: JZ	CHECKED:
			REVISION:

Black X marks damaged strain gauge

Red X marks working gauge

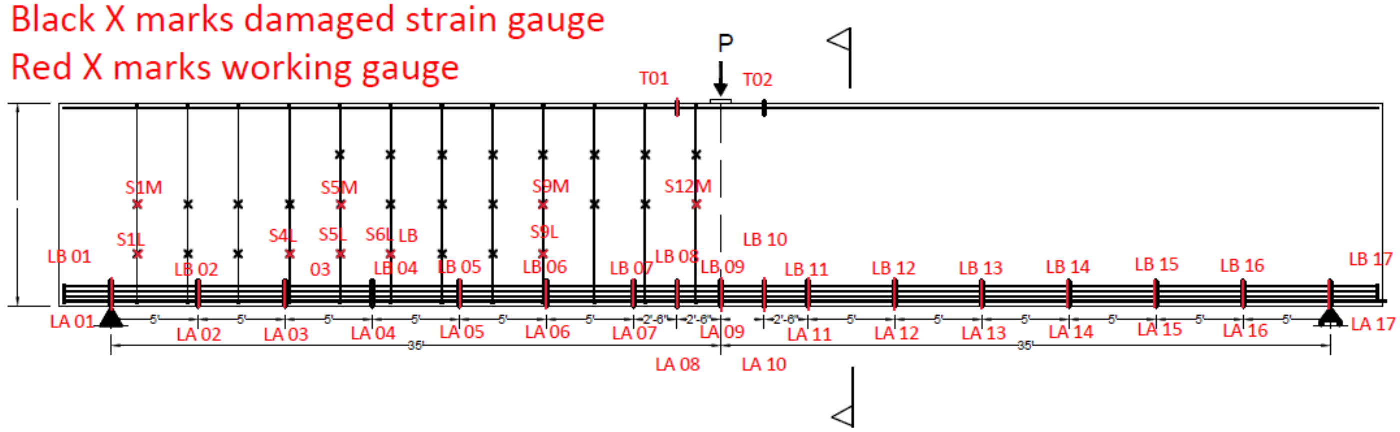

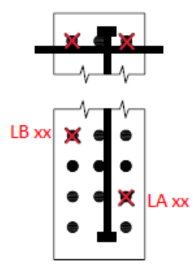

-- STRAIN GAUGE PLANE

-- STRAIN GAUGE LOCATION

STRAIN GAUGE LOCATION NOTES:

Total Count: 72

1. FLEXURAL TENSION REINFORCEMENT
   1.1. GAUGE APPLIED ALONG SIDE ON NEUTRAL AXIS OF REINFORCEMENT
2. SHEAR REINFORCEMENT
   2.1. 1 GAUGE APPLIED TO EACH BAR-ON
   2.2 MIDDLE AND UPPER GAUGE RUN UP, LOWER GAUGE RUN DOWN

PROJECT SHEAR STRENGTH OF THICK FOUNDATION MATS	DRAWN BY MIS	APPROVED	DRAWING NO. SD- 001
CONTENT STRAIN GAUGE LAYOUT	DATE 4/21/2020	SCALE N/A	
FACILITY UNIVERSITY OF CALIFORNIA, BERKELEY STRUCTURAL TESTING LAB, DAVIS HALL	Rev / Date	Description	

A.7. Test Beam 1 (Phase 1 and Phase 2) Construction Photos

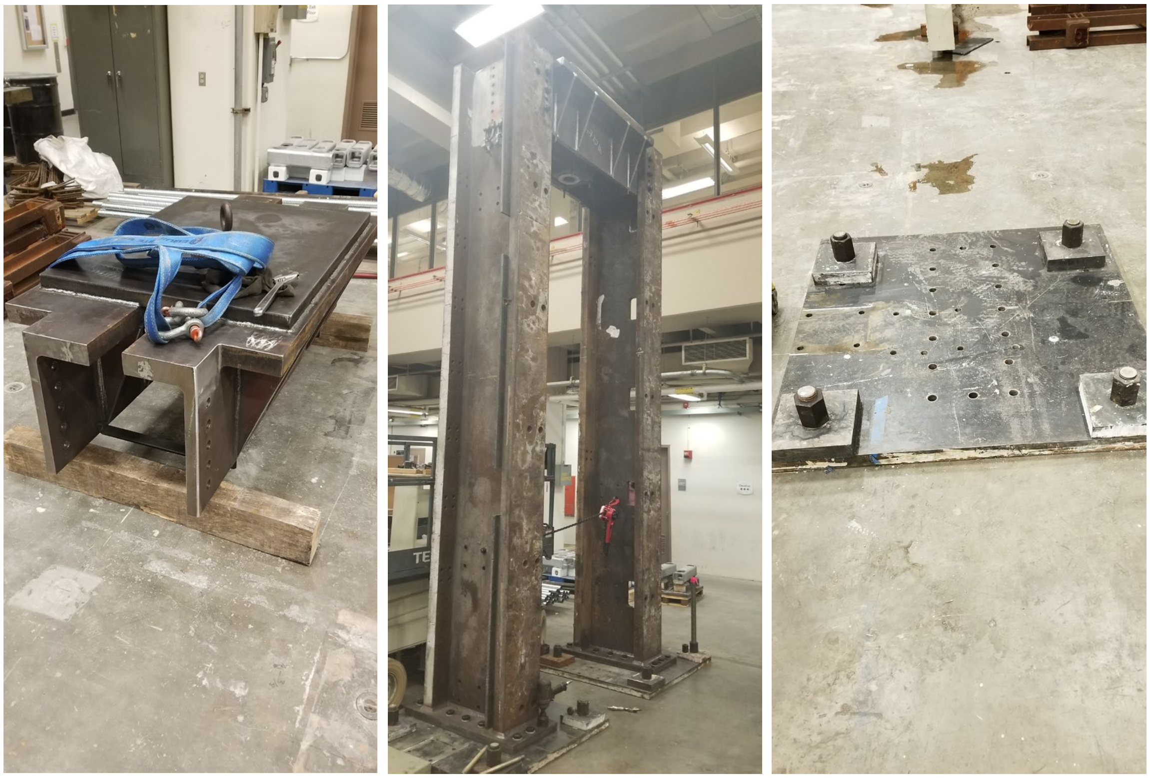

Figure A-19: Central reaction frame. Header beam (left), central frame with jack mounted inside (middle), and base plate (right)

Figure A-20: Lateral A-frames. Retracting arm (left), Overall A-frame (middle), and frame base (right)

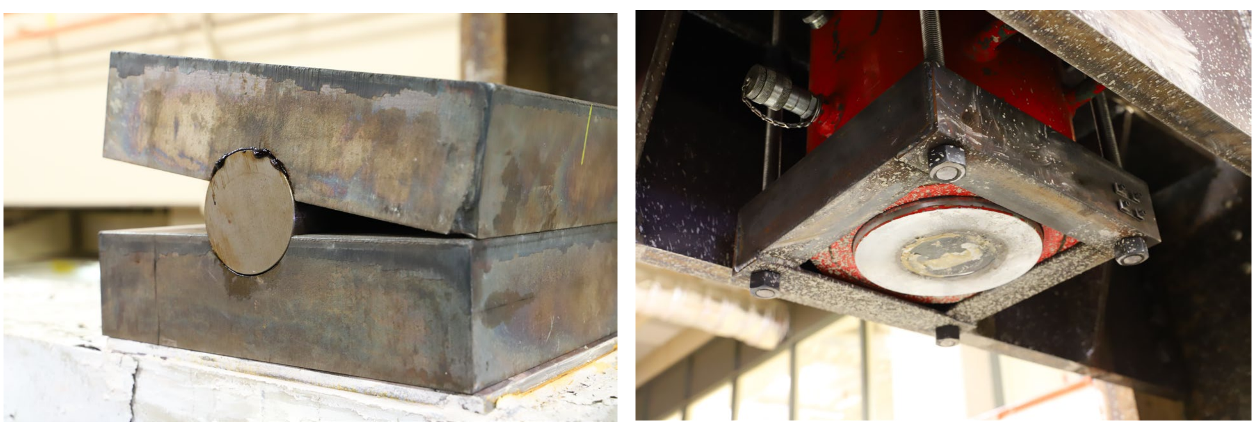

Figure A-21: Rocker block at midspan on top face of beam (left) and hydraulic jack mounted in header beam (right)

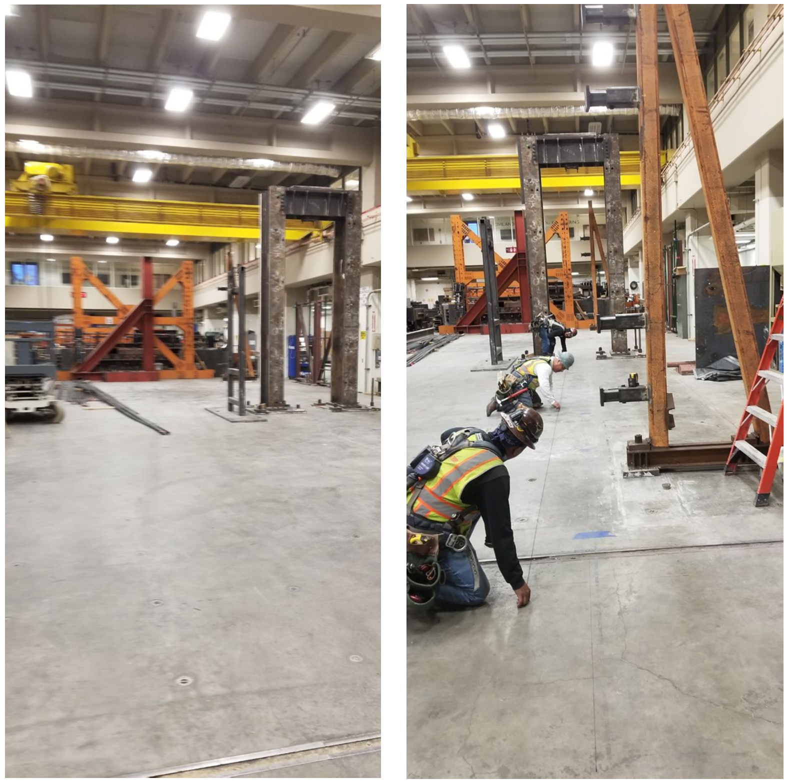

Figure A-22: Empty lab prior to formwork construction (left) and workers marking formwork alignment (right)

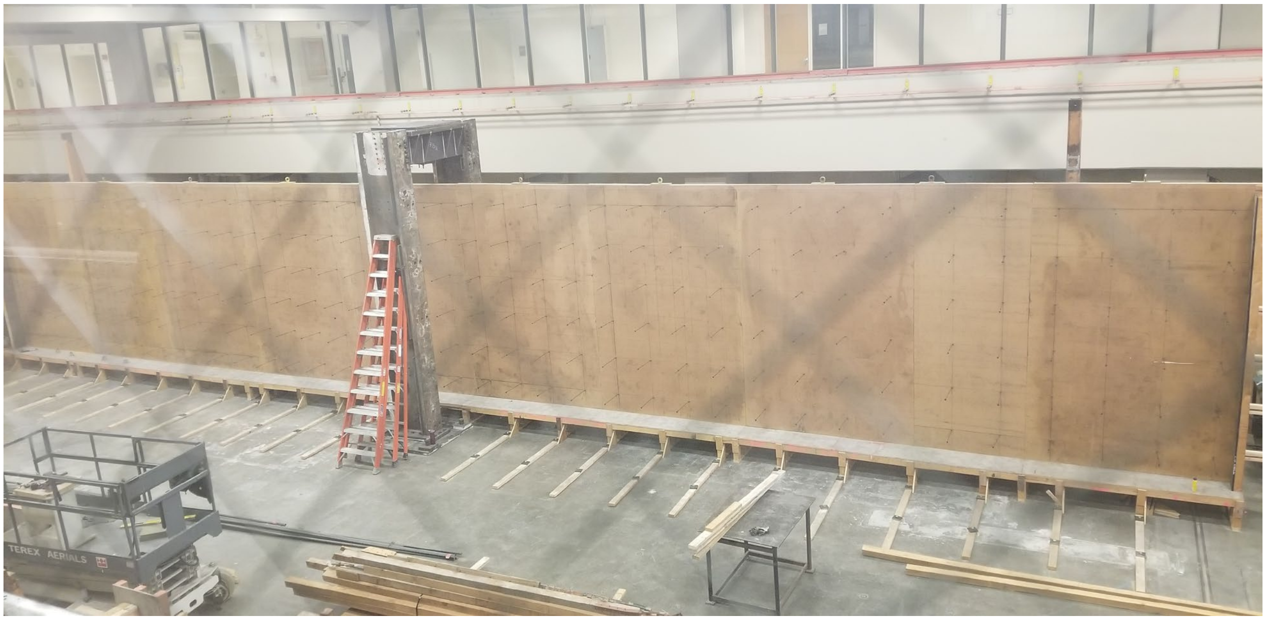

Figure A-23: Formwork with one side up and no steel placed. Central frame in position and lateral A-frames in position on one side

Figure A-24: East end reinforcement and duct exit details. Vents exit duct on side of formwork and ducts exit on ends. Fiber optic strain gauges shown exiting from east end of beam.

Figure A-25: More reinforcement details. Solid block supporting rebar along its length (left), rebar horizontal spacers (middle), and duct plug and vent at midspan (right)

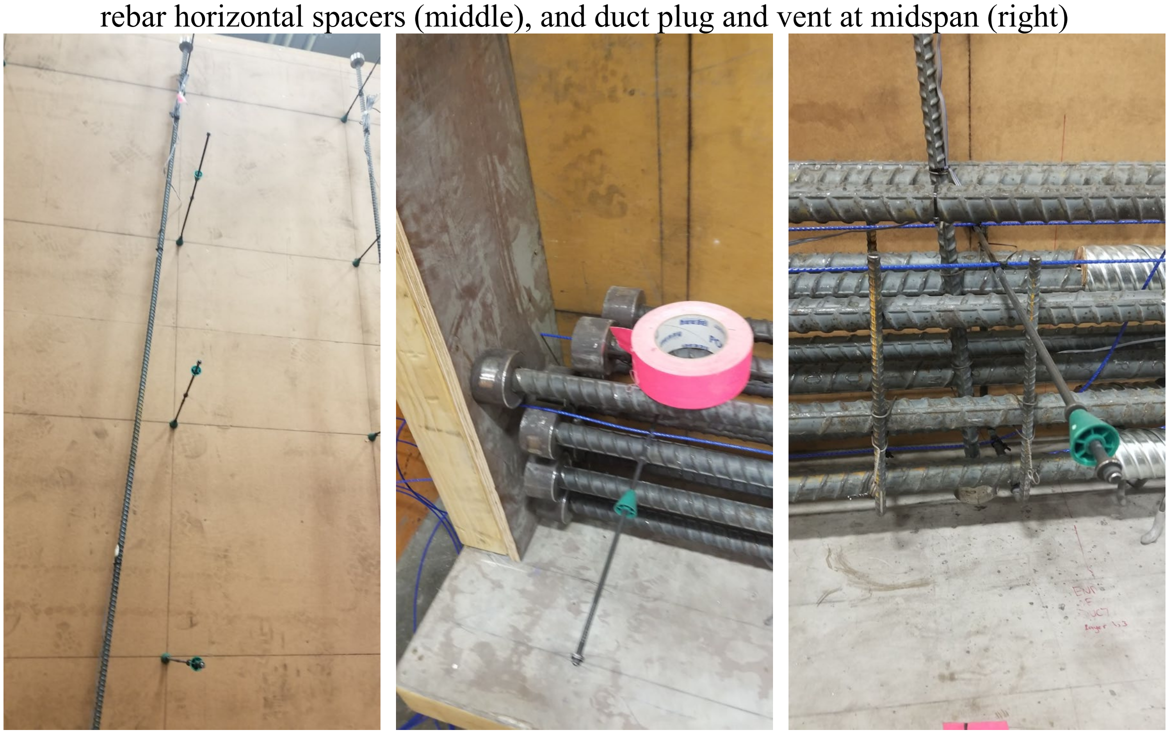

Figure A-26: Shear reinforcement temporarily tied off at top of beam (left), shear reinforcement terminating in rebar cage at bottom (middle), and west beam end (right). Form ties shown sticking out of formwork wall at various locations.

Figure A-27: Formwork closed up once steel reinforcement placed on bottom

Figure A-28: More reinforcement details. Lifting hook held suspended by small wooden plank (left), compression steel layout with last line of rebar suspended for concrete vibrator clearance (mid), and shear reinforcement tied in place on top side (right)

Figure A-29: Cast day. Concrete is pumped into form with 4 inch diameter hose. Hose is suspended from the crane and workers directing hose down the wall.

Figure A-30: Concrete cylinders from 4 trucks of concrete (right), view of top of beam from east end (middle), view of west span of beam from the midspan with shear reinforcement strain gauge wires exiting from top (right)

Figure A-31: Formwork panels removed by crane (left), exposed face of beam near A-frames (middle), A-frame arms extended immediately and locked in place to laterally brace beam (right)

Figure A-32: Formwork removed from beam sides while supported at the base to reduce flexural cracking. Lateral bracing installed at beam ends and midspan for lateral stability.

Figure A-33: Temporary bracing installed at regular intervals during curing (left), beam "roller" supports on east end (middle), and vents exiting beam at east end for grouting procedure (right).

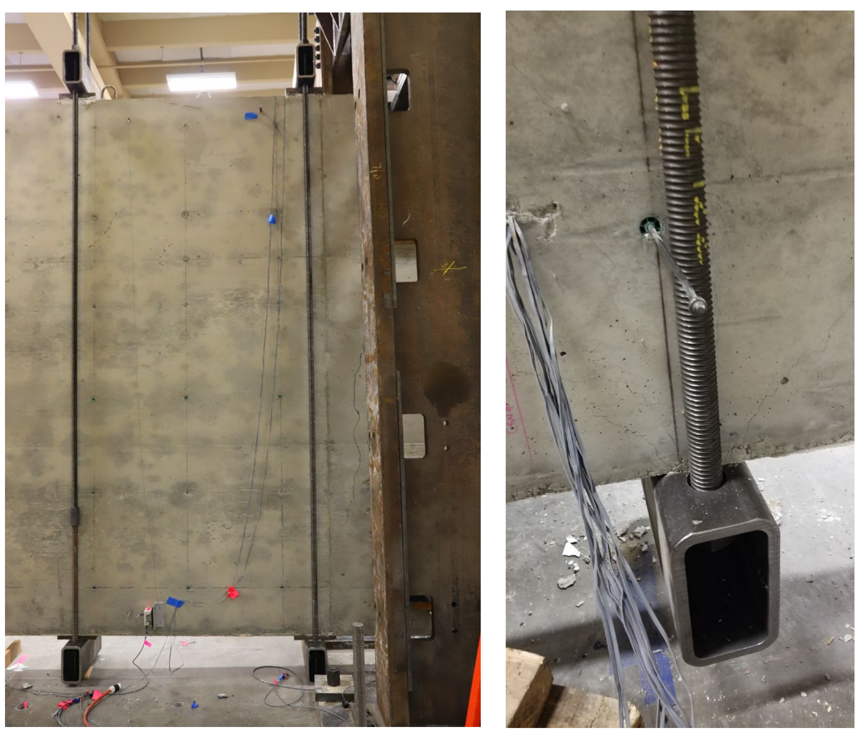

Figure A-34: Shear repair on damaged east span (left) and close-up view of bracket (right). Right image missing bearing plate.

Figure A-35: Beam ready for Phase 2 of testing

Figure A-36: Destroyed state of west span following failure during Phase 2

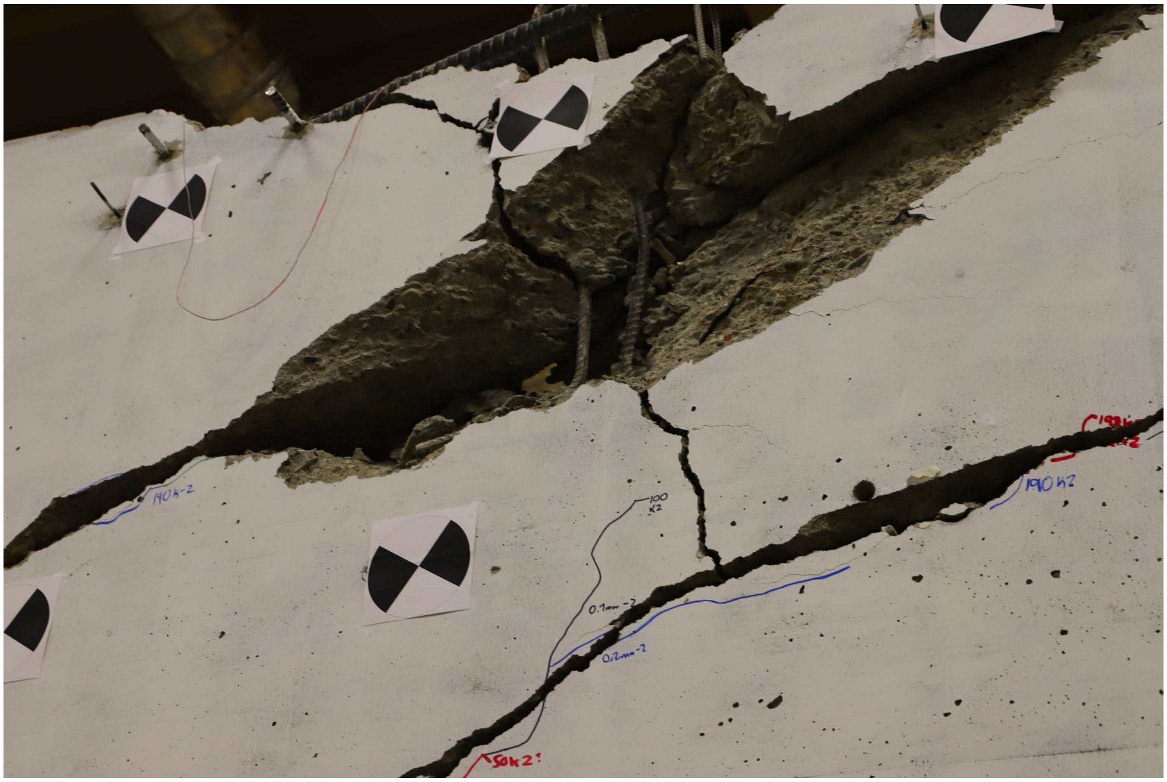

Figure A-37: Destroyed compression zone following failure

Figure A-38: Buckled compression steel at top face of beam

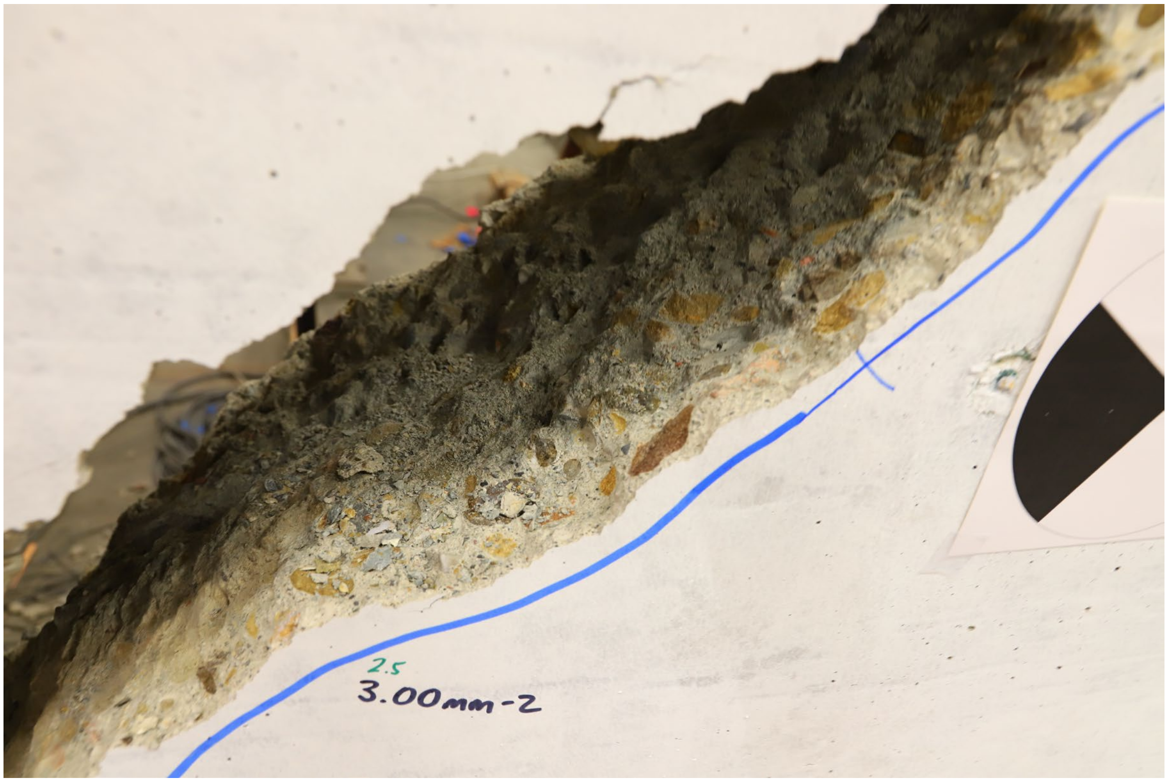

Figure A-39: Crack plane after Phase 2 failure. Signs of multiple aggregate particles shearing

Figure A-40: Damaged dowel zone following failure

Figure A-41: Dowel zone following failure. All concrete cracked diagonally inside of rebar cage

A.8. Test Beam 2 (Phase 3 and Phase 4) Drawings

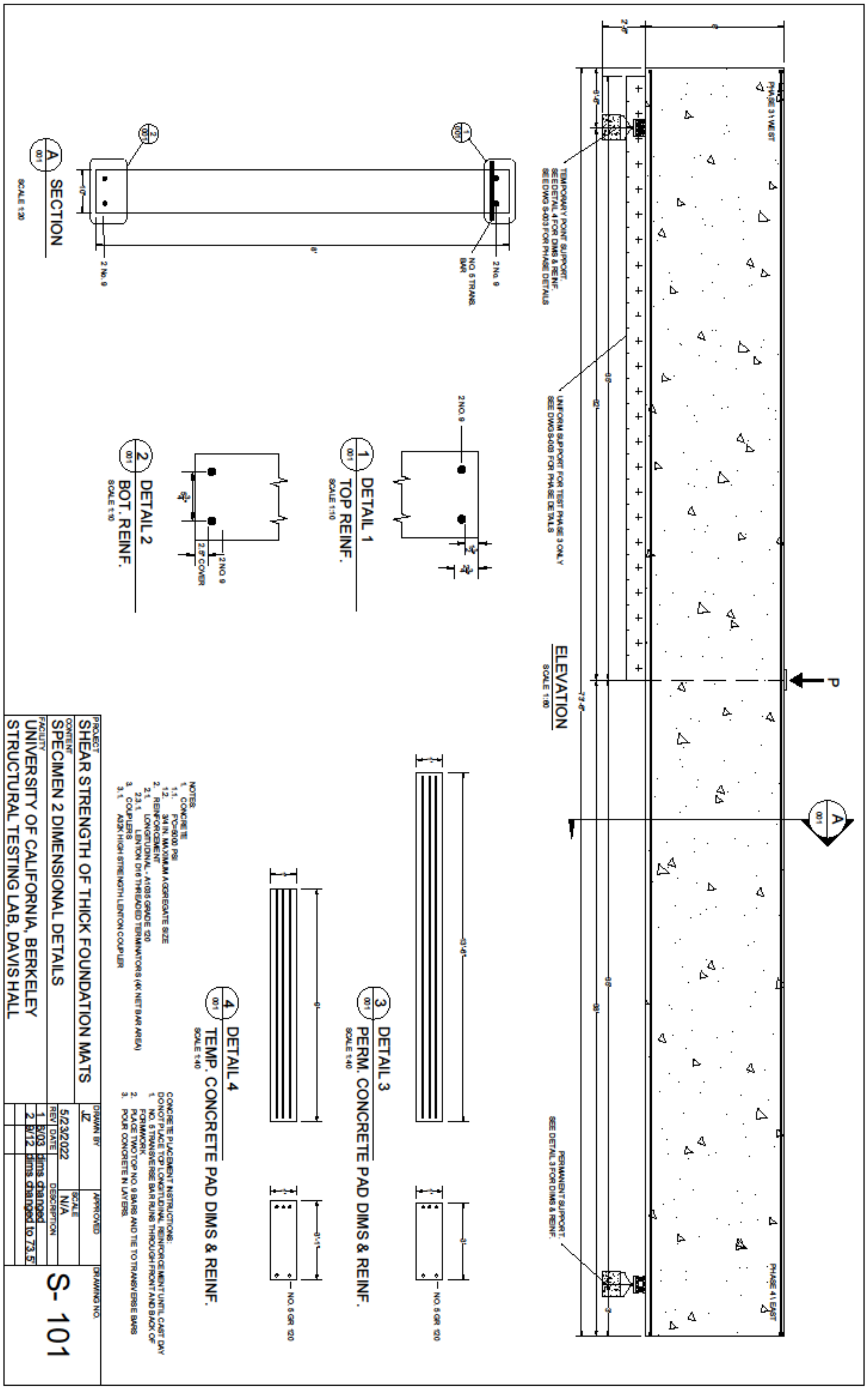

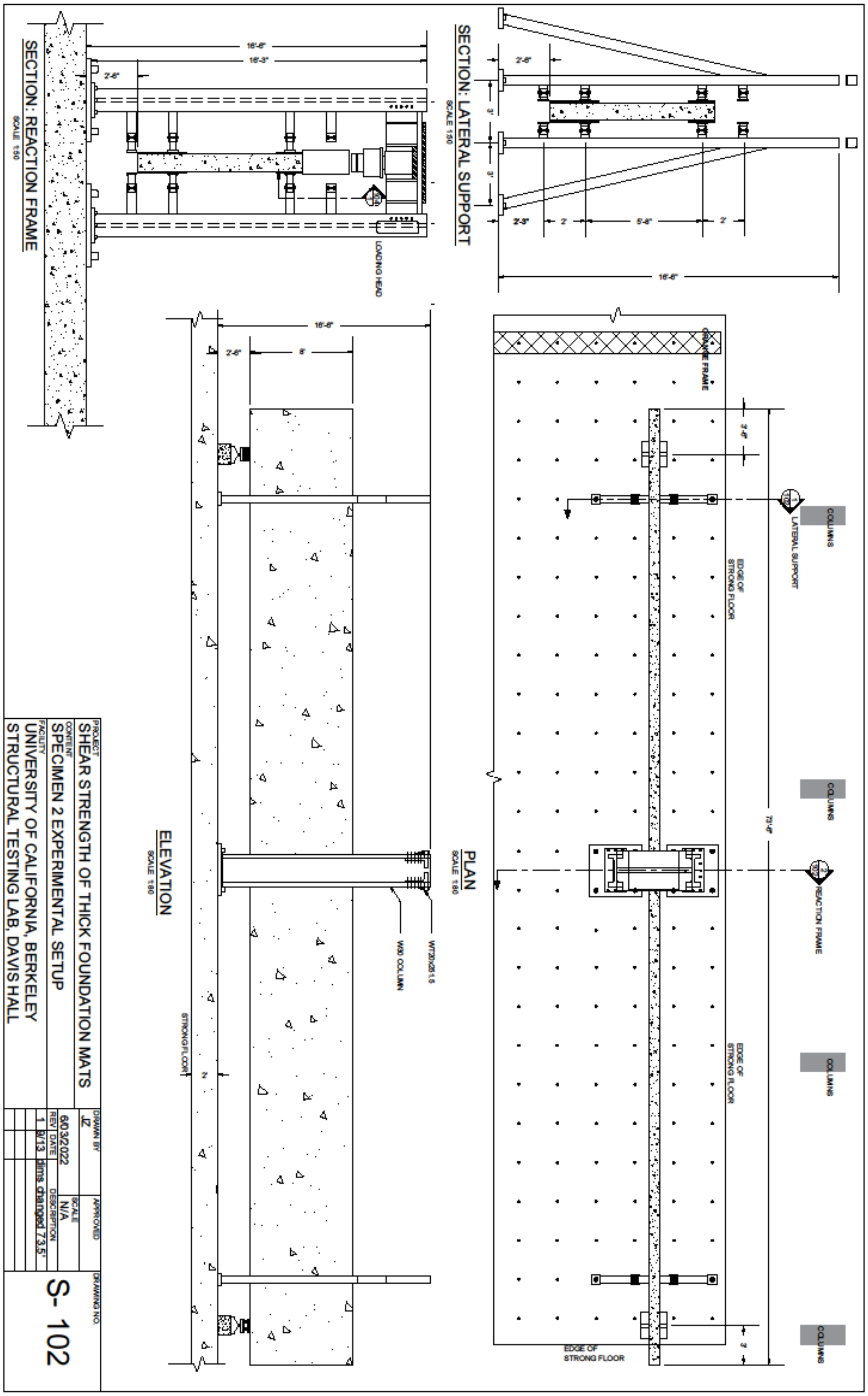
SECTION: LATERAL SUPPORT
SCALE 1:50
SECTION: REACTION FRAME
SCALE 1:50
LOADING HEAD
PLAN
SCALE 1:80
ELEVATION
SCALE 1:80
LATERAL SUPPORT
REACTION FRAME
COLUMNS
EDGE OF STRONG FLOOR
STRONG FLOOR
W30 COLUMN
PROJECT
SHEAR STRENGTH OF THICK FOUNDATION MATS
CONTENT
SPECIMEN 2 EXPERIMENTAL SETUP
FACILITY
UNIVERSITY OF CALIFORNIA, BERKELEY
STRUCTURAL TESTING LAB, DAVIS HALL
DRAWN BY
JZ
APPROVED
DRAWING NO.
6032022
SCALE
N/A
REV DATE DESCRIPTION
1 9/13 dims changed 73.5'
S- 102

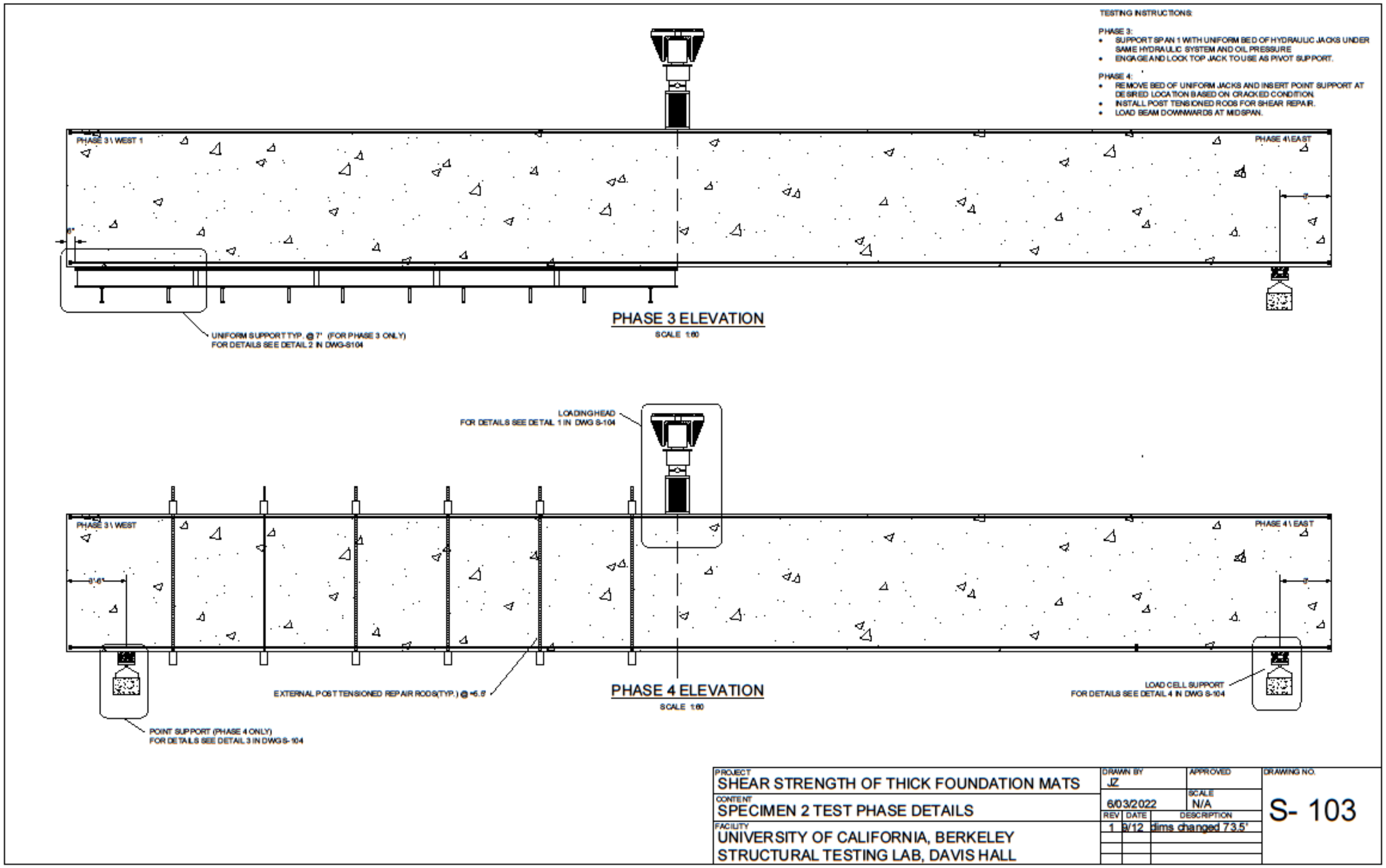

TESTING INSTRUCTIONS:
PHASE 3:
SUPPORT SPAN 1 WITH UNIFORM BED OF HYDRAULIC JACKS UNDER SAME HYDRAULIC SYSTEM AND OIL PRESSURE
ENGAGE AND LOCK TOP JACK TO USE AS PIVOT SUPPORT.
PHASE 4:
REMOVE BED OF UNIFORM JACKS AND INSERT POINT SUPPORT AT DESIRED LOCATION BASED ON CRACKED CONDITION.
INSTALL POST TENSIONED RODS FOR SHEAR REPAIR.
LOAD BEAM DOWNWARDS AT MIDSPAN.
PHASE 3 \ WEST 1
PHASE 4 \ EAST
UNIFORM SUPPORT TYP. @ 7' (FOR PHASE 3 ONLY)
FOR DETAILS SEE DETAIL 2 IN DWG-S104
PHASE 3 ELEVATION
SCALE 1:60
LOADING HEAD
FOR DETAILS SEE DETAIL 1 IN DWG S-104
PHASE 3 \ WEST
3'-6"
EXTERNAL POST TENSIONED REPAIR RODS(TYP.) @ ≈5.5'
PHASE 4 ELEVATION
SCALE 1:60
LOAD CELL SUPPORT
FOR DETAILS SEE DETAIL 4 IN DWG S-104
POINT SUPPORT (PHASE 4 ONLY)
FOR DETAILS SEE DETAIL 3 IN DWG S-104
PROJECT
SHEAR STRENGTH OF THICK FOUNDATION MATS
CONTENT
SPECIMEN 2 TEST PHASE DETAILS
FACILITY
UNIVERSITY OF CALIFORNIA, BERKELEY
STRUCTURAL TESTING LAB, DAVIS HALL
DRAWN BY
JZ
APPROVED
SCALE
6/03/2022
N/A
REV
DATE
DESCRIPTION
1
9/12
dims changed 73.5'
DRAWING NO.
S- 103

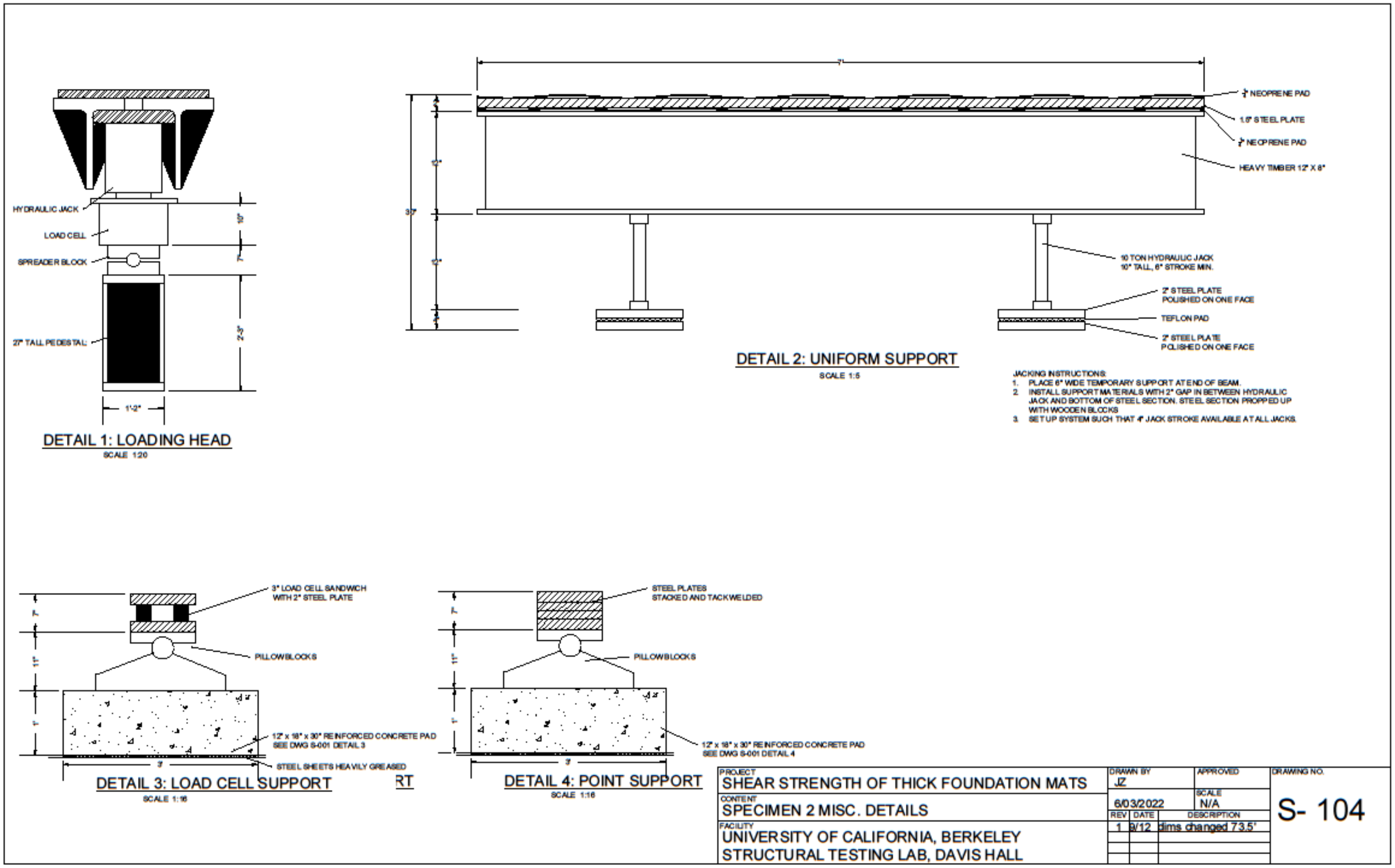
HYDRAULIC JACK
LOAD CELL
SPREADER BLOCK
27" TALL PEDESTAL
10"
7"
2'-3"
1'-2"
DETAIL 1: LOADING HEAD
SCALE 1:20
7'
37"
NEOPRENE PAD
1.5" STEEL PLATE
NEOPRENE PAD
HEAVY TIMBER 12" X 8"
10 TON HYDRAULIC JACK
10" TALL, 6" STROKE MIN.
2" STEEL PLATE
POLISHED ON ONE FACE
TEFLON PAD
2" STEEL PLATE
POLISHED ON ONE FACE
DETAIL 2: UNIFORM SUPPORT
SCALE 1:5
JACKING INSTRUCTIONS:
1. PLACE 6" WIDE TEMPORARY SUPPORT AT END OF BEAM.
2. INSTALL SUPPORT MATERIALS WITH 2" GAP IN BETWEEN HYDRAULIC JACK AND BOTTOM OF STEEL SECTION. STEEL SECTION PROPPED UP WITH WOODEN BLOCKS
3. SET UP SYSTEM SUCH THAT 4" JACK STROKE AVAILABLE AT ALL JACKS.
3" LOAD CELL SANDWICH
WITH 2" STEEL PLATE
PILLOWBLOCKS
12" x 18" x 30" REINFORCED CONCRETE PAD
SEE DWG S-001 DETAIL 3
STEEL SHEETS HEAVILY GREASED
7"
11"
1'
3'
DETAIL 3: LOAD CELL SUPPORT
SCALE 1:16
RT
STEEL PLATES
STACKED AND TACKWELDED
PILLOWBLOCKS
12" x 18" x 30" REINFORCED CONCRETE PAD
SEE DWG S-001 DETAIL 4
DETAIL 4: POINT SUPPORT
SCALE 1:16
PROJECT
SHEAR STRENGTH OF THICK FOUNDATION MATS
CONTENT
SPECIMEN 2 MISC. DETAILS
FACILITY
UNIVERSITY OF CALIFORNIA, BERKELEY
STRUCTURAL TESTING LAB, DAVIS HALL
DRAWN BY
JZ
APPROVED
6/03/2022
SCALE
N/A
REV DATE DESCRIPTION
1 9/12 dims changed 73.5'
DRAWING NO.
S- 104

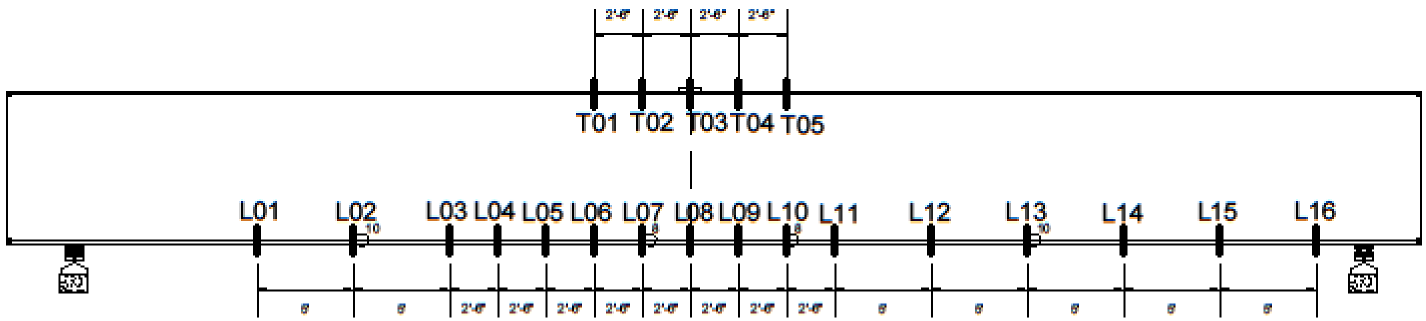

ELEVATION: STRAIN GAUGE DETAILS

SCALE 1:90

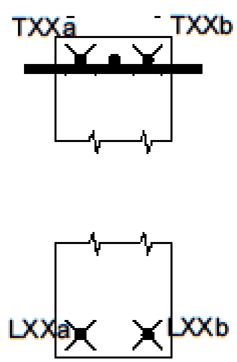

| – STRAIN GAUGE PLANE

x – STRAIN GAUGE LOCATION

– STRAIN GAUGE EXIT LOCATION (n = number of wires exiting)

- Strain gauge to exit from side of forms, horizontal exit location approximate, vertical exit location at 4 inches above bottom of beam.

STRAIN GAUGE LOCATION NOTES:

Total Count: 50

1. FLEXURAL REINFORCEMENT
   1.1. GAUGE APPLIED ALONG SIDE ON NEUTRAL AXIS OF REINFORCEMENT AND RUN OUT OF BACK SIDE OF FORMWORK

PROJECT SHEAR STRENGTH OF THICK FOUNDATION MATS	DRAWN BY JZ	APPROVED	DRAWING NO. S- 105
CONTENT SPECIMEN 2 STRAIN GAUGE LAYOUT	DATE 6/03/2022	SCALE N/A	
FACILITY UNIVERSITY OF CALIFORNIA, BERKELEY STRUCTURAL TESTING LAB, DAVIS HALL	Rev 1 / Date 9/12	Description: dims changed 73.5'	

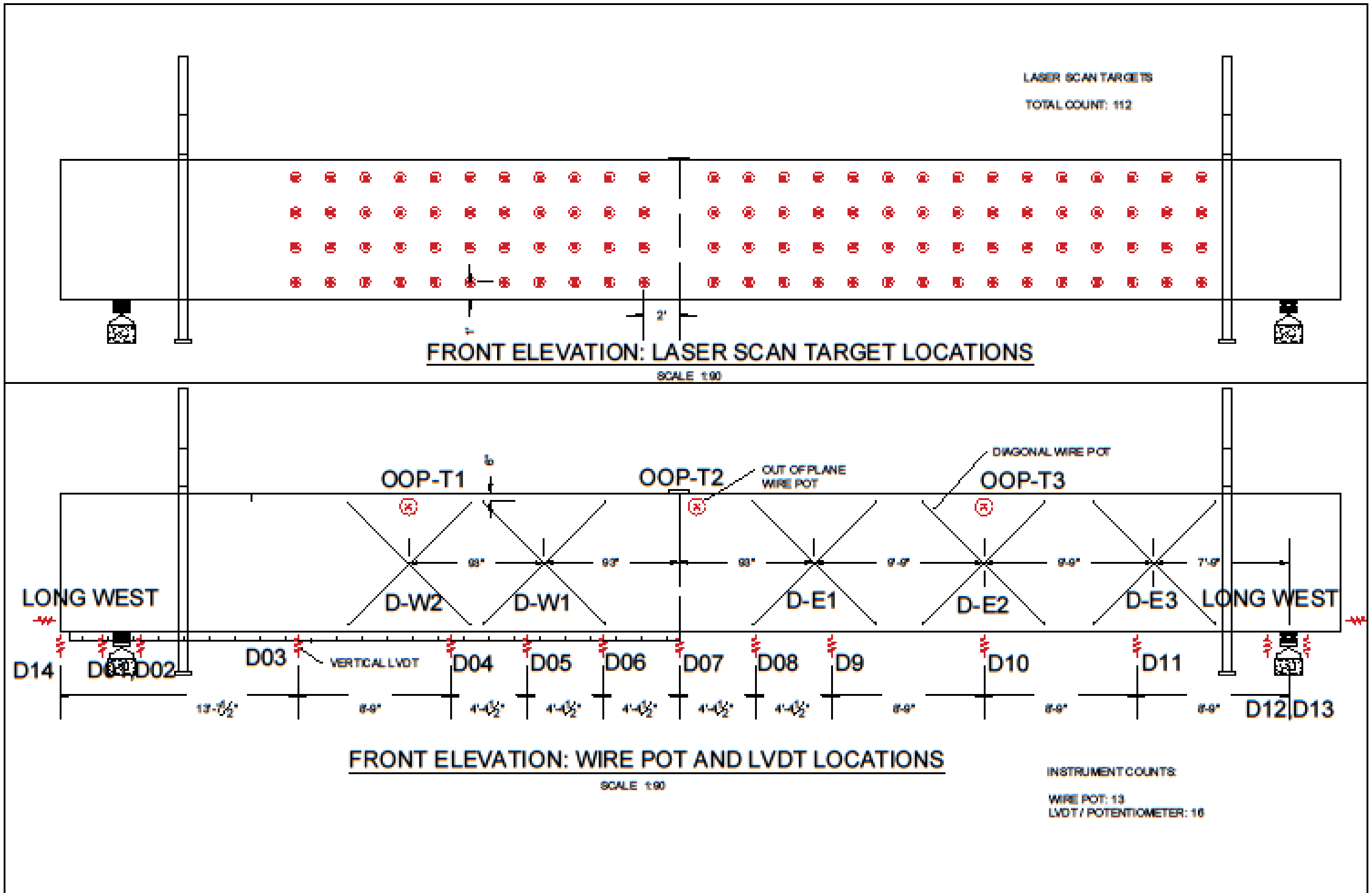

PROJECT SHEAR STRENGTH OF THICK FOUNDATION MATS	DRAWN BY jz	APPROVED	DRAWING NO. S- 106
CONTENT SPECIMEN 2 EXT. INSTRUMENT LAYOUT	DATE 3/21/2023	SCALE N/A	
FACILITY UNIVERSITY OF CALIFORNIA, BERKELEY STRUCTURAL TESTING LAB, DAVIS HALL	Rev / Date	Description	

A.9. Test Beam 2 (Phase 3 and Phase 4) Construction Photos

Figure A-42: Formwork constructed with backside of formwork put up first

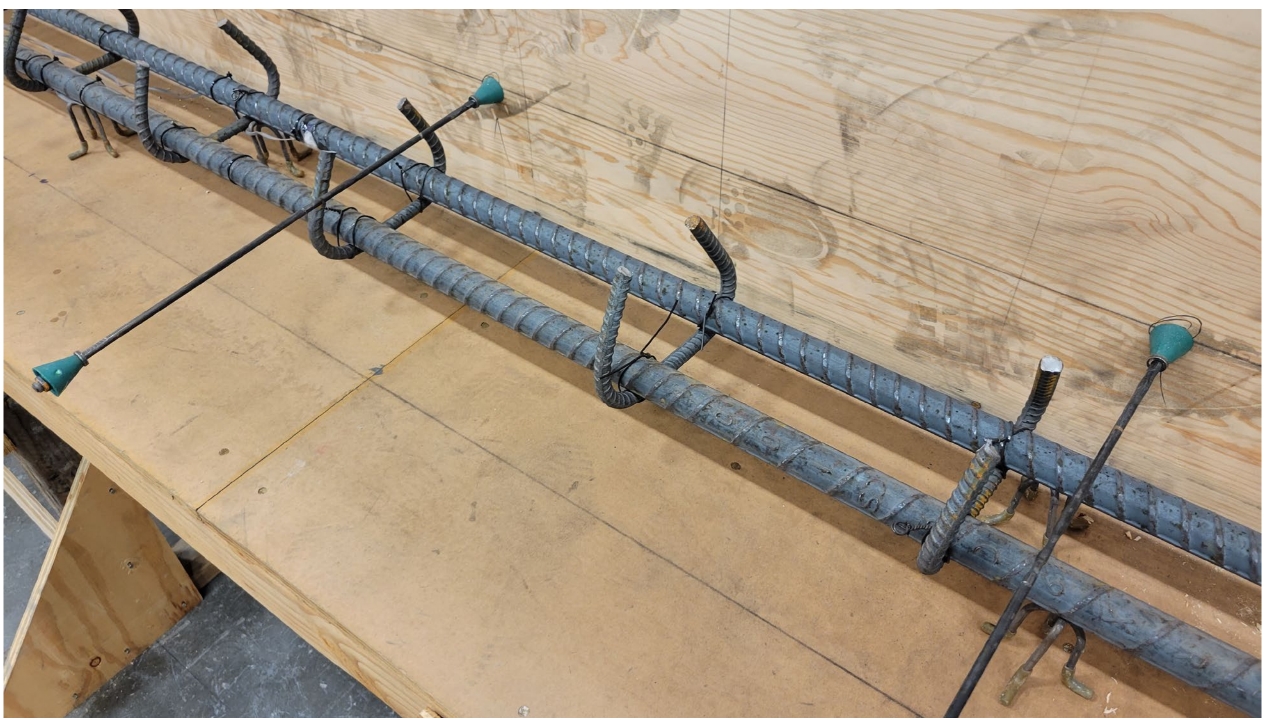

Figure A-43: Longitudinal tension steel placed with transverse ties to prevent splitting

Figure A-44: East span of beam

Figure A-45: Formwork panel closed up and ready for casting

Figure A-46: Concrete cylinders ready to go for casting

Figure A-47: Casting beam with pump hose attached to crane

Figure A-48: Casting concrete cylinders

Figure A-49: Compression steel pushed to the side for pump hose clearance

Figure A-50: Concrete at bottom of beam

Figure A-51: Tying rebar in position before pouring final lift of concrete

Figure A-52: Concrete cast crew

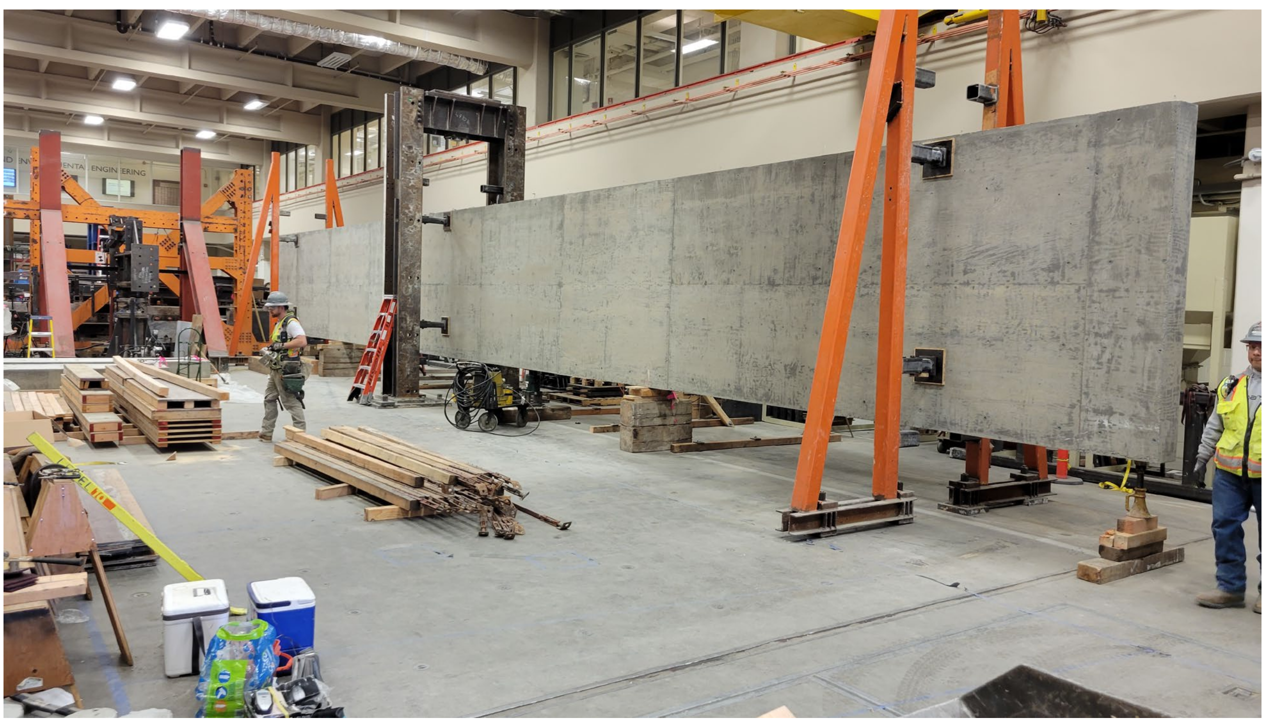

Figure A-53: Concrete beam removed from formwork and placed on temporary supports

Figure A-54: Timber beams used for uniform reaction on west span (jacks not shown). Currently supported by temporary jacks and wood blocks

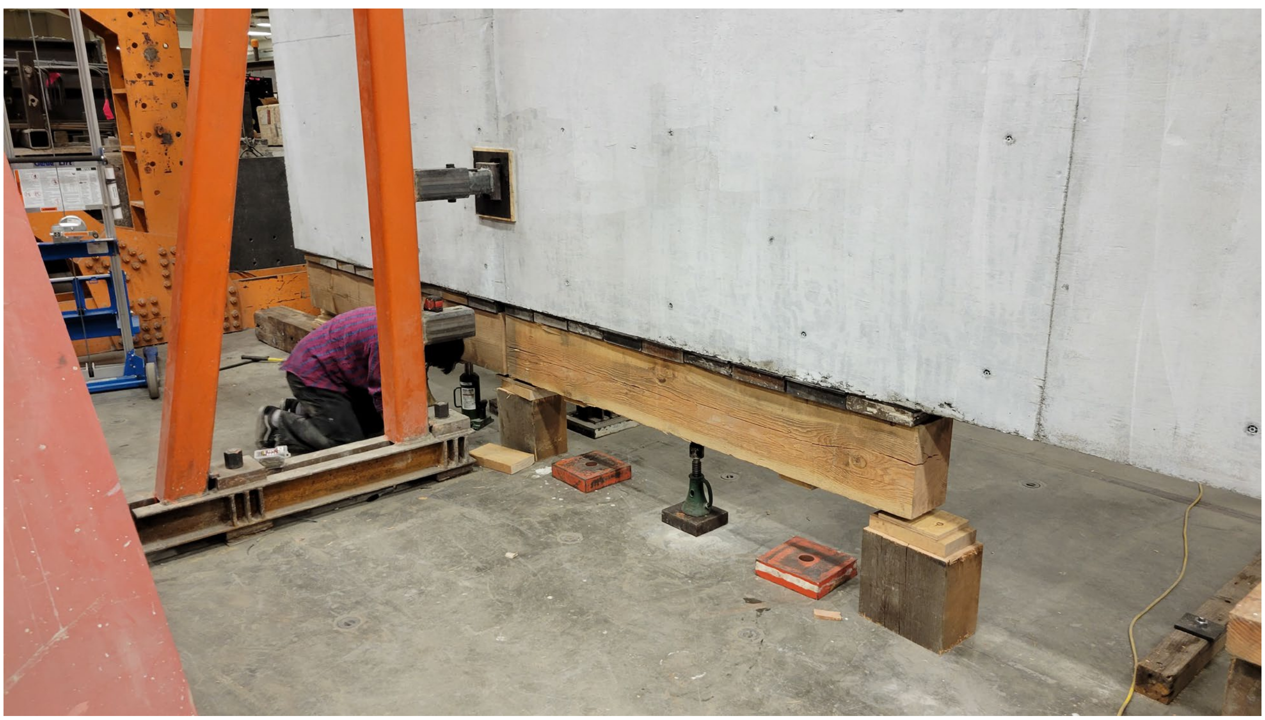

Figure A-55: Additional timber beams used for uniform reaction on west span (jacks not shown). Currently supported by temporary jacks and wood blocks

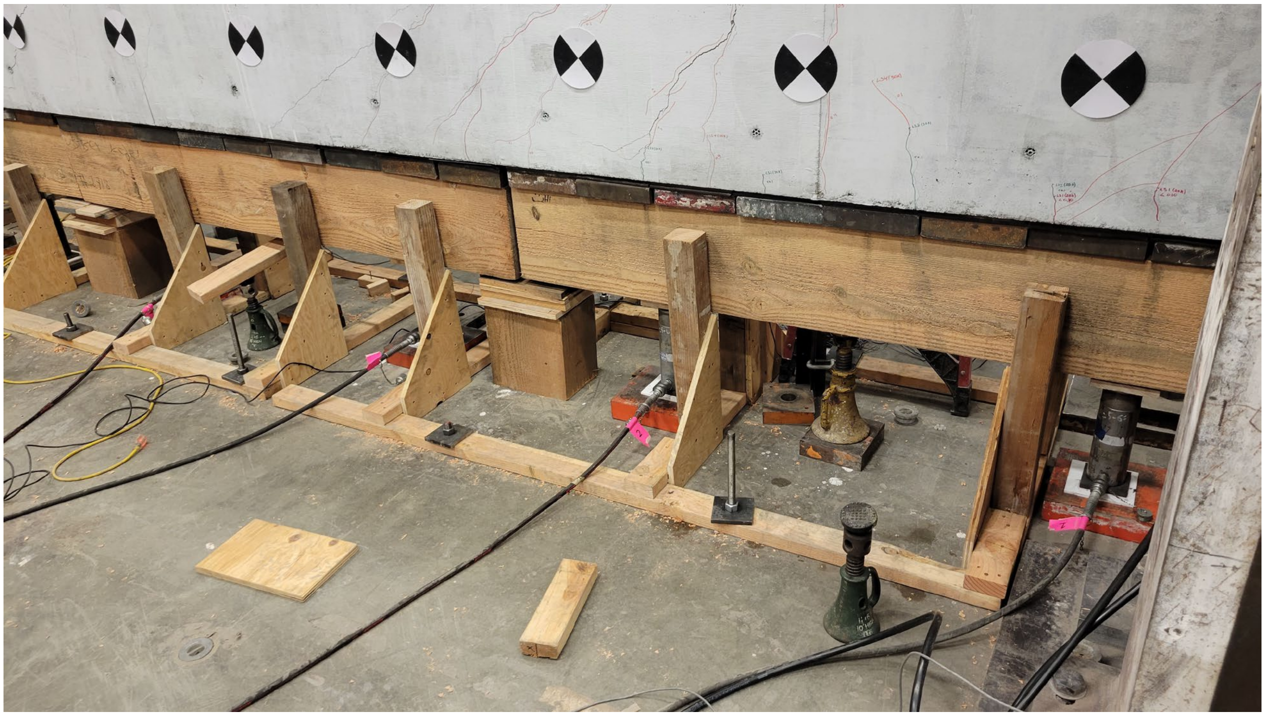

Figure A-56: Uniform reaction setup with jacks and safety mechanism to hold the timber beams from falling sideways

Figure A-57: Uniform reaction jacks supporting beam

Figure A-58: Hydraulic hand pump and switch board connection to each of the hydraulic jacks (hoses not attached)

Figure A-59: Shear repair

Figure A-60: Instruments at west end

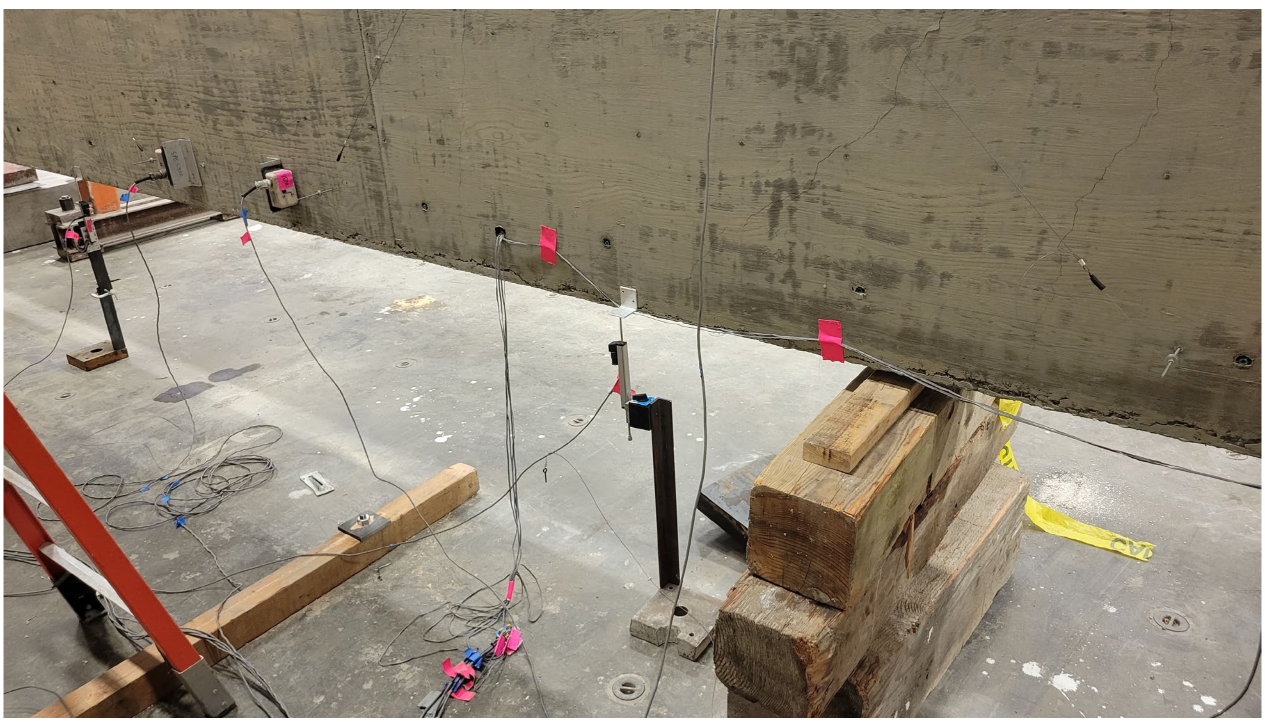

Figure A-61 Various instruments along the span. Dunnage to catch the beam at collapse shown

Figure A-62: "Roller" support on east end. Load cell pack located between support and beam. Companion Beam 3 located underneath the greased slip layer

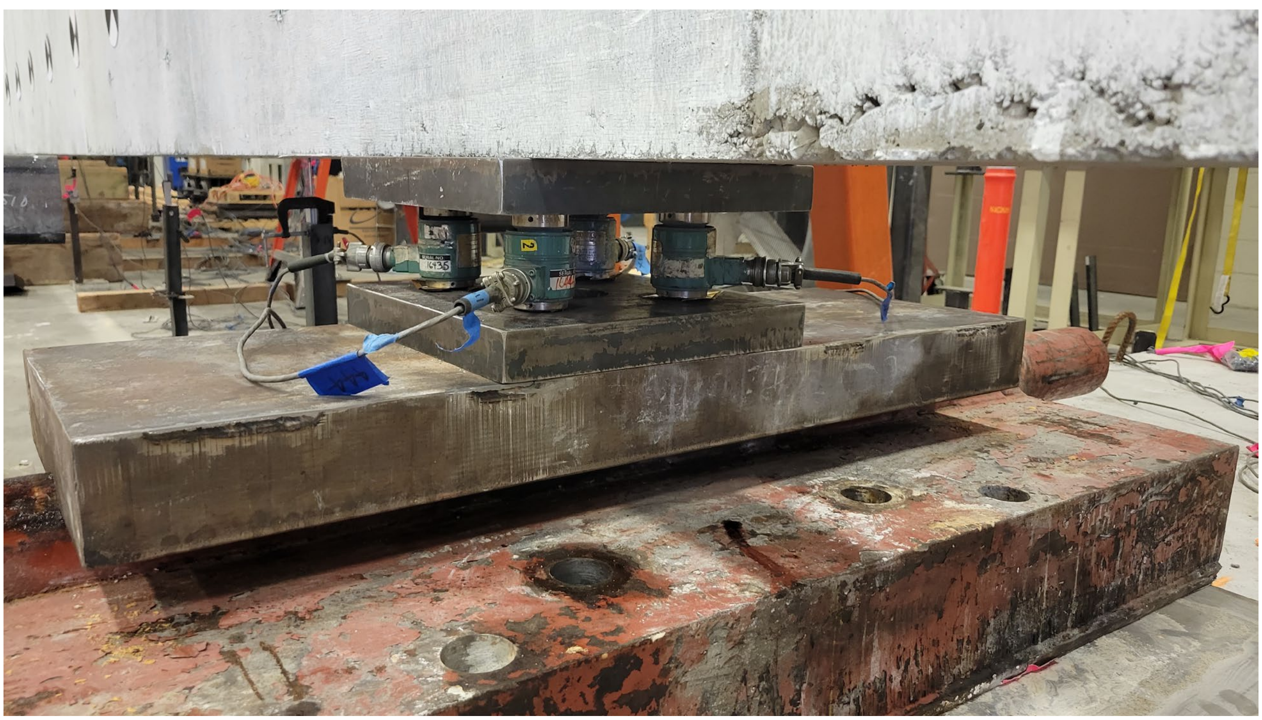

Figure A-63: Load cell pack under east support

Figure A-64: "Roller" support on west end of beam. Multiple steel plates stacked on top of roller block to match clearance of load cell pack on east support

Figure A-65: Squat column making up clearance between jack and beam

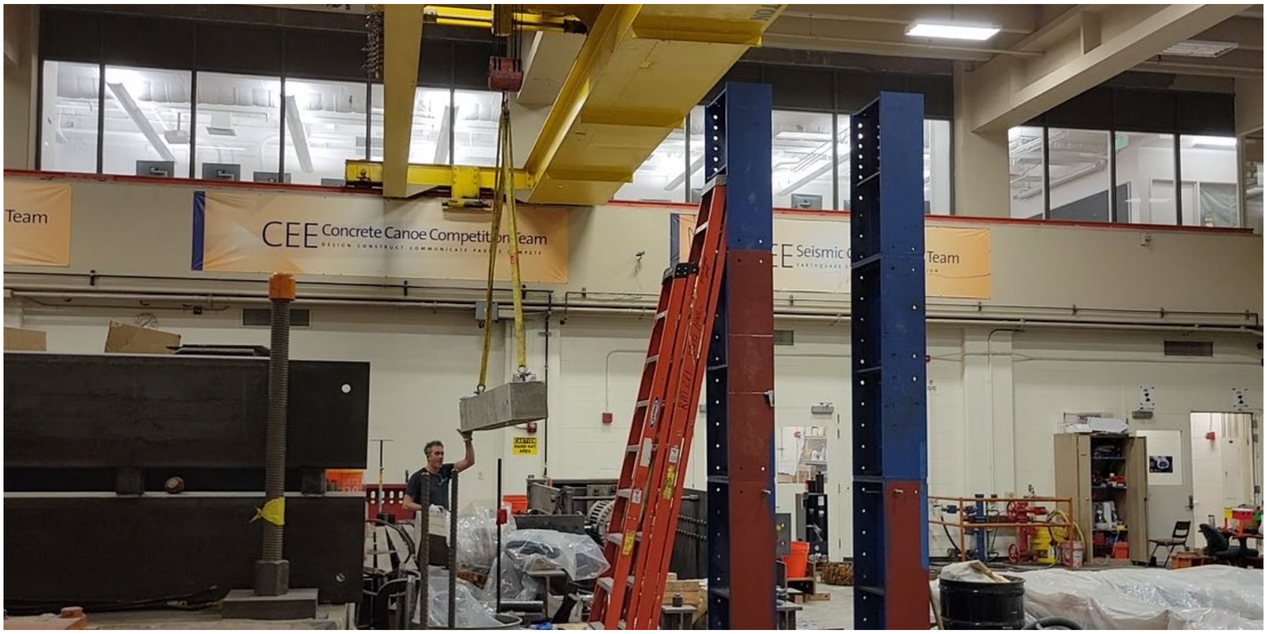

Figure A-66: Moving Companion Beams 1 and 2 into position on the east

Figure A-67: Arched shape of buckled rebar. No aggregate particles observed to be sheared

Figure A-68: Temporary shoring on broken beam

Figure A-69: Crack interface after failure. Some aggregate particles observed to be sheared, but majority intact

Figure A-70: Dowel action keeping beam from fully collapsing

Figure A-71: Arched shape of buckled rebar. Zone where the compression face rips off the top due to bar buckling ends at the top loading plate

A.10. Uniform Support Apparatus Validation

Ten single acting hydraulic jacks of the same model were rented as part of the uniform support. The load is controlled from a singular point via a hand pump. To monitor the loads applied, the jacks are calibrated in a Baldwin UTM to obtain the load versus oil pressure curve. These jacks are tested in two groups of 5 to obtain the average response of all jacks and also individually on a select few jacks to make sure that the responses are consistent. The plots from each test are shown below and the responses are nearly identical.

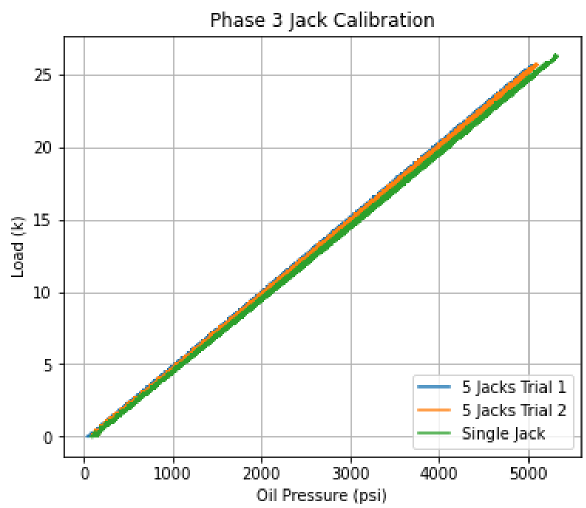

Figure A-72: Phase 3 jack calibration data

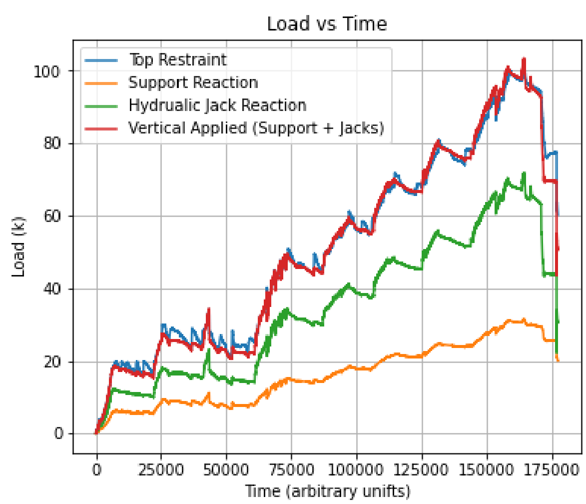

Figure A-73: Phase 3 setup validation from measured jack, top restraint, and support reactions

To check the experimental setup, various independent force readings are summed to verify that vertical equilibrium is satisfied. Independent measurements are made for the load cell at the top restraint, the load cells measuring the east support reaction, and the forces corresponding to the hydraulic jacks, measured by proxy using the oil pressures and calibrated pressure vs. load charts.

The sum of the two support reactions (Support Reaction, Hydraulic Jack Reaction) should equal the restraint provided at the top (Top Restraint) based on the vertical equilibrium of the test setup. When loading, the sum of the reactions agrees very well with the measured top restraint, validating the test response. Accordingly, estimates of shear force and applied load are taken with the measured load cell reactions since those are more accurate.

There is some deviation between the sum of the reactions and the measured restraint when loading is paused. This is attributed to relaxation in the specimen as well as relaxation in the hoses of the jacks. Because the hoses are long, it is possible that small dilations in the hose diameters as well as a little bit of oil leaking back into the pump could result in the observed deviation of the load. Additionally, the top restraint is displacement controlled with a jack to impose no movement rather than having the top restraint directly bear on the central frame. Oscillations in the control of the displacement could also result in the deviations in load when loading is paused due to minor oscillations in the control of the jack. This can cause oil pressures to not respond uniformly in the hydraulic system since the pressure is not applied by the hand pump but imposed by a few jacks near the top restraint.

A.11. Companion Beam Drawings and Construction Photos

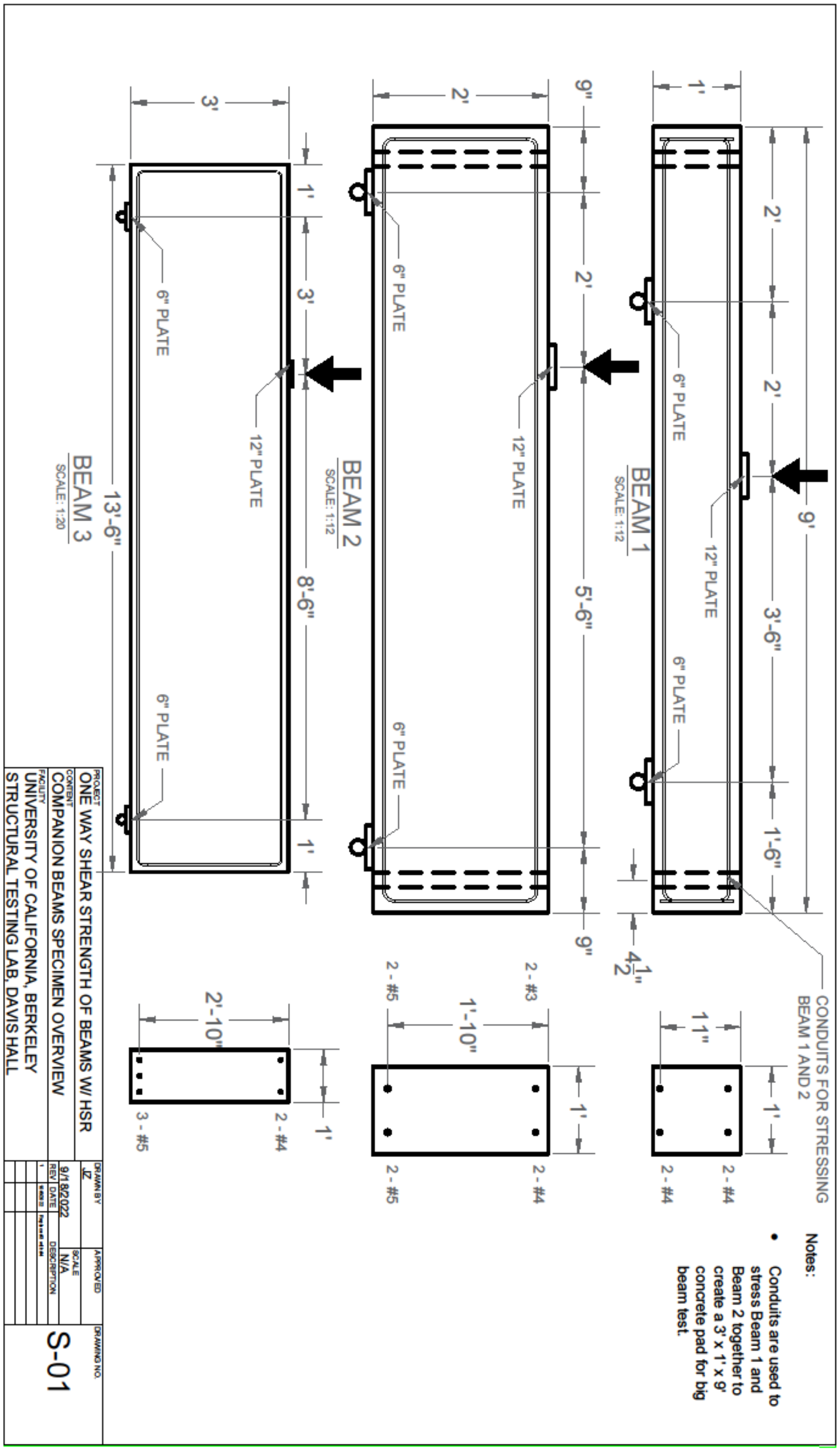

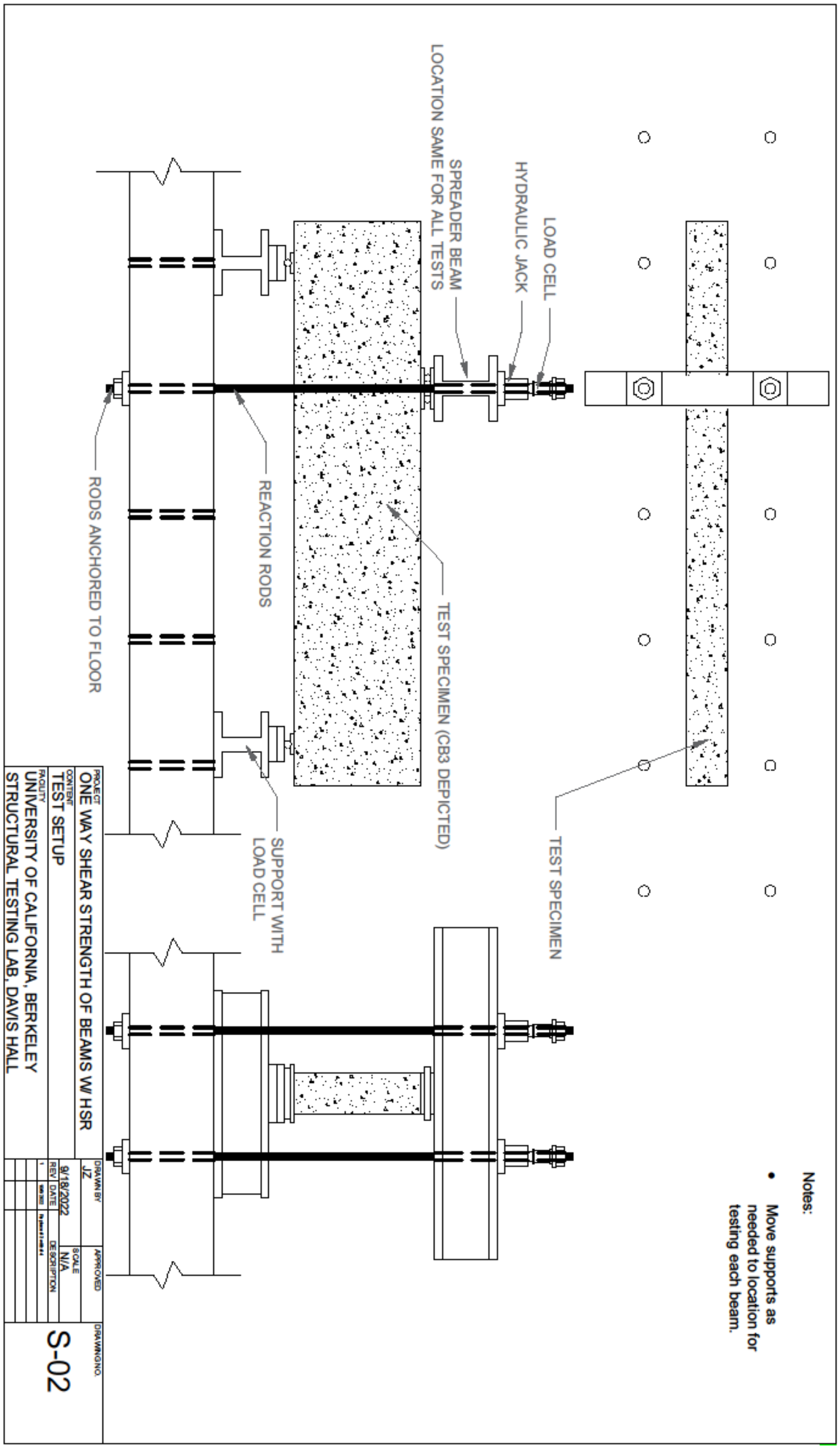
LOAD CELL
HYDRAULIC JACK
SPREADER BEAM
LOCATION SAME FOR ALL TESTS
TEST SPECIMEN (CB3 DEPICTED)
TEST SPECIMEN
REACTION RODS
RODS ANCHORED TO FLOOR
SUPPORT WITH LOAD CELL
Notes:
Move supports as needed to location for testing each beam.
PROJECT
ONE WAY SHEAR STRENGTH OF BEAMS W/ HSR
CONTENT
TEST SETUP
FACILITY
UNIVERSITY OF CALIFORNIA, BERKELEY
STRUCTURAL TESTING LAB, DAVIS HALL
DRAWN BY
JZ
APPROVED
9/18/2022
SCALE
N/A
REV DATE DESCRIPTION
DRAWING NO.
S-02

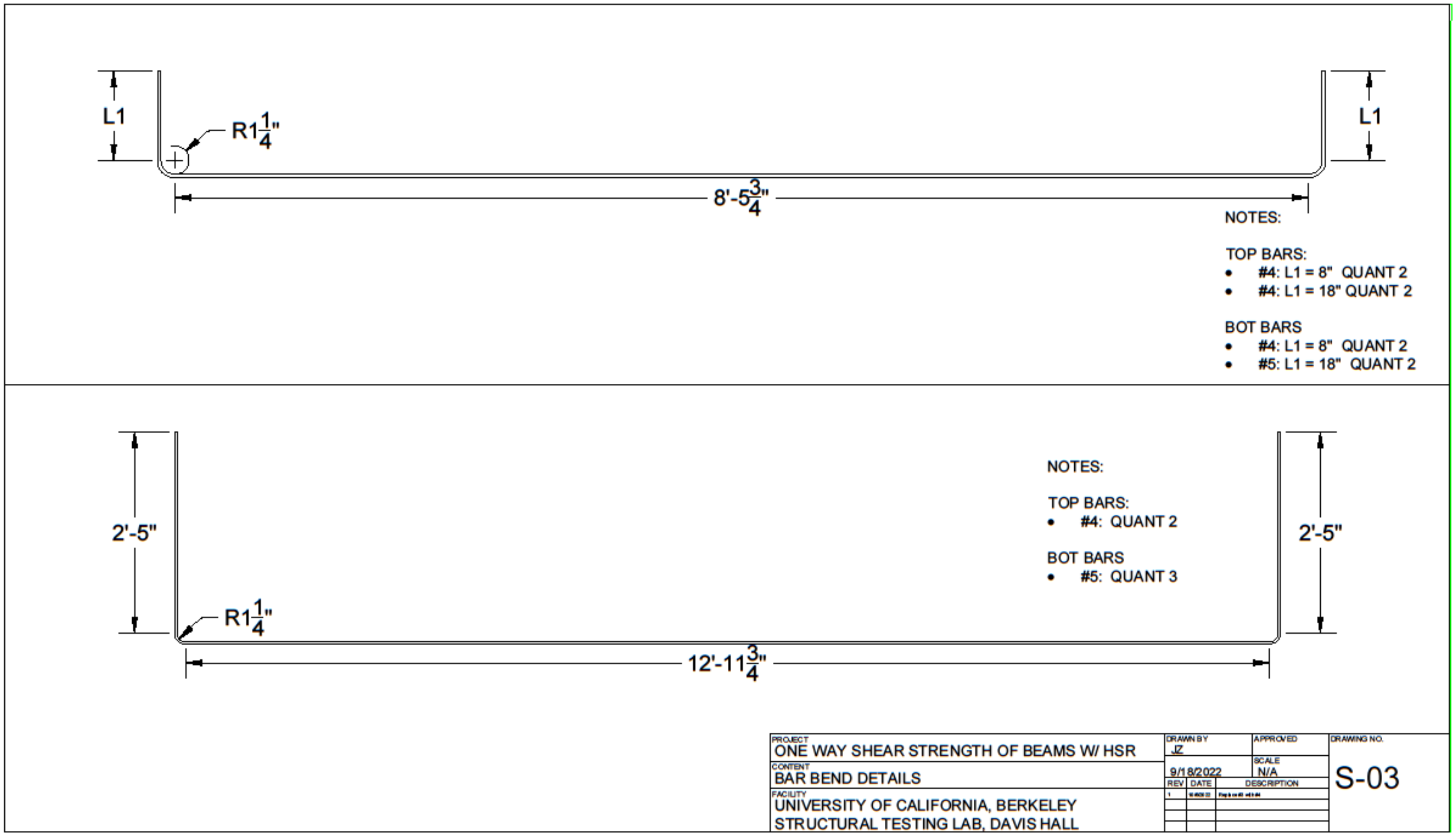
L1
R1$\frac{1}{4}$"
L1
8'-5$\frac{3}{4}$"
NOTES:
TOP BARS:
• #4: L1 = 8" QUANT 2
• #4: L1 = 18" QUANT 2
BOT BARS
• #4: L1 = 8" QUANT 2
• #5: L1 = 18" QUANT 2
2'-5"
NOTES:
TOP BARS:
• #4: QUANT 2
BOT BARS
• #5: QUANT 3
2'-5"
R1$\frac{1}{4}$"
12'-11$\frac{3}{4}$"
PROJECT
ONE WAY SHEAR STRENGTH OF BEAMS W/ HSR
CONTENT
BAR BEND DETAILS
FACILITY
UNIVERSITY OF CALIFORNIA, BERKELEY
STRUCTURAL TESTING LAB, DAVIS HALL
DRAWN BY
JZ
APPROVED
SCALE
N/A
9/18/2022
REV DATE DESCRIPTION
DRAWING NO.
S-03

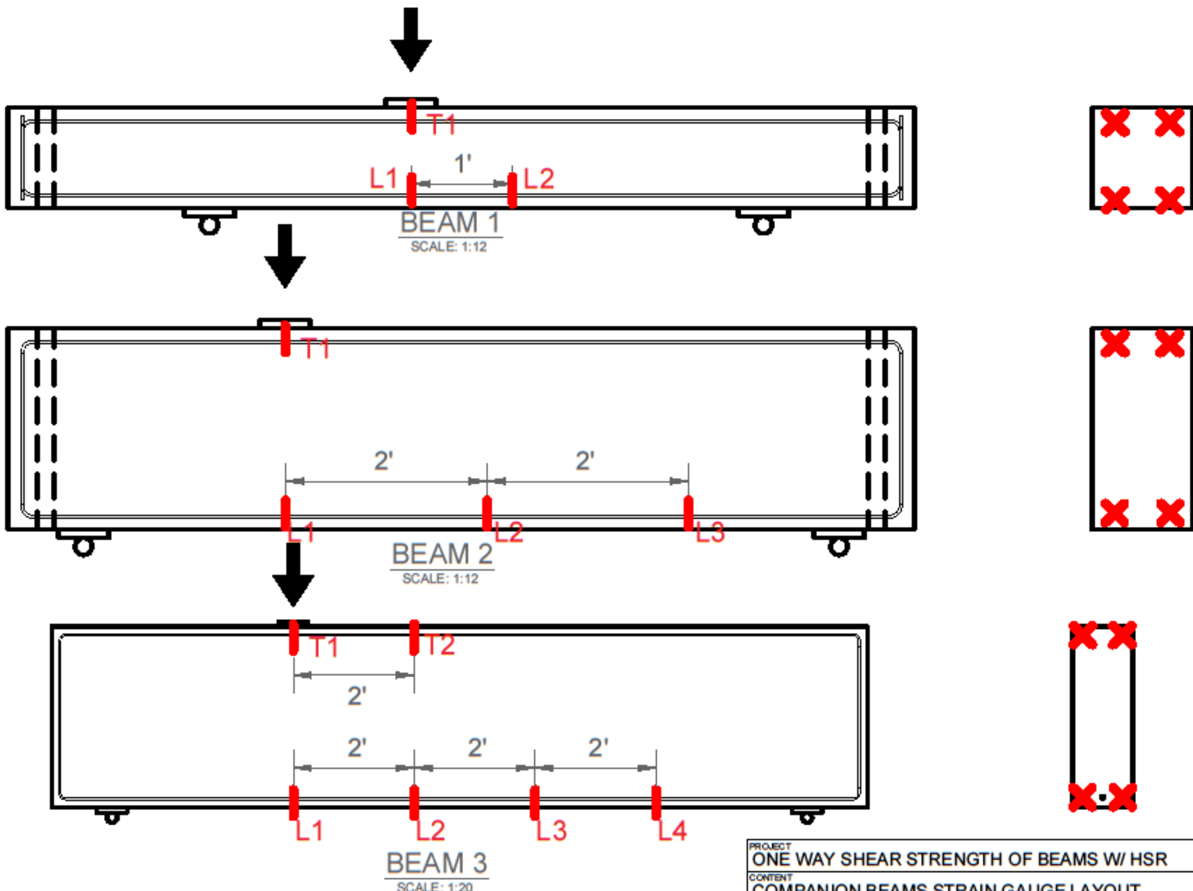

Notes:

- Install strain gauge on side of reinforcement (neutral axis)

PROJECT ONE WAY SHEAR STRENGTH OF BEAMS W/ HSR	DRAWN BY JZ	APPROVED	DRAWING NO.
CONTENT COMPANION BEAMS STRAIN GAUGE LAYOUT	9/18/2022	SCALE N/A	S-04
FACILITY UNIVERSITY OF CALIFORNIA, BERKELEY STRUCTURAL TESTING LAB, DAVIS HALL	REV DATE	DESCRIPTION	

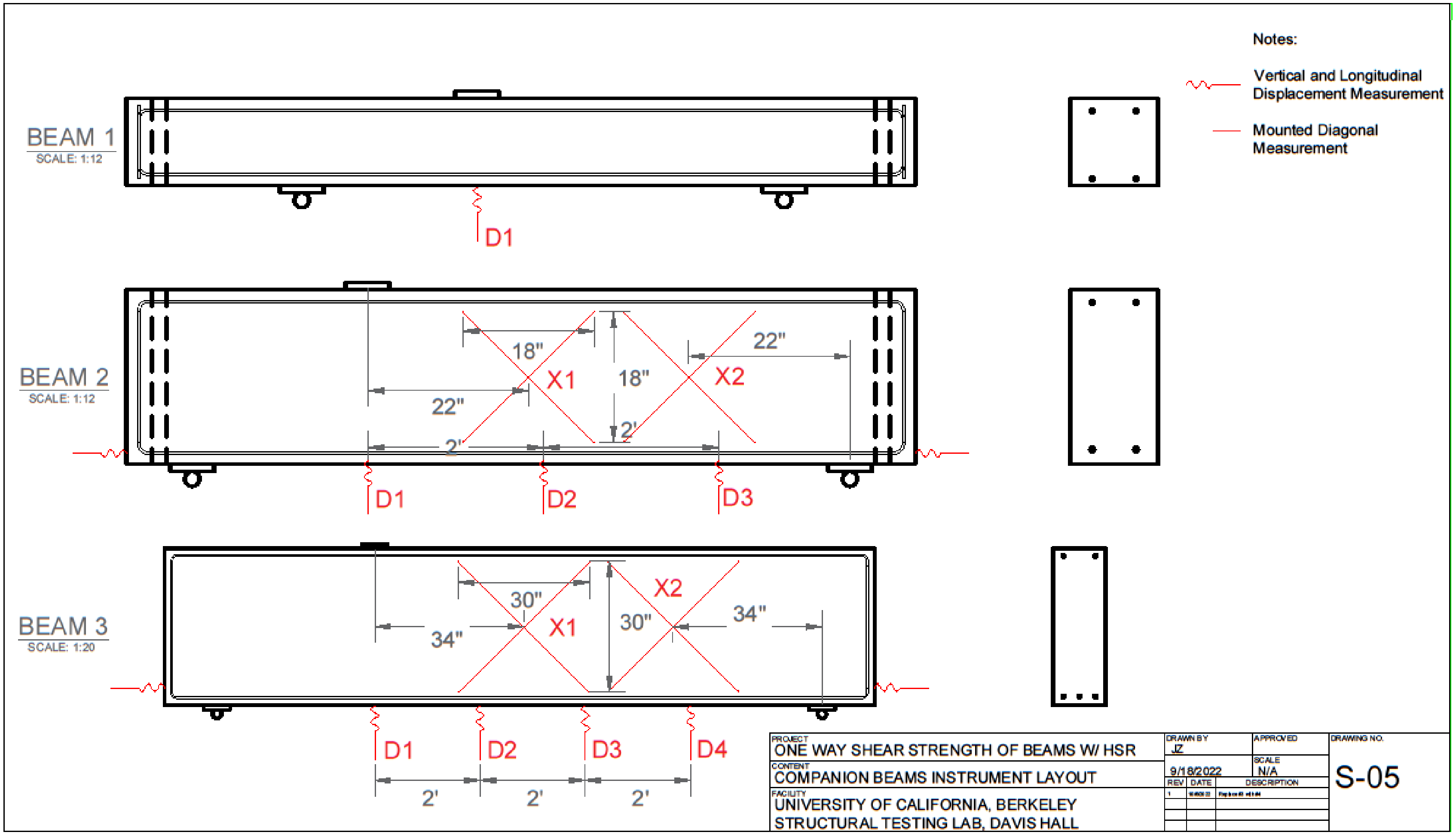
BEAM 1
SCALE: 1:12
D1
BEAM 2
SCALE: 1:12
18"
X1
18"
X2
22"
22"
2'
2'
D1
D2
D3
BEAM 3
SCALE: 1:20
30"
X2
X1
30"
34"
34"
D1
D2
D3
D4
2'
2'
2'
Notes:
Vertical and Longitudinal Displacement Measurement
Mounted Diagonal Measurement
PROJECT
ONE WAY SHEAR STRENGTH OF BEAMS W/ HSR
CONTENT
COMPANION BEAMS INSTRUMENT LAYOUT
FACILITY
UNIVERSITY OF CALIFORNIA, BERKELEY
STRUCTURAL TESTING LAB, DAVIS HALL
DRAWN BY
JZ
APPROVED
9/18/2022
SCALE
N/A
REV
DATE
DESCRIPTION
DRAWING NO.
S-05

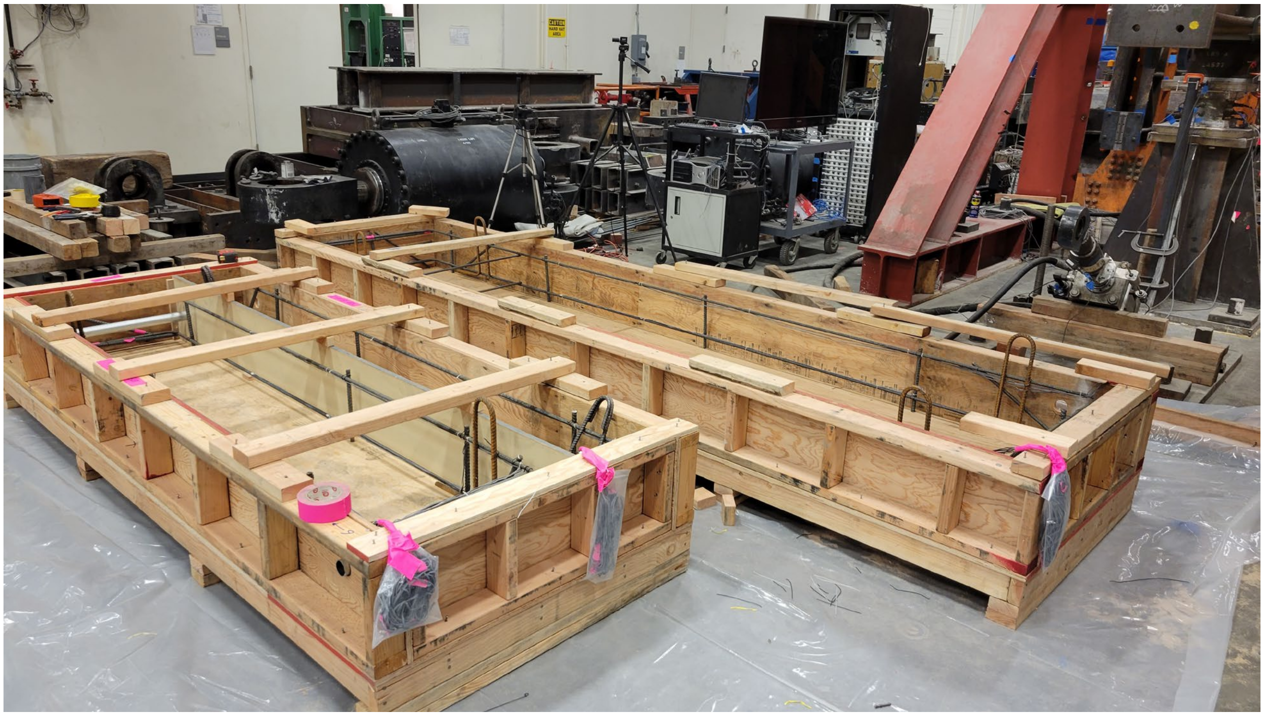

Figure A-74: Formwork for Companion Beams 1 and 2 on left, Companion Beam 3 on right

Figure A-75: Companion Beam 1 and 2 with hollow tubes (silver tubes) for stressing together

Figure A-76: Casting Companion Beams

Figure A-77: Troweling and finishing companion beams

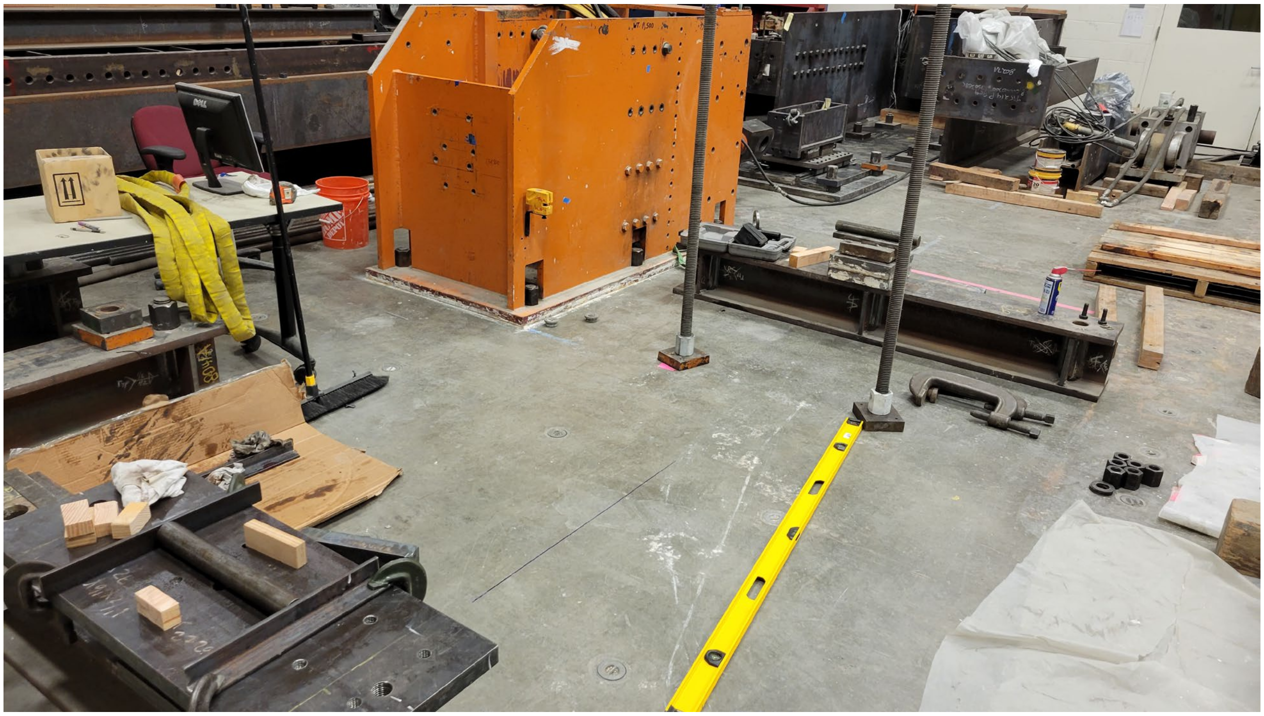

Figure A-78: Testing location for Companion Beams 1, 2, and 3. Supports can be freely relocated based on desired support location

Figure A-79: Load cell underneath support on long span to record shear force carried on the span

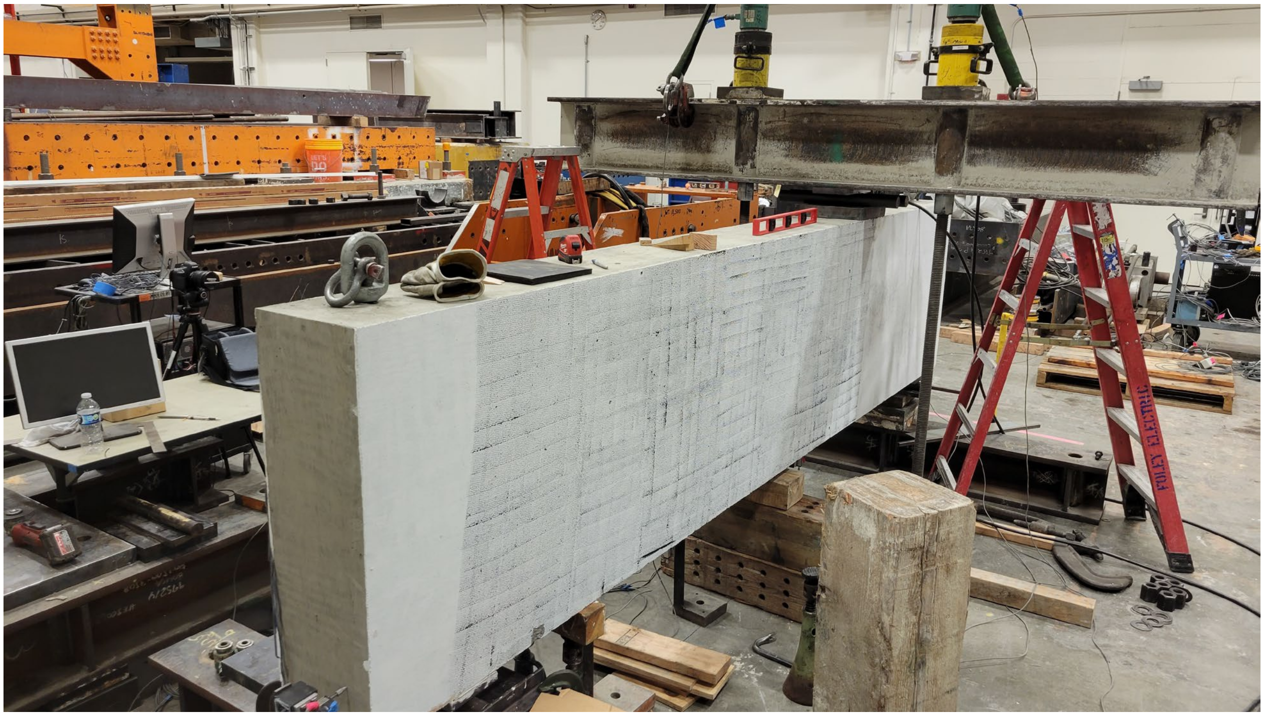

Figure A-80: Test setup with Companion Beam 3 in place

Figure J-1: Double roller setup for additional stability during loading. It was found that a single roller was unstable

Figure J-2: Compression zone of CB3 after failure. Failure cracked sheared through compression zone

Figure J-3: Dowel zone of CB3 after failure

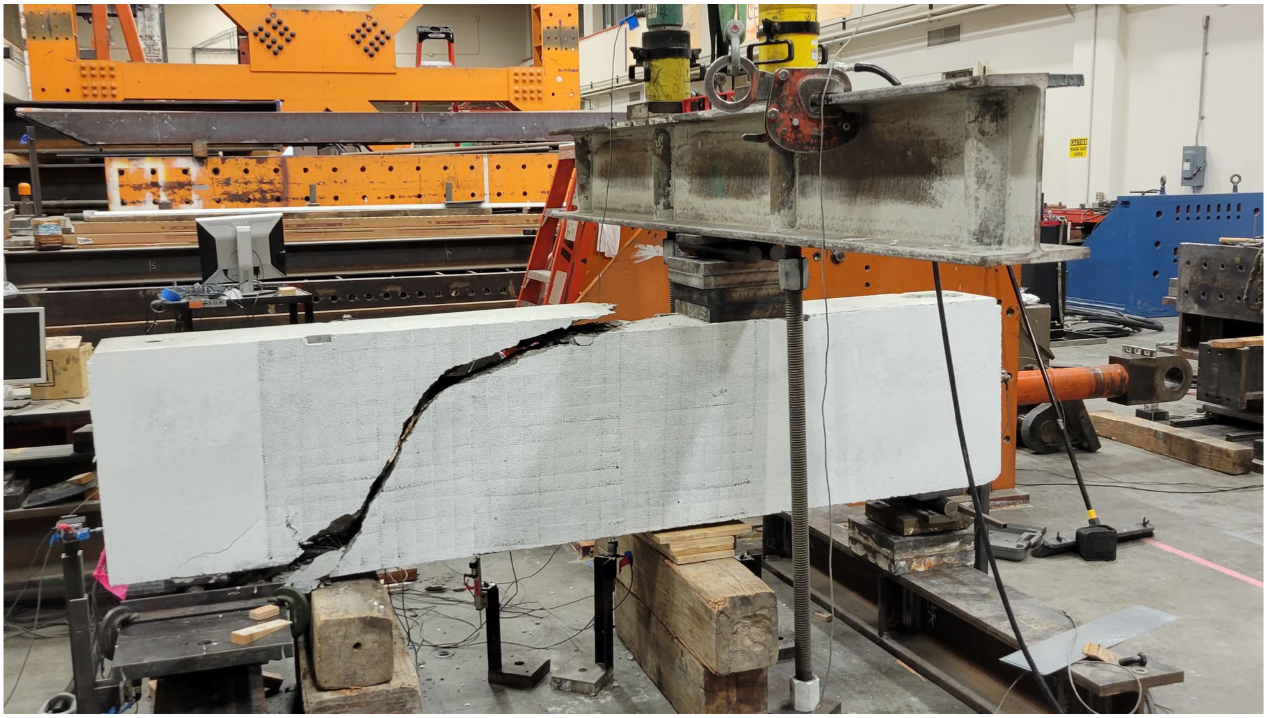

Figure J-4: Companion Beam 2 in test setup after failure

Figure J-5: Dowel zone of CB2 after failure

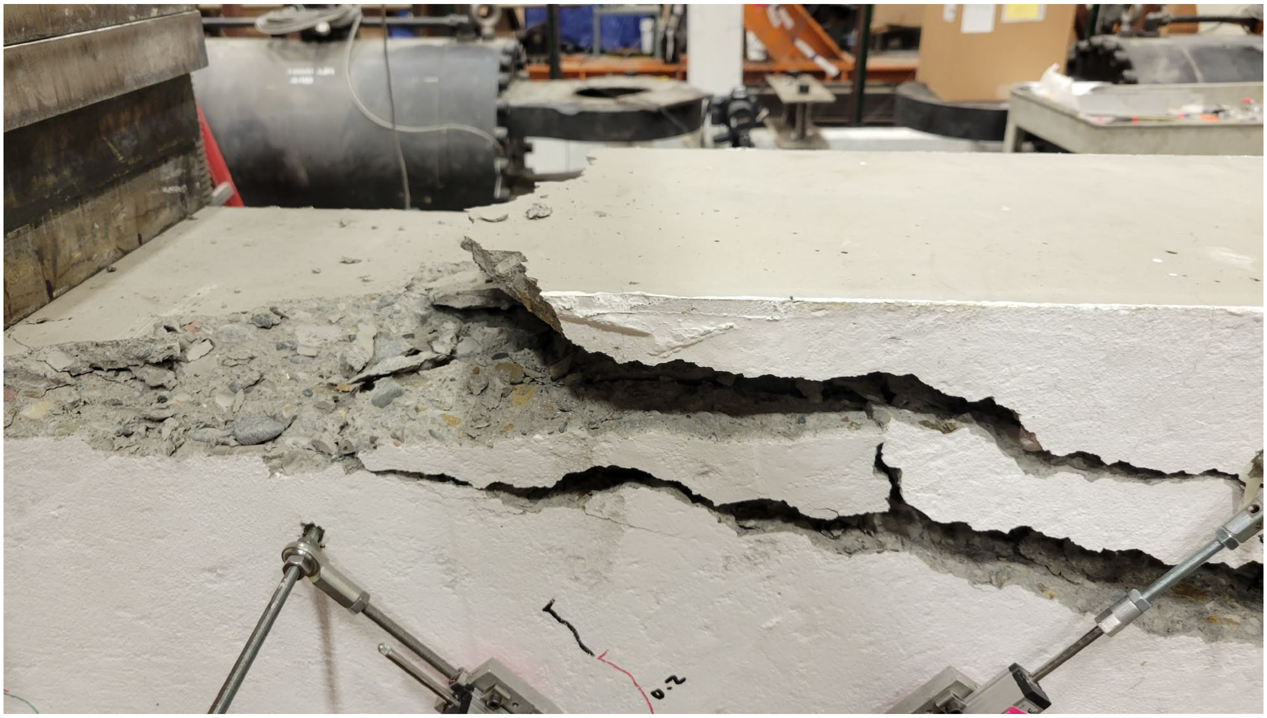

Figure J-6: Compression zone of CB2 after failure

Figure J-7: Companion Beam 1 in test setup

Figure J-8: Failure crack on short span in CB1

Figure J-9: Another view of failure crack in CB1 on short span

A.12. Data Documentation

This section contains all the data in plot form, including data that is not discussed but included for documentation. If uncertain which instrument the data refers to, please refer to the appropriate engineering drawings for phase of the referenced data.

A.12.1. Phase 1

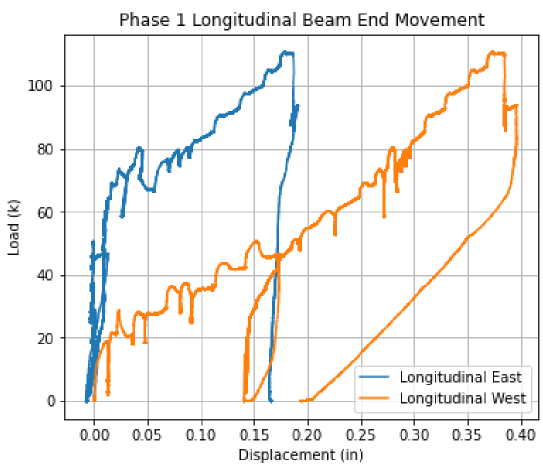

Figure K-1: Phase 1 Longitudinal beam end movement

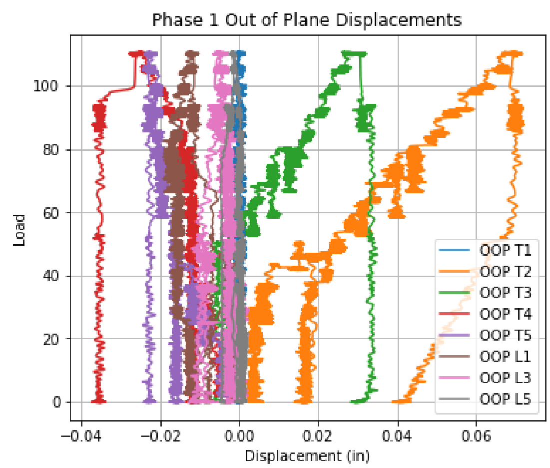

Figure K-2: Phase 1 out of plane displacements

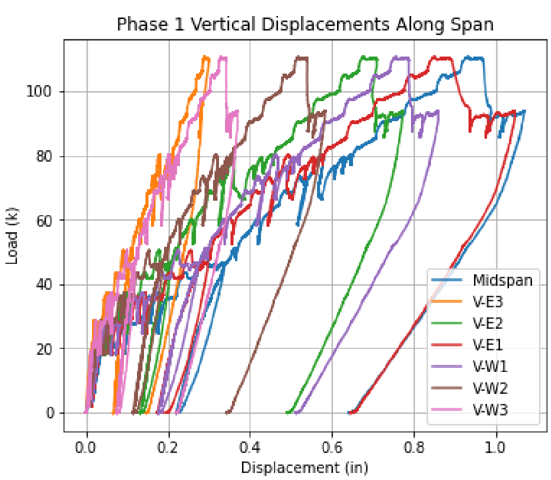

Figure K-3: Phase 1 vertical displacements along span

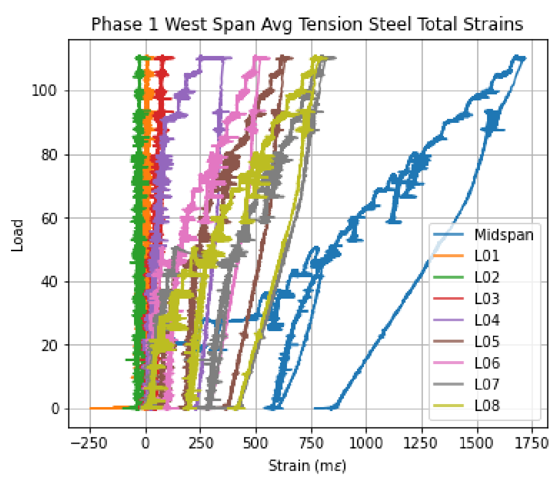

Figure K-4: Phase 1 west span average tension steel total strains

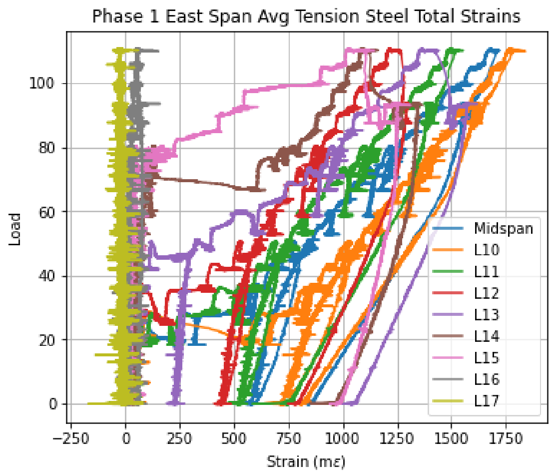

Figure K-5: Phase 1 east span average tension steel total strains

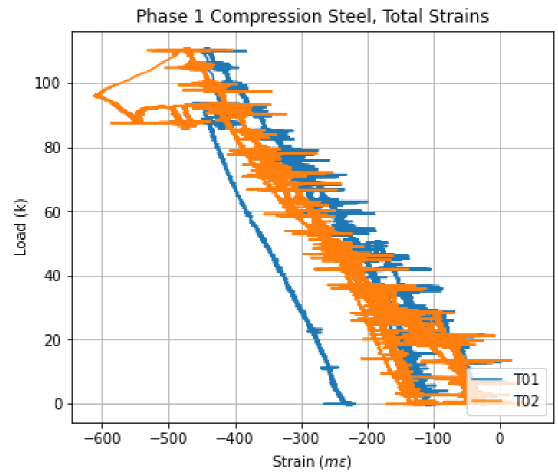

Figure K-6: Phase 1 average compression steel total strains

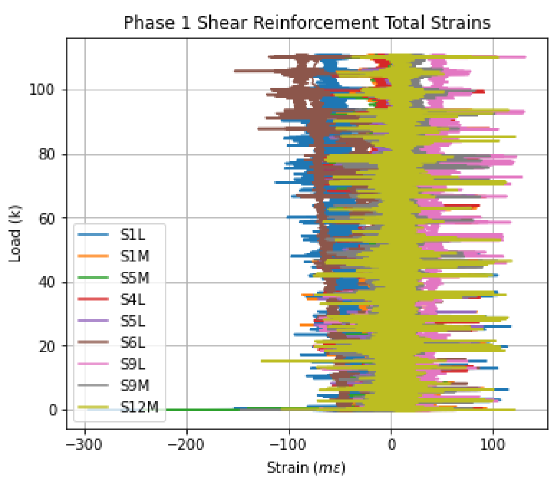

Figure K-7: Phase 1 shear reinforcement strains

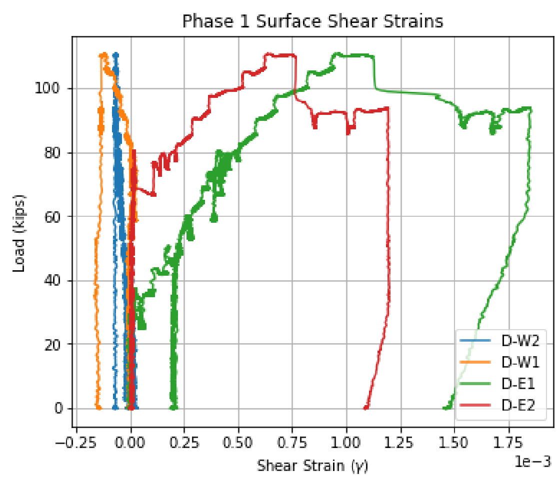

Figure K-8: Phase 1 surface shear strains

Figure K-9: Phase 1, Load Stage 1

Figure K-10: Phase 1, Load Stage 2

Figure K-11: Phase 1, Load Stage 3

Figure K-12: Phase 1, Load Stage 4

Figure K-13: Phase 1, Load Stage 5

Figure K-14: Phase 1, Load Stage 6

Figure K-15: Phase 1, Load Stage 7a

Figure K-16: Phase 1, Load Stage 7b

A.12.2. Phase 2

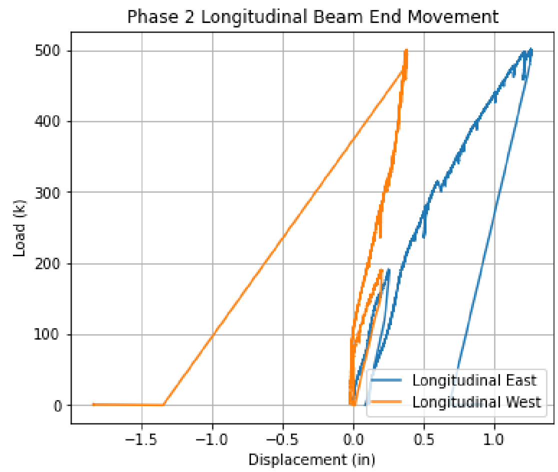

Figure K-17: Phase 2 longitudinal beam end movement

Figure K-18: Phase 2 out of plane movement

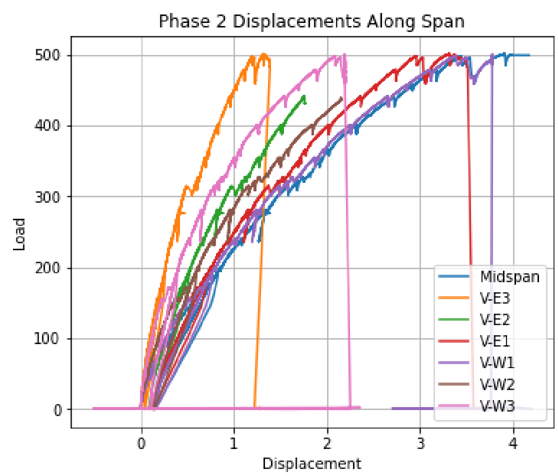

Figure K-19: Vertical displacement along span

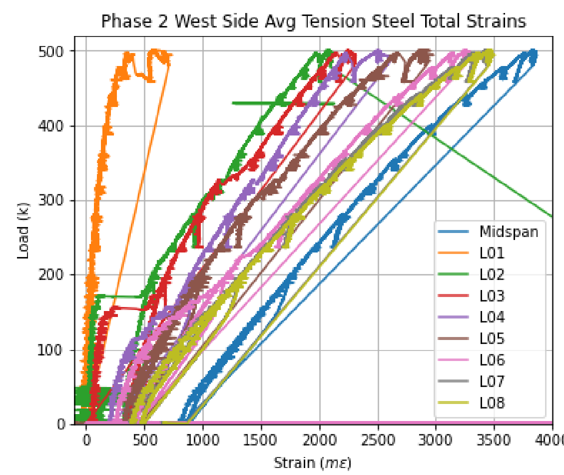

Figure K-20: Phase 2 west side average tension steel total strains

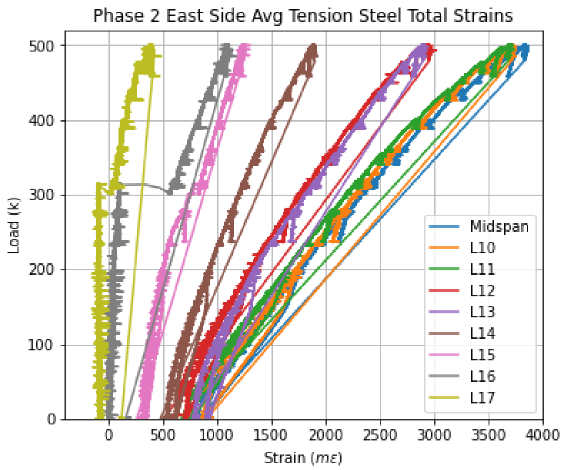

Figure K-21: Phase 2 east side average tension steel total strains

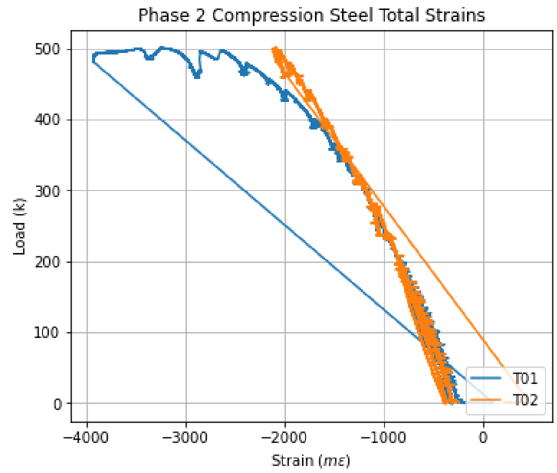

Figure K-22: Phase 2 average compression steel strains

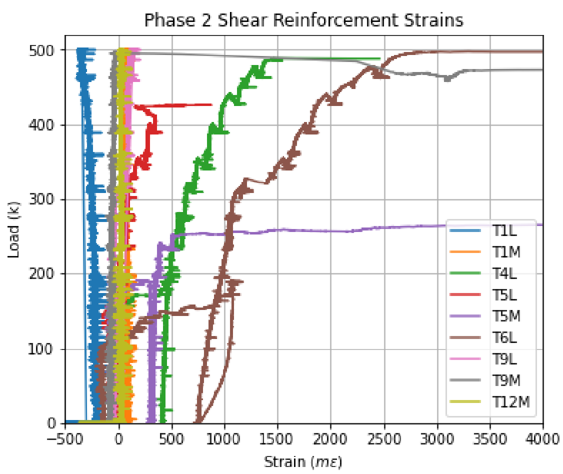

Figure K-23: Phase 2 shear reinforcement strains

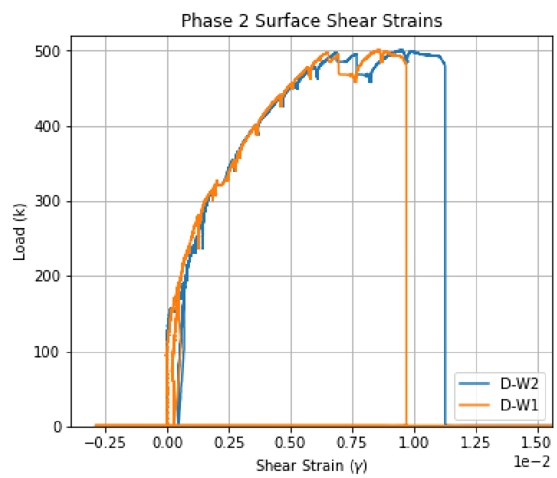

Figure K-24: Phase 2 shear strains

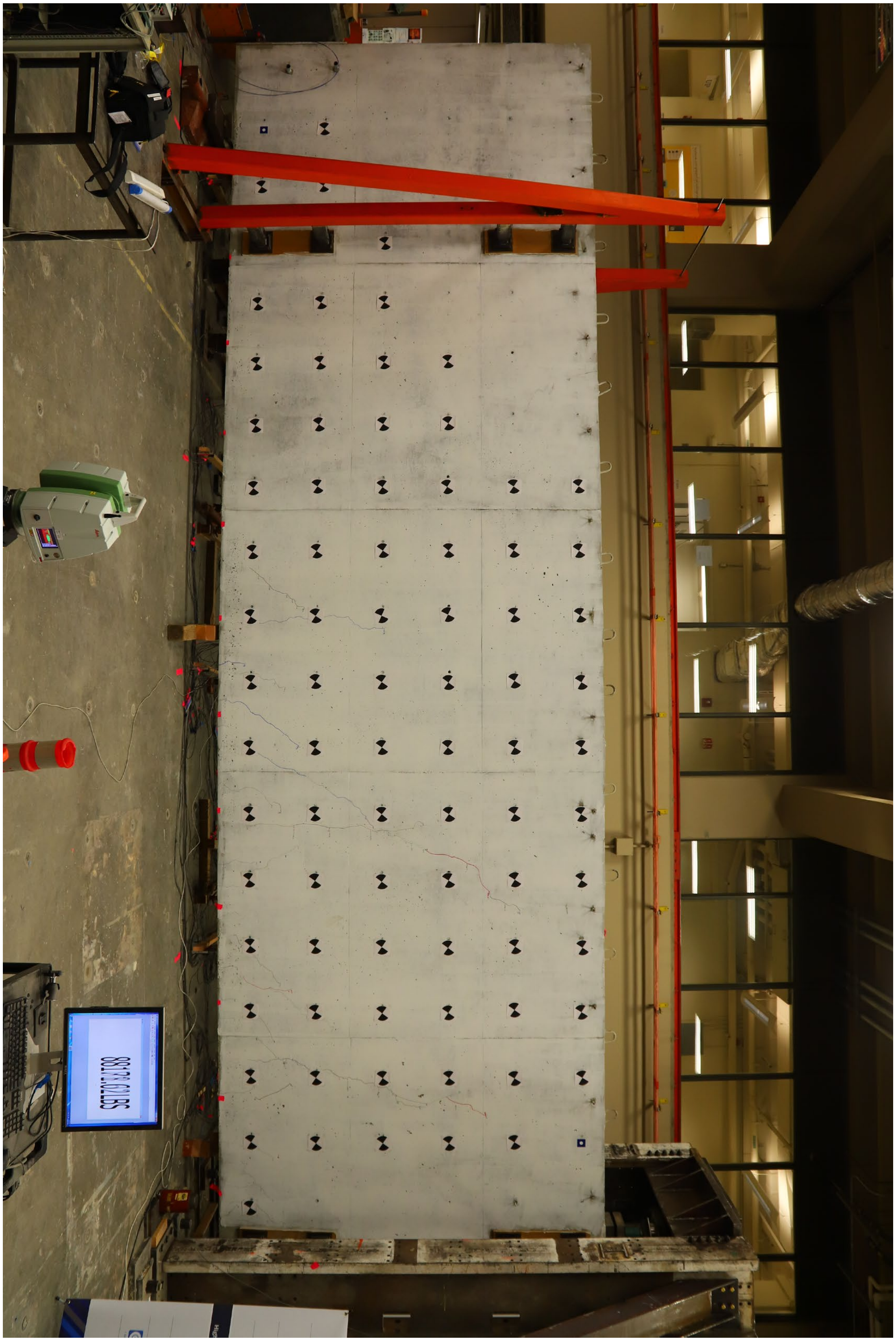

Figure K-25: Phase 2, Load Stage 8

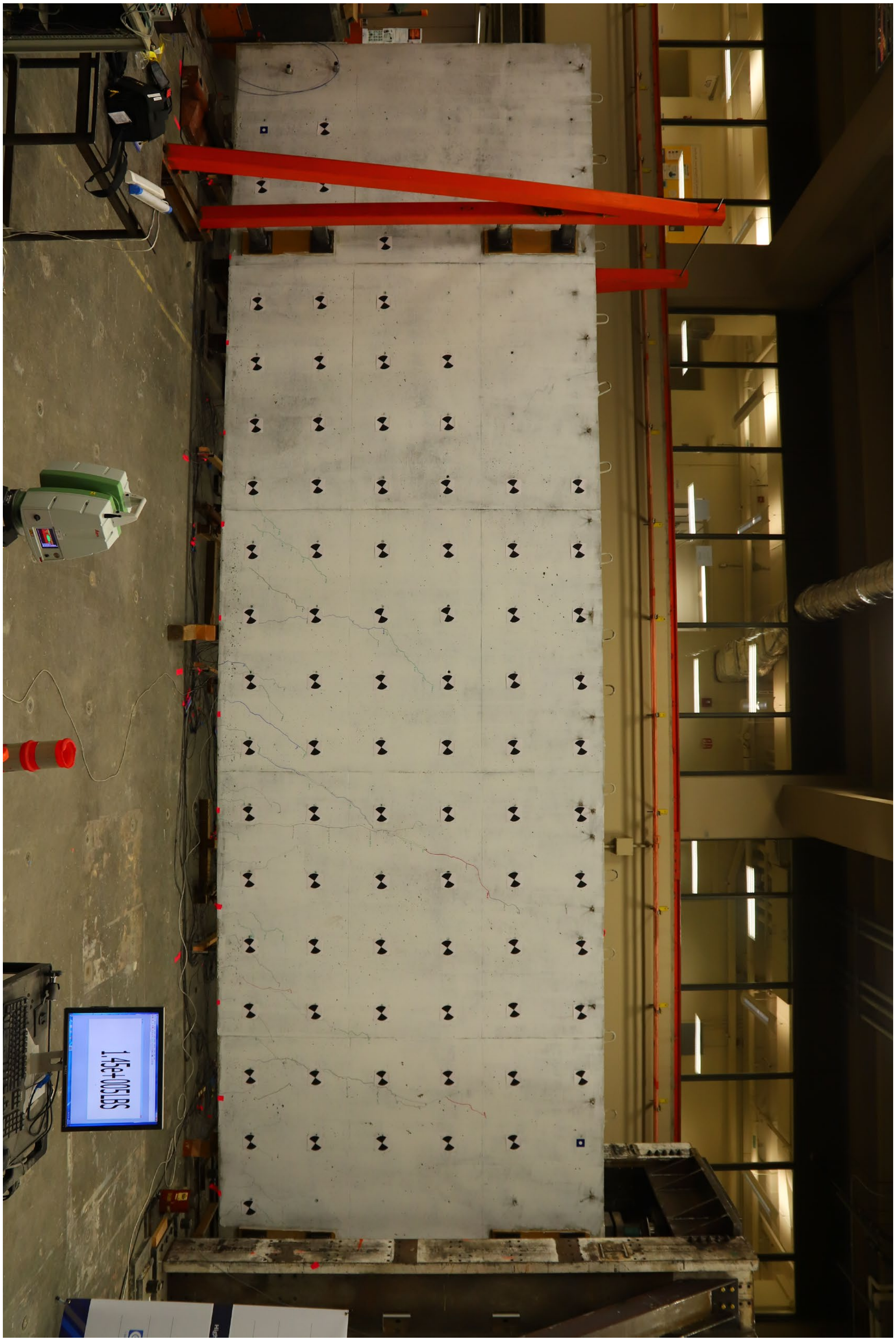

Figure K-26: Phase 2, Load Stage 9

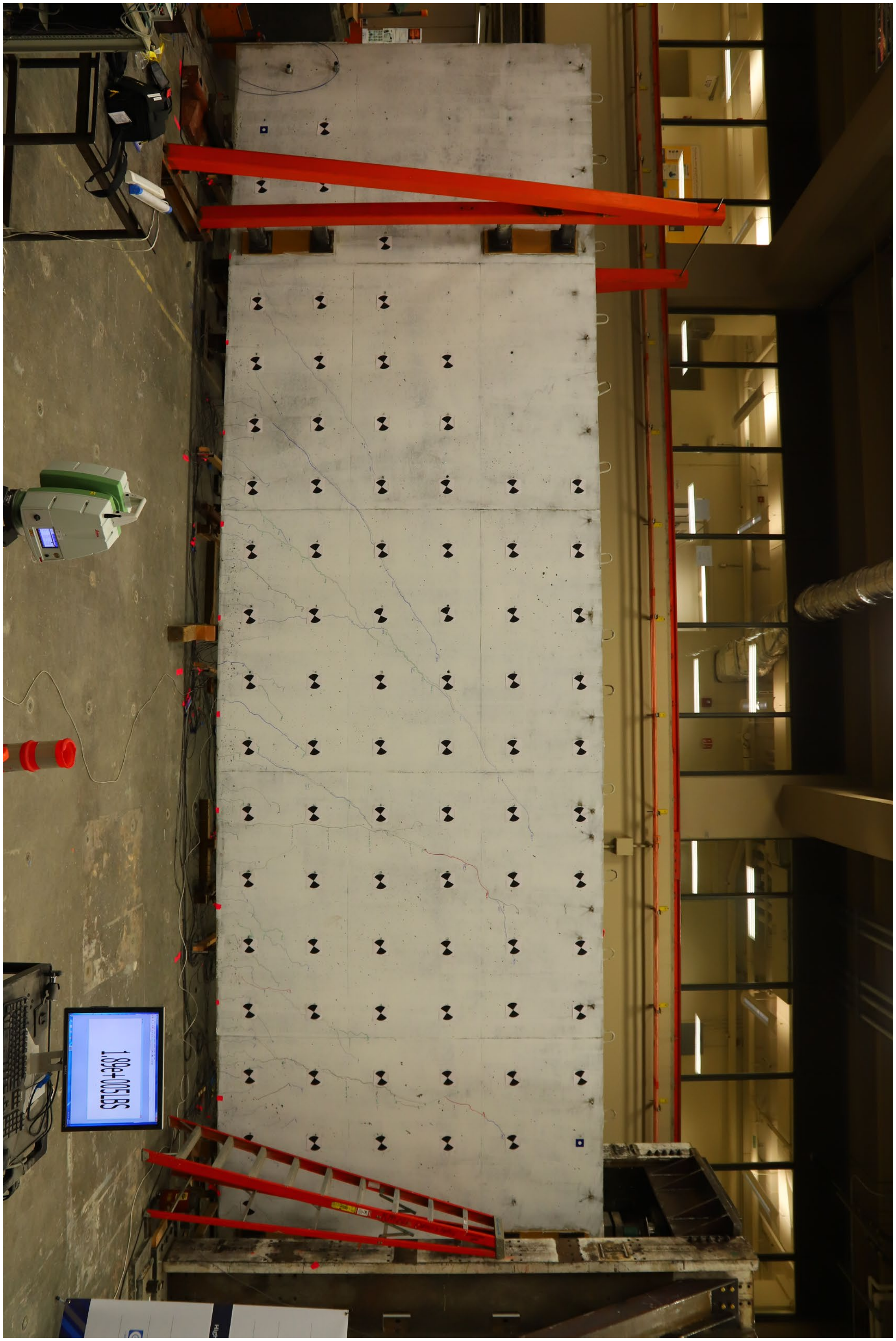

Figure K-27: Phase 2, Load Stage 10

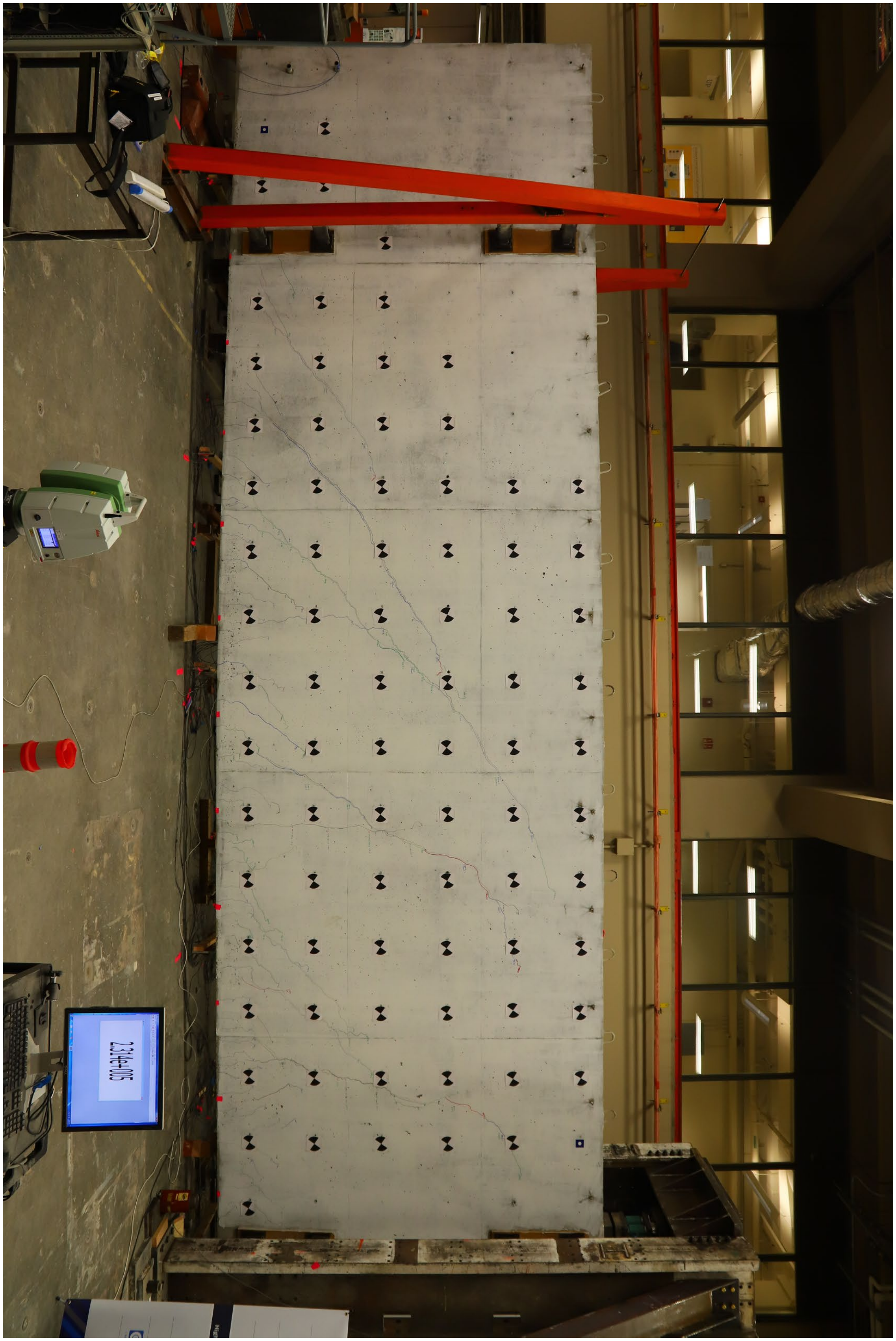

Figure K-28: Phase 2, Load Stage 11

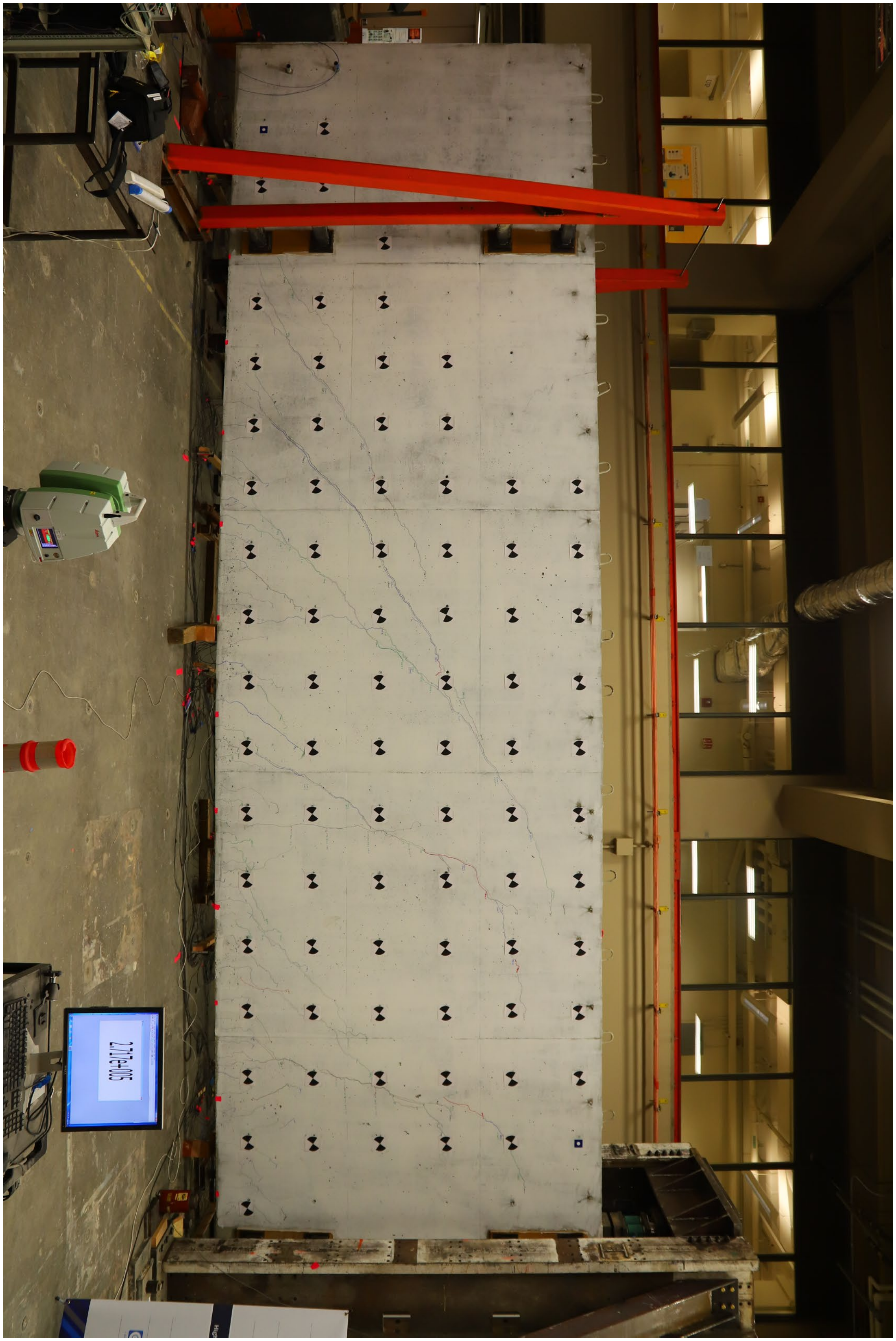

Figure K-29: Phase 2, Load Stage 12

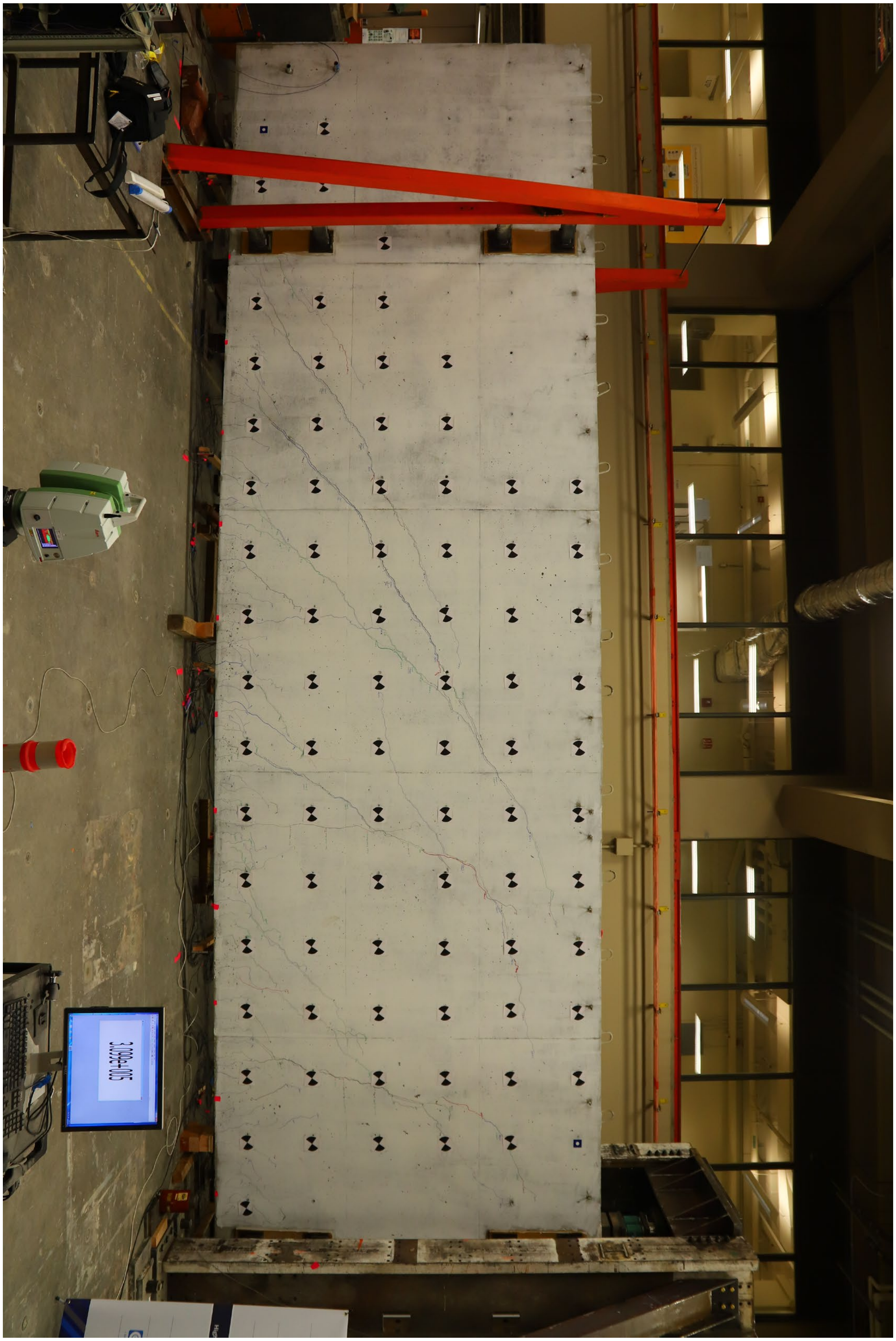

Figure K-30: Phase 2, Load Stage 13

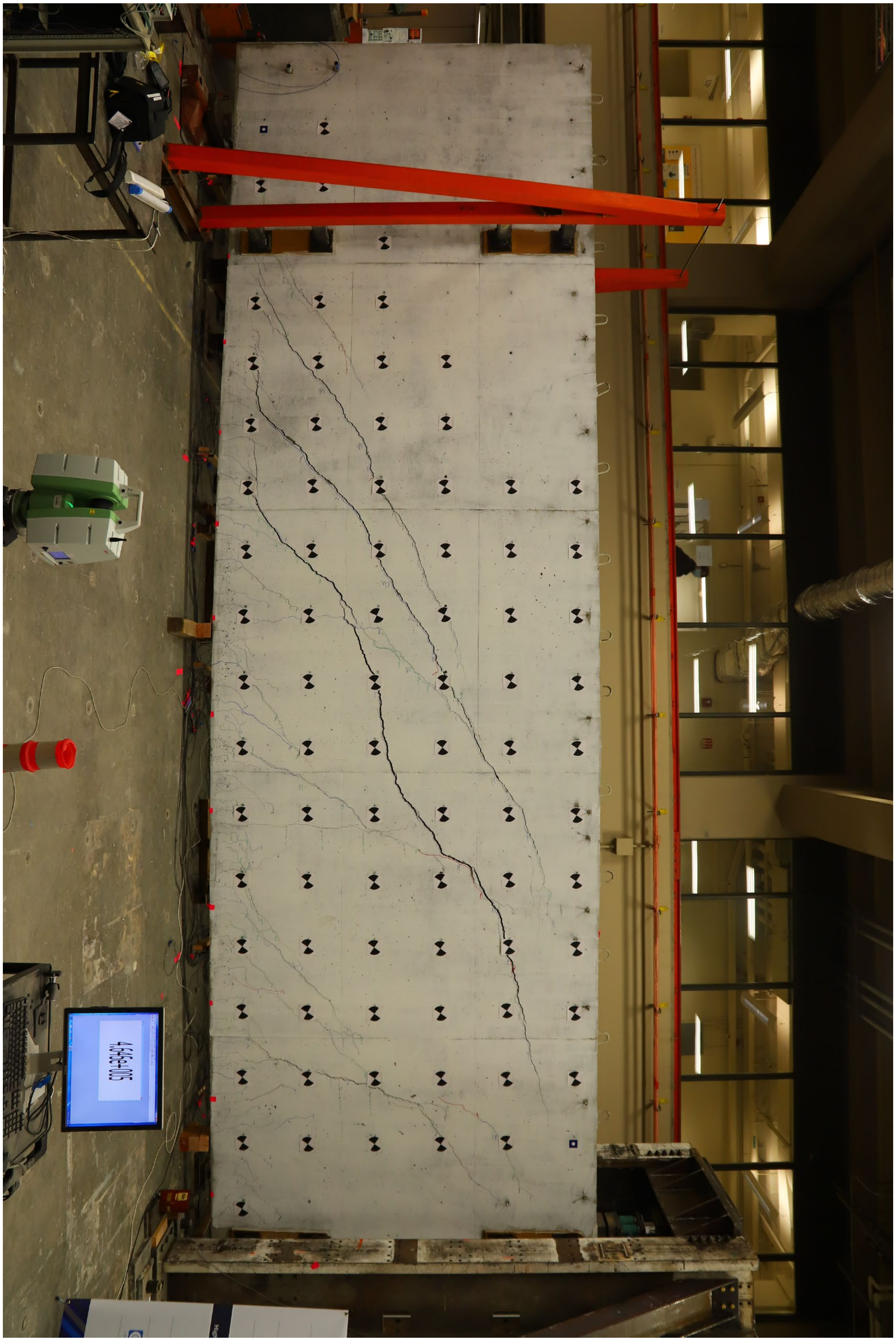

Figure K-31: Phase 2, Load Stage 14

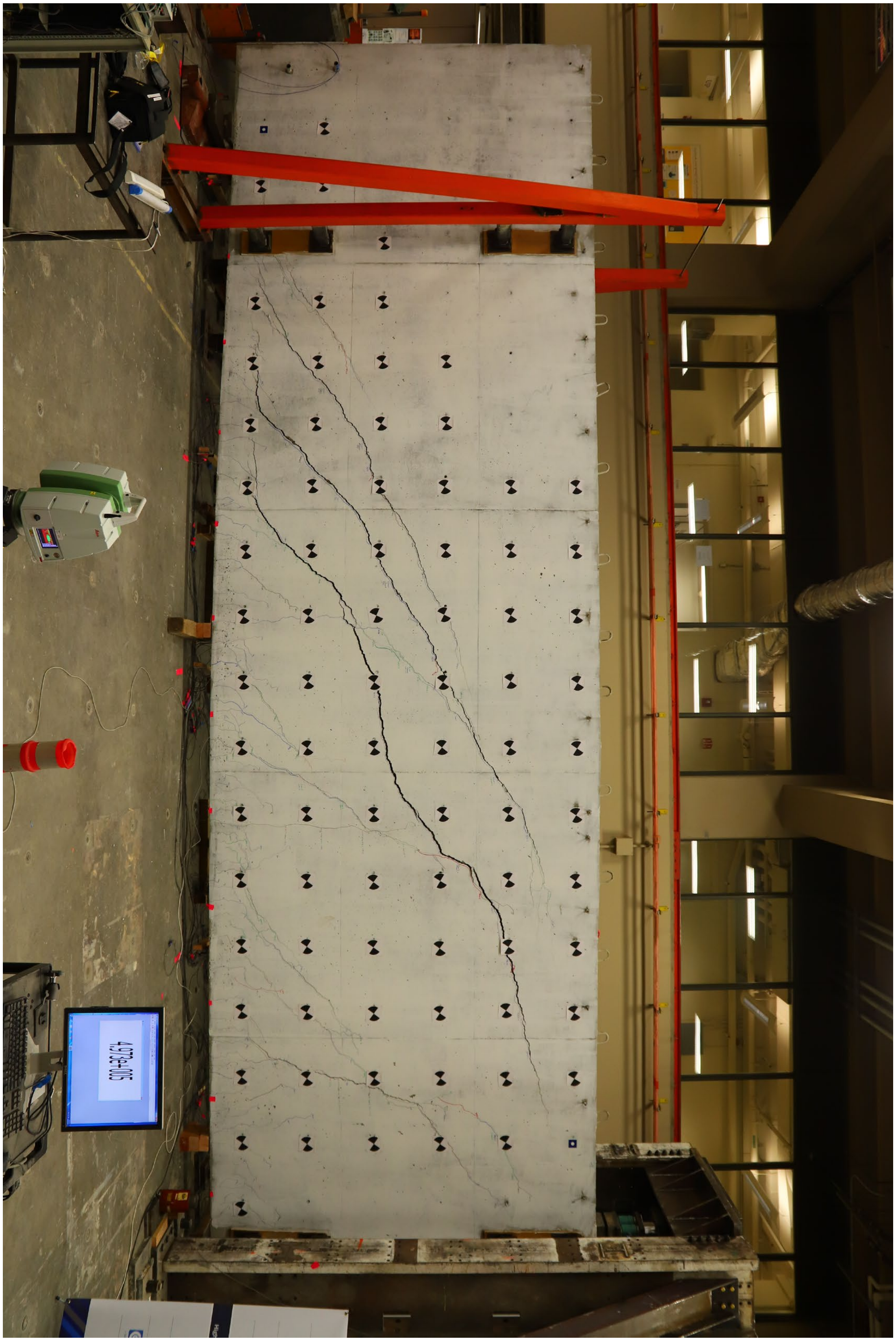

Figure K-32: Phase 2, Load Stage 15a

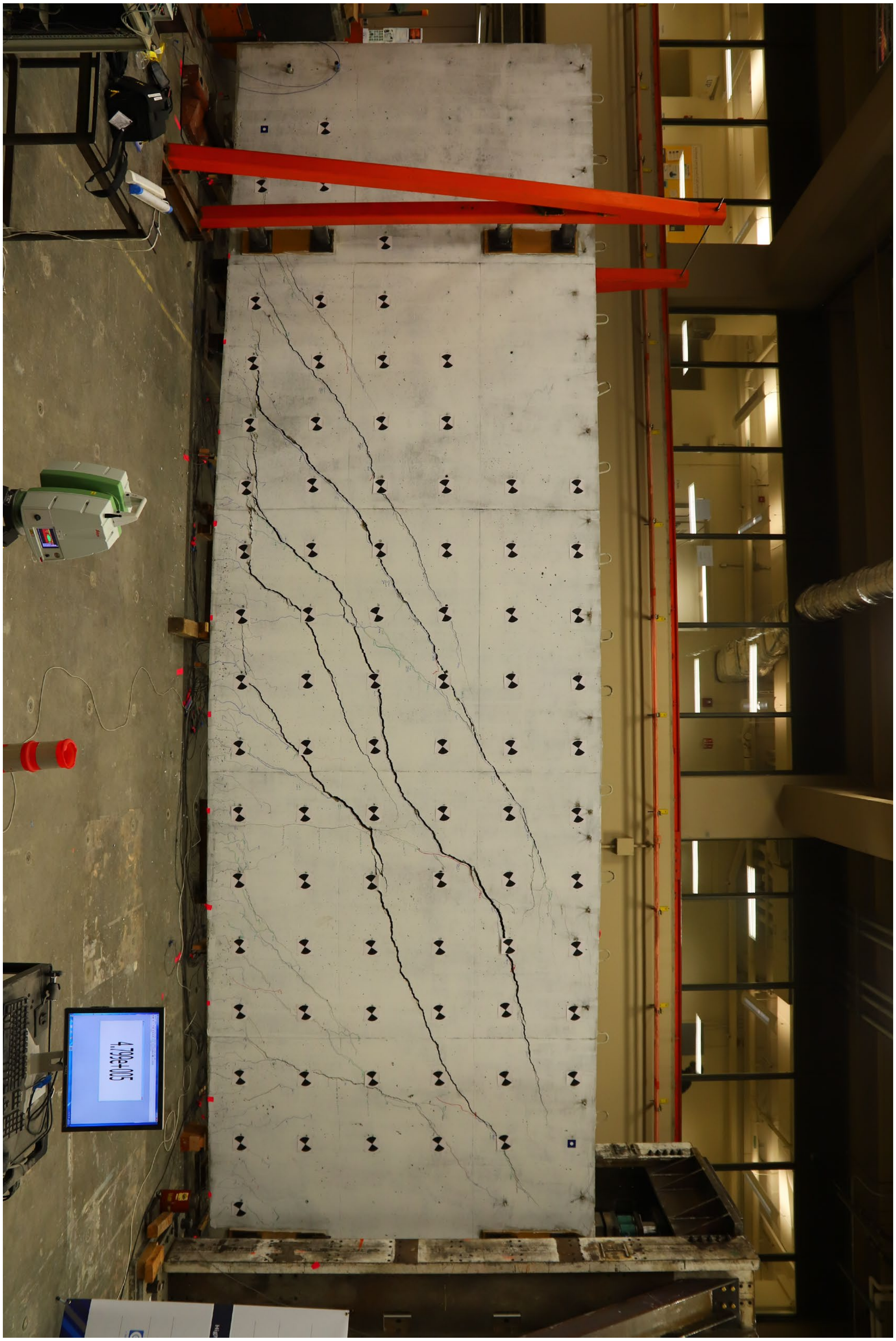

Figure K-33: Phase 2, Load Stage 15b

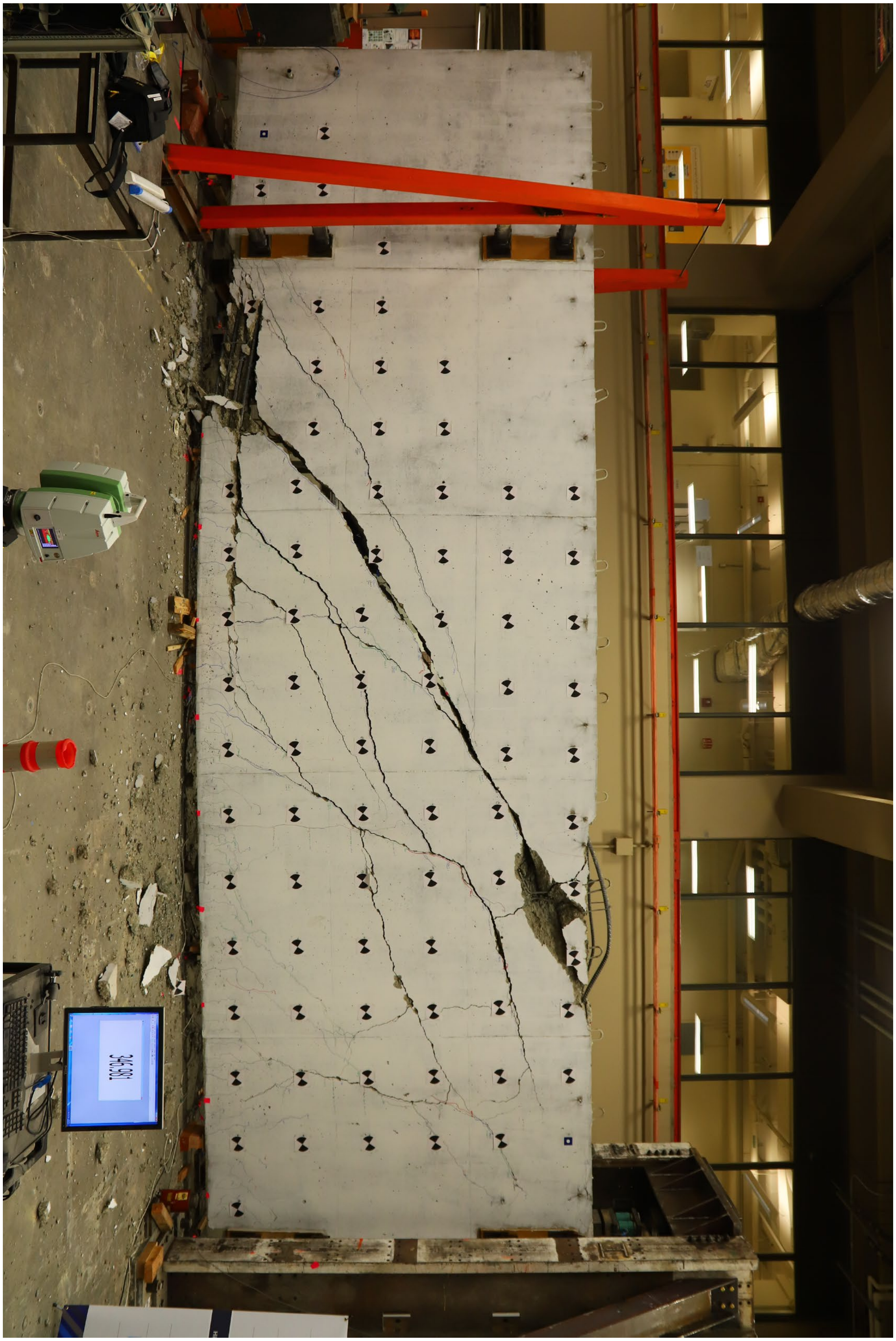

Figure K-34: Phase 2, Failure

A.12.3.<u>Phase 3</u>

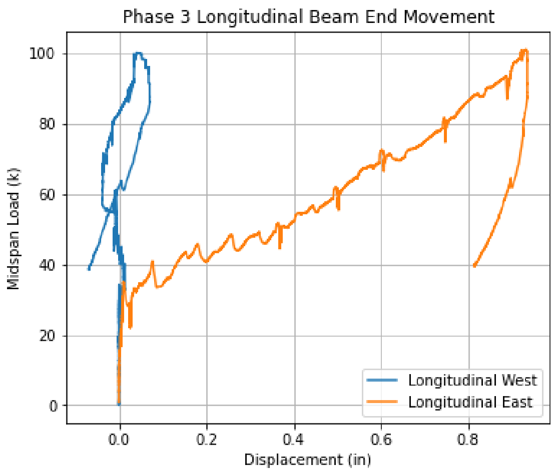

Figure K-35: Phase 3 longitudinal beam end movement

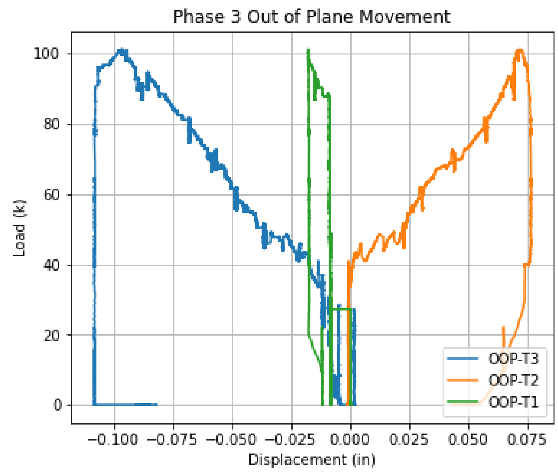

Figure K-36: Phase 3 out of plane movement

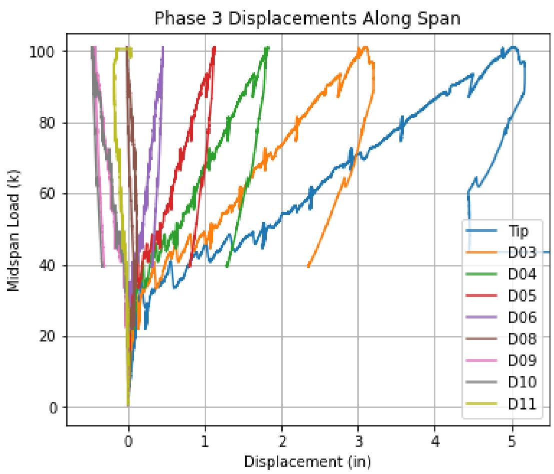

Figure K-37: Phase 3 displacements along span

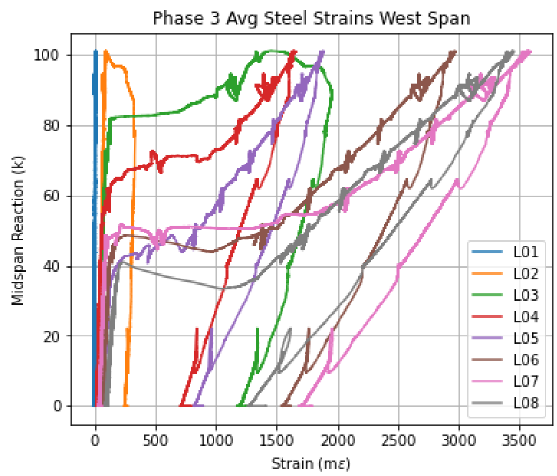

Figure K-38: Phase 3 average tension steel strains on west span

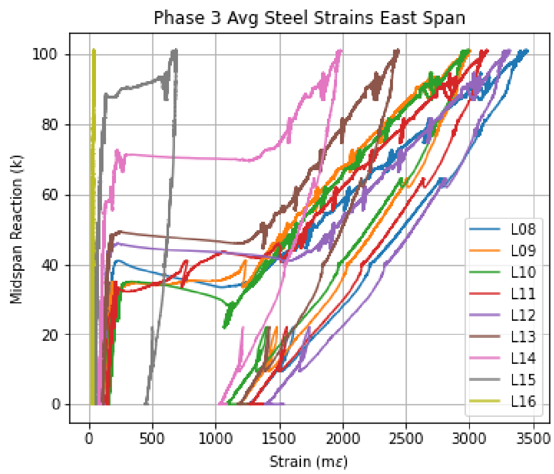

Figure K-39: Phase 3 average tension steel strains on east span

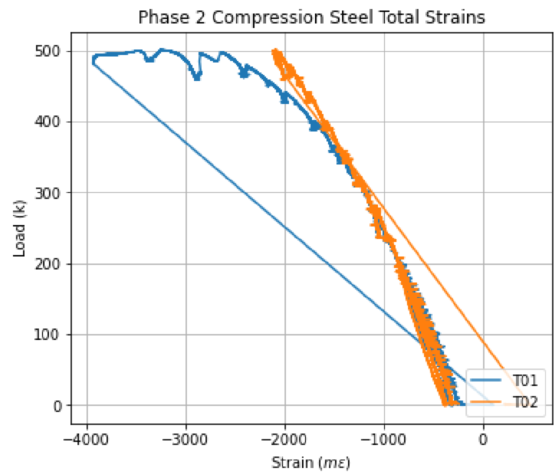

Figure K-40: Phase 3 average compression steel strains

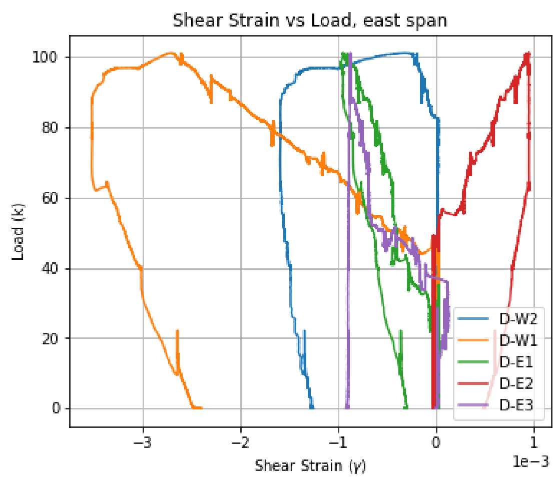

Figure K-41: Phase 3 surface shear strains

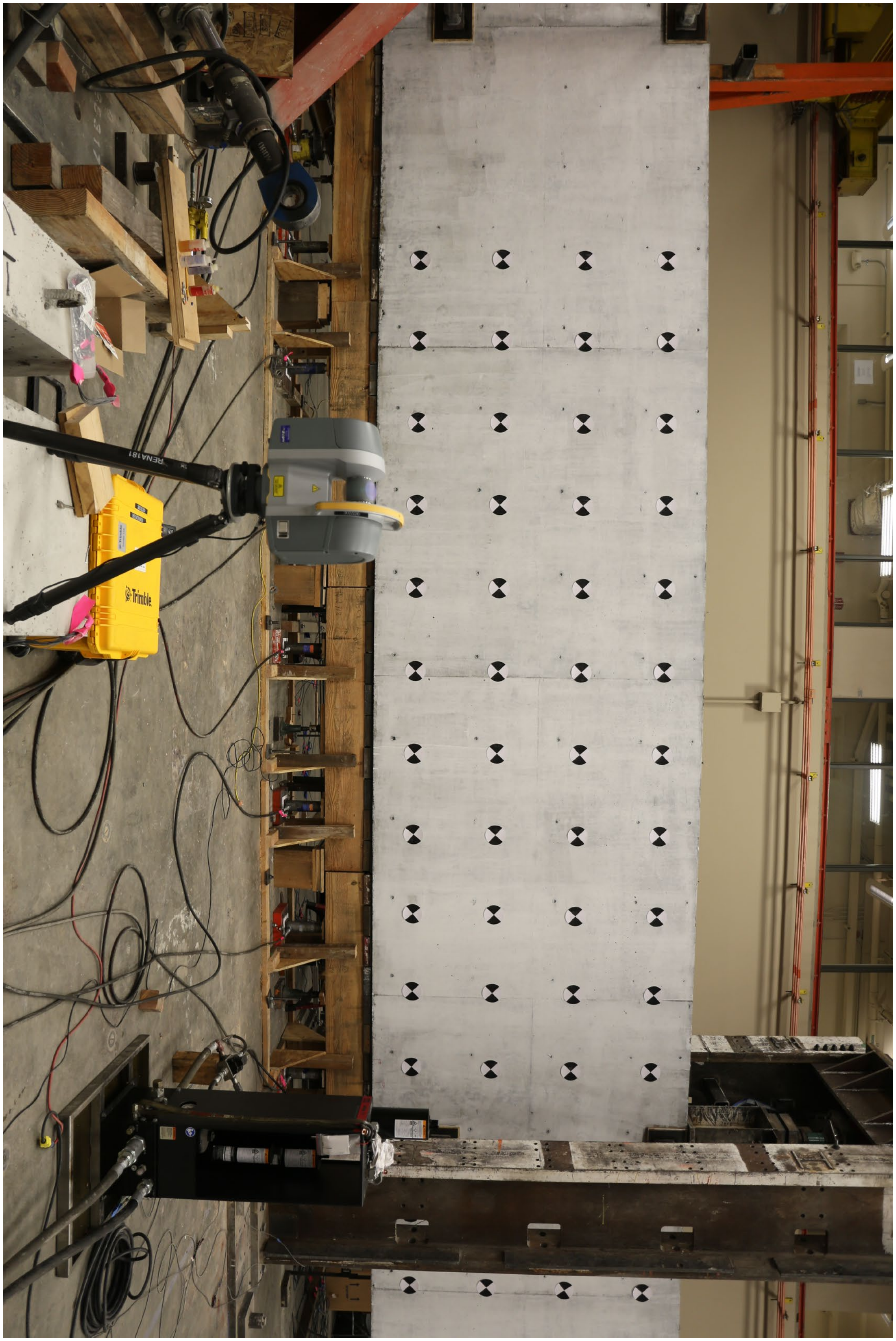

Figure K-42: Phase 3, Load Stage 1

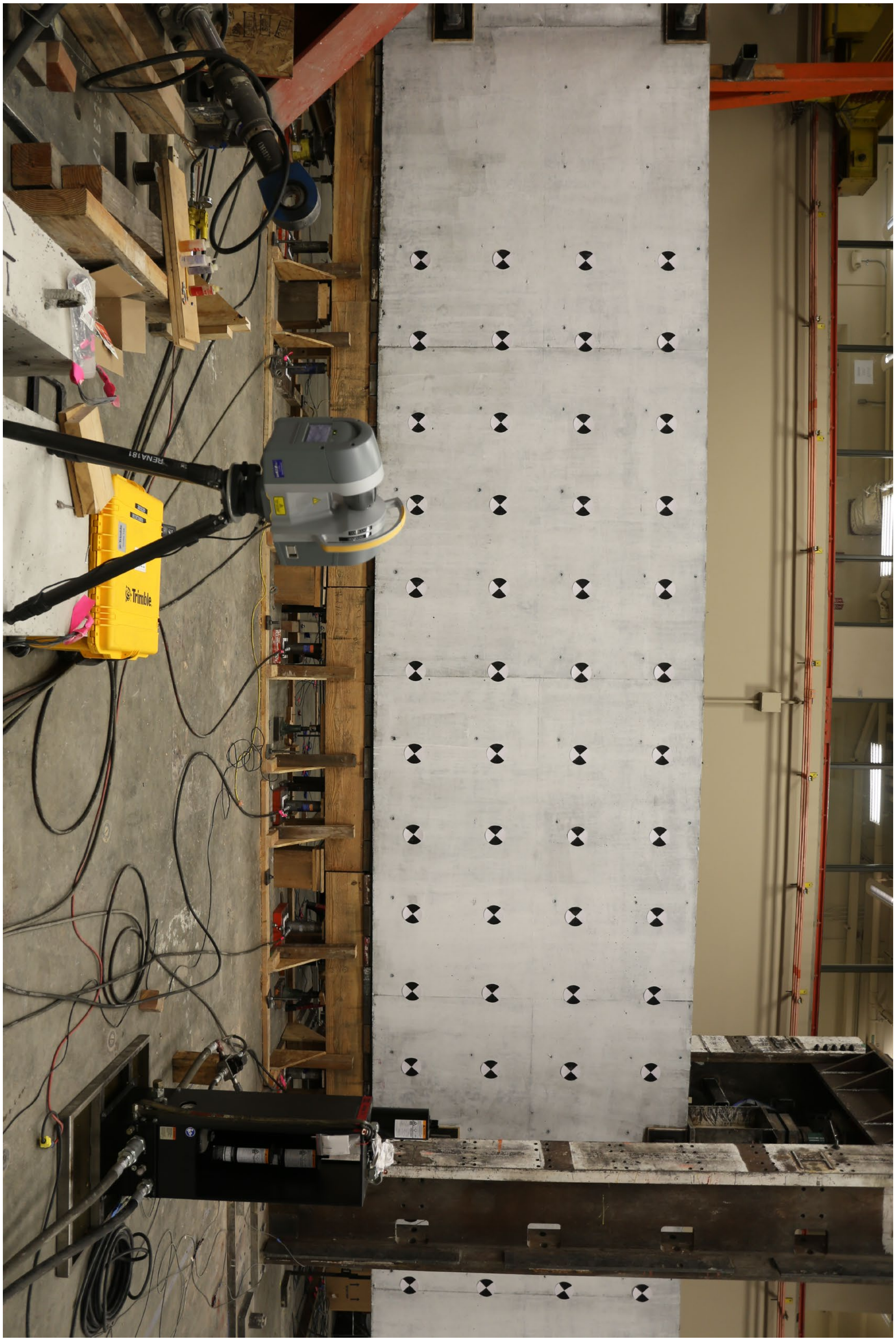

Figure K-43: Phase 3, Load Stage 2

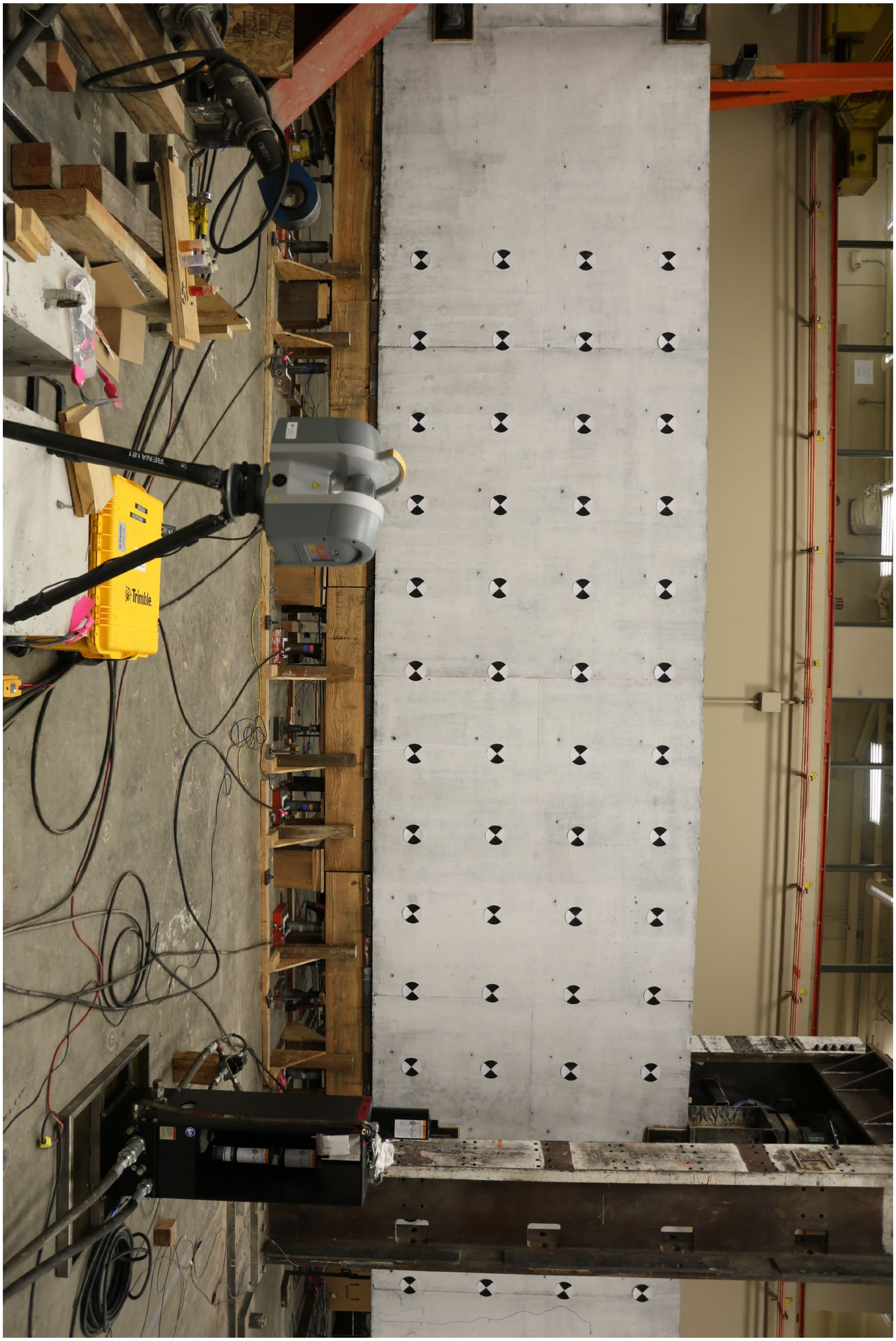

Figure K-44: Phase 3, Load Stage 3

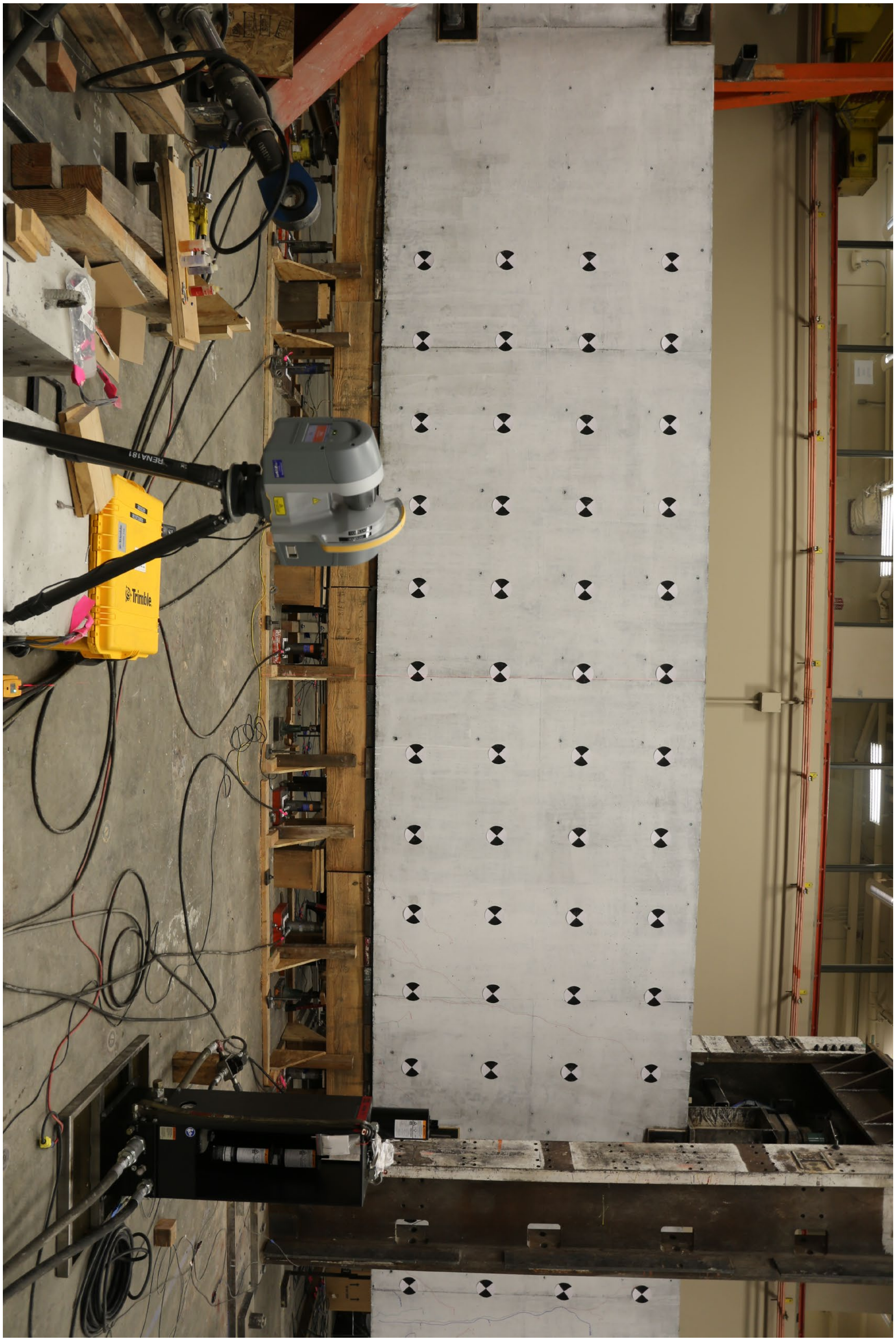

Figure K-45: Phase 3, Load Stage 4

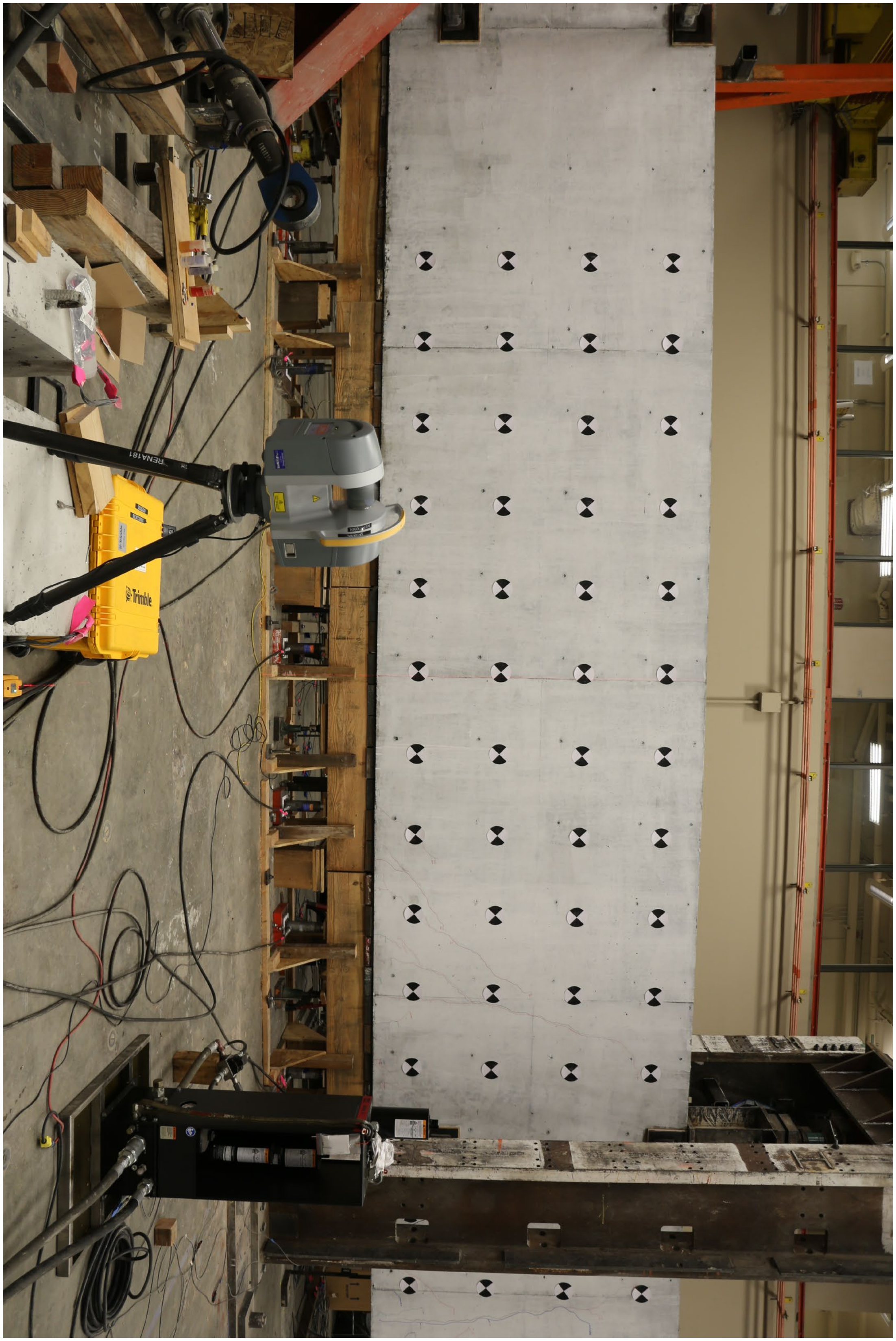

Figure K-46: Phase 3, Load Stage 5

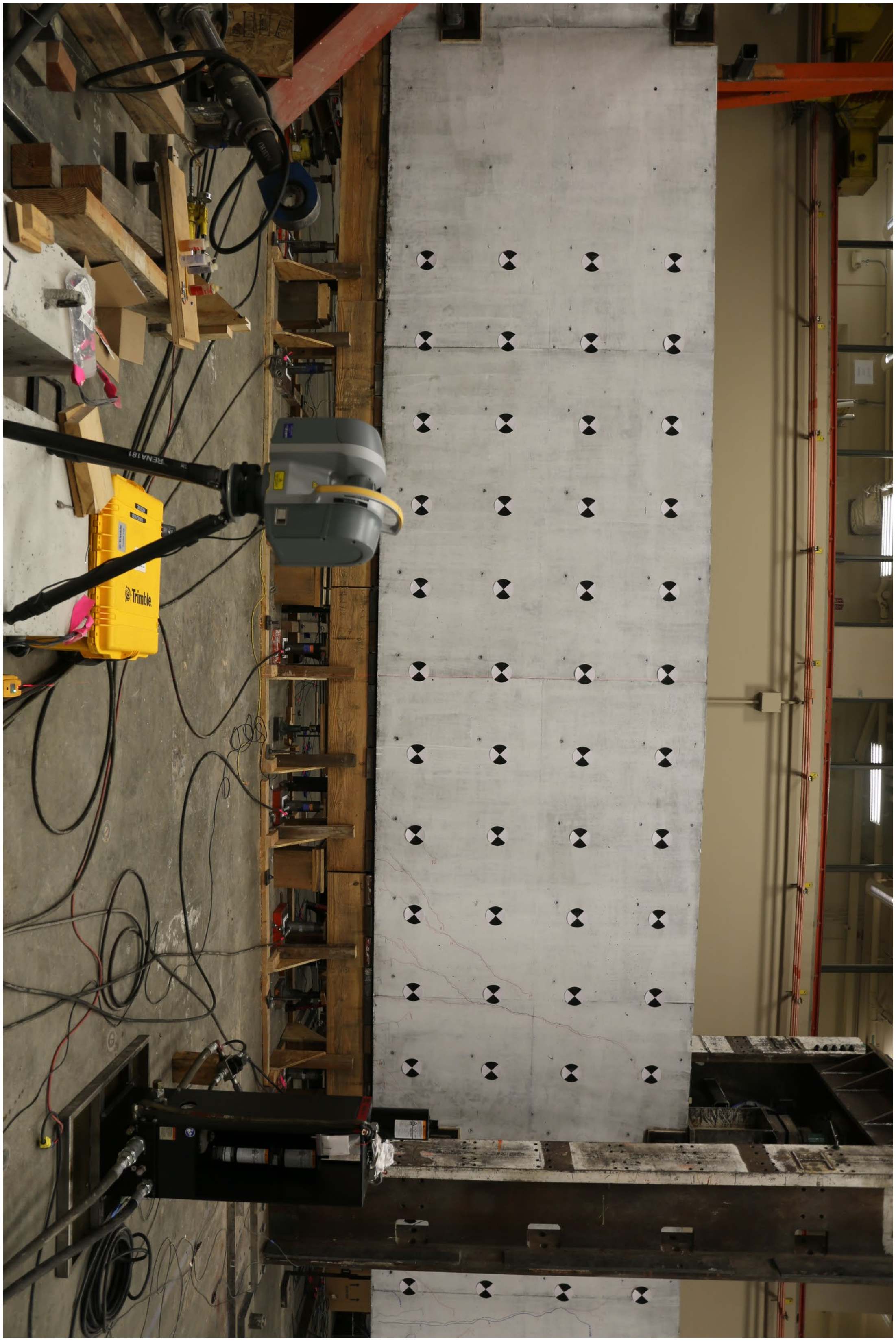

Figure K-47: Phase 3, Load Stage 6

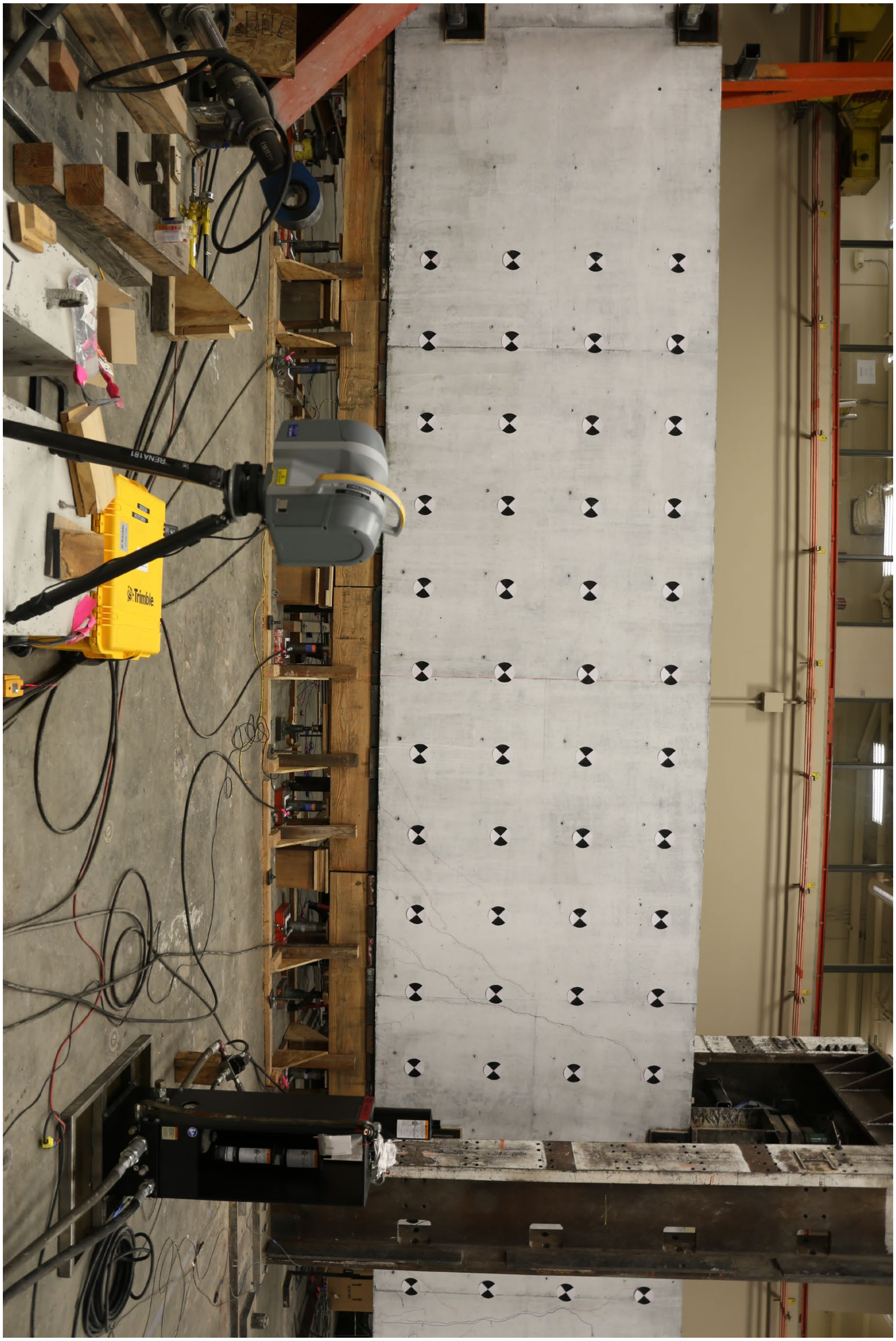

Figure K-48: Phase 3, Load Stage 7

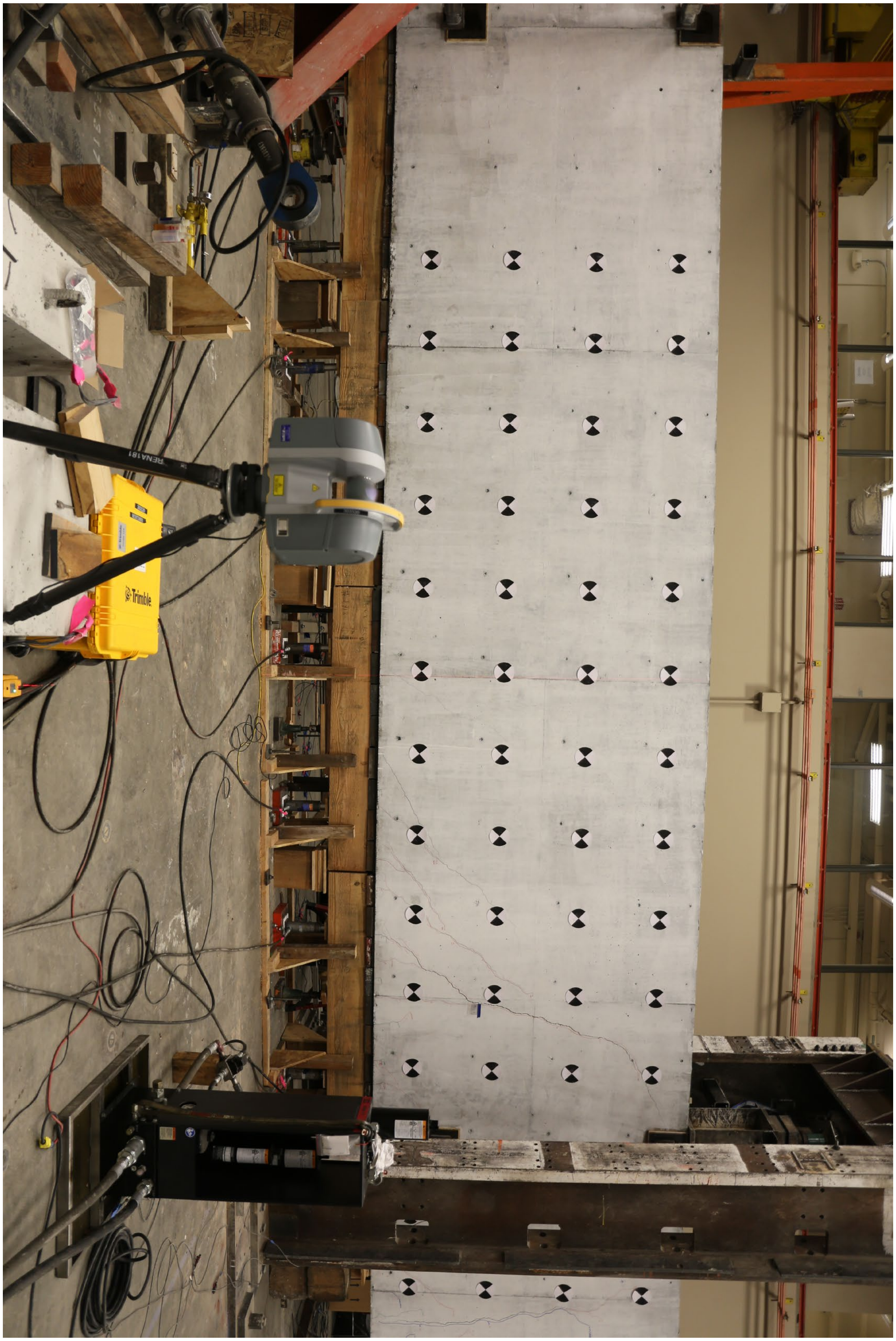

Figure K-49: Phase 3, Load Stage 8a

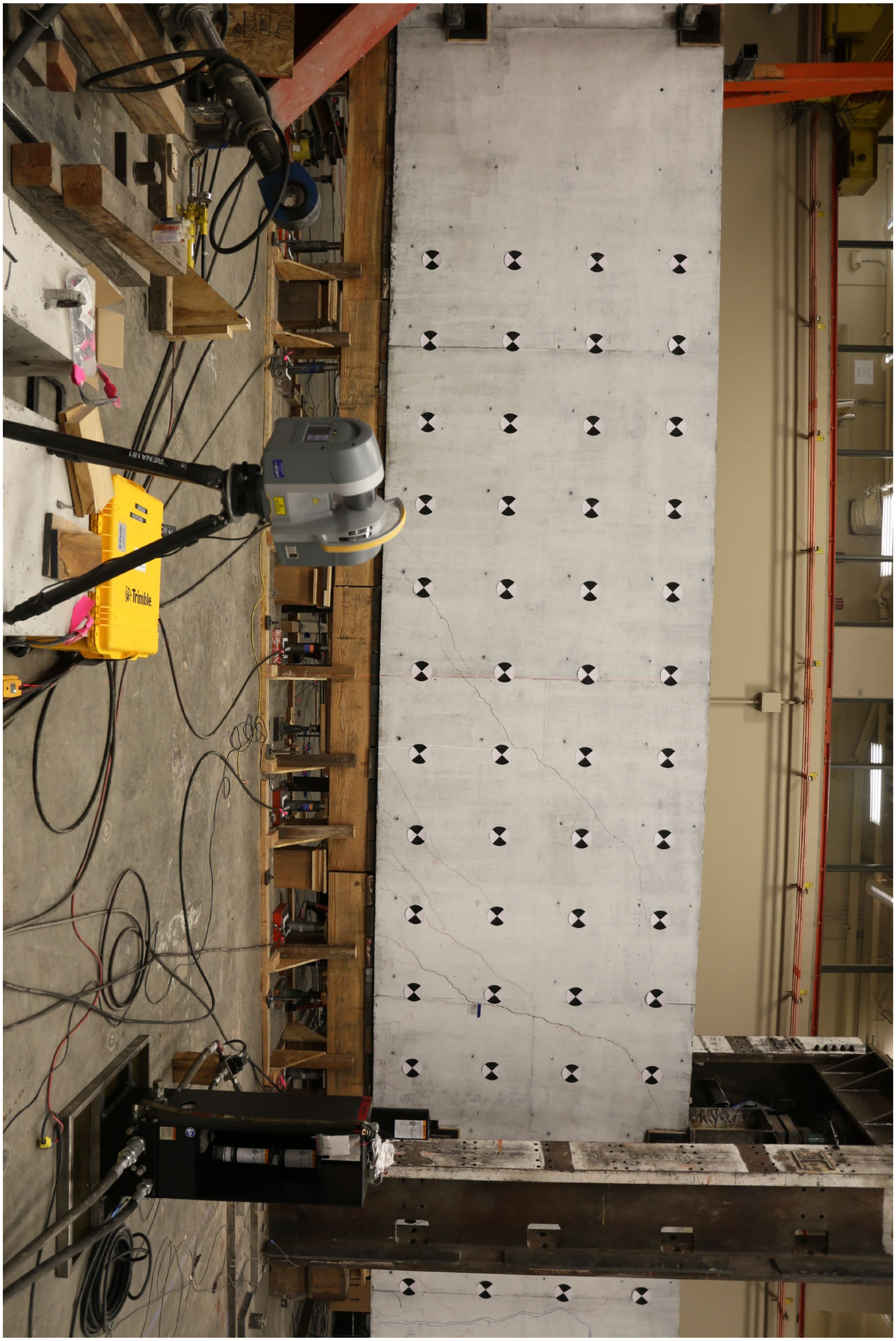

Figure K-50: Phase 3, Load Stage 8b

A.12.4. Phase 4

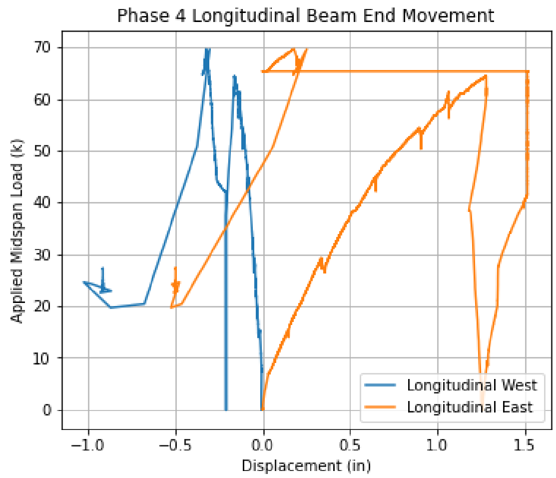

Figure K-51: Phase 4 longitudinal beam end movement (some errors due to very large longitudinal movements resulted in instruments bottoming out)

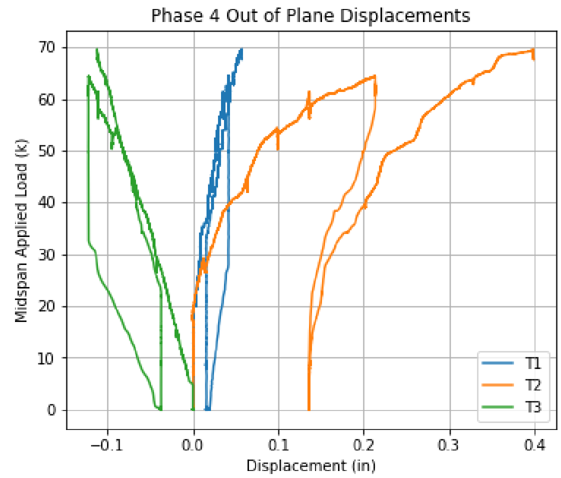

Figure K-52: Phase 4 out of plane displacements

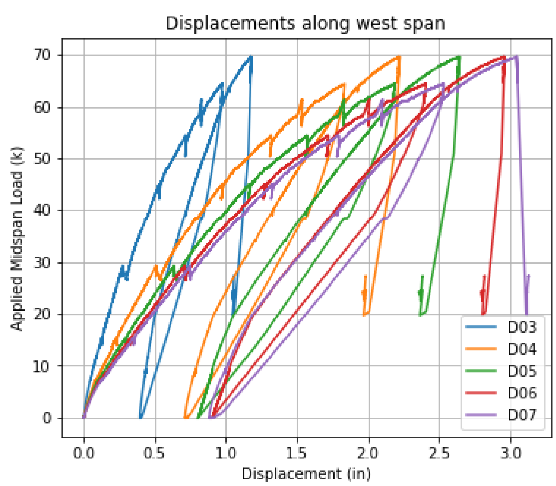

Figure K-53: Phase 4 vertical displacements along west span (some errors due to very large longitudinal movements resulted in instruments sliding off the displacement measuring mount)

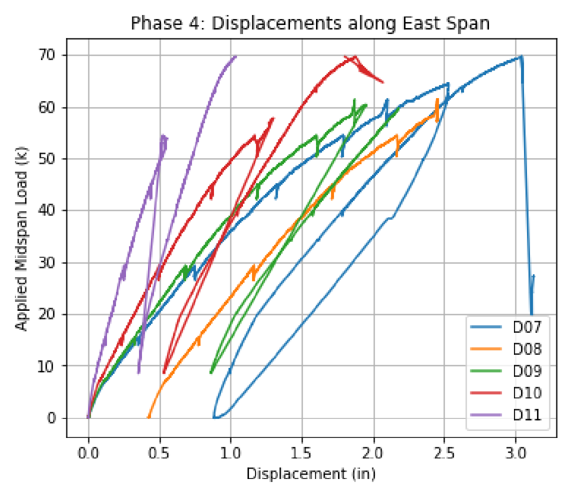

Figure K-54: Phase 4 vertical displacements along east span (some errors due to very large longitudinal movements resulted in instruments sliding off the displacement measuring mount)

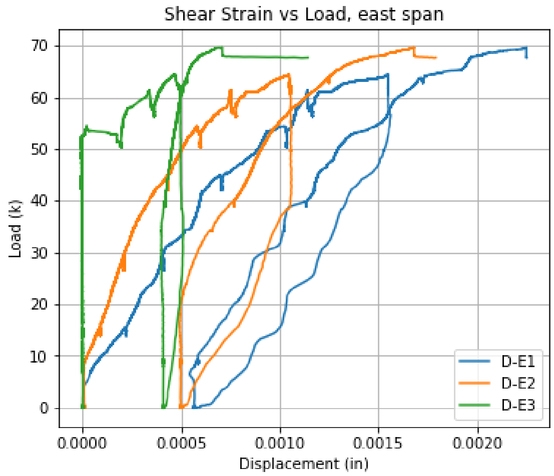

Figure K-55: Phase 4 shear strains on panel zones

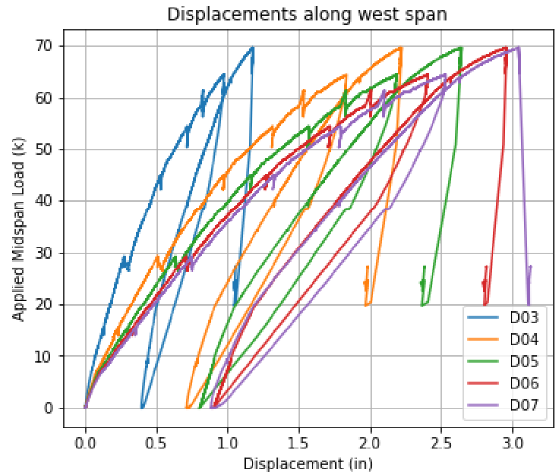

Figure K-56: Phase 4 longitudinal tension steel strains west span

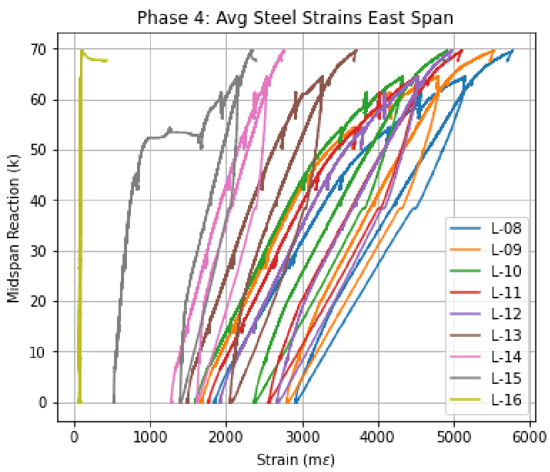

Figure K-57: Phase 4 longitudinal tension steel strains east span

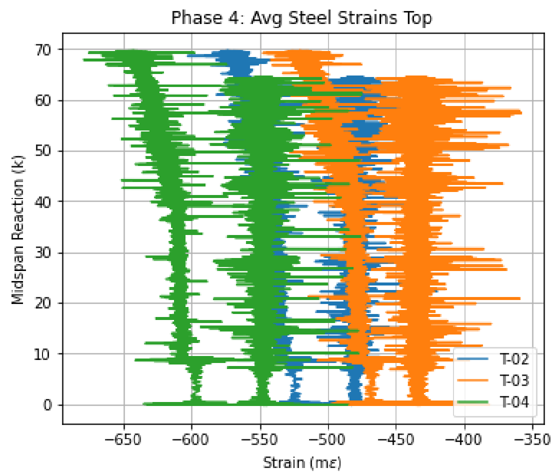

Figure K-58: Phase 4 longitudinal compression steel strains

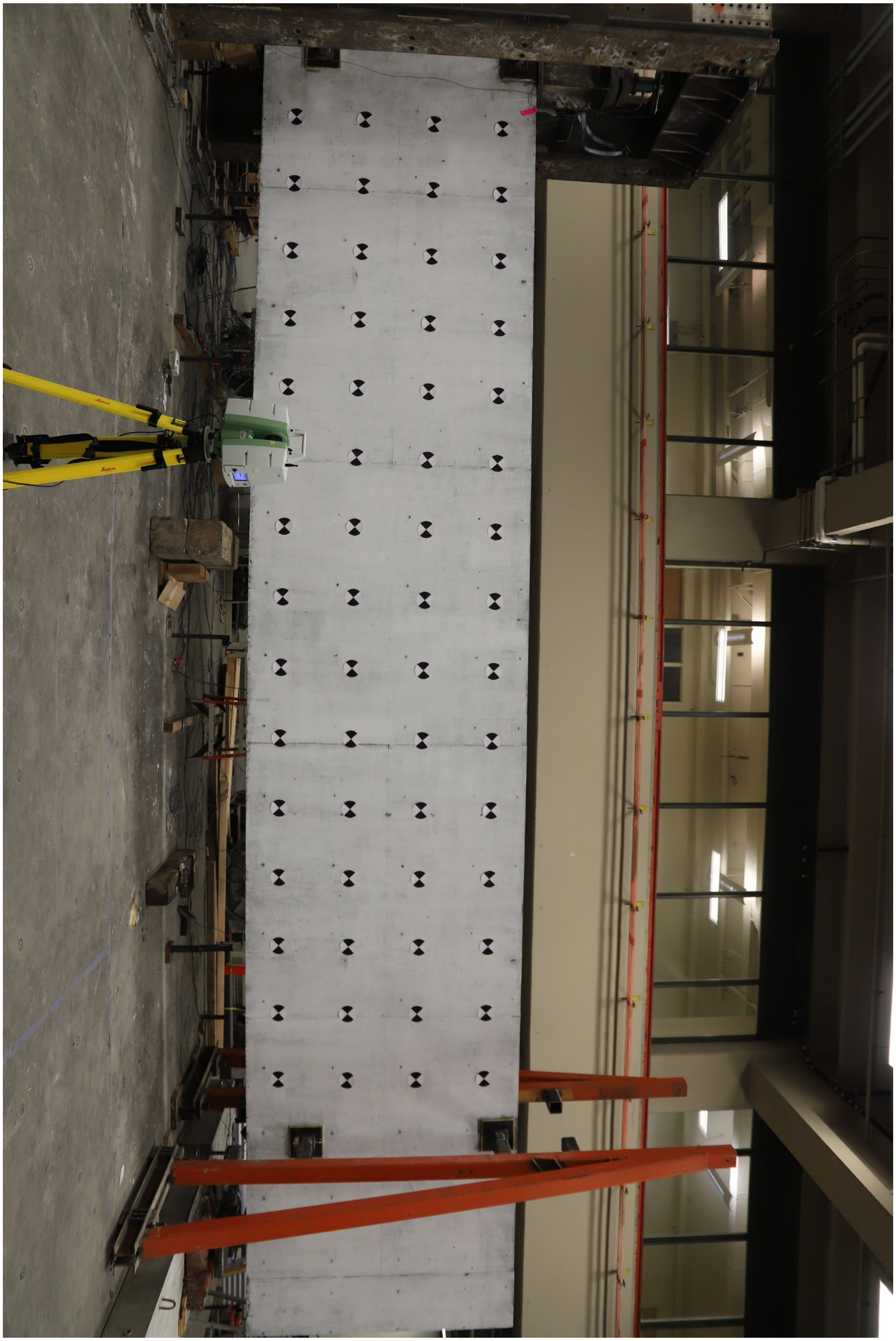

Figure K-59 : Phase 4, Load Stage 1

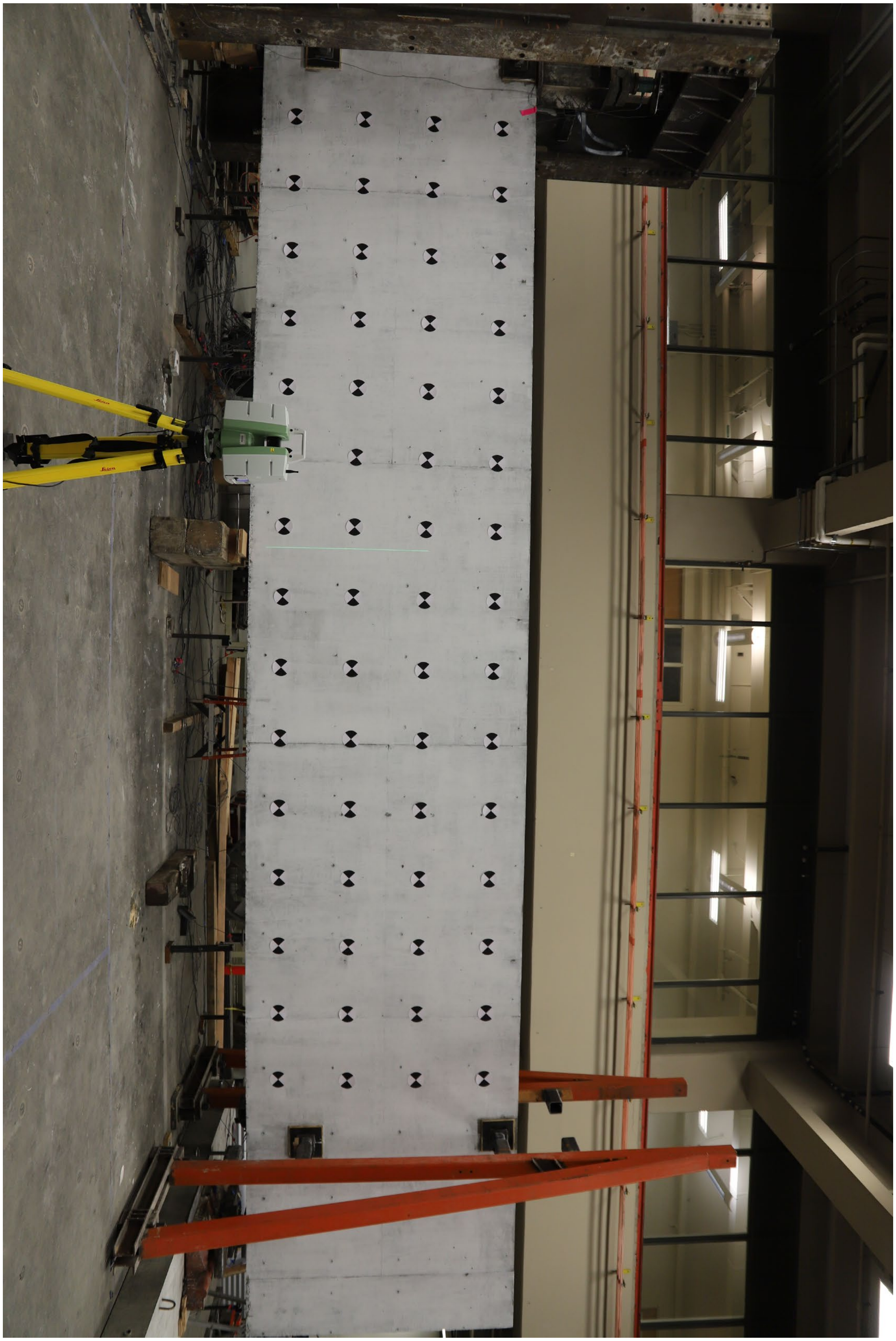

Figure K-60 : Phase 4, Load Stage 2

Figure K-61 : Phase 4, Load Stage 3

Figure K-62 : Phase 4, Load Stage 4

Figure K-63 : Phase 4, Load Stage 5

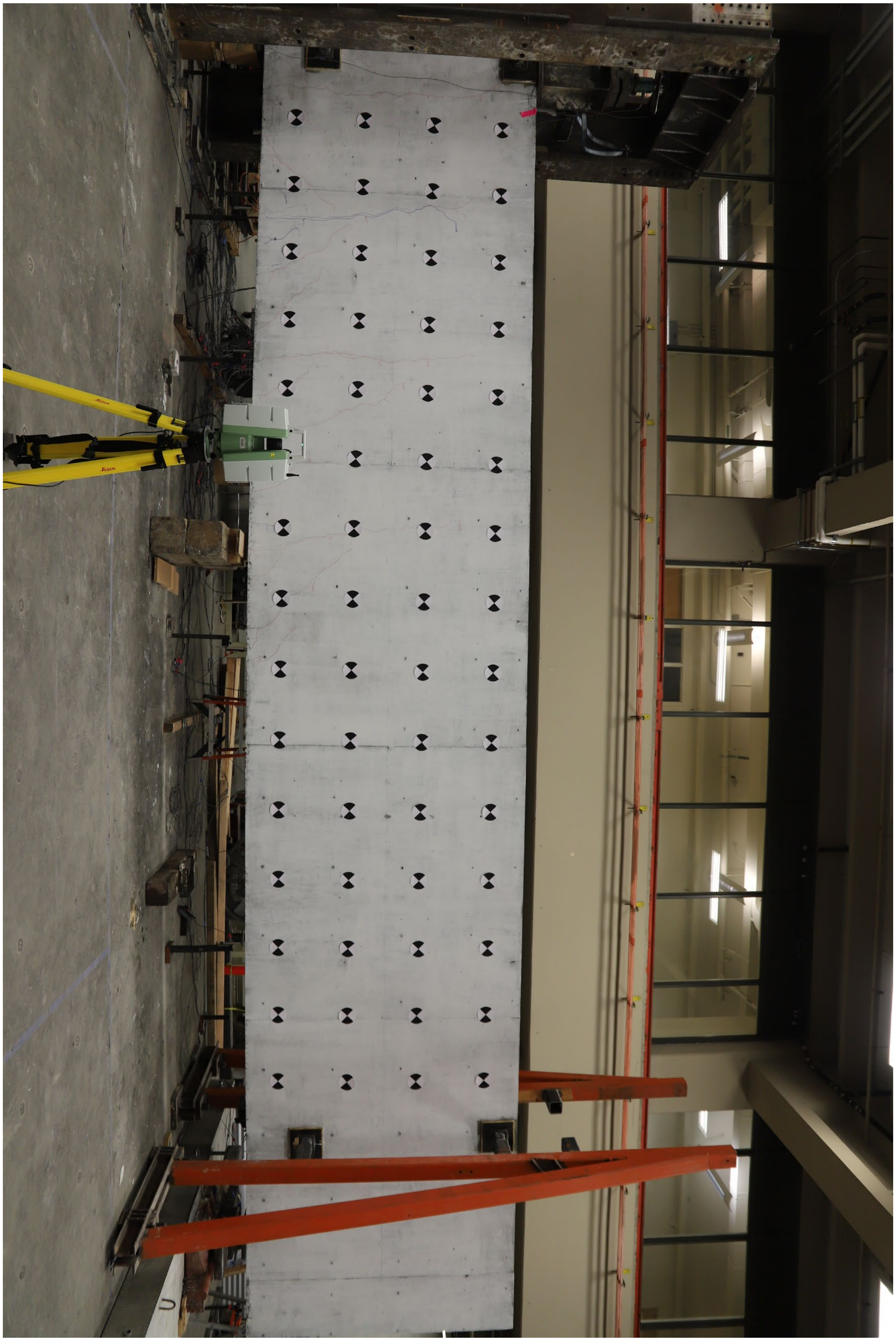

Figure K-64 : Phase 4, Load Stage 6

Figure K-65 : Phase 4, Load Stage 7

Figure K-66 : Phase 4, Load Stage 8

Figure K-67 : Phase 4, Load Stage 9

Figure K-68 : Phase 4, Load Stage 10

Figure K-69 : Phase 4, Load Stage 11

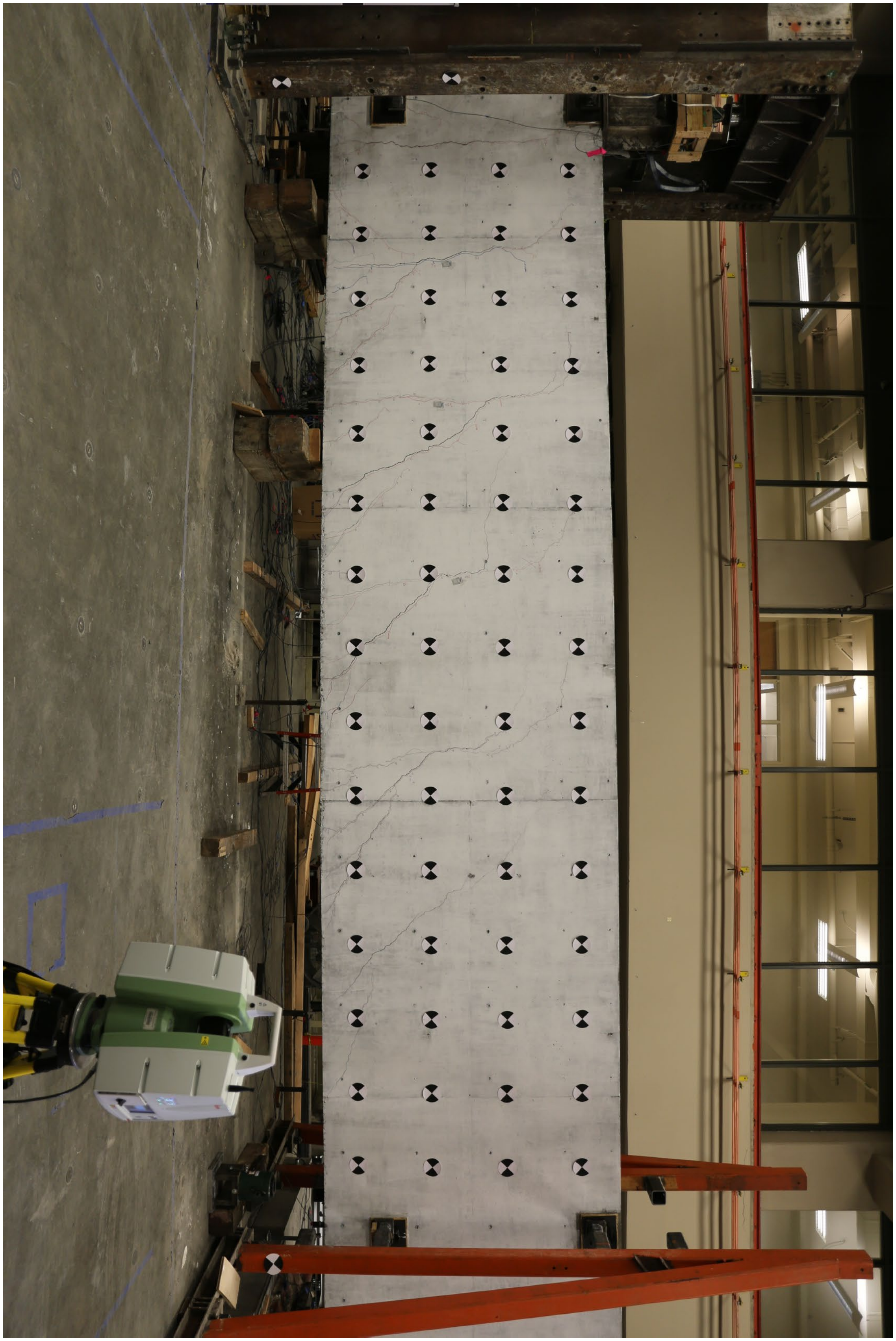

Figure K-70 : Phase 4, Load Stage 12

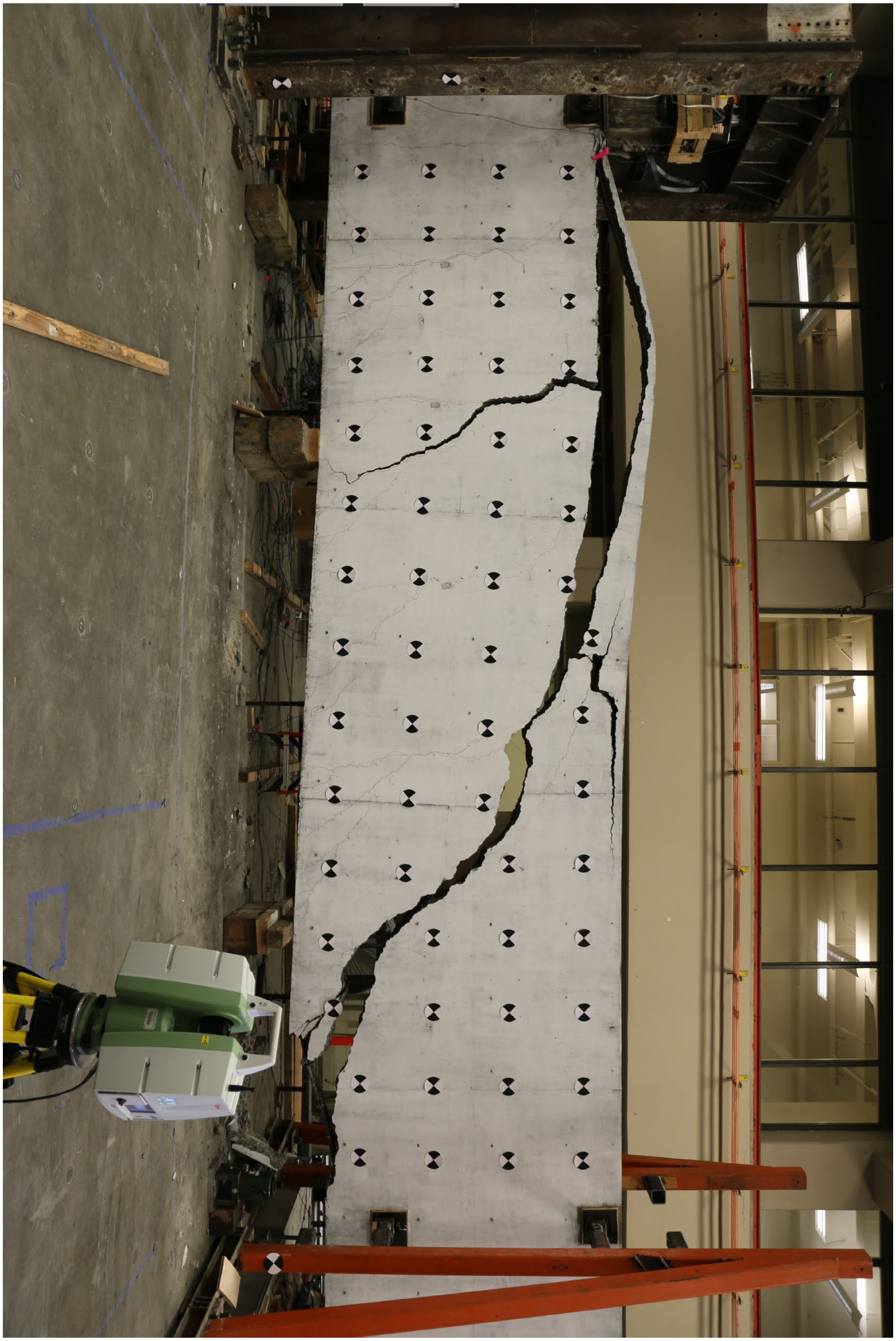

Figure K-71 : Phase 4, Failure

A.12.5. Companion Beam 1

J- 1: Companion Beam 1, Load Stage 1

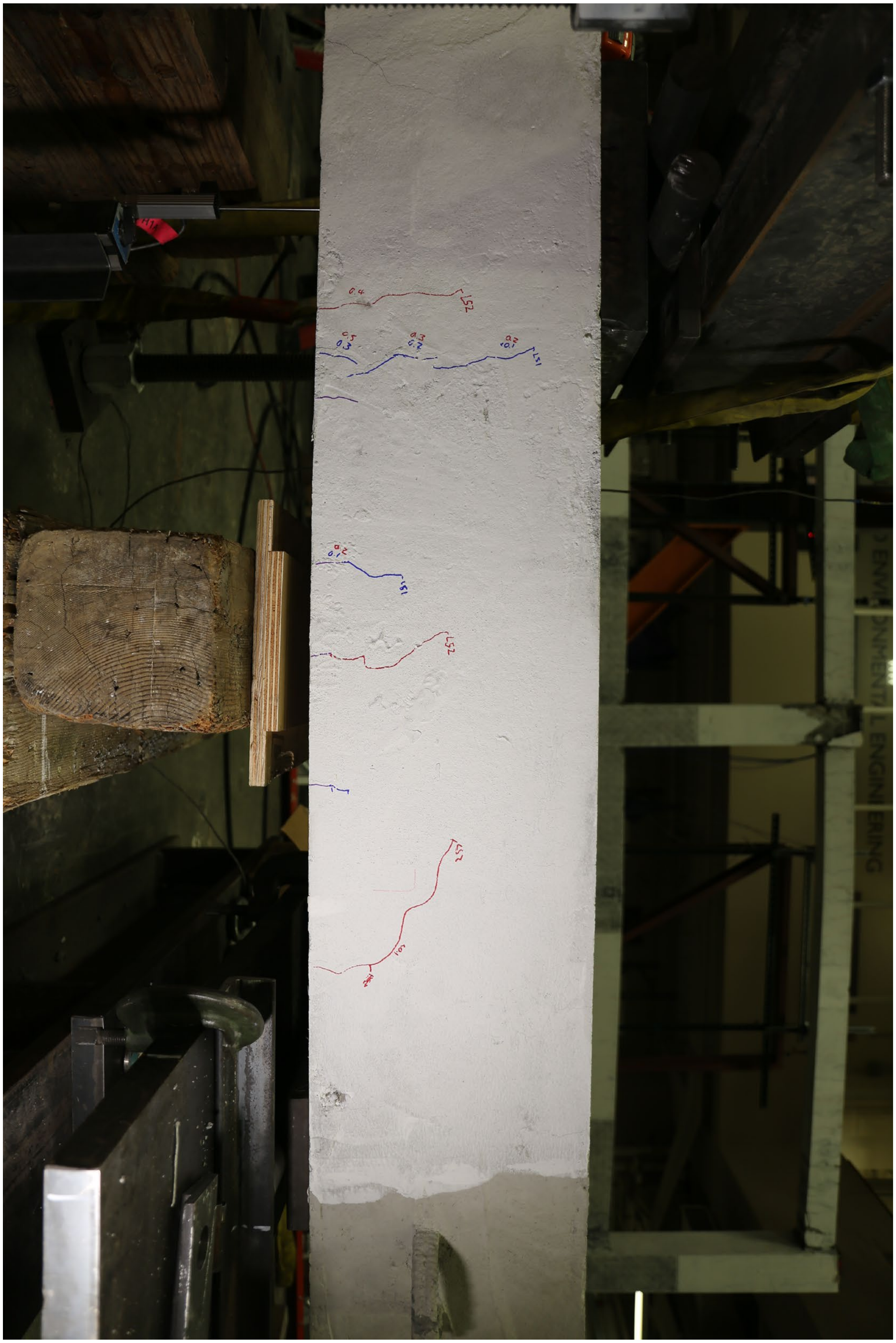

J- 2: Companion Beam 1, Load Stage 2

J- 3: Companion Beam 1, Load Stage 3

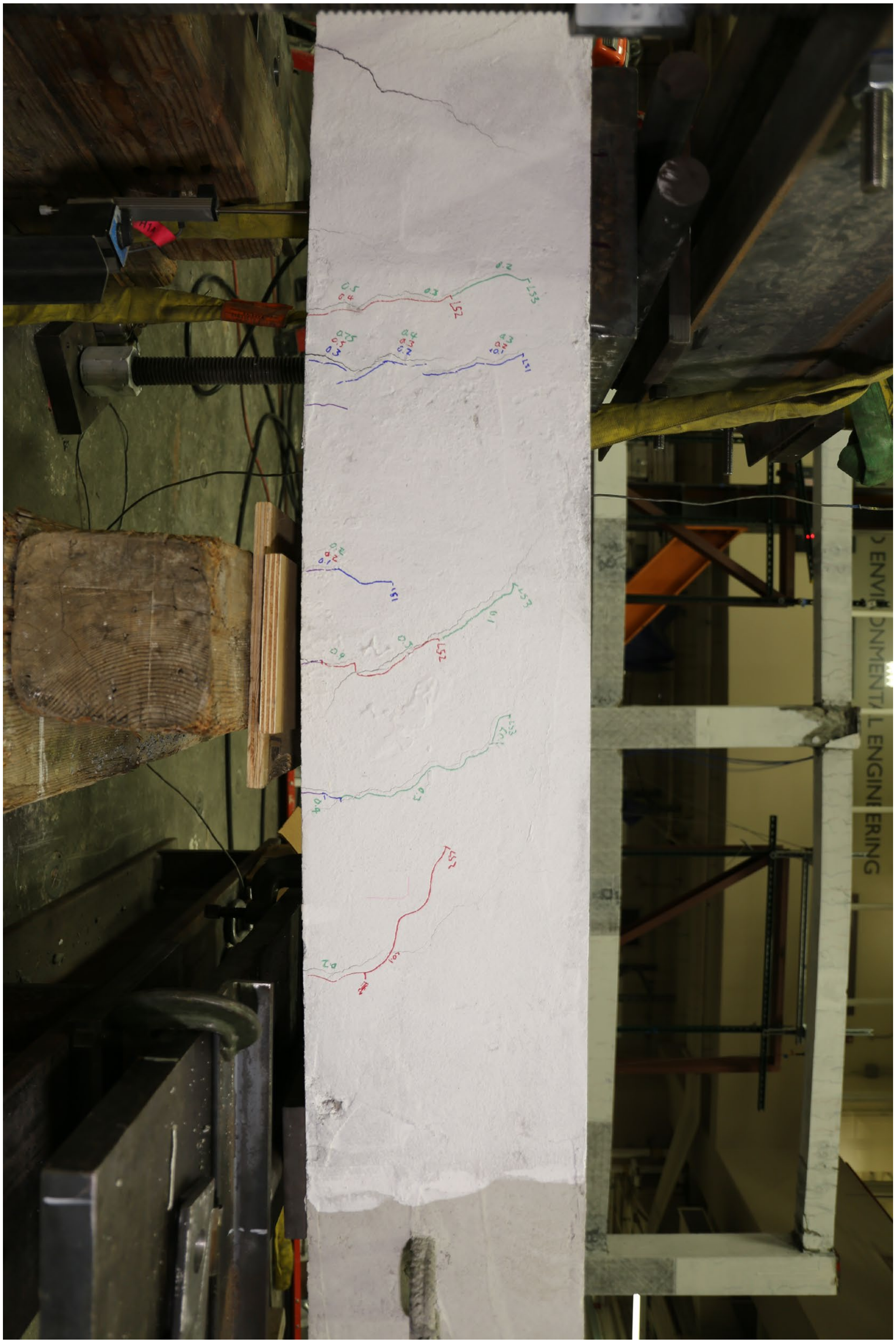

J- 4: Companion Beam 1, Load Stage 4

J- 5: Companion Beam 1, failure

A.12.6. <u>Companion Beam 2</u>

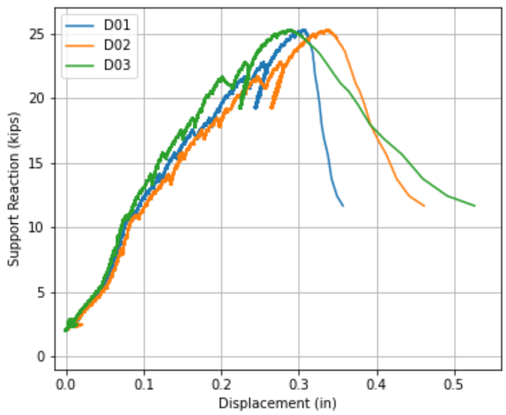

Figure K-72: Companion Beam 2 displacements along span

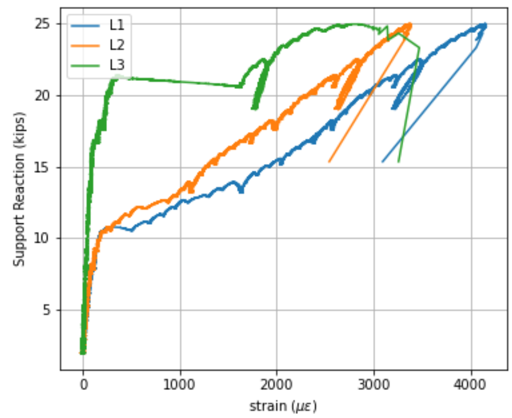

Figure K-73: Companion Beam 2 tension strains along span

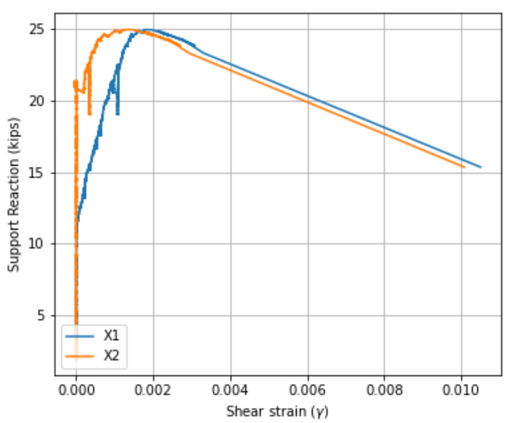

Figure K-74: Companion Beam 2 shear strain on panel zone

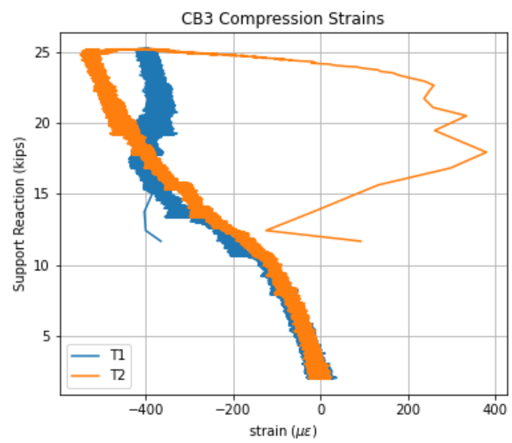

Figure K-75: Companion Beam 2 compression strain along span

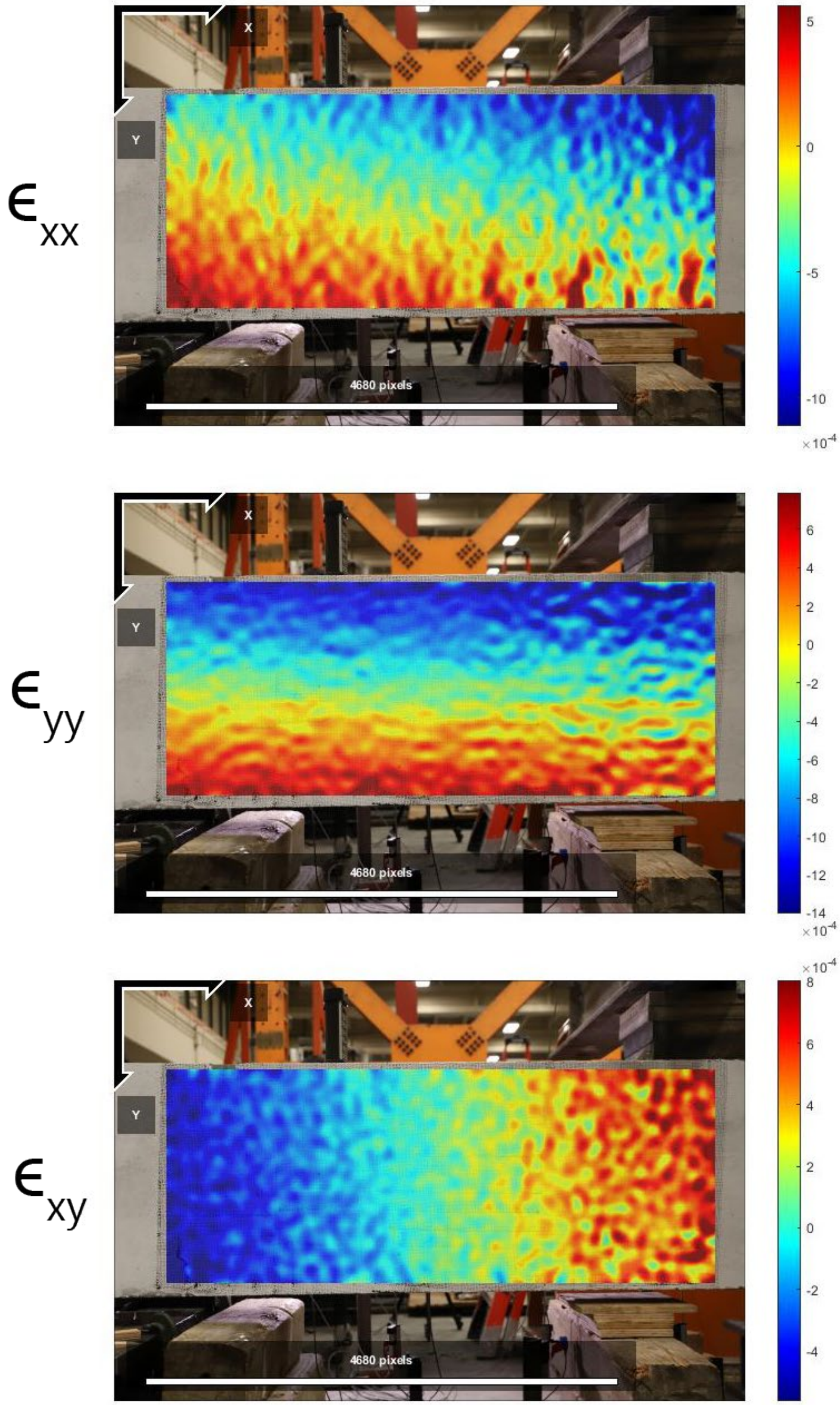

Figure K-76: CB2 DIC Pattern 1

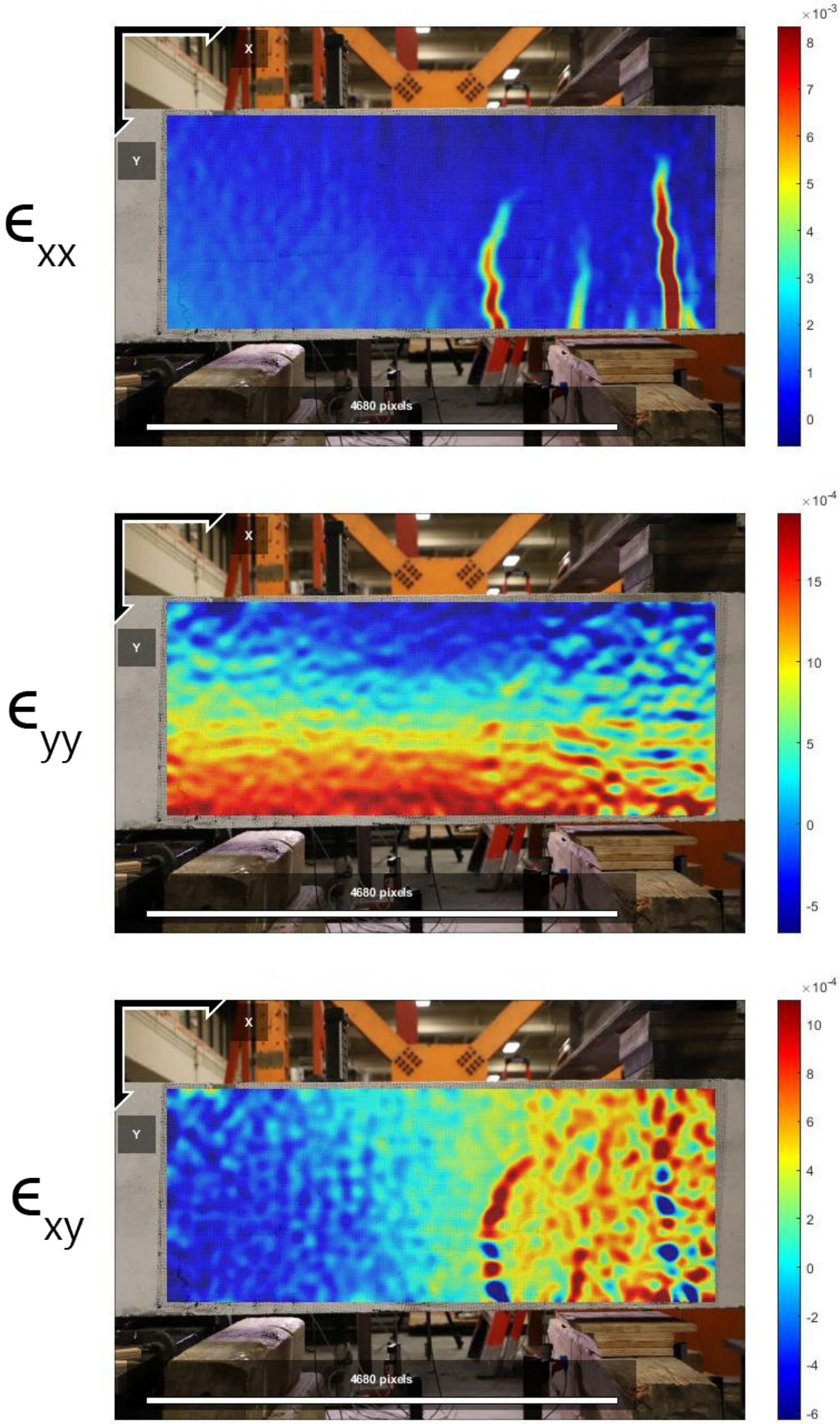

Figure K-77: CB2 DIC Pattern 2

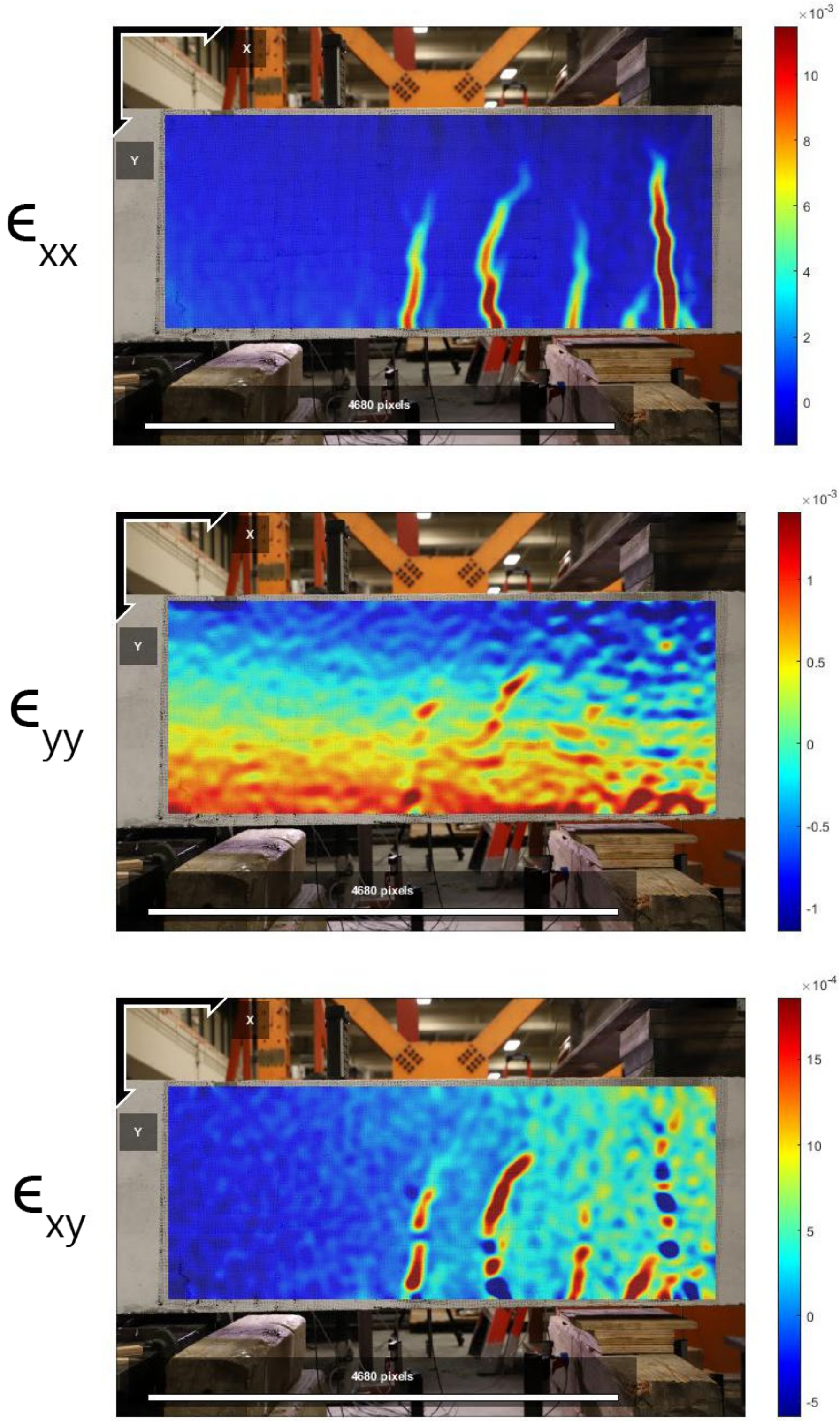

Figure K-78: CB2 DIC Pattern 3

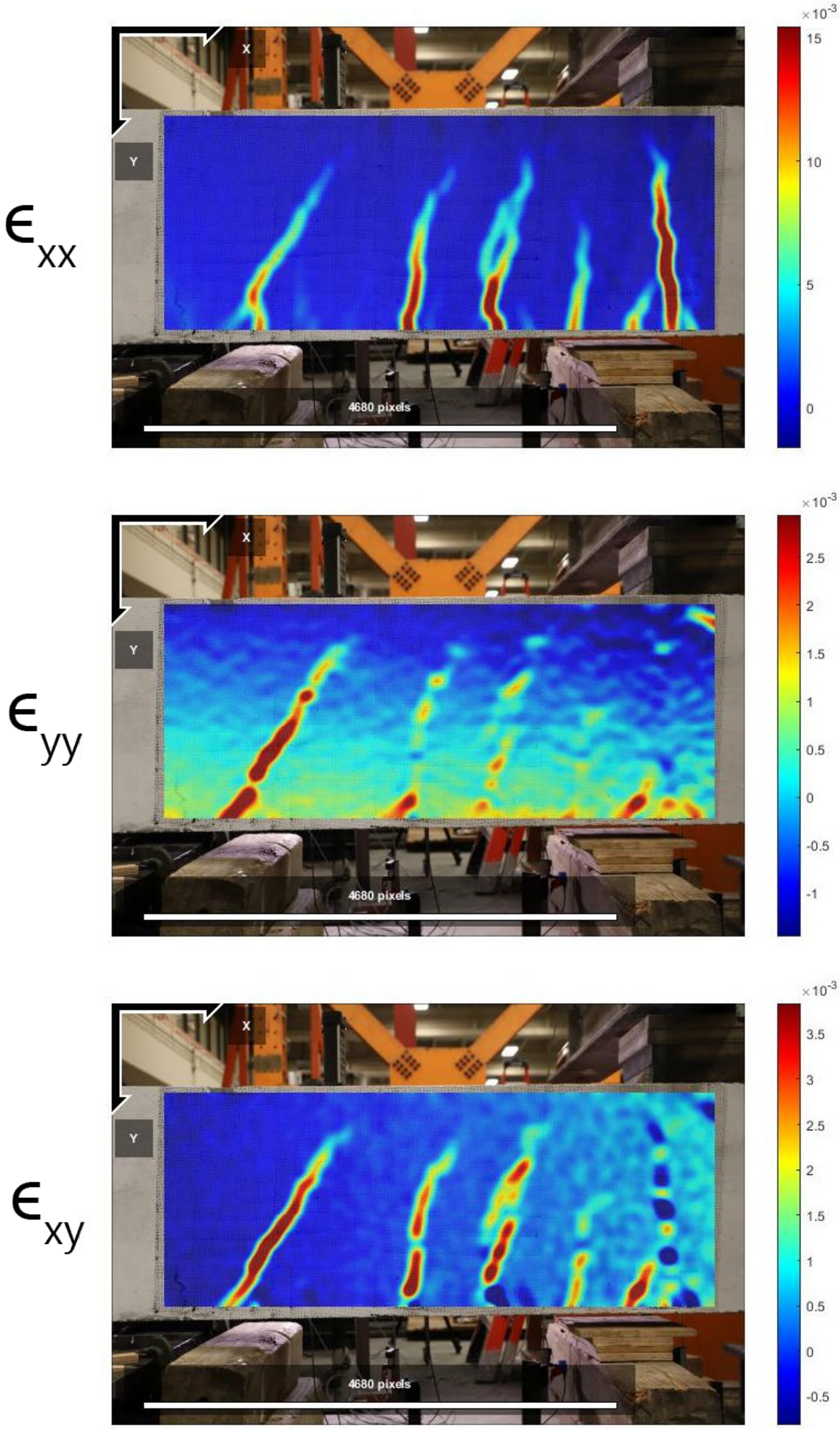

Figure K-79: CB2 DIC Pattern 4

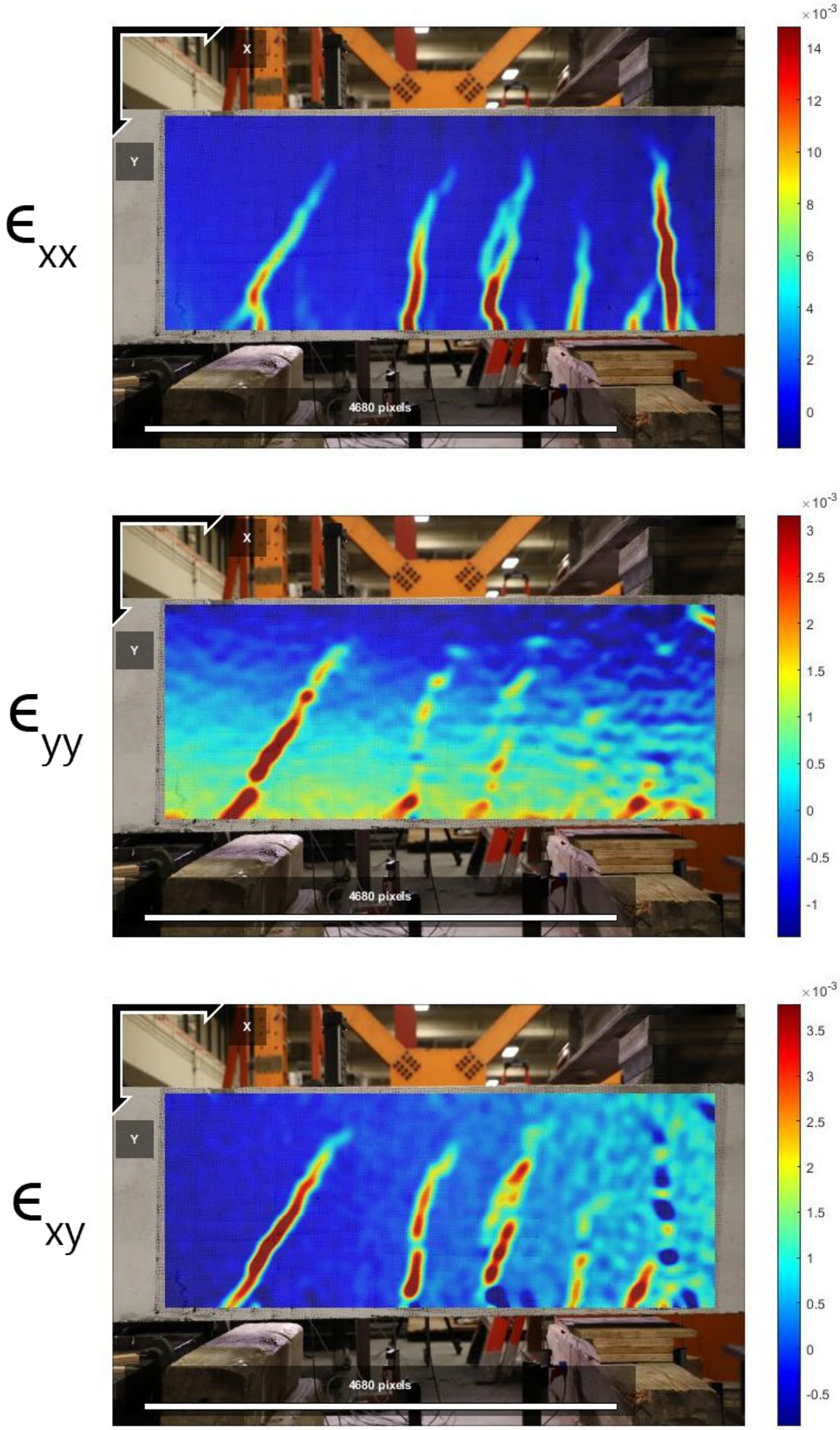

Figure K-80: CB2 DIC Pattern 5

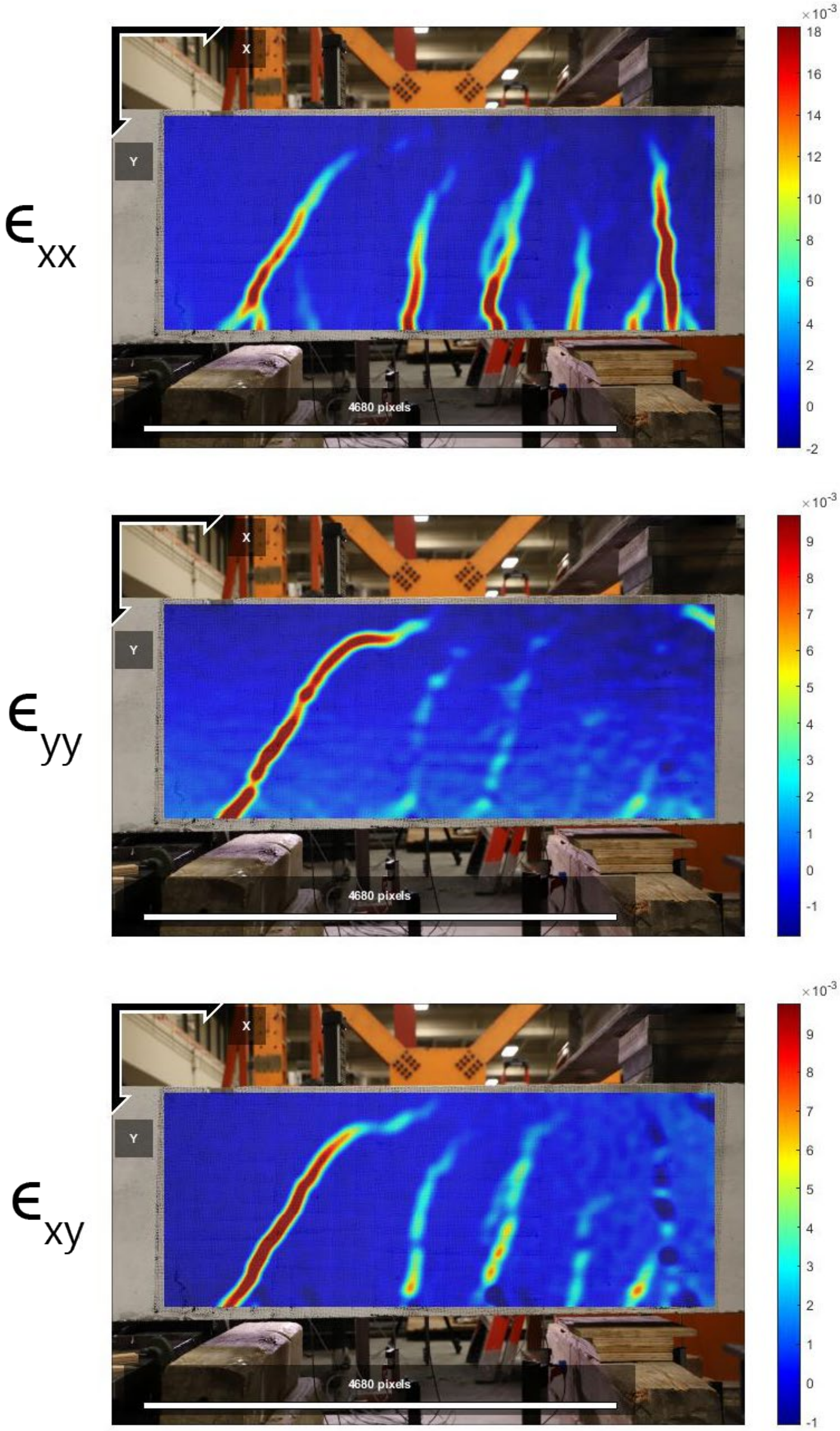

Figure K-81: CB2 DIC Pattern 6

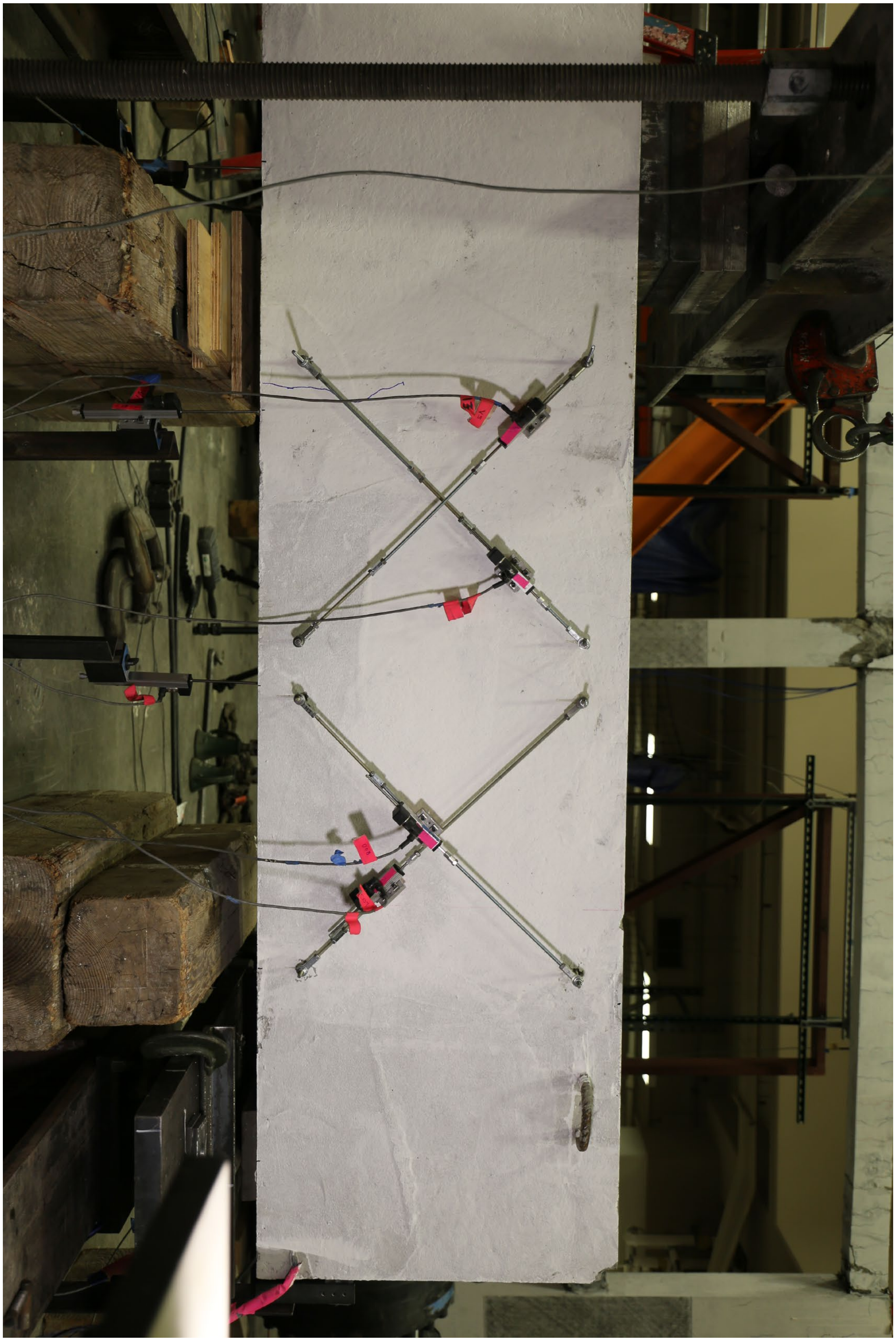

Figure K-82: Companion Beam 2, Load Stage 1

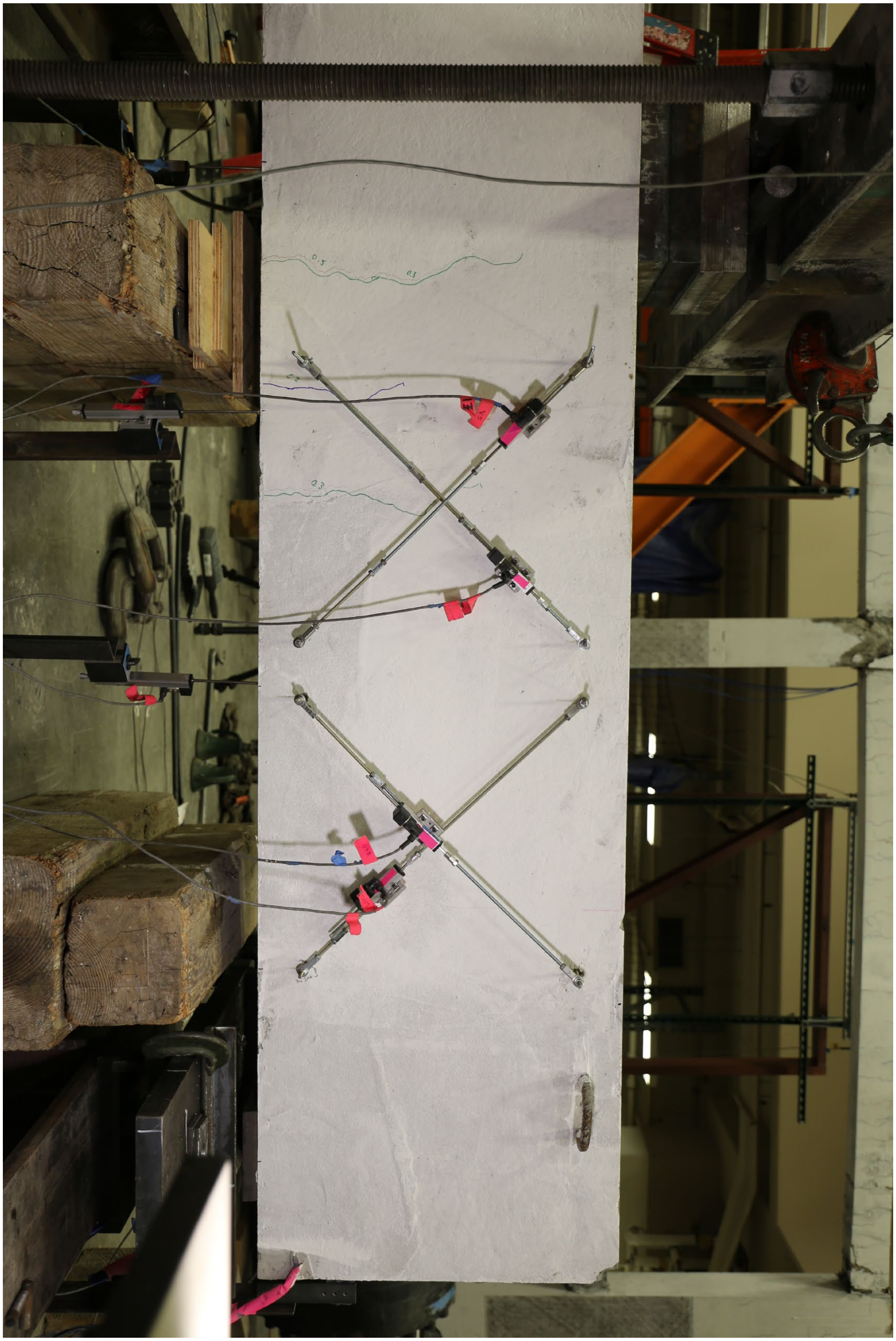

Figure K-83: Companion Beam 2, Load Stage 2

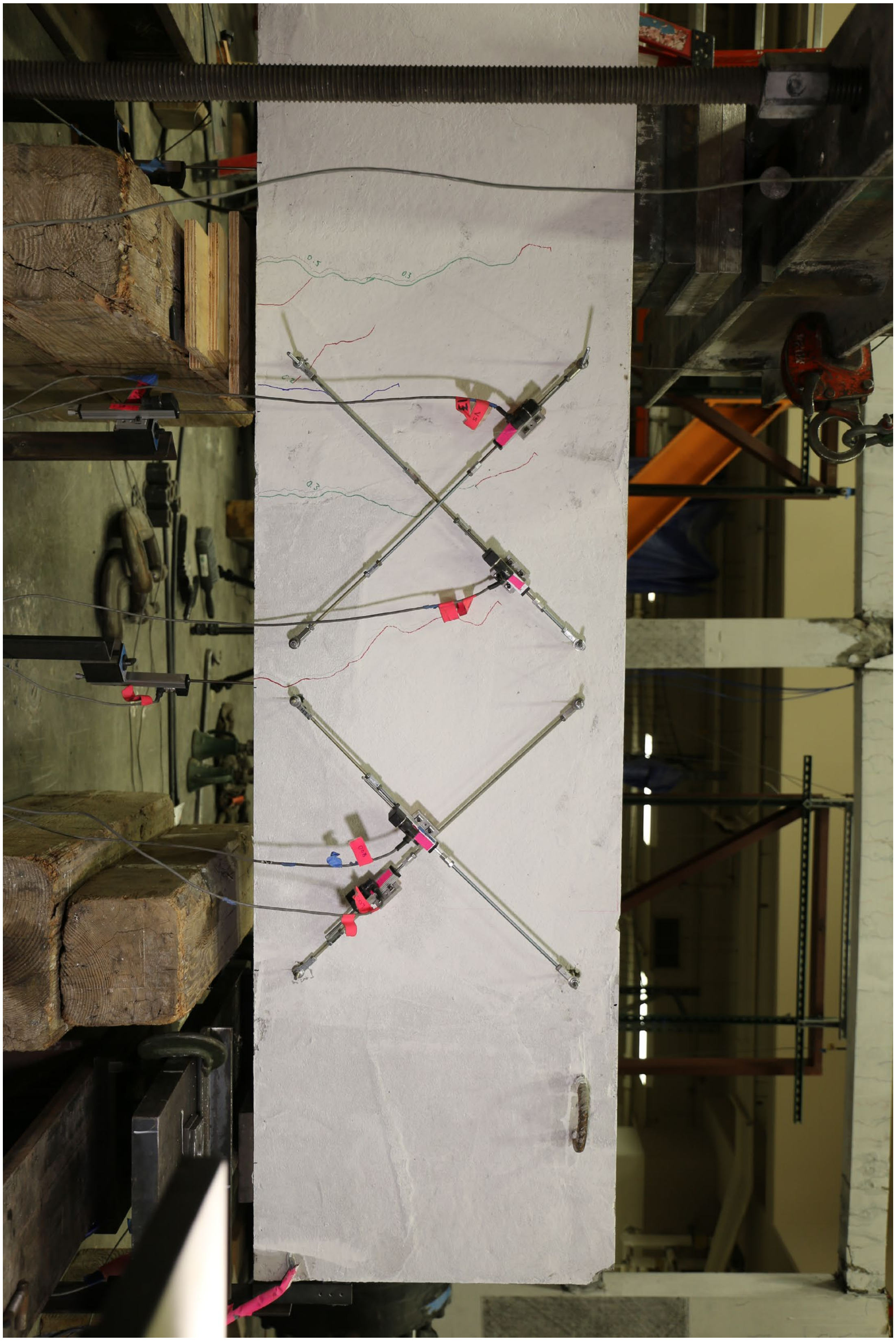

Figure K-84: Companion Beam 2, Load Stage 3

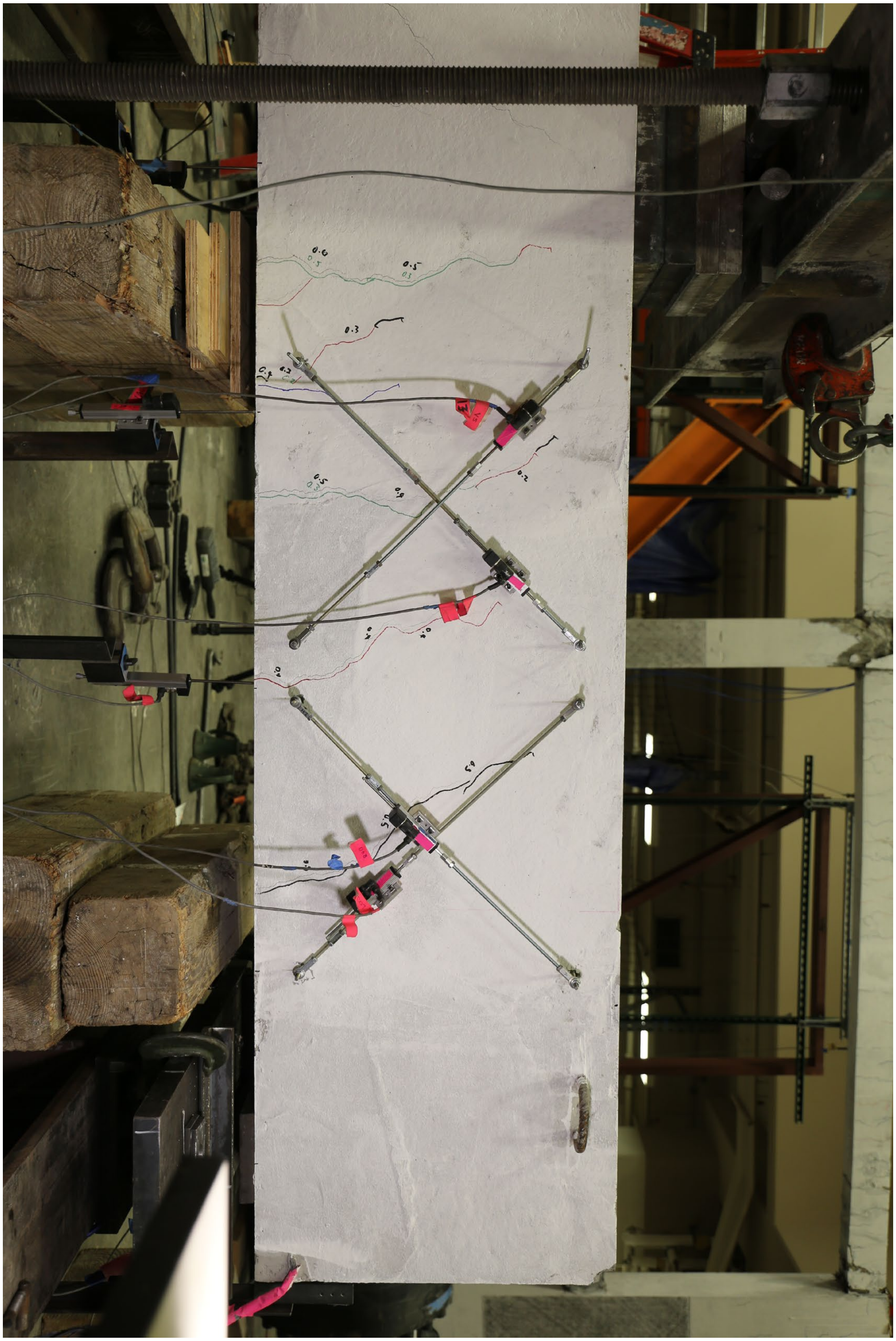

Figure K-85: Companion Beam 2, Load Stage 4

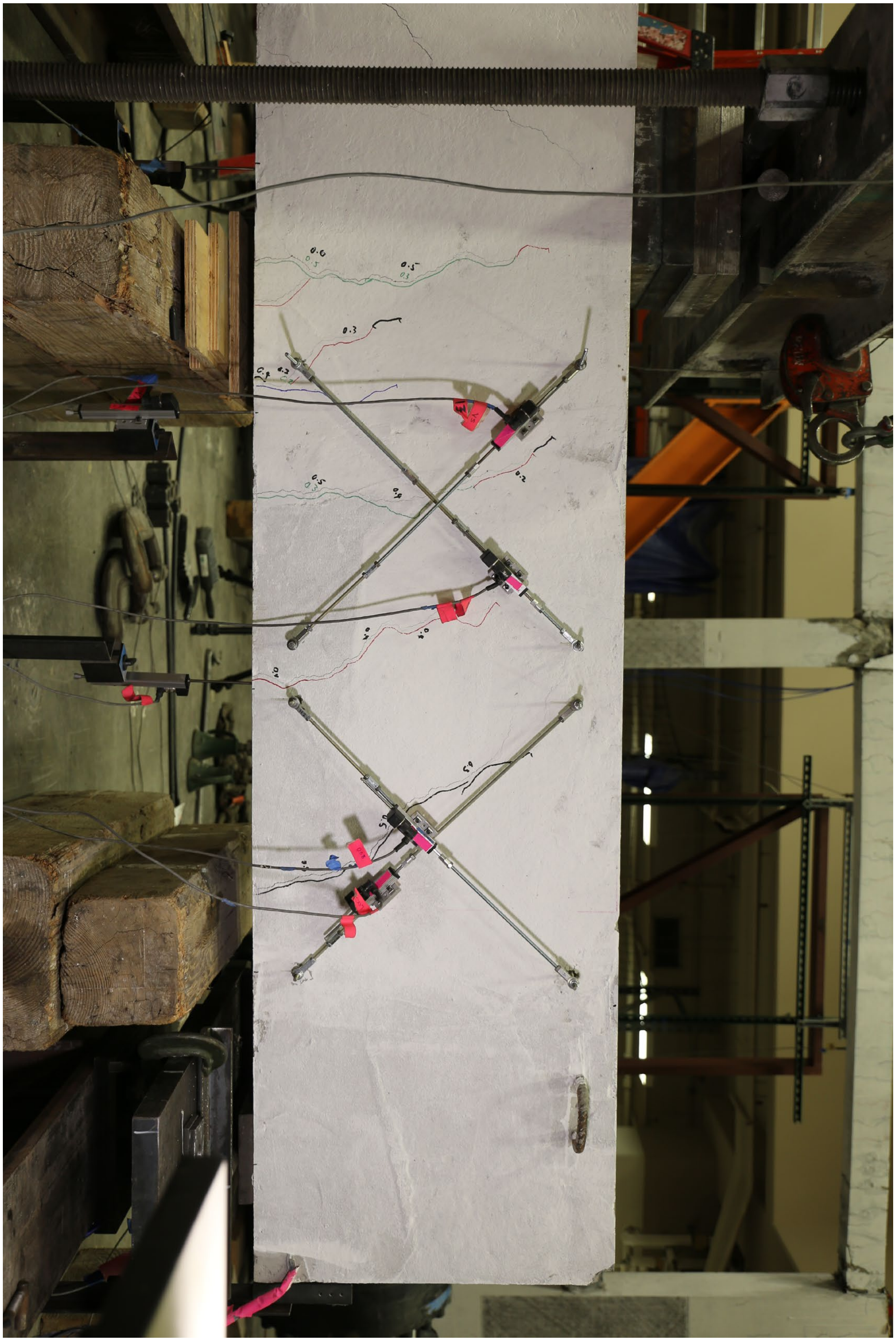

Figure K-86: Companion Beam 2, Load Stage 5

Figure K-87: Companion Beam 2, Failure

A.12.7.Companion Beam 3

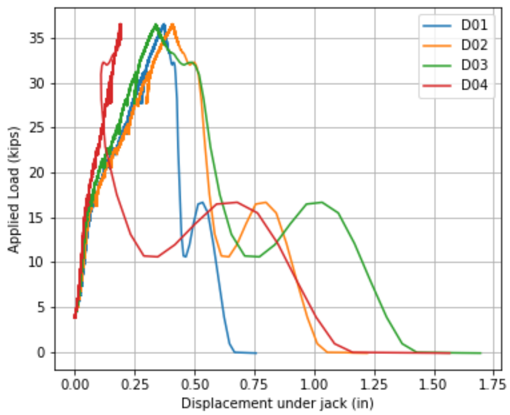

Figure K-88: Companion Beam 3 load vs. displacement along span

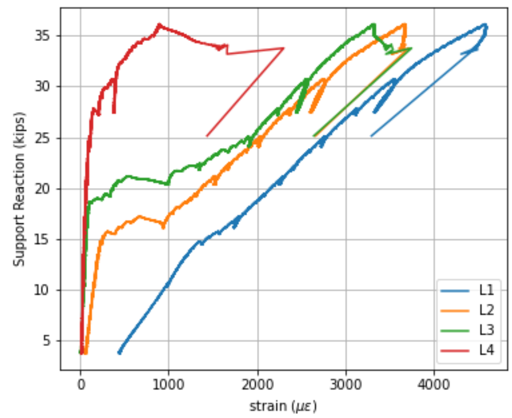

Figure K-89: Companion Beam 3 tension strains along span

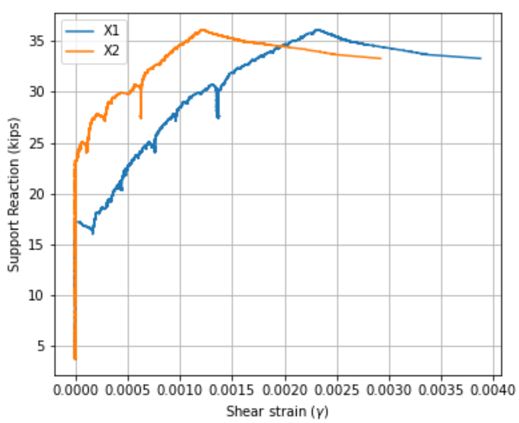

Figure K-90: Companion Beam 3 shear strain on surface panel zone

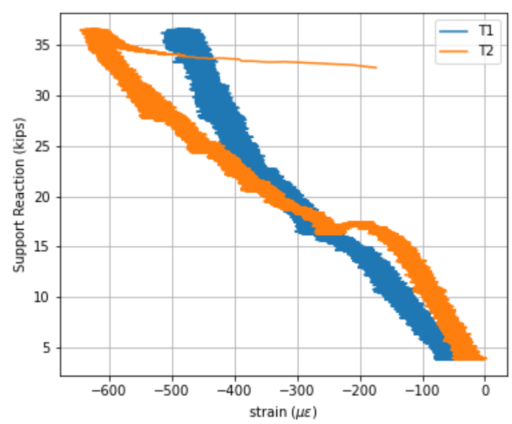

Figure K-91: Companion Beam 3 compression strains along span

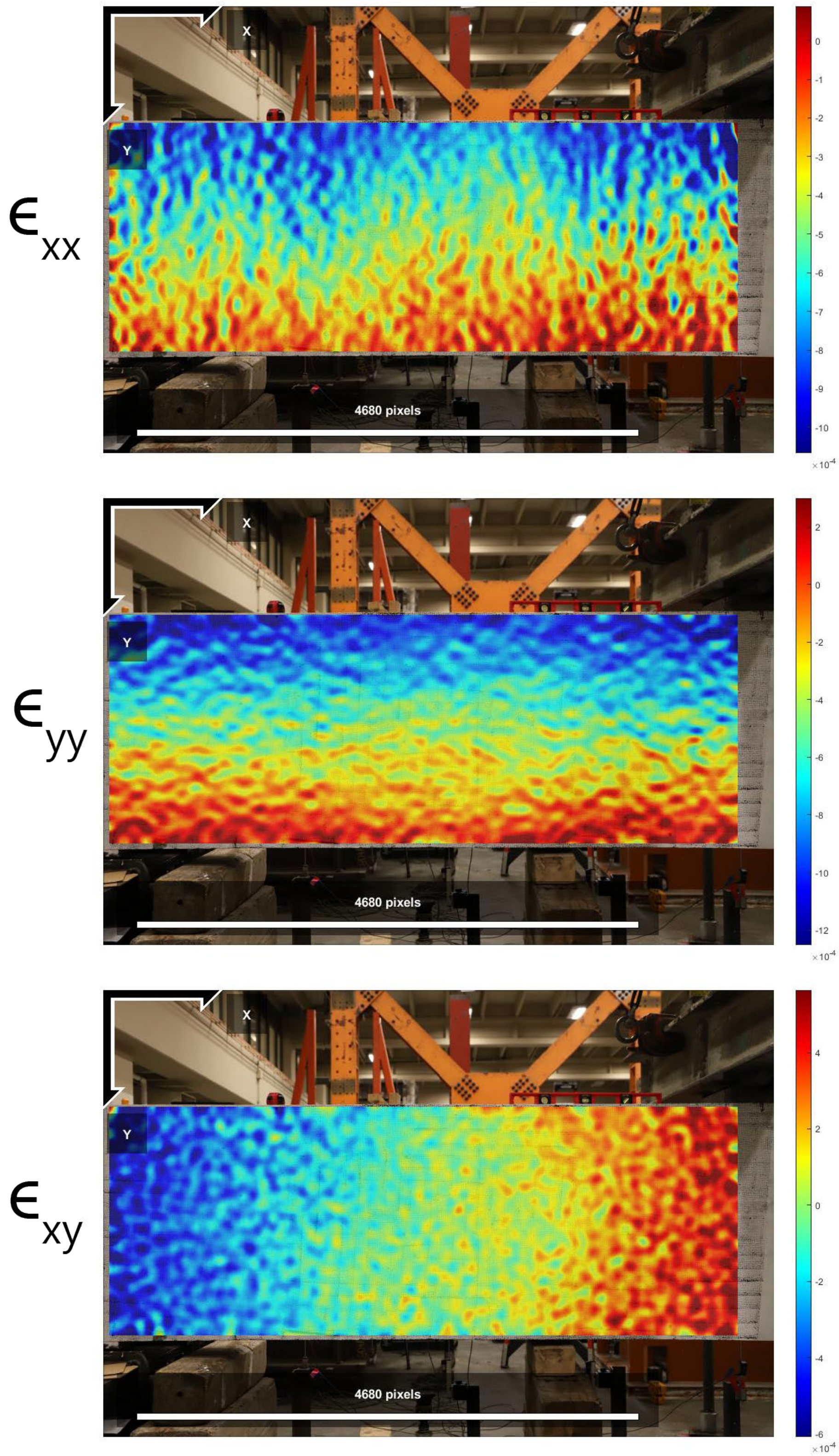

Figure K-92: Companion Beam 3 DIC Pattern 1

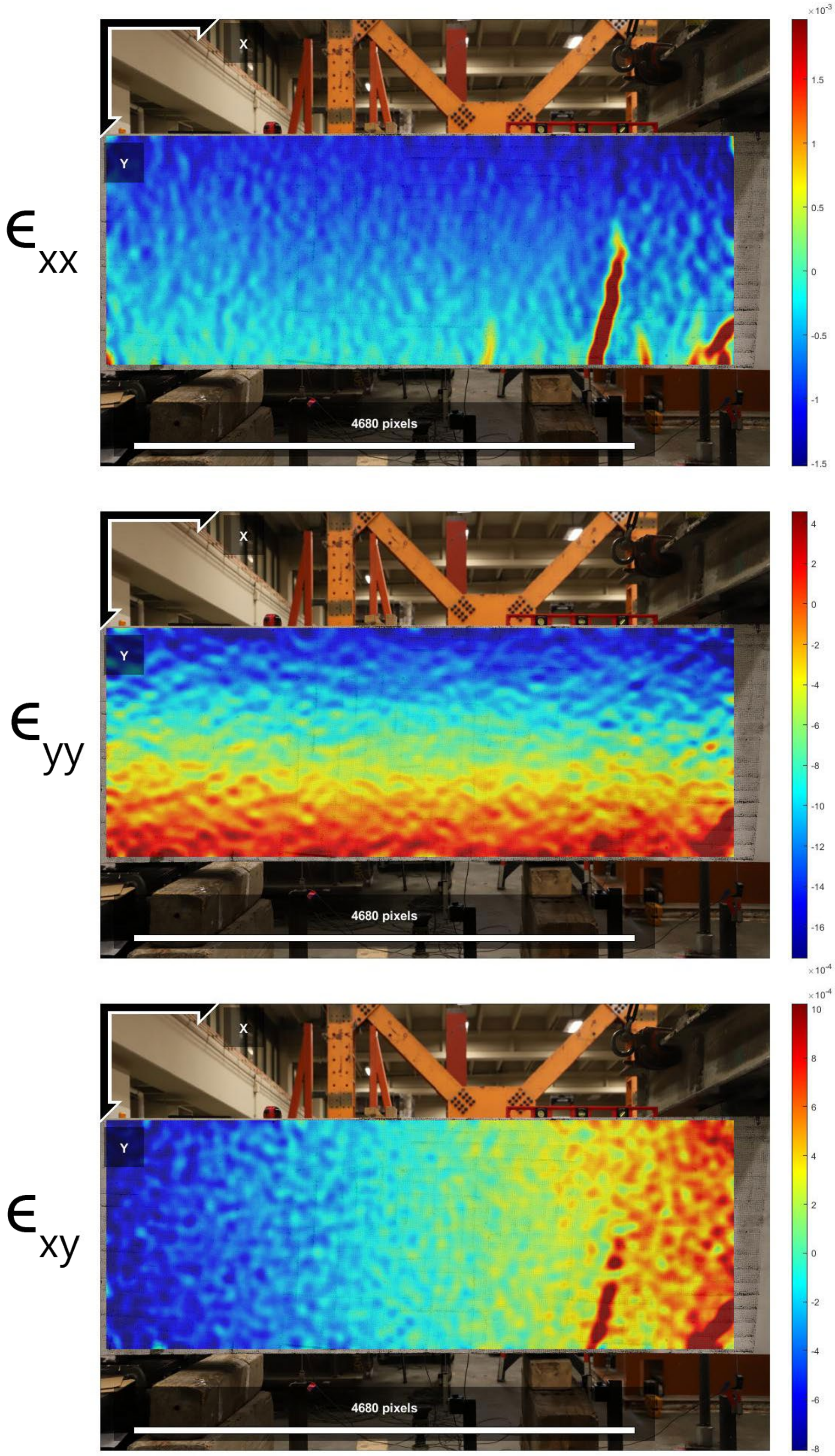

Figure K-93: Companion Beam 3 DIC Pattern 2

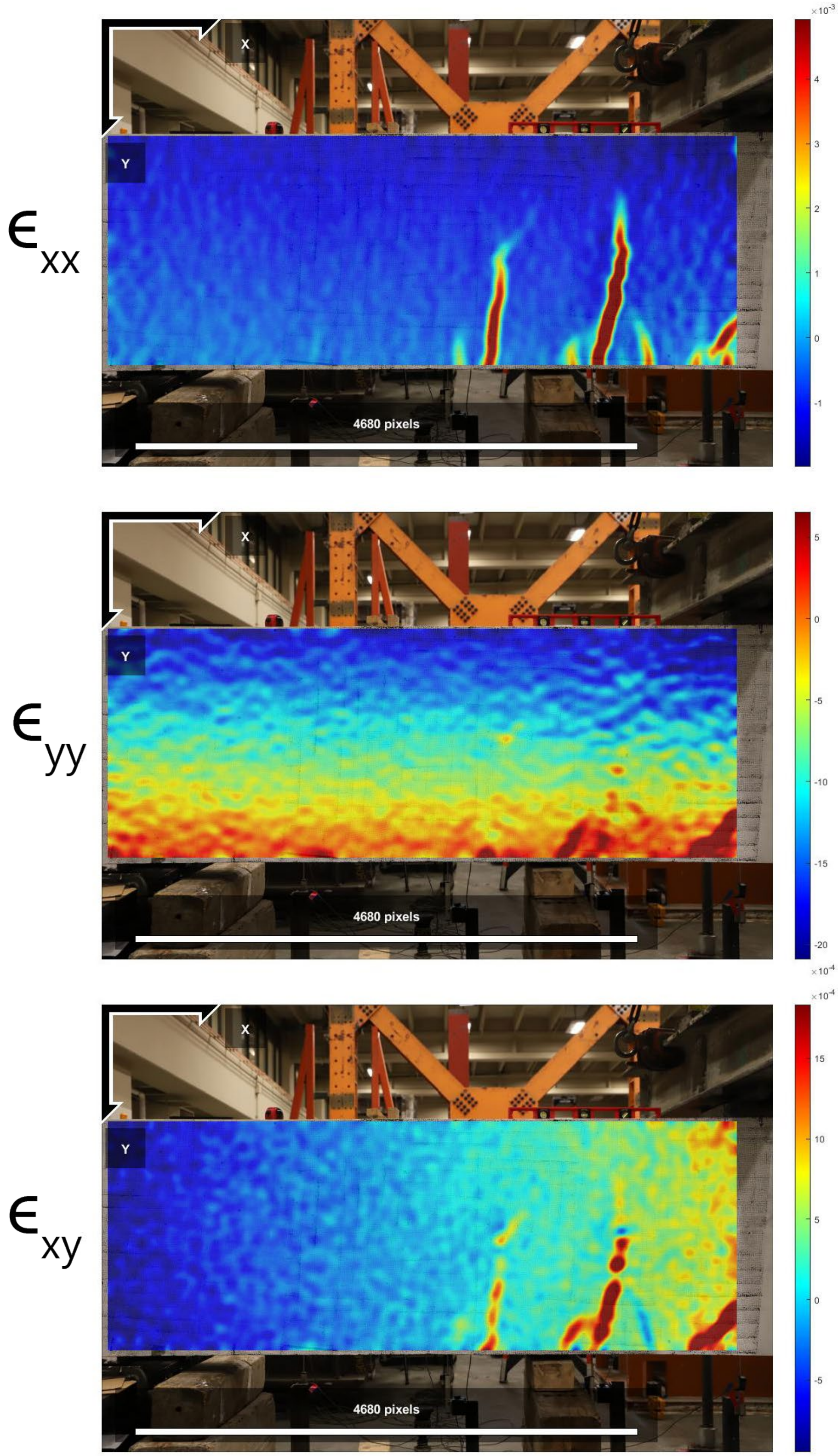

Figure K-94: Companion Beam 3 DIC Pattern 3

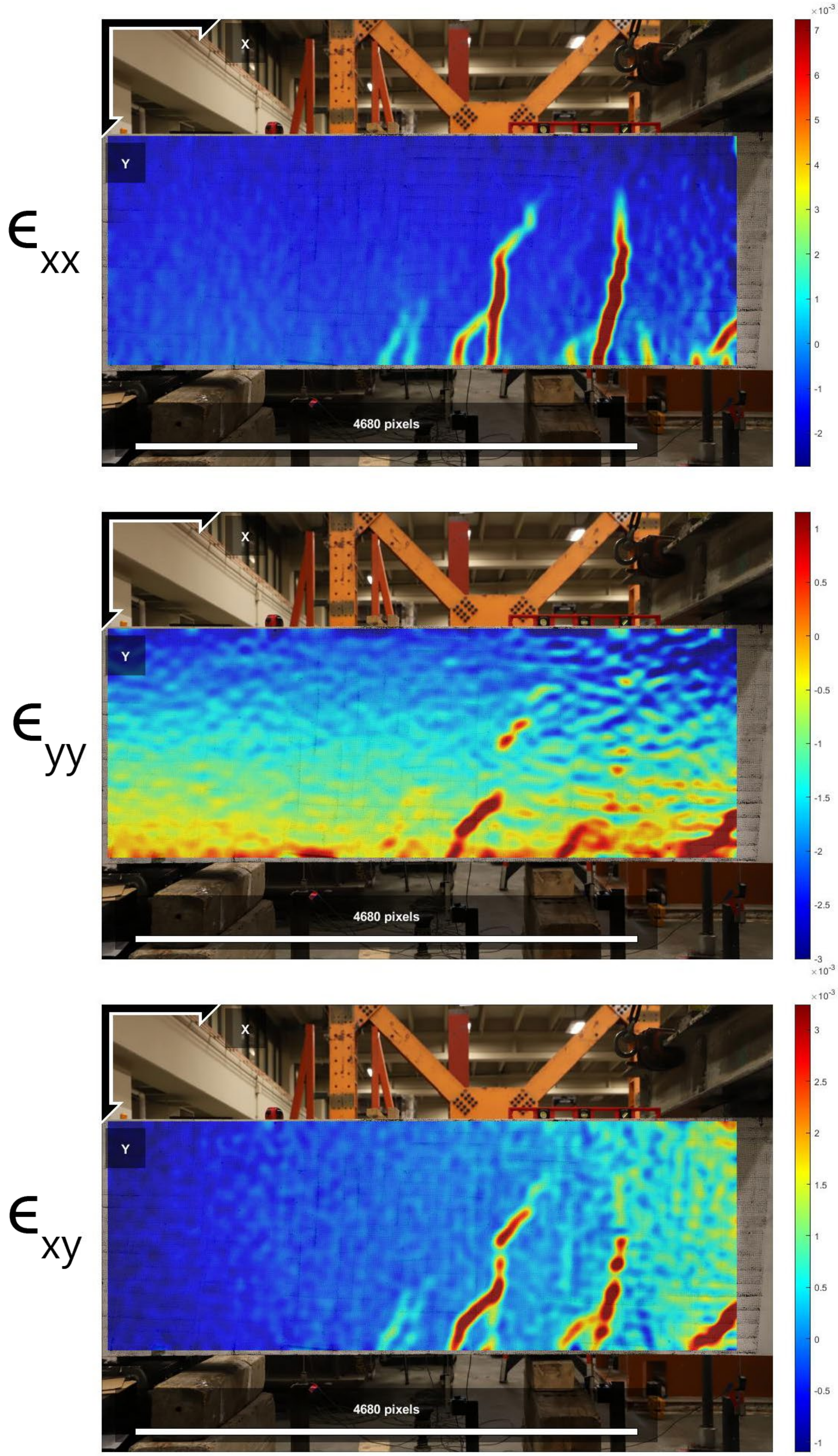

Figure K-95: Companion Beam 3 DIC Pattern 4

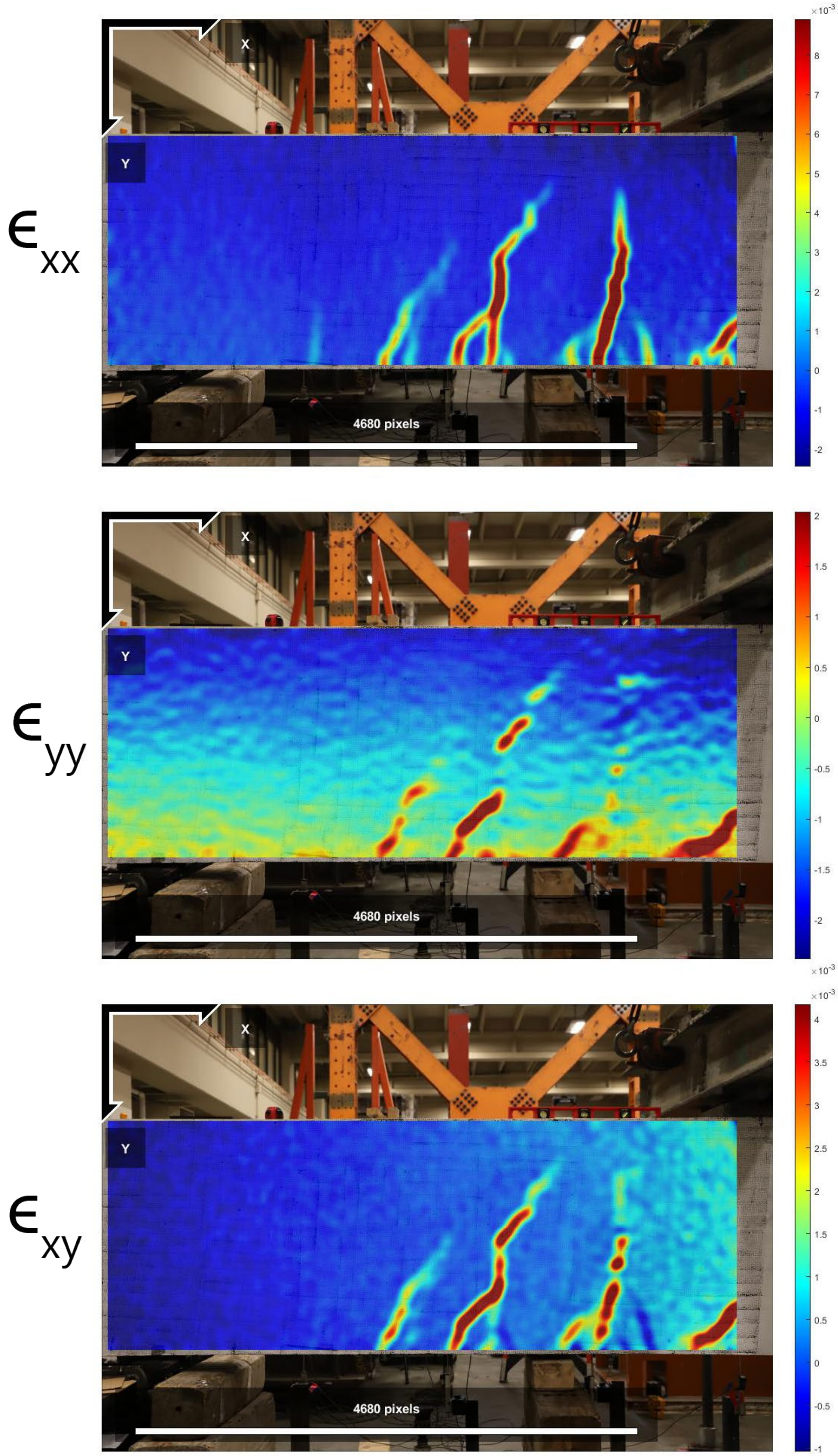

Figure K-96: Companion Beam 3 DIC Pattern 5

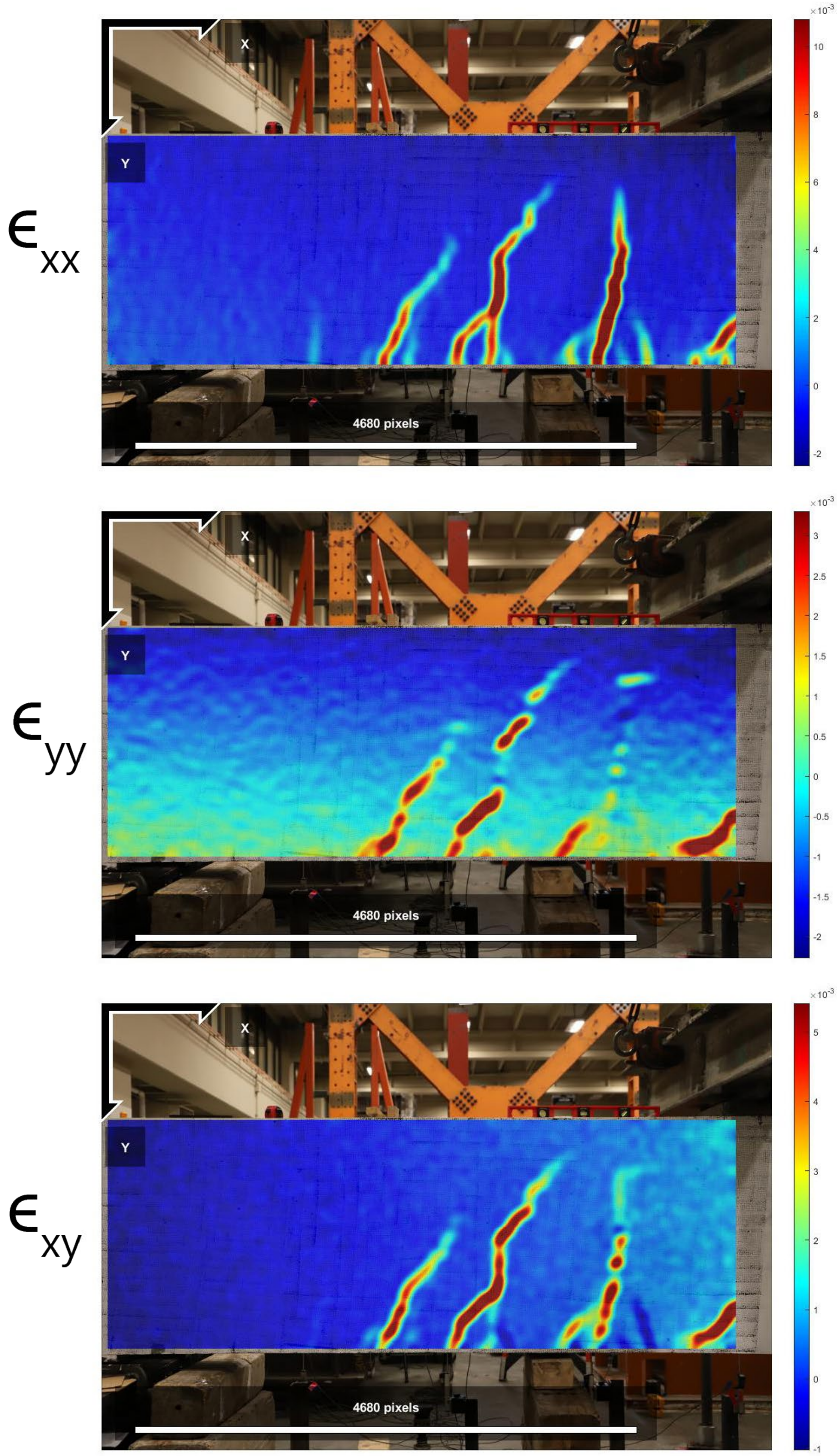

Figure K-97: Companion Beam 3 DIC Pattern 6

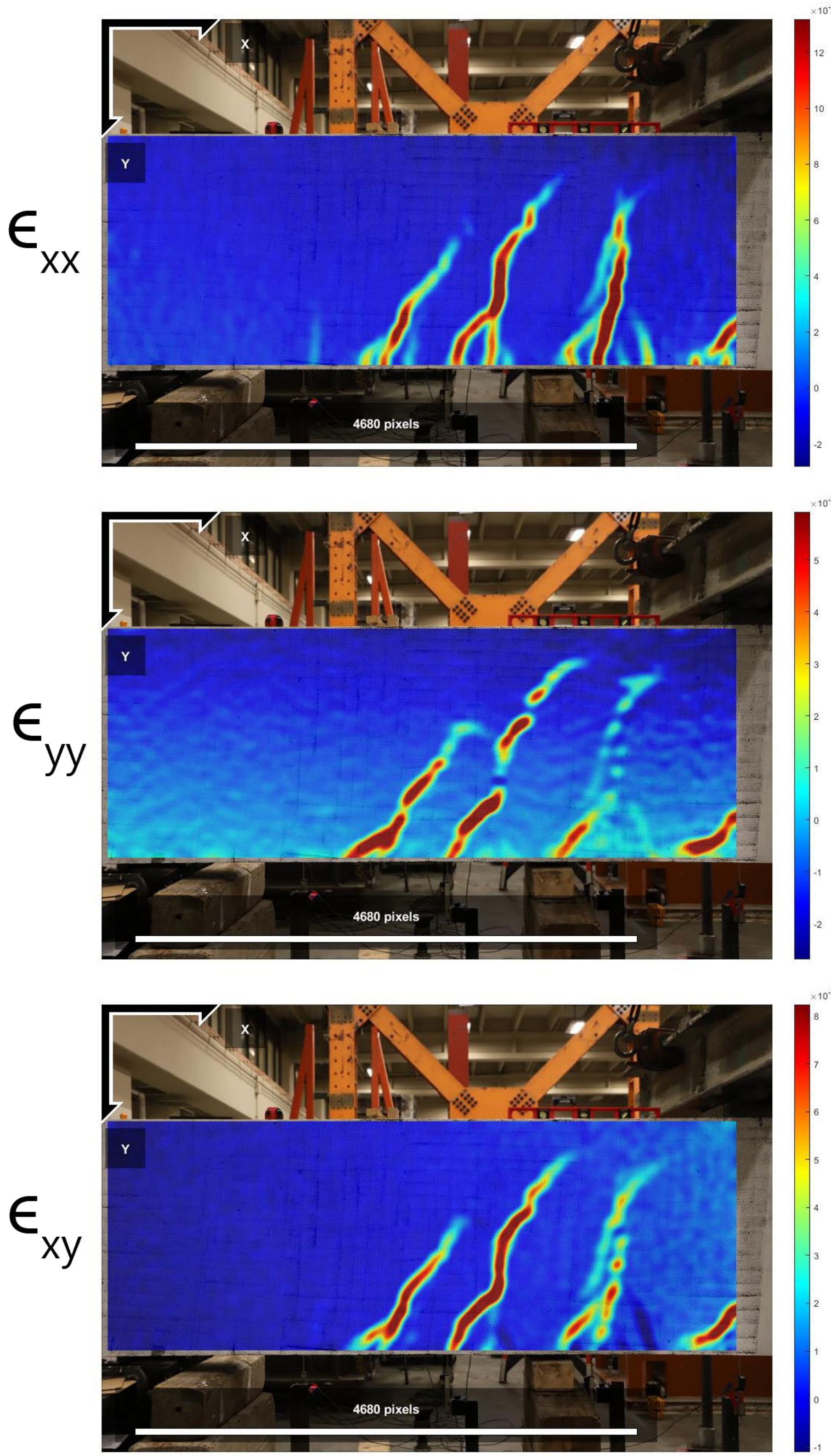

Figure K-98: Companion Beam 3 DIC Pattern 7

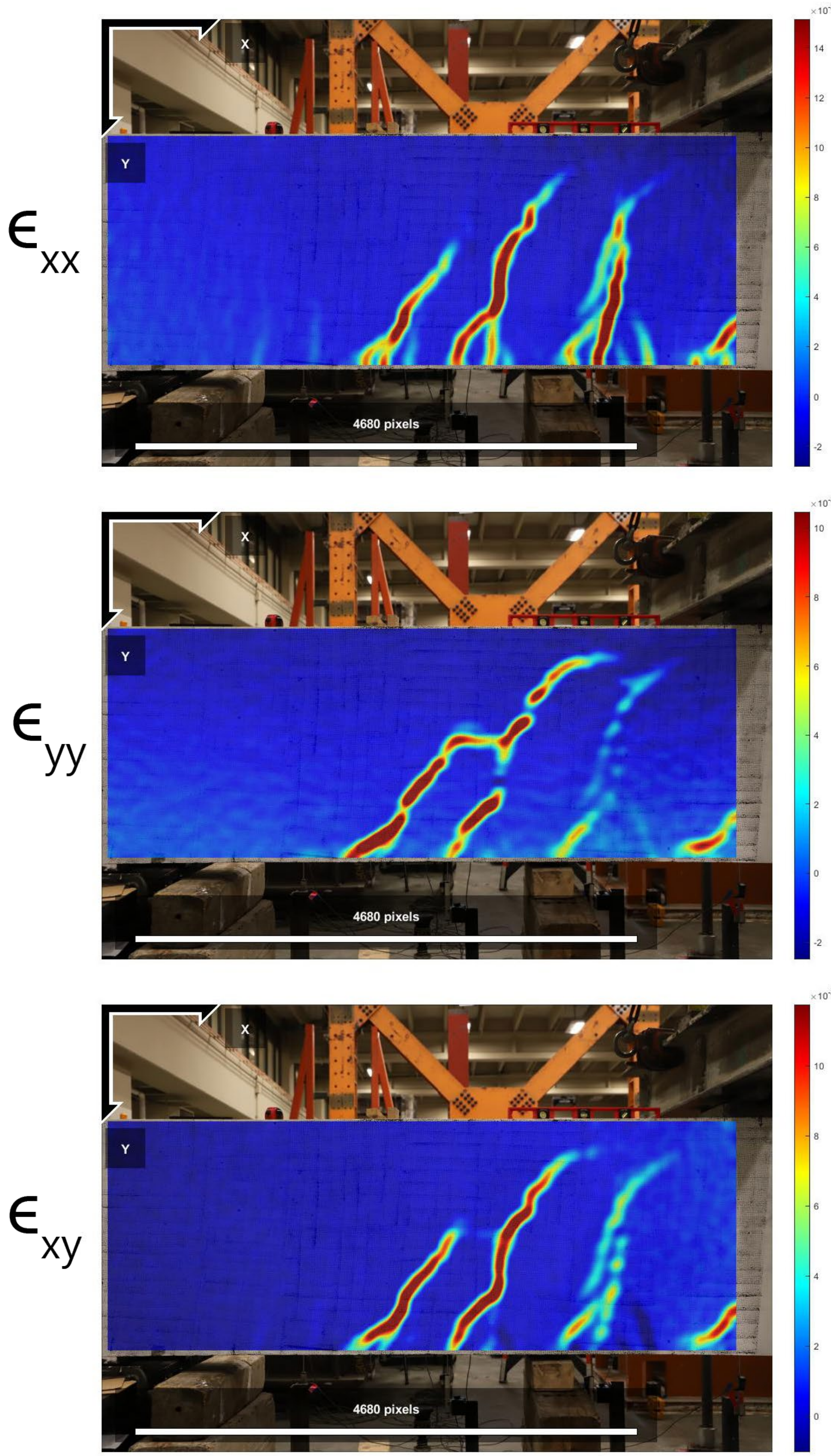

Figure K-99: Companion Beam 3 DIC Pattern 8

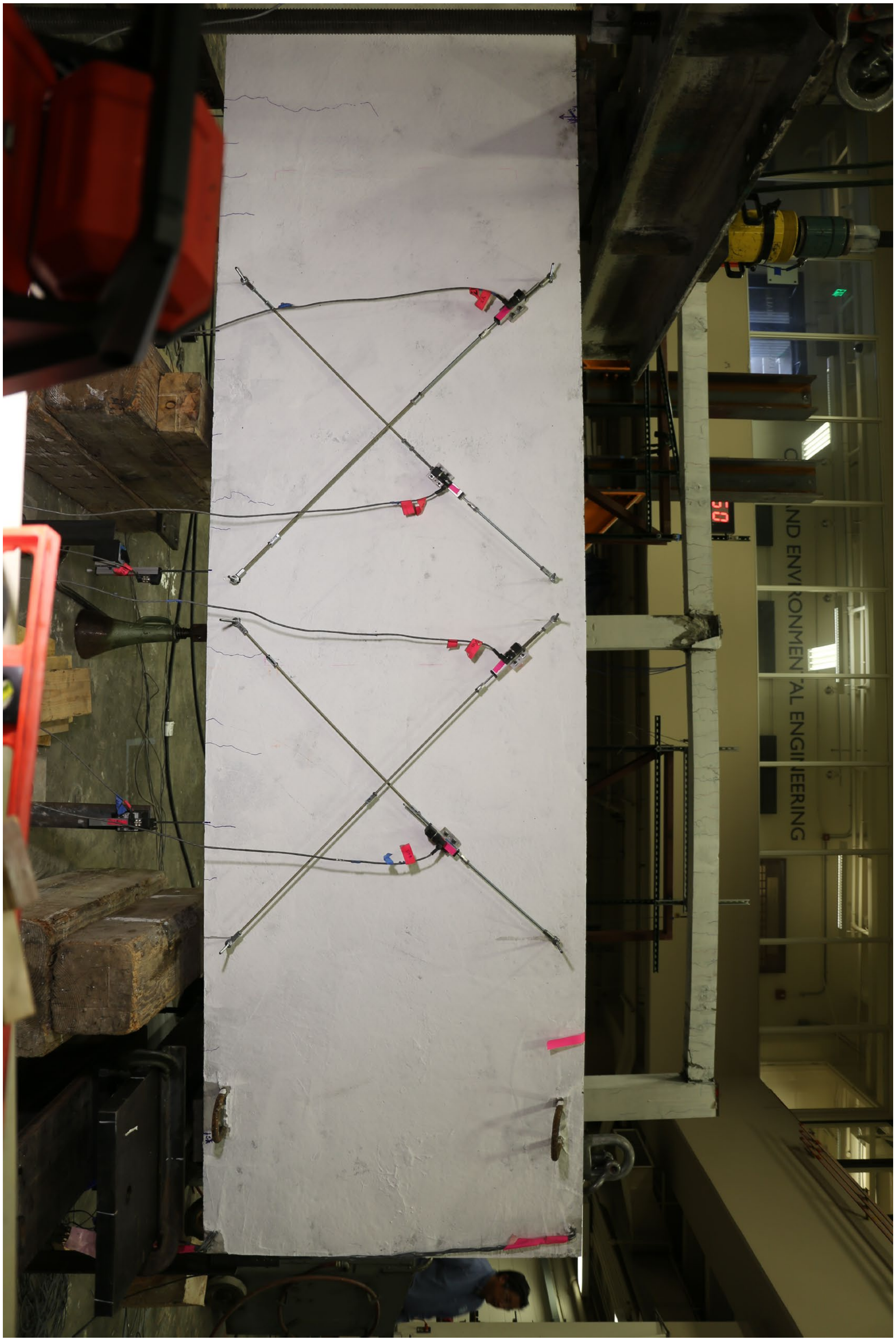

Figure K-100: Companion Beam 3 Load Stage 1

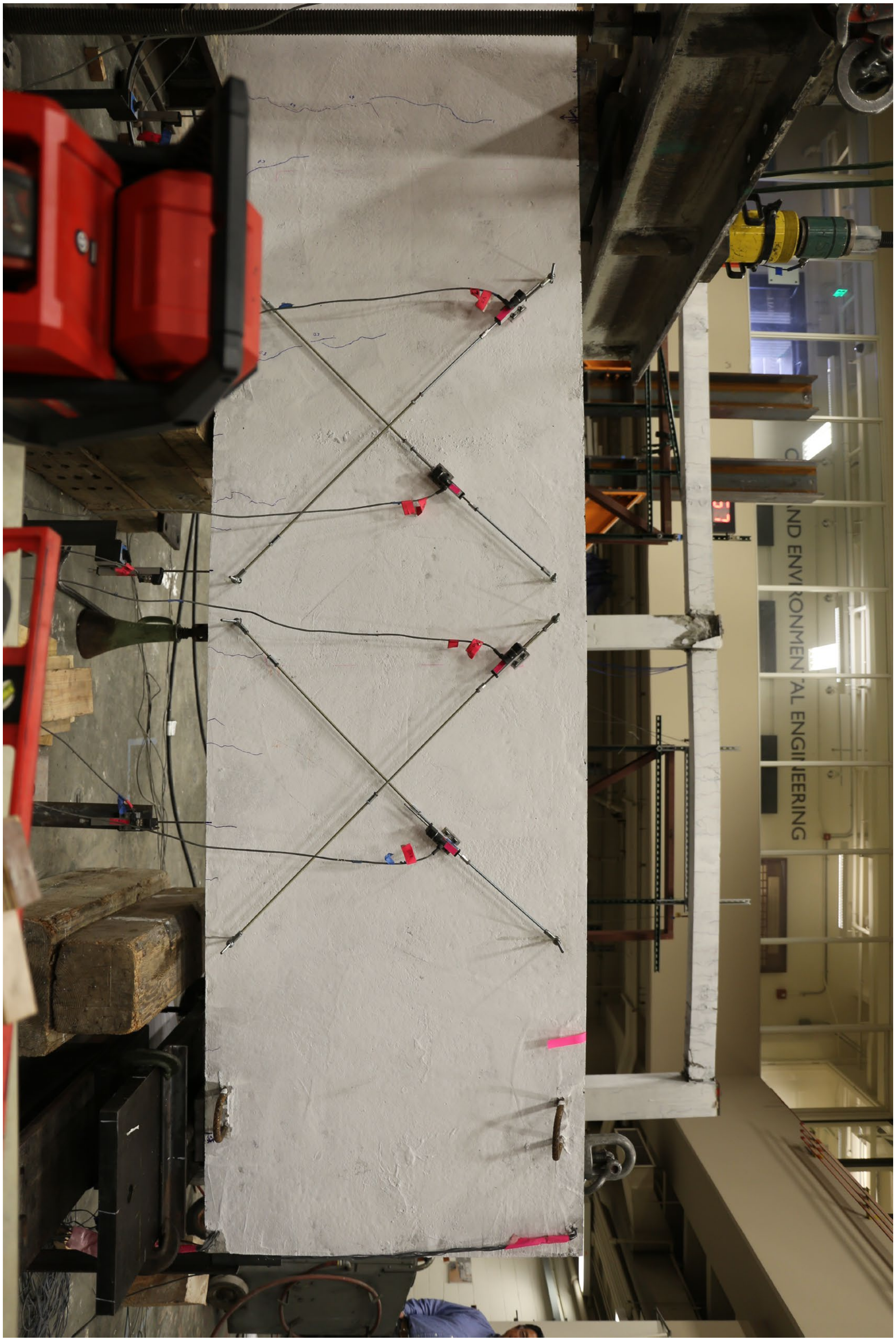

Figure K-101: Companion Beam 3, Load Stage 2

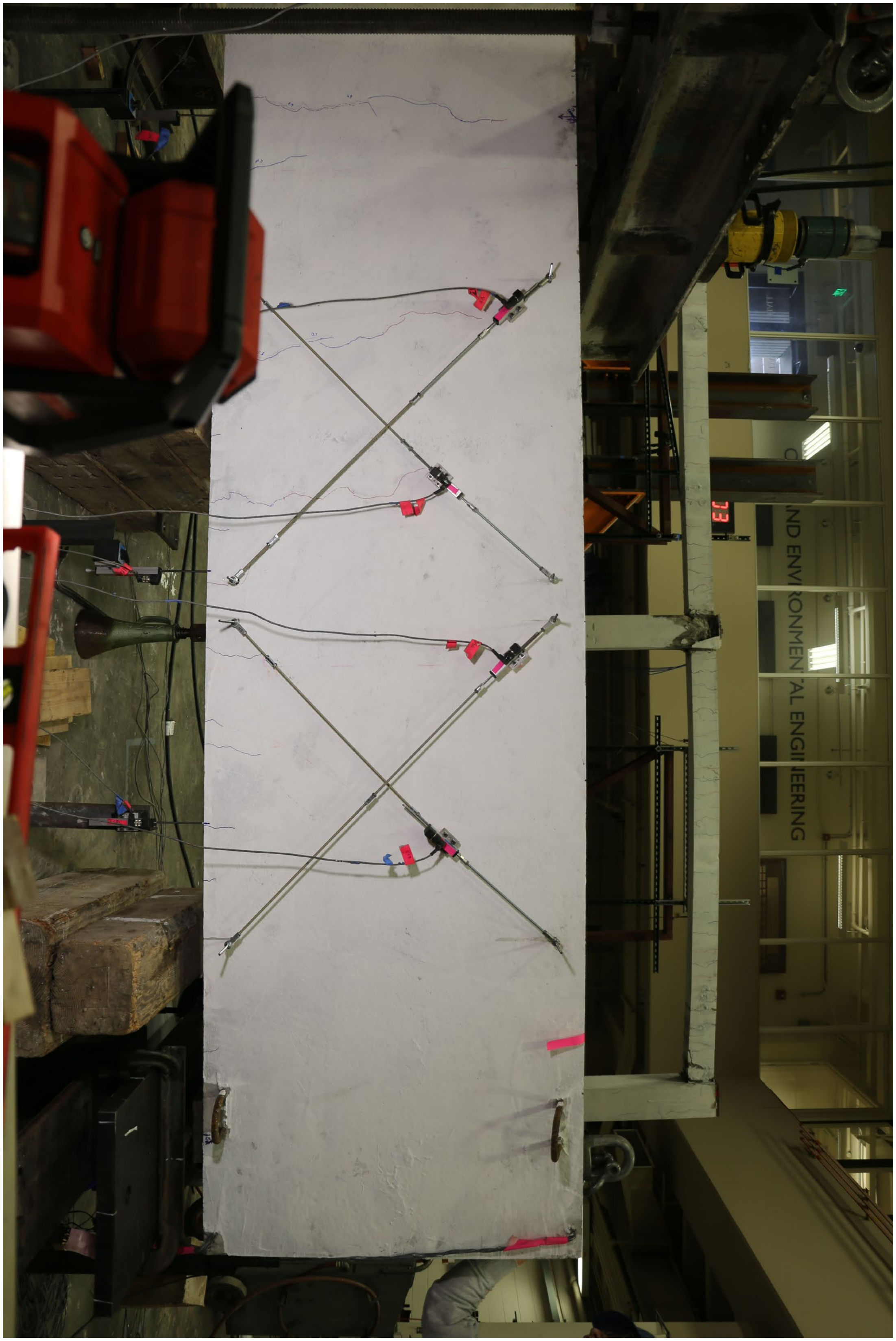

Figure K-102: Companion Beam 3 Load Stage 3

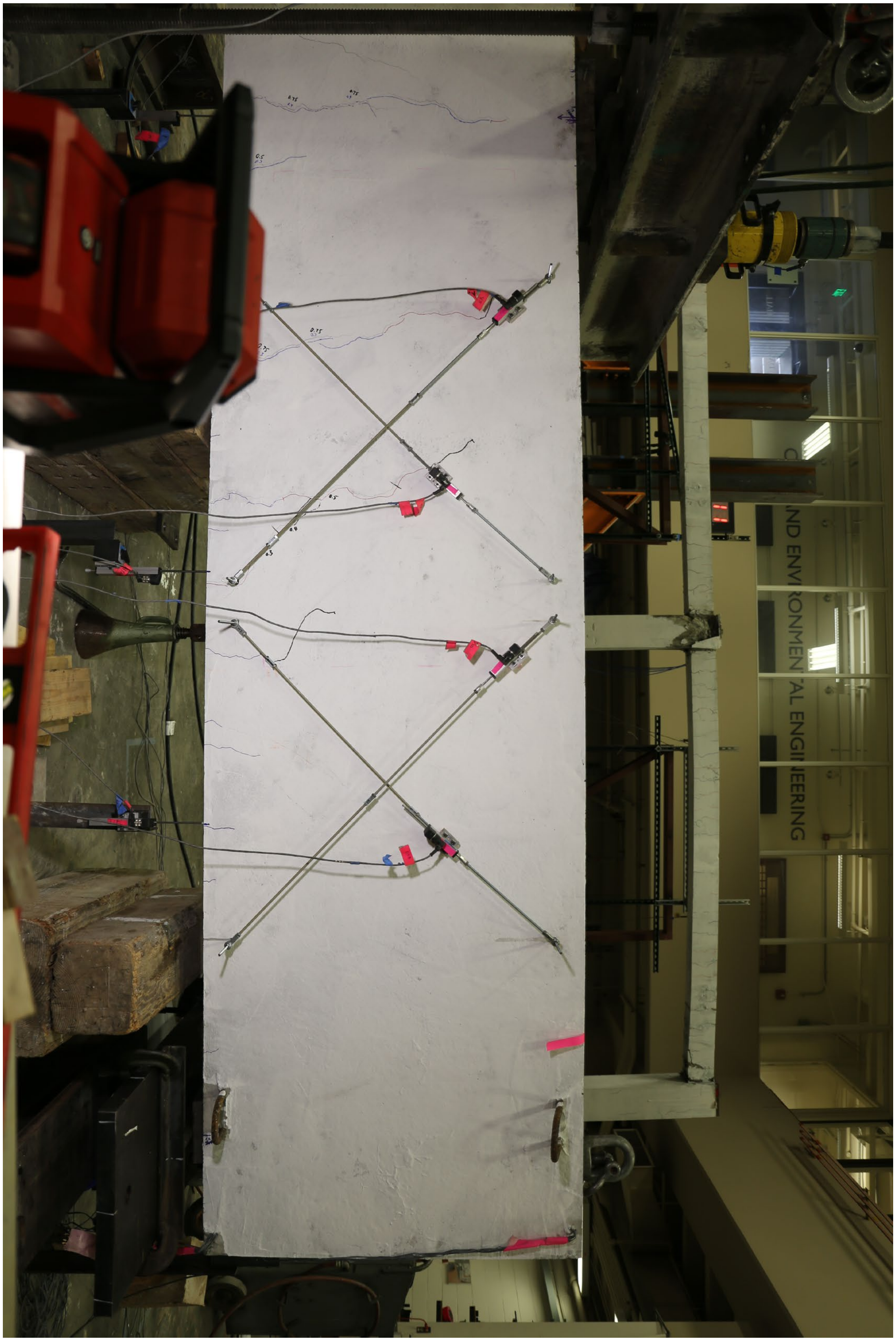

Figure K-103: Companion Beam 3 Load Stage 4

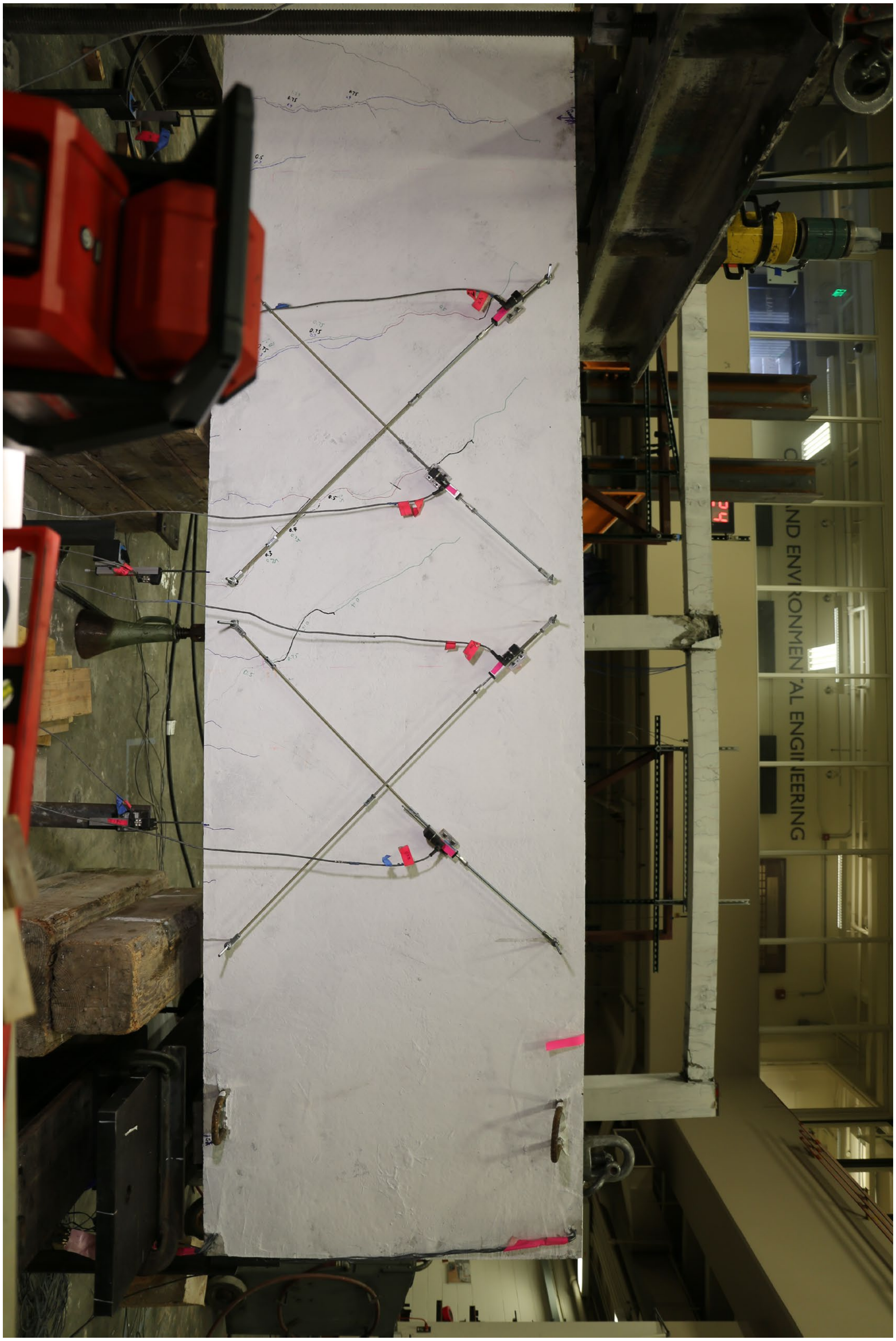

Figure K-104: Companion Beam 3 Load Stage 5

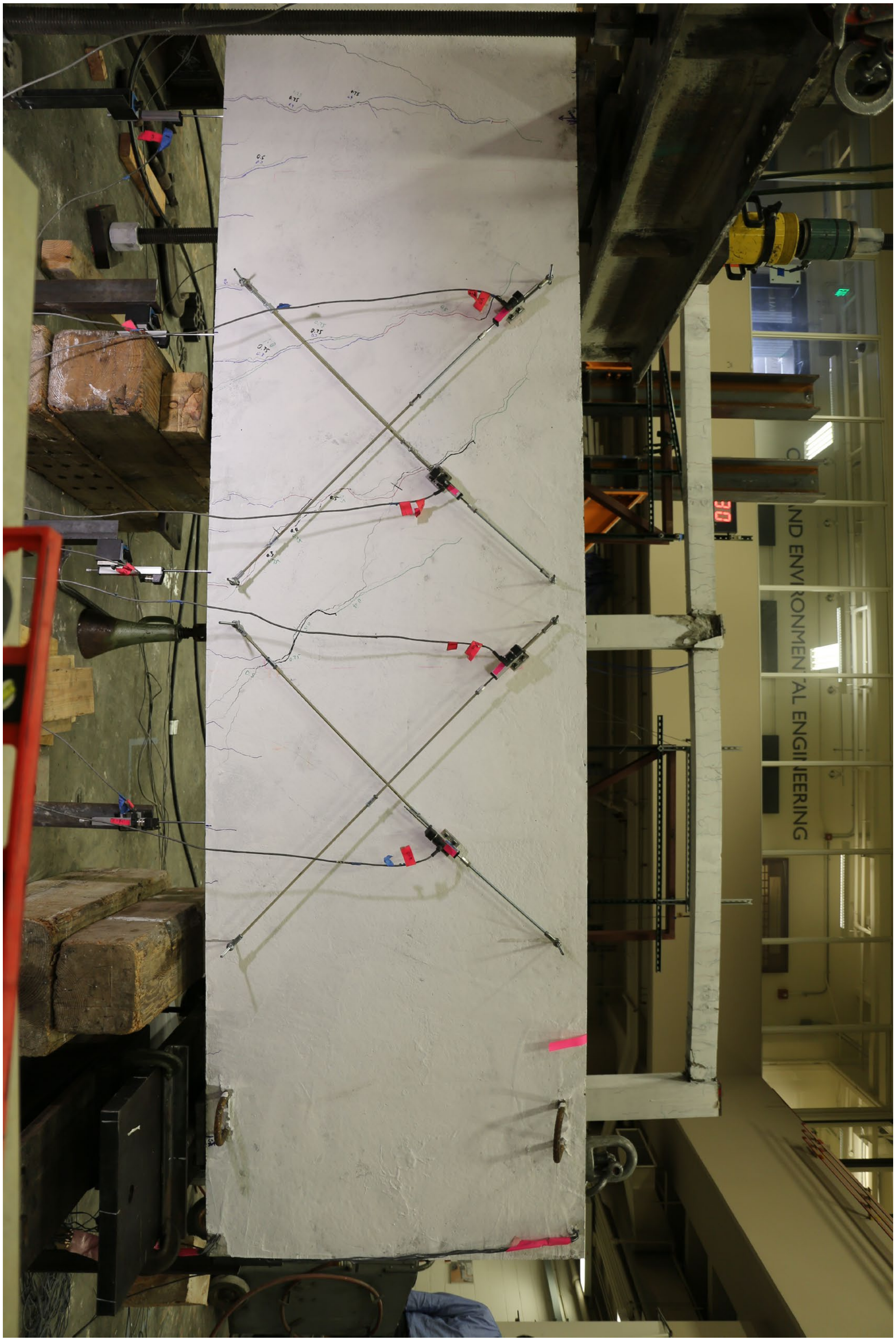

Figure K-105: Companion Beam 3 Load Stage 6

Figure K-106: Companion Beam 3 Failure